NATIONAL AERONAUTICS AND SPACE ADMINISTRATION

Space Programs Summary 37-62, Vol. II

The Deep Space Network

For the Period January 1 to February 28, 1970

JET PROPULSION LABORATORY
CALIFORNIA INSTITUTE OF TECHNOLOGY
PASADENA, CALIFORNIA

March 31, 1970

NATIONAL AERONAUTICS AND SPACE ADMINISTRATION

Space Programs Summary 37-62, Vol. II

The Deep Space Network

For the Period January 1 to February 28, 1970

JET PROPULSION LABORATORY

CALIFORNIA INSTITUTE OF TECHNOLOGY

PASADENA, CALIFORNIA

March 31, 1970

SPACE PROGRAMS SUMMARY 37-62, VOL. II

Preface

The Space Programs Summary is a multivolume, bimonthly publication that presents a review of technical information resulting from current engineering and scientific work performed, or managed, by the Jet Propulsion Laboratory for the National Aeronautics and Space Administration. The Space Programs Summary is currently composed of four volumes:

Vol. I. *Flight Projects* (Unclassified)

Vol. II. *The Deep Space Network* (Unclassified)

Vol. III. *Supporting Research and Advanced Development* (Unclassified)

Vol. IV. *Flight Projects and Supporting Research and Advanced Development* (Confidential)

Foreword

Volume II of the Space Programs Summary reports the results of work performed by the Deep Space Network (DSN). Information is presented, as appropriate, in the following categories:

Introduction
  Description of the DSN
  Description of DSN Systems

Mission Support
  Interplanetary Flight Projects
  Planetary Flight Projects
  Manned Space Flight Project
  Advanced Flight Projects

Advanced Engineering
  Tracking and Navigational Accuracy Analysis
  Communications Systems Research
  Communications Elements Research
  Supporting Research and Technology

Development and Implementation
  Space Flight Operations Facility Development
  Ground Communications Facility Development
  Deep Space Instrumentation Facility Development
  DSN Project and System Development

Operations and Facilities
  DSN Operations
  Space Flight Operations Facility Operations
  Ground Communications Facility Operations
  Deep Space Instrumentation Facility Operations
  Facility Engineering

In each issue, the section entitled "Description of DSN Systems" reports the current configuration of one of the six DSN systems (tracking, telemetry, command, monitoring, simulation, and operations control). The fundamental research carried out in support of the DSN is reported in Vol. III.

Contents

Contents (contd)

Contents (contd)

I. Introduction

A. Description of the DSN

The Deep Space Network (DSN), established by the NASA Office of Tracking and Data Acquisition under the system management and technical direction of JPL, is designed for two-way communications with unmanned spacecraft traveling approximately 10,000 mi from earth to planetary distances. It supports, or has supported, the following NASA deep space exploration projects: *Ranger*, *Surveyor*, *Mariner* Venus 1962, *Mariner* Mars 1964, *Mariner* Venus 67, *Mariner* Mars 1969, *Mariner* Mars 1971 (JPL); *Lunar Orbiter* and *Viking* (Langley Research Center); *Pioneer* (Ames Research Center); *Helios* (West Germany); and *Apollo* (Manned Spacecraft Center), to supplement the Manned Space Flight Network (MSFN).

The DSN is distinct from other NASA networks such as the MSFN, which has primary responsibility for tracking the manned spacecraft of the *Apollo* Project, and the Space Tracking and Data Acquisition Network (STADAN), which tracks earth-orbiting scientific and communications satellites. With no future unmanned lunar spacecraft presently planned, the primary objective of the DSN is to continue its support of planetary and interplanetary flight projects.

To support flight projects, the DSN simultaneously performs advanced engineering on components and systems, integrates proven equipment and methods into the network,[1] and provides direct support of each project through that project's Tracking and Data System. This management element and the project's Mission Operations personnel are responsible for the design and operation of the data, software, and operations systems required for the conduct of flight operations. The organization and procedures necessary to carry out these activities are described in SPS 37-50, Vol. II, pp. 15–17.

By tracking the spacecraft, the DSN is involved in the following data types:

(1) *Metric:* generate angles, one- and two-way doppler, and range.

(2) *Telemetry:* receive, record, and retransmit engineering and scientific data.

---

[1] When a new piece of equipment or new method has been accepted for integration into the network, it is classed as Goldstone duplicate standard (GSDS), thus standardizing the design and operation of identical items throughout the network.

(3) *Command:* send coded signals to the spacecraft to activate equipment to initiate spacecraft functions.

The DSN operation is characterized by six DSN systems: (1) tracking, (2) telemetry, (3) command, (4) monitoring, (5) simulation, and (6) operations control.

The DSN can be characterized as being comprised of three facilities: the Deep Space Instrumentation Facility (DSIF), the Ground Communications Facility (GCF), and the Space Flight Operations Facility (SFOF).

1. Deep Space Instrumentation Facility

a. Tracking and data acquisition facilities. A worldwide set of deep space stations (DSSs) with large antennas, low-noise phase-lock receiving systems, and high-power transmitters provide radio communications with spacecraft. The DSSs and the deep space communications complexes (DSCCs) they comprise are given in Table 1.

Radio contact with a spacecraft usually begins when the spacecraft is on the launch vehicle at Cape Kennedy, and it is maintained throughout the mission. The early part of the trajectory is covered by selected network stations of the Air Force Eastern Test Range (AFETR) and the MSFN of the Goddard Space Flight Center.[2] Nor-

---

[2]The 30-ft-diam-antenna station established by the DSN on Ascension Island during 1965 to act in conjunction with the MSFN orbital support 30-ft-diam-antenna station was transferred to the MSFN in July 1968.

mally, two-way communications are established between the spacecraft and the DSN within 30 min after the spacecraft has been injected into lunar, planetary, or interplanetary flight. A compatibility test station at Cape Kennedy (discussed later) monitors the spacecraft continuously during the launch phase until it passes over the local horizon. The deep space phase begins with acquisition by either DSS 51, 41, or 42. These and the remaining DSSs given in Table 1 provide radio communications to the end of the flight.

To enable continuous radio contact with spacecraft, the DSSs are located approximately 120 deg apart in longitude; thus, a spacecraft in deep space flight is always within the field-of-view of at least one DSS, and for several hours each day may be seen by two DSSs. Furthermore, since most spacecraft on deep space missions travel within 30 deg of the equatorial plane, the DSSs are located within latitudes of 45 deg north or south of the equator. All DSSs operate at S-band frequencies: 2110–2120 MHz for earth-to-spacecraft transmission and 2290–2300 MHz for spacecraft-to-earth transmission.

To provide sufficient tracking capability to enable useful data returns from around the planets and from the edge of the solar system, a 210-ft-diam-antenna network will be required. Two additional 210-ft-diam-antenna DSSs are under construction at Madrid and Canberra, which will operate in conjunction with DSS 14 to provide this capability. These stations are scheduled to be operational by early 1973.

Table 1. Tracking and data acquisition stations of the DSN

DSCC	Location	DSS	DSS serial designation	Antenna		Year of initial operation
				Diameter, ft	Type of mounting	
Goldstone	California	Pioneer	11	85	Polar	1958
		Echo[a]	12	85	Polar	1962
		(Venus)[b]	13	(85)	(Az–El)	(1962)
		Mars	14	210	Az–El	1966
Canberra	Australia	Woomera[c]	41	85	Polar	1960
		Tidbinbilla[c]	42	85	Polar	1965
—	South Africa	Johannesburg[c]	51	85	Polar	1961[d]
Madrid	Spain	Robledo[c]	61	85	Polar	1965
		Cebreros[c]	62	85	Polar	1967

[a]Established in 1959 to support NASA's *Echo* Project to explore the feasibility of transcontinental two-way communications using a passive satellite; DSS 12 was originally configured with an 85-ft-diam az–el-mounted antenna. In 1962, when the need arose for a second 85-ft-diam polar-mounted antenna at the Goldstone site, the 85-ft-diam az–el-mounted antenna was moved to DSS 13, and an 85-ft-diam polar-mounted antenna was constructed at DSS 12.

[b]A research-and-development facility used to demonstrate the feasibility of new equipment and methods to be integrated into the operational network. Besides the 85-ft-diam az–el-mounted antenna, DSS 13 has a 30-ft-diam az–el-mounted antenna that is used for testing the design and operation of the feed system for the DSS 14 210-ft-diam antenna.

[c]Normally staffed and operated by government agencies of the respective countries (except for a temporary staff of the Madrid DSCC), with some assistance of U.S. support personnel.

[d]Between 1958 and 1962, a temporary mobile tracking station was located near Johannesburg to provide L-band communications required by the *Ranger* and *Mariner* Venus 1962 spacecraft.

b. Compatibility test facilities. In 1959, a mobile L-band compatibility test station was established at Cape Kennedy to verify flight-spacecraft DSN compatibility prior to the launch of the *Ranger* and *Mariner* Venus 1962 spacecraft. Experience revealed the need for a permanent facility at Cape Kennedy for this function. An S-band compatibility test station with a 4-ft-diam antenna became operational in 1965. In addition to supporting the preflight compatibility tests, this station monitors the spacecraft continuously during the launch phase until it passes over the local horizon.

Spacecraft telecommunications compatibility in the design and prototype development phases was formerly verified by tests at the Goldstone DSCC. To provide a more economical means for conducting such work and because of the increasing use of multiple-mission telemetry and command equipment by the DSN, a compatibility test area (CTA) was established at JPL in 1968. In all essential characteristics, the configuration of this facility is identical to that of the 85- and 210-ft-diam-antenna stations.

The JPL CTA is used during spacecraft system tests to establish the compatibility with the DSN of the proof test model and development models of spacecraft, and the Cape Kennedy compatibility test station is used for final flight spacecraft compatibility validation testing prior to launch.

2. Ground Communications Facility

The GCF, using, in part, facilities of the worldwide NASA Communications Network (NASCOM),[3] provides voice, high-speed data, and teletype communications between the SFOF and all DSSs, except those of the Goldstone DSCC. Communications between the Goldstone DSCC and the SFOF are provided by a microwave link leased from a common carrier. Early missions were supported with voice and teletype circuits only, but increased data rates necessitated the use of wide-band circuits from all DSSs.

3. Space Flight Operations Facility

Network and mission control functions are performed by the SFOF at JPL. (Prior to 1964, these functions were performed in temporary facilities at JPL.) The SFOF receives data from all DSSs and processes that information required by the flight project to conduct mission operations. The following services are provided: (1) real-

---

[3]Managed and directed by the Goddard Space Flight Center.

time processing and display of metric data; (2) real-time and non-real-time processing and display of telemetry data; (3) simulation of flight operations; (4) near-real-time evaluation of DSN performance; (5) operations control, and status and operational data display; and (6) general support such as internal communications by telephone, intercom, public address, closed-circuit TV, documentation, and reproduction of data packages. Master data records of science data received from spacecraft are generated. Technical areas are provided for flight project personnel who analyze spacecraft performance, trajectories, and generation of commands.

The SFOF is equipped to support many spacecraft in flight and those under test in preparation for flight. Over a 24-h period in 1967, as many as eight in-flight spacecraft or operational-readiness tests for flight were supported by the SFOF.

B. Description of DSN Systems

1. Multiple-Mission Command and Telemetry Systems High-Speed and Wideband Data Formats, W. J. Kinder

a. Introduction. In converging towards a fully centralized control of the DSN Multiple-Mission Command and Multiple-Mission Telemetry Systems, transmission formats defining the principal SFOF/DSS interface have been completed for the support of the 1971-era mission set. From the Mission Support and DSN areas within the SFOF, messages are initialized, formatted for transmission by the SFOF, and reacted upon by the designated DSS. Responses are likewise formatted by the DSS for processing and display by the SFOF. The Multiple-Mission Command System exhibits almost total automatic control from the SFOF, while the Multiple-Mission Telemetry System still retains manual participation by the DSSs. This article describes the established message types.

b. Command message. The command message will contain the command data along with DSIF Telemetry and Command Subsystem processing instructions, time of execution and accountability information. This command message originates in the SFOF Mission Support area and will be displayed in the SFOF Mission Support and Command Operations Analysis Group areas.

c. Command verification message. This message will be a repetition of the command data except for a reversal of the source and destination codes. This message is sent

automatically upon receipt of a command message by the DSIF Telemetry and Command Subsystem and will be displayed in the SFOF Mission Support and Command Operations Analysis Group areas.

d. Command instruction translate table input message. This message will contain the actual command data to be preloaded into the DSIF Telemetry and Command Subsystem along with processing and accountability information. The DSIF Telemetry and Command Subsystem will automatically return a repetition of this message to the SFOF, except for reversal of source and destination codes. This instruction originates in the SFOF Mission Support area and will be displayed in the SFOF Mission Support and Command Operations Analysis Group areas.

e. Command instruction configuration table input message. This message will contain information to automatically configure the DSIF Telemetry and Command Subsystem for a particular mission. The DSIF Telemetry and Command Subsystem will return a repetition of this message to the SFOF, except for reversal of source and destination codes. This instruction message will be originated in the Command Operation Analysis Group area and be displayed in the SFOF Mission Support and Command Operatons Analysis Group areas. Explicit in this message are mode instructions, frequency shift (if applicable), modulation abort limits, and command symbol rate.

f. Command instruction standards and limits message. This message will be sent from the SFOF to the DSIF and contain both DSN and project-supplied standards, with attendant limits, to enable the DSIF Telemetry and Command Subsystem to automatically monitor its operation. The DSIF Telemetry and Command Subsystem will return a repetition of this message to the SFOF, except for reversal of source and destination codes. This message will be originated in the Command Operation Analysis area and be displayed in the SFOF Mission Support and Command Operations Analysis Group areas. Such standards as maximum time of execution, frequency shift limits, symbol rates, exciter frequency, and spacecraft numbers are contained in this format.

g. Command enable/disable message. This message will be sent to the DSIF from the SFOF and list processing instructions for the DSIF Telemetry and Command Subsystem's storage of commands. The DSIF Telemetry and Command Subsystem will return a repetition of this message to the SFOF, except for reversal of source and

destination codes. This message will originate in the SFOF Mission Support area and be displayed in the SFOF Mission Support and Command Operations Analysis Group areas.

h. Command confirm/abort message. This message contains confirmation on the results of processing commands by the DSIF Telemetry and Command Subsystem. This message originates automatically at the DSS and is displayed in the SFOF Mission Support and Operations Analysis Group areas. It contains command accountability and time of first bit transmission or abort reason code.

i. Command recall request message. This message interrogates the DSIF Telemetry and Command Subsystem for current status as to configuration, standards and limits, command and translate table stacks, and system checks. It originates in the SFOF Mission Support area and is displayed in the SFOF Mission Support and Command Operations Analysis Group areas.

j. Command recall response message. This message is the answer to the recall request message. It originates in the DSIF Telemetry and Command Subsystem and is displayed in the SFOF Mission Support and Command Operations Analysis Group areas.

k. Command alarm message. This message contains system alarms and is originated automatically by the DSIF Telemetry and Command Subsystem. It is displayed in the SFOF Mission Support and Command Operations Analysis areas.

l. Telemetry configuration messages. These messages, containing telemetry system standards/limits, are composed in the SFOF by the Telemetry Operations Analysis Group and transmitted via high-speed data service before a DSS track. These messages are to be displayed on the line printer at the DSS.

m. Telemetry high-speed–wideband data block messages. The Multiple-Mission Telemetry System high-speed and wideband data messages originating at the DSS and transmitted to the SFOF contain the following DSN and spacecraft data for a specific high-speed–wideband data block:

(1) DSS receiver and demodulator lock status.

(2) DSS block decoder, symbol synchronizer, and bit sync loop lock status.

(3) DSS ground receiver automatic gain control and signal-to-noise ratio samples.

(4) Time tags for telemetry data in ms.

(5) Spacecraft engineering or science telemetry data bits.

(6) DSS configuration and partial status bits.

The formats for the high-speed and wideband data services are identical; the amount of spacecraft data is in keeping with project data response requirements.

n. Concluding remarks. Operations at the DSSs in response to multimission command and multimission telemetry requests will be essentially automated for the 1971-era mission set. Complete configuration control by the respective DSN operations analysis groups will characterize the multimission concept. However, the project/SFOF interface for command activity and display interaction will be preserved.

2. DSN Tracking System High-Speed Data Formats,
R. E. Holzman

a. Introduction. A design goal of the DSN Tracking System is to provide for centralized control of the system from the SFOF. The first step in the design has been accomplished, i.e., that of definition of the formats of the transmission messages between the SFOF Central Processing System (CPS) and the DSIF Tracking Subsystems (DTS) to be installed at the 210-ft diam antenna DSSs for the 1973–1975 mission era. A new concept in control, that of "stimulus/reaction," is used to enable automatic processing of interrupt messages without excessive overhead in either the CPS or the DTS. This concept is implemented as follows: Before a control or data transmission can be initiated from either the CPS or the DTS, a "stimulus" message must be transmitted to the receiving site. Only after a "reaction" message is returned, signifying readiness to receive, can the message be initiated. The remainder of this article describes the seven established tracking message types.

b. Data transmission messages. Seven formats have been defined to transmit system data from the DTS to the CPS; each format corresponds to a specific data sample rate. These data include partial status data and auxiliary information as well as tracking data.

c. Predict messages. Predicts are sent from the CPS to the DTS as variably time-tagged data points; these points are interpolated in the DTS to the 1/s interval required for the antenna pointing function. The predicts are sent in two distinct formats: One contains three time-related predicted points per block, while the other (the predict control block) contains the frequency and control information necessary to use a set of blocks (predict set). As many blocks as required are generated of each format. Fifteen types of special events can be listed in the predict control blocks, i.e., DSS rise, set, enter occultation, exit occultation, maximum elevation, etc.

d. General control messages. Formats for these control messages are the same regardless of origin (DTS or CPS). These formats are described in the remainder of this paragraph.

Stimulus and reaction. These messages are used to determine ability or willingness to communicate. A full block of repeated code (to be determined) is sent (stimulus) and immediately returned (reaction) if the receiving subsystem is able to receive a message.

Retransmission request. This message is transmitted whenever the GCF error status code indicates an error in the block or if a block serial number has been skipped. Either the block in error or the skipped block serial number is requested for retransmission.

Data unrecognizable. This message is sent if internal system checks (rather than the GCF) indicate that the block contains an error.

Operator alert. This message is transmitted from one facility to the other for direction printout to the operator at the distant end. Up to 64 characters can be displayed.

Boresight coefficients. Two formats are used: The CPS sends antenna boresight coefficients (as polynomial coefficients) to the DTS or the DTS can generate its own corrections, which are then transmitted to the CPS for validation.

e. DTS Alarms. This format is used to transmit DTS alarms, which normally are included in the Monitor System alarm message from a DSS to the CPS; it is designed to serve as a backup to the Monitor System, but is sent regardless of Monitor System status.

f. Standards and limits, predict set instructions, and data format instructions. The use of these formats is self-explanatory.

II. Mission Support

A. Planetary Flight Projects

1. Mariner Mars 1969 Extended Operations Mission Support, K. W. Linnes

The *Mariner* Mars 1969 Extended Operations Mission was formally established as a project in January 1970 as a follow-on to the main *Mariner* Mars 1969 Mission. Formal statement of the project requirements for tracking and data system (TDS) support was received in the form of a Support Instrumentation Requirements Document (SIRD), and a NASA support plan was prepared in response. In addition, a DSN operations plan was prepared, detailing the characteristics of the support capabilities committed by the NASA Support Plan. Key features of the support plan provide for tracking coverage from DSSs 62, 12, and 14. The support that has been provided since the end of the main mission on November 1, 1969 will continue on a formal basis.

DSS 62 was used to conserve tracking time of the 210-ft antenna at DSS 14 by commanding the spacecraft to the desired operational mode just prior to the Goldstone DSCC view period. The roundtrip time of the radio signal was in the order of 40 min, and tracking time utilizing the sequential acquisition ranging system at DSS 14 was maximized.

By the end of February, *Mariners VI* and *VII* were about 385,000,000 and 372,000,000 km from the earth, respectively. Since launch, 2229 commands have been sent to *Mariner VI*, and 1575 to *Mariner VII*. Both spacecraft were sending engineering telemetry at 8⅓ bits/s. However, the telemetry was received at DSS 14 only until January 25, 1970, when that station was taken out of service for installation of the tri-cone feed structure and the 400-kW transmitter. At DSS 62, telemetry was below threshold, as was the carrier shortly before that date. Even though the carrier was below threshold, DSS 62 was able to send commands to the spacecraft as necessary to prepare it for the tracking pass over DSS 14; this activity was feasible due to an adequate performance margin in the uplink and the availability of accurate predicts.

Since January 25, tracking has been feasible only at DSS 12 through use of a specially prepared, low-noise feed cone on the 85-ft antenna. The cone temperature

in the diplex mode is about 24°Kelvin and 17°Kelvin in the listen-only mode. Using a 3-Hz loop bandwidth in the listen-only mode, the spacecraft signal was received satisfactorily at −174 dBmW, i.e., usable two-way doppler data was obtained. In the diplex mode, the receivers were in lock only about one data point out of three. Periods of two-way doppler data were, therefore, obtained by turning on the ground transmitter for about 40 min, or one round-trip light time, and then turning it off a few moments before the signal arrived back from the spacecraft. Usable two-way doppler data was obtained for the length of time the transmitter was on. This process was repeated in a checkerboard pattern, providing about six periods of good data per tracking pass. Although telemetry data was only about 0.5 dB above threshold, the subcarrier demodulator assemblies were able to be locked up; the data was quite noisy, producing about one error in ten. Nevertheless, some insight into the spacecraft condition was maintained through analysis of this data. This mode of tracking will continue until the return of DSS 14 to service about March 1, 1970. During this time, no commands will be sent to the spacecraft. Ranging data was not received after January 25, since that equipment is operable only at DSS 14.

Model 8 of the real-time telemetry computer program for the IBM 7044 computer was incorporated into the operating system in the Space Flight Operations Facility. This model introduced no change to the *Mariner* Mars 1969 operations, but permitted simultaneous operation with the *Pioneer* Project in the same computer string. The previous model, Model 7, permitted simultaneous operation of only the two *Mariners*.

2. Mariner Mars 1971 Mission Support,
R. P. Laeser and E. C. Gatz

a. Introduction. In SPS 37-60, Vol. II, pp. 4–6, changed plans for the SFOF data processing configuration were described. This new plan was called configuration C. During this reporting period, plans were again changed, and the result is the Mark III SFOF central processing system which will be a phased development with a preplanned set of capabilities for the *Mariner* Mars 1971 mission.

One of the features of the SFOF central processing system, in conjunction with other DSN elements, is the capability for production of master data records (MDRs). Experiment data records (EDRs) that apply to specific science experiments can be extracted from the MDRs.

b. Definitions. Definitions of the various types of data records follow.

Log. Local record made at any point in the system.

Original data record (ODR). Digital log made at initial point of entry or definition of data in the system, maintained only until permanently recorded elsewhere.

System data. All data that flows within a DSN system, i.e., between the interface with the spacecraft (at the DSS antenna feed) and the interface(s) where the data is transferred to or from the user. The user in this context may be either a flight project, another DSN system, or a scientific project.

System data record (SDR). Log made at the central point of the system (one log for each DSN System). Repository is maintained until an agreed MDR transfer is accomplished.

Master data record. Records obtained, through specialized processing techniques, from the original data records. They contain the original experiment information and supporting information, such as orbital position, spacecraft attitude, and command and housekeeping data. Ground time and, where applicable, spacecraft time will have been correlated with these data. Extraneous and duplicate segments have been removed and the remainder is an organized, identified set of records, usually in digital form and capable of direct entry into a computer.

DSN MDR. Subset of the system data that the DSN provides to the project. The subset definition will be negotiated with the project. (Another log, or ODR, may be transferred as well, if agreeable and negotiated, even though such transfer may affect performance of the system.)

Experiment data record (EDR). Records extracted from the MDR to provide the principal investigator with data associated only with his experiment.

DSN EDR. Same as EDR, except that it contains only those records extracted from the DSN MDR.

c. System records. To accomplish its functions in providing the direct support of a flight project, the DSN has established six DSN systems: (1) tracking, (2) telemetry, (3) command, (4) monitoring, (5) simulation, and (6) operations control. The first four systems provide

the various data records of interest to a flight project. The records made as part of each system are described in the following paragraphs. The operations control system, while not described in detail here, includes the functions of central repository of MDR/ODRs and the transfer of these records to flight projects.

Tracking system records. Principal tracking records are shown schematically in Fig. 1. This diagram is abbreviated to show only those portions of the tracking system that contribute to records. The primary output is the SDR, available in real-time on disk or off-line on tape. This record is also by definition a DSN MDR. The MDR would consist of orbit position data computed by the project from this record. The tracking SDR (DSN MDR) contains at least the negotiated metric data (angles, doppler, and range data) plus data quality indications—such as ground configuration, statistical varia-

tions, and DSN status and performance codes. Also in the SDR are significant event records, station location data, frequencies, and calibration parameters. The SDR may be organized according to spacecraft, and also according to other parameters, and ground transmission errors may be corrected.

Other tracking logs, as indicated in Fig. 1, are available only by recall (replay) from the recording facility. The one exception to this is the set of paper tape records made at the 85-ft DSSs.

Telemetry system records. Telemetry system records are shown schematically in Fig. 2. The ODRs recorded at each station are digital recordings compatible with both DSS and SFOF computers. They contain all received telemetry data, spacecraft and station IDs, time references, and station status and performance parameters.
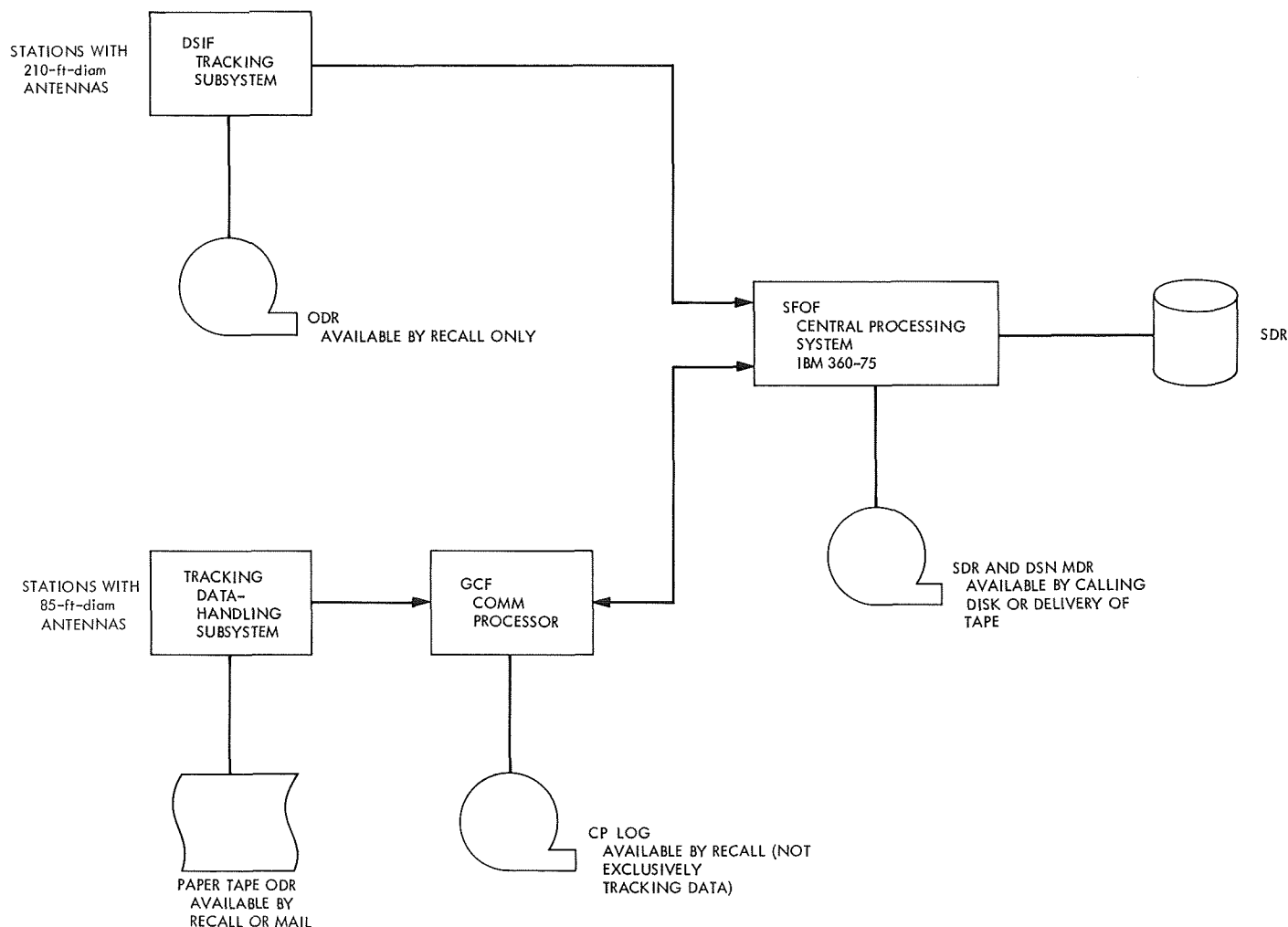
Fig. 1. Tracking system records
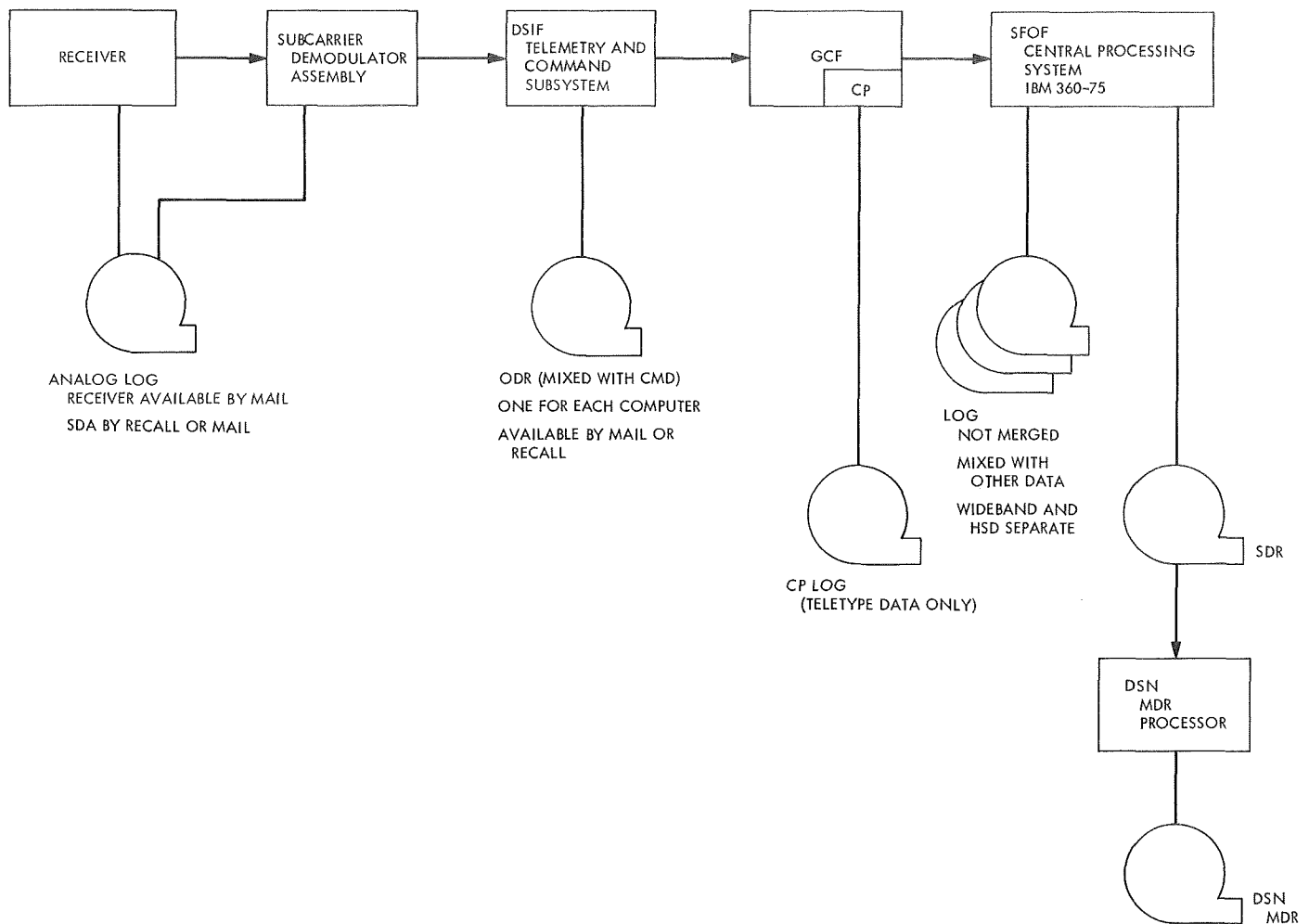
Fig. 2. Telemetry system records

The backup analog tapes contain similar telemetry data, with time tags. The SDA recording is available for playback. The receiver recording is available by mail for non-DSN processing.

The telemetry SDR is a record of all received telemetry data, with data from overlapping stations merged and duplicate data removed. Data from separate telemetry streams (such as engineering and science or data from more than one spacecraft of the same project) may be merged as appropriate. The record is arranged and identified according to spacecraft and data type. It includes DSN status and performance codes and statistical data.

Command system records. Command system records are shown schematically in Fig. 3. Command ODRs are made at both the SFOF and the various tracking sta-

tions, since some of the messages are originated at each. DSS ODRs are available by mail or replay through the station. The command SDR contains at least all transmitted command data with time tags. Included also are control data, DSN status, and verification and confirm/abort data. The SDR is organized according to mission and spacecraft.

As with the telemetry system, a backup analog log can be made at each DSS. However, this log cannot be replayed through the station. Rather it is available, by mail, for project processing.

Monitor system records. Monitor system records are shown schematically in Fig. 4. The ODRs recorded at each DSS are compatible with both DSS and SFOF computers. They contain time-tagged data on station configuration and instrumentation performance. The records
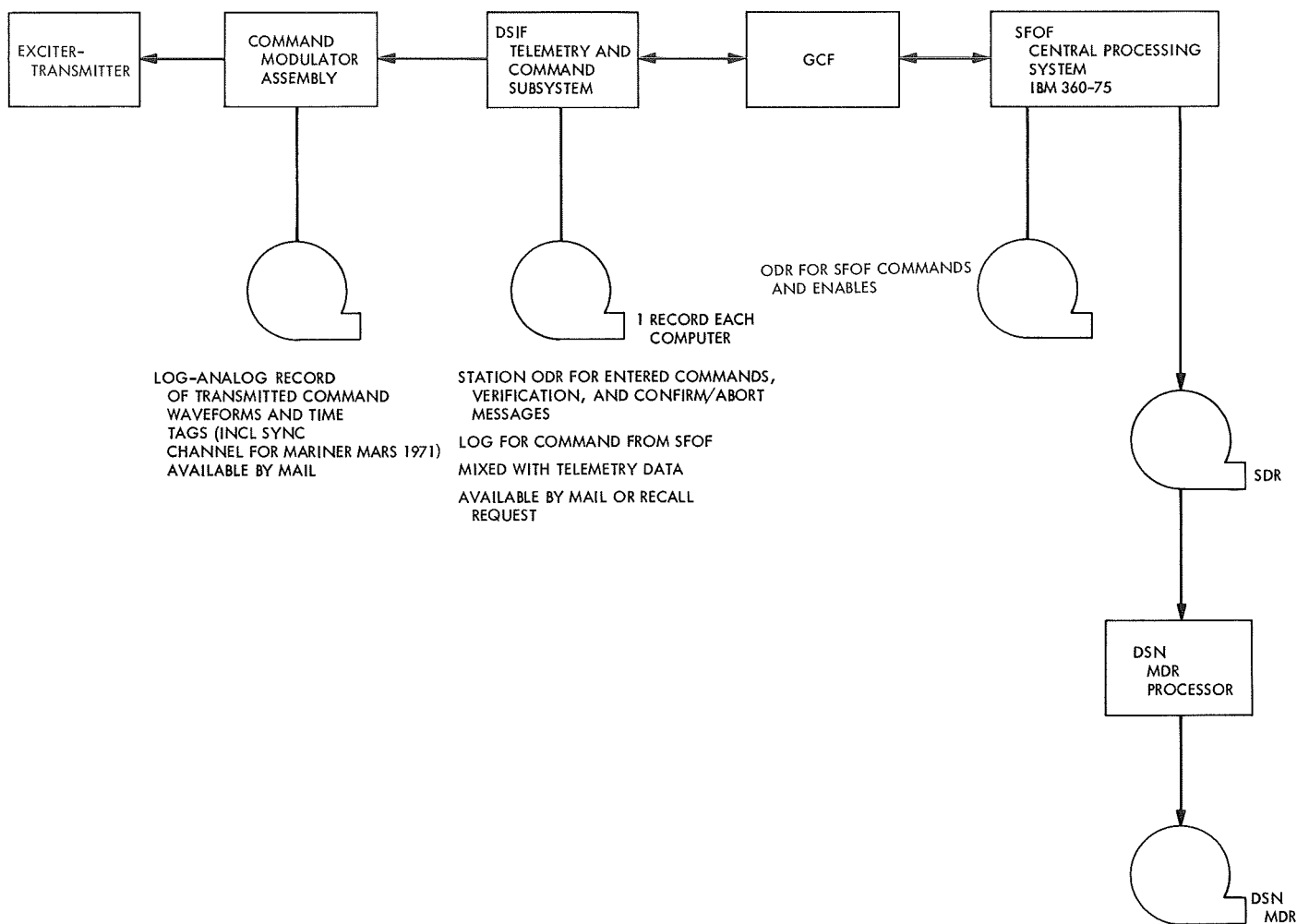
Fig. 3. Command system records

contain information transmitted to the SFOF and facility monitor data of local interest only. These records are available by mail or by replaying from the station.

The ground communications facility (GCF) monitor ODR is processed in the communications processor (CP) in the SFOF. The GCF status data is combined with data from other DSN systems. It contains data on high-speed data (HSD) line performance and CP performance and is available by CP recall.

The SFOF monitor ODR is contained on the DSN status ODR (which is also the DSN monitor SDR). The DSN status ODR contains the DSIF monitor data transmitted from each DSS to the central processing system (CPS) in the SFOF, the GCF monitor data transmitted from the CP to the CPS, and the SFOF monitor data that originates in the SFOF and is processed by the

CPS. It also contains a history of monitor criteria data (MCD) set usage and a history of all monitor alarms. The DSN status MDR is obtained by processing of the SDR.

The DSN status MDR is not normally furnished to the project per se, but an extracted subset of the data on it may be furnished to the project.

d. Guidelines for DSN MDR. The DSN master data record will consist of a set of digital magnetic tapes containing data for each DSN system, plus related statistical and accounting data delivered on microfilm.

The contents of the MDR tapes are negotiable with respect to the following:

(1) Separation of data from several spacecraft or vehicles; for example, orbiters, landers, flybys, probes.

Fig. 4. Monitor system records

ᵃALSO KNOWN AS DSN STATUS ODR

IT ALSO CONTAINS THE SFOF
MONITOR ODR
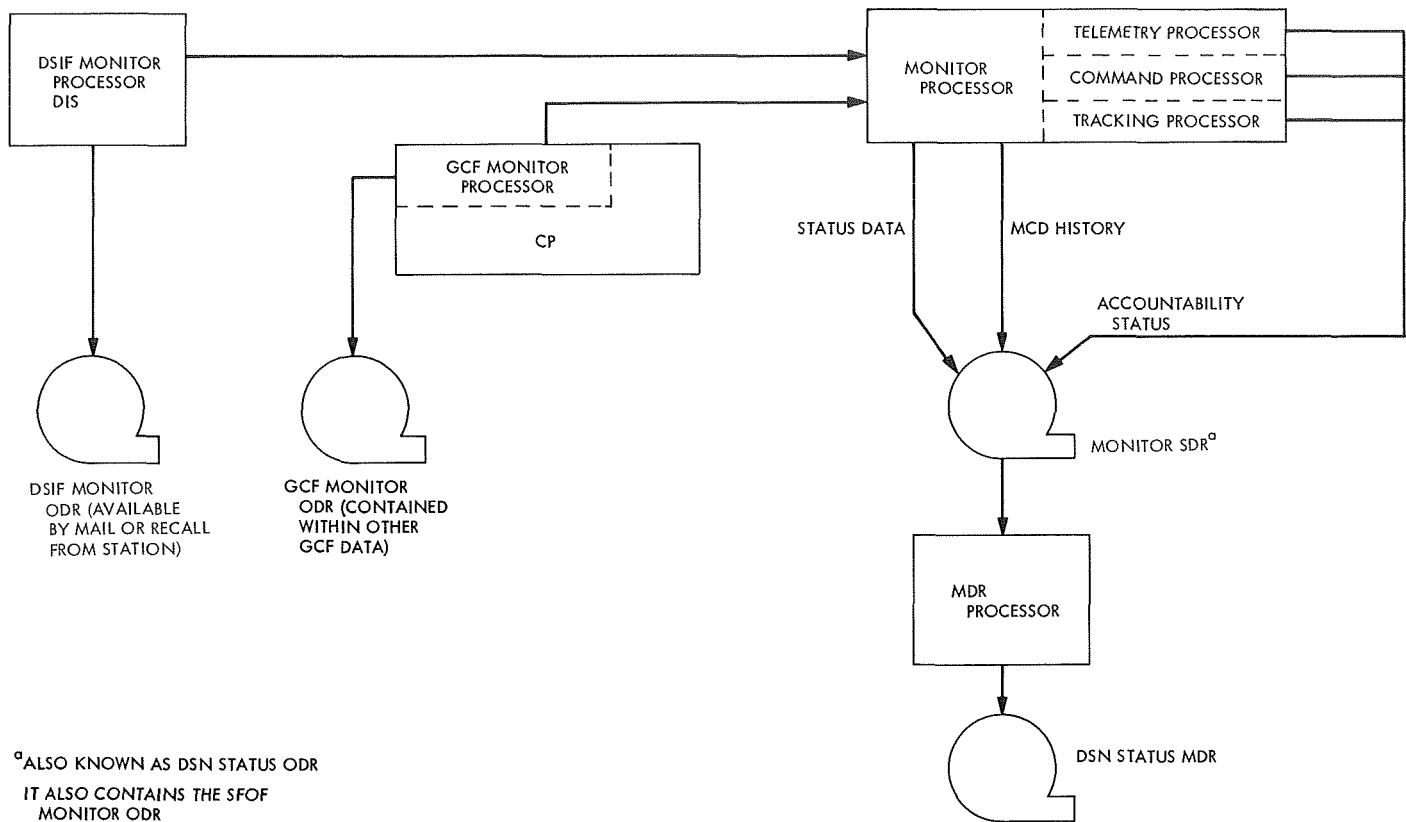
(2) Separation of several subcarriers, for example, engineering, coded science, uncoded science. (Combination of data from different spacecraft or subcarriers, if needed, shall be accomplished on the SDR).

(3) Inclusion of negotiated, ground-derived data; for example, ground receiver AGC, SPE, and SNR, which were included in data transmitted to the SFOF.

(4) Frequency and accuracy of time tagging. Time tagging of data will not exceed that frequency or accuracy negotiated for the real-time transmission of data from the DSS to the SFOF. All data in the DSN MDR will be ordered by time of receipt or generation on the ground.

(5) The quantity of data on the DSN MDR is negotiable within the following constraints:

(a) Quantity will be expressed in terms of percentage of data after initial receiver-in-lock indication.[1]

(b) Maximum size of gaps in the data may be specified.

(c) Percentage and gap size requirements may vary with mission phase. In general, stricter requirements should apply for shorter periods of time. Requirements may be changed to a more strict category at any time prior to data acquisition and up to some negotiated time after data acquisition (nominally 30 days).

(6) The DSN will provide a quality indicator on all data based on DSN-specified partial status.

(7) Quantity of data on each tape, within the limits of efficient tape utilization; for example, a specific number of frames, number of days, number of passes, or full tape.

(8) Sample rate for tracking data.

Telemetry data will be synchronized to the frame level, but not further decommutated. Tracking data will be structured in standard sample formats. Command and status data will be arranged in standard message formats.

---

[1]Receiver-in-lock periods should satisfy negotiated coverage plans as stated in the DSN Operations Plan, Vol. I. Violation of this plan should result in the scheduling of compensating coverage.

All data acquired during below-threshold periods will automatically receive the least stringent class of MDR processing. Threshold definitions are as follows:

(1) Tracking Threshold.[2] The signal level that is defined by the maximum acceptable receiver-loop cycle-slipping as defined by the sum of the negative tolerances in the telecommunications interface design.

(2) Telemetry Threshold.[2] The signal-to-noise ratio that provides the minimum acceptable bit error rate as defined by the sum of the negative tolerances in the telecommunications interface design.

(3) Command. No threshold.

(4) Monitor. No threshold.

Errors introduced in the spacecraft-to-ground telecommunications links, as well as ground errors not detected by the DSN systems in real-time, are excluded from DSN MDR considerations.

DSN MDRs will be completed within 24 h after the end of the station track on which the data was acquired or within 24 h after a change of category, whichever is later. MDRs that require the return of data logs by mail from deep space stations, however, will be completed on a schedule consistent with mail schedules.

The DSN MDR production system will undergo performance demonstration and acceptance at the same time as the real-time data processing systems. When accepted by the project, the system will operate without further acceptance of the end product.

e. Guidelines for the DSN EDR. The DSN contribution to EDRs will consist of digital magnetic tapes containing negotiable extracts from the various DSN MDRs. Telemetry will be decommutated, if required, but not converted to engineering units. Tracking, command, and status data, if required, will be in standard formats. The frequency and accuracy of time tags will be consistent with the MDR time requirements. The quantity and quality requirements will not exceed those for the DSN MDR. The DSN contribution to EDRs will be completed within 72 h of the receipt of assurance that no further MDR category changes will be made for

---

[2]Below threshold, additional data may be extracted by spectral analysis or other techniques, but this is not part of the MDR, nor even DSN, activity in general.

the applicable time period (72 h after 30 days, if no assurance is supplied).

f. Worst-case design for Mariner Mars 1971. Negotiations with the *Mariner* Mars 1971 Project are taking place at this time, using the above guidelines. The most likely results of these negotiations will be a set of requirements which makes maximum use of DSN capability —designation of the DSN MDR as the total MDR, and extraction from this MDR to form EDRs. Any information required on EDRs that is outside the scope of what the DSN will provide under the guidelines, would be supplied by the Project on a separate tape that would accompany EDR tapes.

This set of requirements would require development of a three-phase MDR/EDR production system. Phase I would produce SDRs in real-time on the SFOF CPS IBM 360/75 computer. Phase II would produce the DSN MDR according to Project-specified extract criteria, using a batch-operated IBM 360/75 program. Gap-filling using post-pass replay from ODRs would be provided, according to the criticality of the data. Phase II output would be complete within 24 h. Phase III would produce the DSN EDRs, using another batch-operated IBM 360/75 program. Phases I and II might be required to be repeated as a result of raising the MDR category by an experimenter based on his observation of real-time data.

3. Viking Mission Support, D. J. Mudgway

A DSN capabilities planning team (CPT) for the *Viking* Project was formed late in 1969 to make a detailed study of the functional capabilities needed to satisfy the 1973 *Viking* mission design in the areas of telemetry, tracking and command.

Starting with the general capabilities given in SPS 37-61, Vol. II, pp. 26–28, the CPT developed a set of functional block diagrams and supporting notes describing the hardware and software capabilities required by each of the subsystems of the DSIF, GCF, and SFOF.

The capabilities reflected by these documents are consistent with the long-range development plans of the DSN and are constrained by the planned capabilities of each of the DSN Systems.

The diagrams depicting the telemetry, tracking, and command systems for the 210-ft antenna subnetwork for *Viking* 1973, together with the supporting software and hardware notes, are given in Figs. 5 to 7.
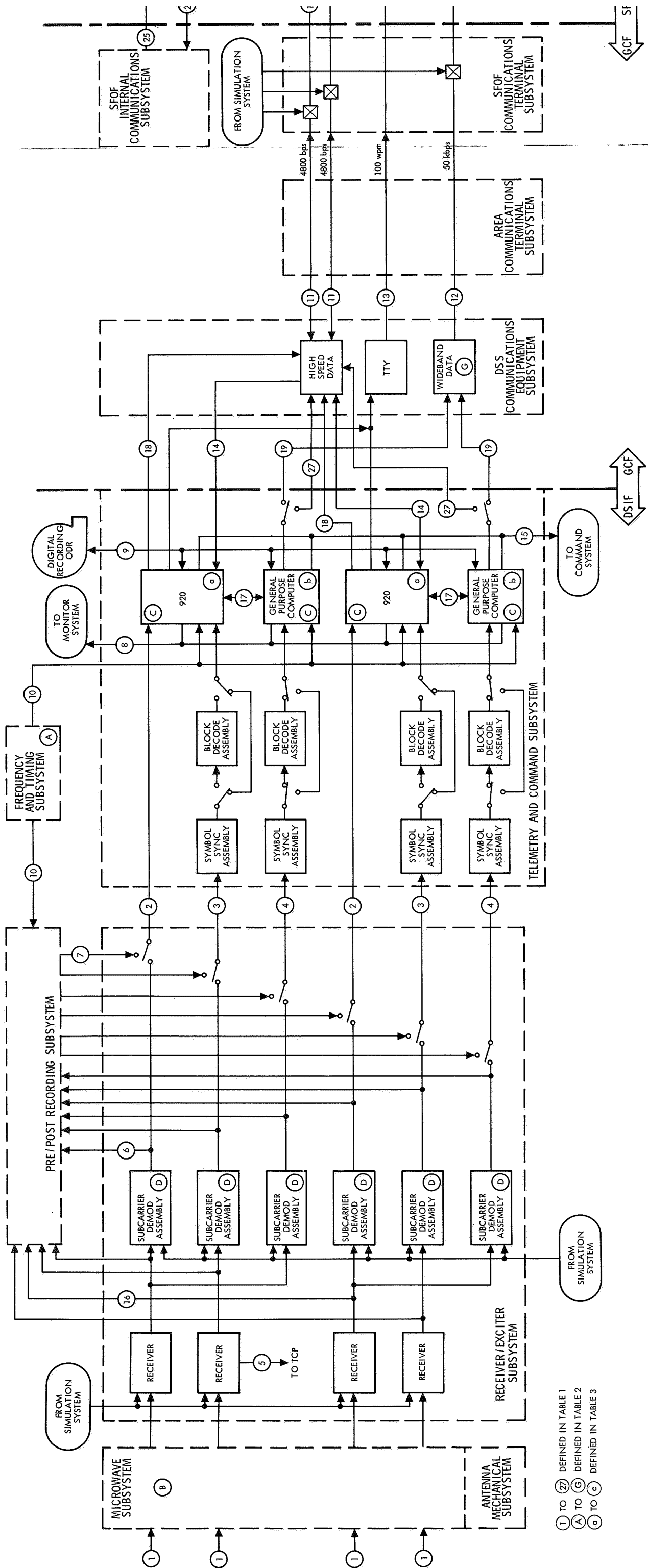
Fig. 5. Viking telemetry system
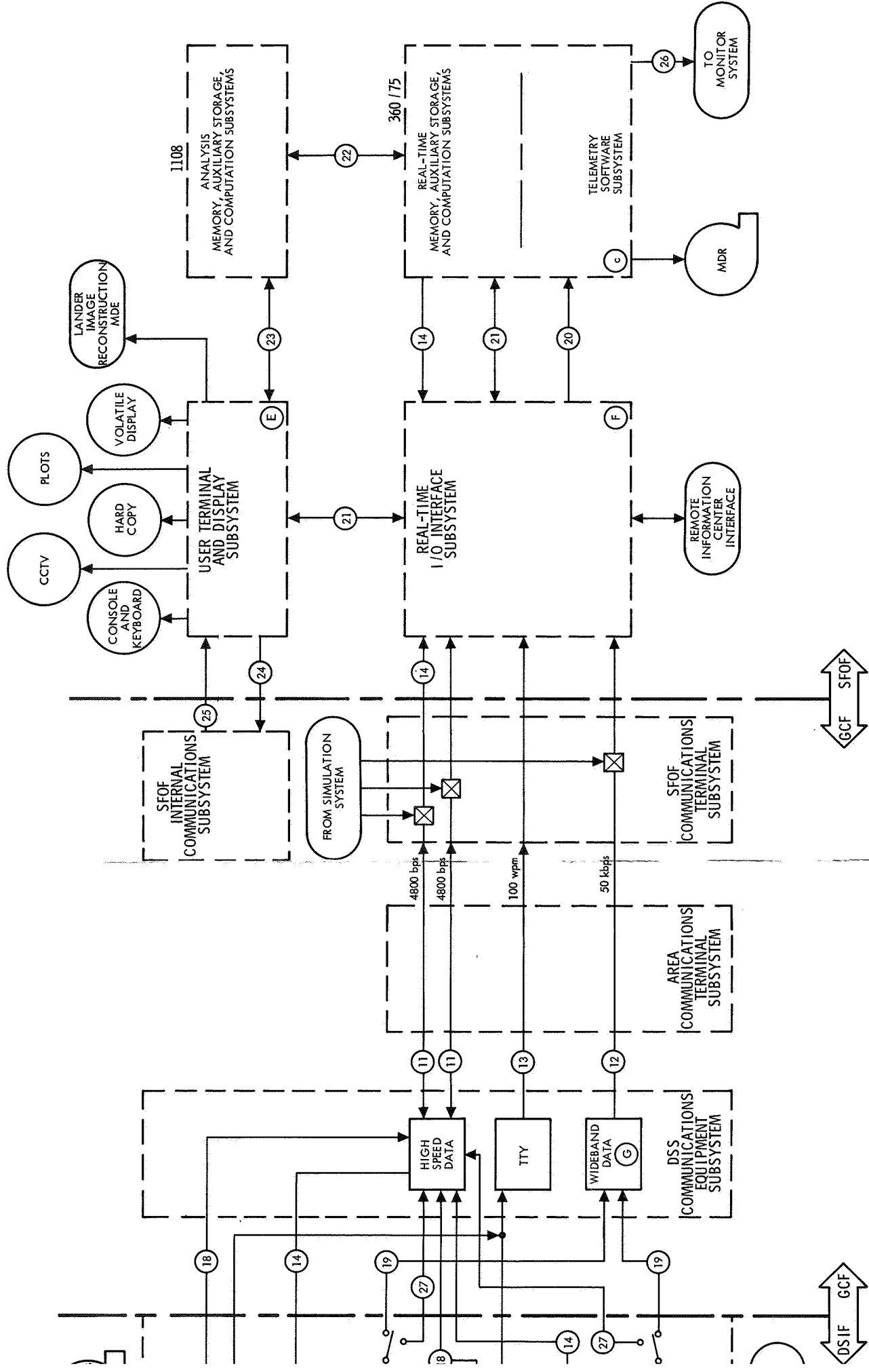
Fig. 5. *Viking telemetry system (210-ft-diam-antenna subnetwork) baseline functional requirements block diagram*

13
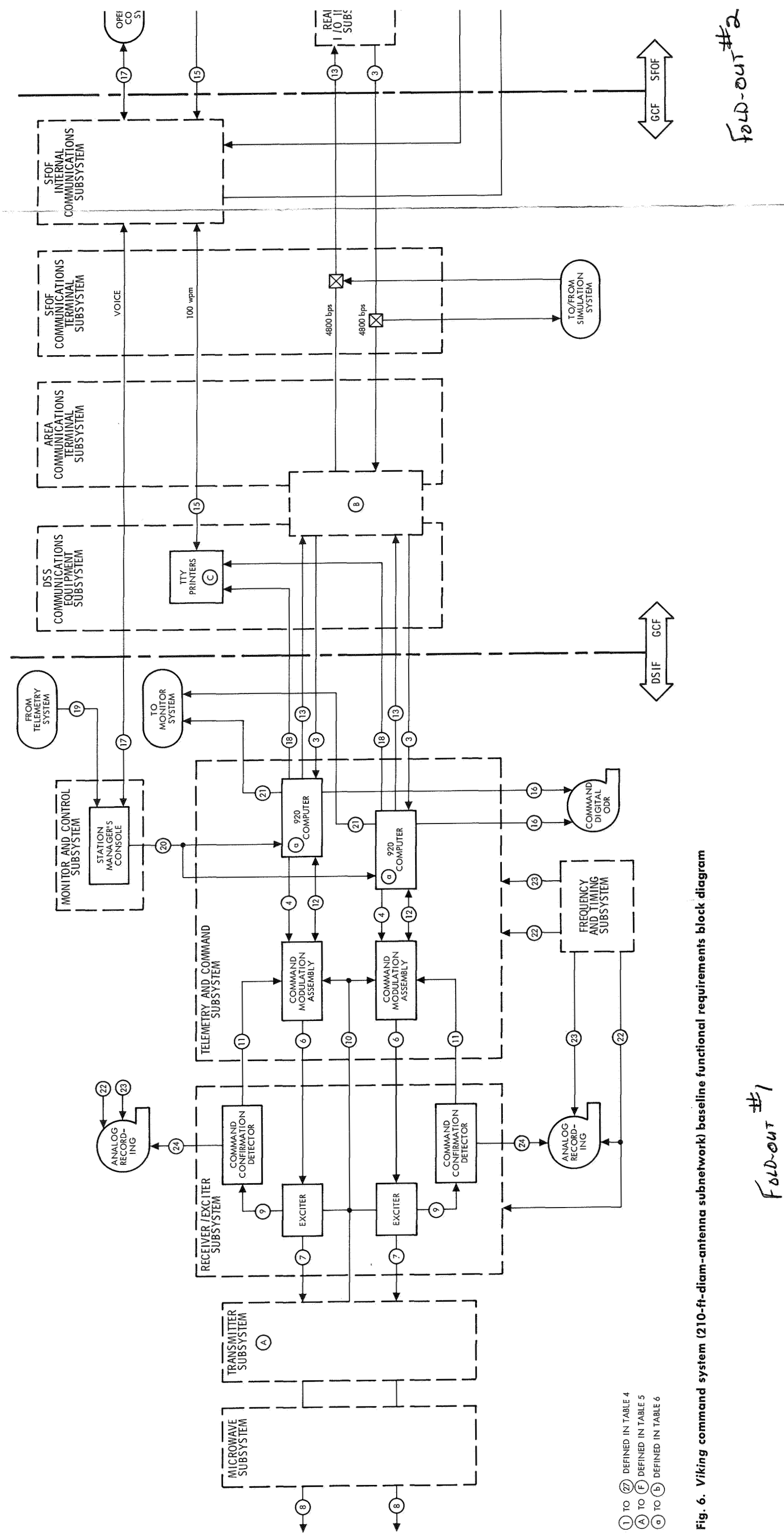
FOLD-OUT #2

Fig. 6. *Viking command system (210-ft-diam-antenna subnetwork) baseline functional requirements block diagram*

fold-out #2

1108

ANALYSIS
MEMORY, AUXILIARY STORAGE,
AND COMPUTATION SUBSYSTEMS
(COMGEN)

360/75

REAL-TIME
MEMORY, AUXILIARY STORAGE
AND COMPUTATION SUBSYSTEMS

SFOF TELEMETRY AND
COMMAND SOFTWARE
SUBSYSTEM

MDR

TO MONITOR SYSTEM

REAL-TIME
I/O INTERFACE
SUBSYSTEM

USER TERMINAL
AND DISPLAY
SUBSYSTEM

VOLATILE DISPLAY

HARD COPY

CCTV

KEYBOARD AND CONSOLE

TO OPERATIONS CONTROL SYSTEM

SFOF INTERNAL COMMUNICATIONS SUBSYSTEM

GCF   SFOF

SFOF COMMUNICATIONS TERMINAL SUBSYSTEM

VOICE

100 wpm

4800 bps

4800 bps

TO/FROM SIMULATION SYSTEM

AREA COMMUNICATIONS TERMINAL SUBSYSTEM

Fig. 7. Viking tracking system (210-ft-diam-antenna subnetwork) baseline functional requirements block diagram

Page intentionally left blank
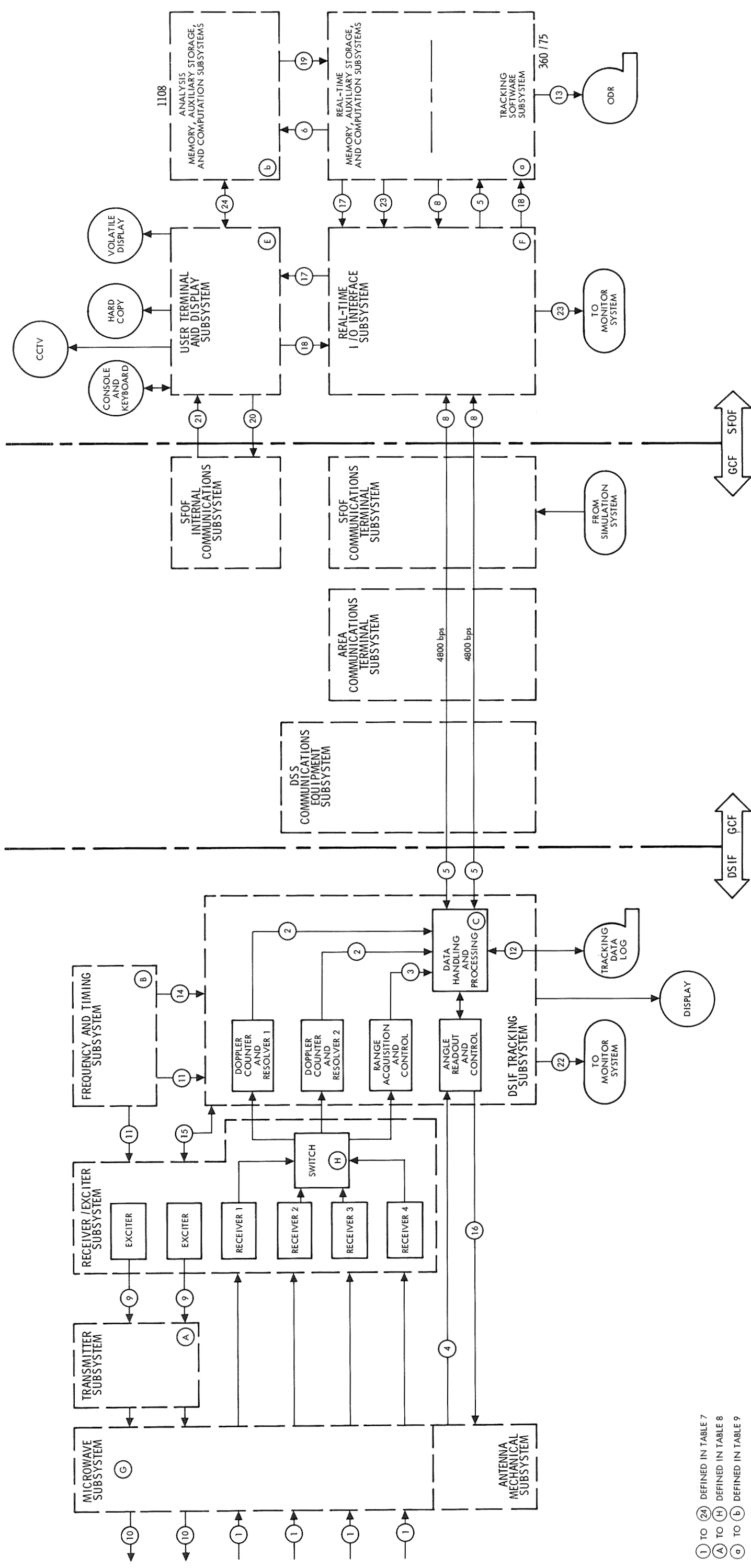
A complementary milestone schedule and program evaluation and review technique (PERT) chart were also prepared to afford some visibility into the interplay of the implementation and testing processes necessary to meet the Project launch readiness date in July 1973. It was intended that this schedule be used by the implementation, interface, testing, and operations team in planning their work, in order that the entire flow of *Viking*-related activity throughout the DSN be carried out in a coordinated and timely fashion, with minimum perturbation to technical activity related to the support of other projects.

At this point, budgetary considerations necessitated a redirection of the Project activity toward the 1975 launch opportunity.

Because of the resulting changes in the mission design, further progress in developing the DSN capability for *Viking* is being continued at a somewhat slower pace to permit the Project to consolidate a new mission plan.

Flow paths and capabilities for Fig. 5 are outlined in Tables 1 to 3; for Fig. 6 in Tables 4 to 6; for Fig. 7 in Tables 7 to 9; and abbreviations are defined in Table 10.

Table 1. Telemetry system data flow paths: 210-ft-diam antenna network (Fig. 5)

(1)	From one to four downlink carriers but limited to six simultaneous subcarriers	(15)	Spacecraft AGC and SPE from telemetry data to station Manager's console for command system operations
(2)	Low-rate telemetry data, uncoded, up to 50 bps (bit sync done in 920)	(16)	Predetection recordings, output of all receivers, no playback capability
(3)	Medium-rate telemetry data, uncoded, from 8 1/3 bps to 2000 bps or block coded up to 2000 bps from one lander at a time	(17)	Provides for program loading and transfer of control information from 920 to the general-purpose computer and monitor information from the general-purpose computer to the 920
(4)	Block-coded data, from 250 bps to 16.2 kbps or 4 kbps uncoded	(18)	Telemetry data, including partial status, formatted for high-speed data line transmission to SFOF
(5)	Illustrates ground AGC available from any receiver to the 920 and general-purpose computers for transmission to the SFOF with telemetry data streams	(19)	Telemetry data, including partial status, formatted for wideband data circuit transmission to SFOF
(6)	Output of all SDAs is recorded	(20)	Routing of all telemetry data to the 360/75 for decommutation, formatting, and processing for display. Master data record production
(7)	Playback of recorded SDA output	(21)	Control for telemetry data processing from user terminal and display subsystem (UTDS) to 360/75 and processed data from 360/75 to UTDS for display
(8)	Periodic status, S/N calculations, data/tape loss alarms	(22)	Telemetry data/MDR transfer from 360/75 to 1108. Control information and telemetry standards and limits output from 1108 to 360/75
(9)	Digital recordings of 920/general-purpose computers' output. Prime ODR for telemetry data. Also, replay of taped data.	(23)	Project input control to telemetry data analysis programs and analysis programs output for display
(10)	Time	(24)	Control to SFOF internal communications subsystem for CCTV display
(11)	Telemetry data transmission to the SFOF via two high-speed data lines, including telemetry system partial status and post-pass tape replays	(25)	CCTV signals
(12)	Telemetry data transmission to the SFOF via wideband data circuit, assuming availability of NASCOM-provided satellite circuits for overseas 210-ft stations, one wideband circuit per complex. Duplex to DSS 14 only.	(26)	SFOF telemetry system alarms, periodic status, errors detected, data loss alarms, etc.
(13)	Not used	(27)	Telemetry data formatted for HSDL transmission
(14)	DSS initialization conditions and telemetry standards and limits from the SFOF to the DSS via high-speed data line		

Table 2. Equipment/subsystem capabilities (Fig. 5)

(A) Output time accurate to 5 ms

(B) System temperature estimated to be 25°K in diplex mode and 18°K in listen mode at near zenith; 40°K in diplex mode and 33°K in listen mode at 10 deg elevation.

(C) Two 920 computers (shared with command system) and two general-purpose computers for DSS telemetry processing

(D) As illustrated, six subcarrier demodulator assemblies required at each 210-ft station to handle a maximum of six simultaneous subcarriers, two from each of two orbiters and one lander

(E) UTDS provides consoles, input-output processors, and displays required to interface with 360/75 and 1108 and the SFOF internal communications subsystem. Interface with the 360/75 is via the real-time I/O interface subsystem. The UTDS has a direct interface with the 1108.

(F) The SFOF real-time I/O interface subsystem includes hardware and software for I/O processing of telemetry and associated data via high-speed, wideband, and TTY circuits, and channels for display and control information.

(G) Wideband data circuit to each complex, duplex to DSS 14 only

Table 3. Software capabilities (Fig. 5)

Input processing	Internal processing	Output processing
(a) and (b) DSIF telemetry and command subsystem		
Will accept input to four different combinations of telemetry bit streams Will handle two commands simultaneously with any one combination of telemetry streams Ground AGC Time reference Hardware lock status Operator messages through the computer console Standards and limits messages from SFOF	Performs bit synchronization and detection on engineering data 8⅓ or 33⅓ bps direct from SDA Frames synchronization of engineering data Decommutation of engineering data Calculates SNR and ground AGC in decibels	Formats and outputs for transmission to SFOF via wideband, high-speed, and TTY circuits Spacecraft AGC Subsystem instrumentation status to monitor system Data to digital magnetic log tape
(c) Central processing system IBM 360/75 computer		
Accept data simultaneously from up to four high-speed and two wide-band circuits Separates telemetry and partial status data Routes data for internal processing Accepts messages from remote information center	Frame sync, decommutate, and format telemetry data streams Processes and analyzes DSN status and alarm data Reconstructs video data for mission operations control purposes Provides mass storage for nonserial video data and data recall for reconstruction of video image Generates standards and limits Generates MDR	Prints, plots, and graphics to UTDS Outputs video data for CRT display in MSA MDR tapes DSN status and alarms to telemetry analysis group, monitor system, and MSA DSN log tape of data received Data to the Univac 1108, as called Selected data to remote information centers

Table 4. Command system data flow paths: 210-ft-diam antenna subnet (Fig. 6)

①	Control of command message and instruction message generation
②	Command generation via COMGEN programs and transmitted to IBM 360/75 command file
③	Command message, command instruction messages, and command recall request messages for any spacecraft
④	SFOF- or DSIF-generated command bits for single or dual up-link carrier
⑤	Not used
⑥	Command modulated subcarrier for single or dual uplink
⑦	Transmitter drive, single or dual uplink carrier
⑧	Amplified, modulated S-band single or dual uplink carrier
⑨	Modulator output for command confirmation
⑩	Transmitter, exciter, modulator status
⑪	Command detection for confirmation or abort
⑫	Controls, status, and command bits for closed loop comparison
⑬	Command verification, confirm/abort, alarm, and recall response messages
⑭	Command system status and alarms
⑮	Transmission of commands via TTY for manual input, as backup to high-speed data (if required)
⑯	Digital recording, original data record of command activity
⑰	Voice circuit for backup command transmission coordination
⑱	DSS local display of commands, verification, and confirmation/abort
⑲	Spacecraft AGC, SPE, and other parameters from telemetry data required to verify DSS command system readiness
⑳	Verbal instructions to TCP operator for manual command control (bit rate, mode select, operate/test, normal/emergency, request verification, transmit, stop)
㉑	Command system configuration, status, and alarms
㉒	Reference signals
㉓	DSS time
㉔	As required by project and if FR 1400 recorder tape tracks are available, command composite waveform on subcarrier
㉕	Control messages for command processing and display recall response messages, and display data (hard copy and volatile)
㉖	Control to SFOF internal communications subsystem for TTY and CCTV display
㉗	TTY and CCTV display data

Table 5. Equipment/subsystem capabilities (Fig. 6)

Ⓐ	A 400-kW power amplifier that provides about 40 kW RF power for each of two S-band carriers transmitted simultaneously, and about 400 or 20 kW S-band power transmitted via one carrier (at all 210-ft stations)
Ⓑ	DSS/area communications processor that handles high-speed data formatting, address identification, and routing to and from station assemblies, e.g., command data is routed to the appropriate 920 as addressed
Ⓒ	Located at the station manager's console
Ⓓ	Not used
Ⓔ	UTDS provides consoles, input-output processors, and displays required to interface with the 360/75 and 1108 and the SFOF internal communications subsystem. Interface with the 360/75 is via the real-time I/O interface subsystem. The UTDS has a direct interface with the 1108
Ⓕ	The SFOF real-time I/O interface subsystem includes hardware and software for input-output processing of high-speed data, wideband data, TTY data, display data, and control information

Table 6. Software capabilities (Fig. 6)

(a) SDS 920 TCP program for command (one spacecraft sharing TCP with telemetry system)		
Input processing	**Output processing**	**Internal processing**
HSD command messages and *enable/disable* messages from SFOF Command messages and *enable/disable* messages via local DSS manual input (backup) Command instruction messages Command recall request via HSD or operator input Command verification from waveform generator and mode control for bit-by-bit comparison Computer reference time	Output process and format for HSD and TTY: Command verification messages to inform SFOF command message reception by 920 with or without bit error Command recall response messages to inform SFOF of status of equipment of multi-mission command system and TCP; current command messages stored in TCP still unprocessed; and command confirmation/abort messages to SFOF Output process and format for transmission to DIS computer via 24-bit parallel register: Hardware status indicator information from multi-mission command; error indication of bit-by-bit between command waveform generator and TCP; error indicator that HSD command message or request blocks show ADSS HSD error Output process and format teletype messages to SMC of: Reception of command message or *enable/disable*; command request/response messages; command confirmation/abort messages; command verification message Output process and format digital magnetic log tape (ODR) of all received commands, *enable/disable* messages, command instructions, command confirmation/abort combined tape and telemetry data (ODR) Transmit command bits to waveform generator and mode control	Extract spacecraft number from command instruction message and use to obtain parameters with which to initialize multi-mission command hardware Keep time against computer clock reference until stored command is to be processed to command waveform generator and mode control hardware Extract required parameters from command instruction message; buffer and store for recall response Transmit *enabled* commands at time given in command message, or immediately if specified Perform verification on command message from HSD (GCF error detection) and prepare verification message Compare data in command instruction message and generate alarm if system is out of tolerance Remove *disabled* command from storage, or inhibit transmission of remaining bits if it is in process
(b) IBM 360/75 mission-independent central processing system (two computers)		
Command messages accepted and prepared for HSD transmission Transmit stored command messages to DSS in time sequence so that the storage capability of the DSS command system is not exceeded Examine command recall response messages and extract parameters to be displayed Process verification messages received via HSD from DSS to assure correct receipt and display for Project Accept Project-generated *enable/disable* messages and transmit to DSS. Reject *enable* messages if not valid Accept command recall request messages and prepare for transmission or interrogate CPS buffer and display command recall response messages Compare command message parameters with predetermined standard and limits and display detected errors as alarms Maintain a message (command) accountability system		

Table 7. DSN tracking system data flow paths: 210-ft antenna network (Fig. 7)

(1)	S-band downlink from one to four spacecraft
(2)	Doppler data from either one or two spacecraft
(3)	Ranging data from one of the spacecraft in (2)
(4)	*Actual antenna pointing angles*
(5)	High-speed tracking data from DSIF Tracking Subsystem
(6)	Tracking data (ODR) to 1108 for processing and ephemeris data generation
(7)	Not used
(8)	Predicts, acquisition messages, and standard and limits
(9)	Transmitter drive, modulated with ranging signals when required. Range modulation of only one carrier at a time
(10)	Amplified, modulated S-band carrier
(11)	Reference frequency
(12)	Digital logs of all subsystem data output (doppler, range, angles, frequency references, station parameters, and calibration data), with near-real time or post-pass capability to play back a selected number of samples at the same or a lesser sample rate than that originally recorded at the DSS
(13)	Tracking data ODR, digital tape form
(14)	Time
(15)	Frequency references and ranging modulation
(16)	Antenna drive signals
(17)	Tracking software subsystem display data, pseudo-residuals, ODR, predictions, status
(18)	Control messages for tracking data processing and display
(19)	Validated spacecraft ephemeris data, either initial conditions or actual trajectory points
(20)	Control to SFOF internal communications subsystem for CCTV display
(21)	CCTV signals
(22)	DSS detected alarms to monitor system
(23)	Tracking system alarms to monitor system
(24)	Project input control to tracking data analysis programs and analysis programs output for display

Table 8. Equipment/subsystem capabilities (Fig. 7)

(A)	400-kW power amplifier that provides approximately 40 kW RF power for each of two S-band carriers transmitted simultaneously, and either approximately 400 kW or 20 kW S-band power transmitted via one carrier (at all 210-ft stations)
(B)	Accurate to ± 5 μs in relation to universal time (calibration function not shown)
(C)	Multipurpose computer that provides: (1) Antenna pointing control (2) Predicts processing (3) Doppler extraction and counting (4) Ranging control (5) Data formatting and commutation (6) Logging and recall (7) On-line request processing (8) Validation (9) Selection (10) Status
(D)	Not used
(E)	User terminal and display subsystem (UTDS) provides consoles, I/O processor, and displays required to interface with the 360/75 and 1108 and the internal communications subsystem. Interface with the 360/75 is via the I/O interface subsystem. The UTDS has a direct interface with the 1108
(F)	The SFOF real-time I/O interface subsystem includes hardware and software for I/O processing of high-speed data lines, wideband data circuits, TTY circuits, and channels for display and control information
(G)	210-ft antennas do not have autotrack capability; operation is in listen only or diplex modes
(H)	This switch is a simplification of the actual patching capability between receivers and doppler/ranging extractors. Any one of the four receivers may be patched to the range acquisition and control if that receiver is also patched to one of the doppler counters and resolvers. Receivers 1 and 2 may be switched only to doppler counter and resolver 1. Receivers 3 and 4 may be switched only to doppler counter and resolver 2

Table 9. Software capabilities (Fig. 7)

(a) IBM 360/75 mission-dependent software		
Input processing	**Output processing**	**Internal Processing**
Tracking data from DSS via HSDL Messages for controlling the printing and plotting of pseudoresiduals Spacecraft ephemeris data to be used in prediction calculation Control information for transmission of predictions Control information for operation of the tracking software subsystem Input requests and control message from the DSIF tracking subsystem	ODR to the 1108 Pseudoresiduals to the UTDS Predictions or predictions data for transmission to DSS via HSDL Tracking software subsystem generated displays Request and control messages to DSIF tracking subsystem SFOF tracking subsystem alarm messages to the monitor program Error or acceptance messages to operators	Subtract actual tracking data from predictions on a point-by-point basis to generate pseudoresiduals When pseudoresidual is out of the given plot, the appropriate (high or low) designation (H or L) is given to the value and plotted at the appropriate limit Accumulate all tracking and related data into an ODR Generate predictions or prediction data
(b) All project tracking system programs are run on the 1108.		

Table 10. Definition of abbreviations

AGC	automatic gain control
CCTV	closed-circuit television
CPS	central processing subsystem
HSD	high-speed data
HSDL	high-speed data line
I/O	input/output
MDR	master data record
ODR	original data record
SDA	subcarrier demodulator assembly
SMC	station monitor and control
S/N	signal-to-noise
SPE	static phase error
TCP	telemetry and command processor
TTY	teletype
UTDS	user terminal and display subsystem

III. Advanced Engineering

A. Tracking and Navigational Accuracy Analysis

1. Introduction, *T. W. Hamilton and D. W. Trask*

The DSN Inherent Accuracy Project was formally established by the DSN Executive Committee in July 1965. The objectives of the project are:

(1) Determination (and verification) of the inherent accuracy of the DSN as a radio navigation instrument for lunar and planetary missions.

(2) Formulation of designs and plans for refining this accuracy to its practical limits.

Achievement of these goals is the joint responsibility of the Telecommunications and Mission Analysis Divisions of JPL. To this end, regular monthly meetings are held to coordinate and initiate relevant activities. The project leader and his assistant (from the Mission Analysis and Telecommunications Divisions, respectively) report to the DSN Executive Committee, and are authorized to task project members to (1) conduct analyses of proposed experiments, (2) prepare reports on current work, and (3) write descriptions of proposed experiments. The project is further authorized to deal directly with those flight projects using the DSN regarding data-gathering procedures that bear on inherent accuracy.

The various data types and tracking modes provided by the DSIF in support of lunar and planetary missions are discussed in SPS 37-39, Vol. III, pp. 6–8. Technical work directly related to the Inherent Accuracy Project is presented in SPS 37-38, Vol. III, and in subsequent *Deep Space Network* SPS volumes, and is continued in the following subsections of this volume.

For most upcoming planetary missions, such as *Mariner* Mars 1971, the tightest bounds on the allowable errors for a number of parameters arise from the navigational accuracy requirements during encounter support. In particular, encounter navigational accuracy is most sensitive to error sources that cause a diurnal signature on the radio tracking data (SPS 37-39, Volume II, pp. 18–24). These sources of error are of two classes: Those parameters that define the locations of the DSS in inertial space and those phenomena that directly affect the DSS tracking data. The first category includes the location of the DSS with respect to the earth's crust; universal time (UT1); polar motion (the motion of the earth's crust with respect to the spin axis); precession and nutation (orientation of the earth's spin axis with respect to inertial space); and the ephemerides of the earth, moon, and target body. Of these, uncertainties in the first three are currently the major limitations to the encounter support

of navigation accuracy. Utilizing the information on UT1 supplied by the U. S. Naval Observatory (USNO) and the Bureau International l'Heure (BIH) and the information on polar motions supplied by the BIH and the International Polar Motion Service (IPMS), the DSN has actively supported efforts to reduce the operational uncertainties of these parameters while improved DSS location determinations result from continuing post-flight analysis of DSS radio tracking data. Improvements of the remaining ephemeris-related parameters have been primarily supported by non-DSN efforts.

The dominant sources of error in the second category are those affecting the tracking data directly, including charged particles (ionosphere and space plasma), troposphere, frequency system instability, and electrical phase path variations (through both the spacecraft and the DSS). The reduction of the effect of all these error sources, except those due to the spacecraft, is directly supported by the DSN.

The first article (Subsection 2) describes the possible orbit determination error for the Mariner Mars 1971 approach trajectory due to space plasma effects on the tracking data. Although the effect of the space plasma will be one of the major limitations to the navigation support of the Mariner Mars 1971 mission encounter phase, these effects can be kept below 25 km (the total 1σ budget for all navigation-related errors is 50 km) provided the space plasma activity is no worse than anything experienced during the Mariner V mission. However, solar flares such as those detected during Pioneer missions could cause orbit determination errors greater than 50 km. Consequently, some means of calibration for these charged particles in the space plasma is desirable. One such method, which is discussed in Subsections 3 and 4, is called "difference range versus integrated doppler," (DRVID), i.e., charged particles affect an electromagnetic wave such that the group velocity (ranging code) is retarded and the phase velocity (doppler) is advanced. The DRVID method, which makes use of these principles, is receiving increased interest as a charged particle calibration technique for radio tracking data. Therefore, as background to past and intended future articles, Subsection 3 is primarily tutorial in nature and describes the theoretical basis underlying this method. The following article (Subsection 4) describes the DRVID charged particle measurements using a binary-coded sequential acquisition ranging system while tracking during the Mariner Mars 1969 extended operations. The quality of

the resultant data indicates that charged particle effects can be determined to within 0.6 m of range change over intervals of 5 to 8 h, which would be a significant contribution to the radio navigation goals for the 1971 era.

A companion article in Section B-1 of this chapter describes a series of tests conducted at DSS 14 to accurately assess the performance of the ranging system used during the DRVID demonstrations described in Subsection 4.

The last three articles of this section (Subsections 5, 6, and 7) pertain to navigation errors of the first category, called "platform parameters," i.e., the location of the DSS with respect to inertial space. Subsection 5 describes the progress that has been made in comparing DSS locations as inferred by the Smithsonian Astrophysical Observatory from Baker–Nunn and laser tracking of earth satellites, and DSS locations as determined by JPL from analyzing DSN radio tracking data itself. The two sets of results have an average difference of 0.3 m with a scatter of 7 m in the distance of the earth's spin axis component; in the longitude direction, there is an average difference of 21 m and a scatter of 4.5 m. This is an improvement of up to a factor of three since the initial comparisons made in 1966 and is well within the predicted statistics. However, there is an unexplained drift of 1–2 m/yr in the longitude solutions as derived from the DSN tracking data. Subsection 6 considers suspected errors in precession, nutation, equinoxial drift, and UT1 as possible causes. However, no known sources of error in these quantities can produce the apparent westward drift observed in these solutions.

The final article in this section (Subsection 7) describes the technique of very-long baseline radio interferometry. The basic equations are developed for two data types— time delay and fringe rate. The partials of these two data types are developed with respect to DSS positions, source position, UT1, polar motion, and two constants of precession and nutation. It is anticipated that the very-long baseline interferometry technique will provide data allowing a significant reduction in the uncertainties of these platform parameters.

2. An Example of the Space Plasma Effect on the Mariner Mars 1971 Encounter Accuracy, G. W. Reynolds, N. A. Mottinger, and V. J. Ondrasik

a. Introduction. The Mariner Mars 1971 missions are designed to study the dynamic characteristics of Mars from an orbiting spacecraft for a minimum period of

90 days. To place the *Mariner* spacecraft into Mars orbit requires an orbit insertion maneuver to transfer from the approach hyperbolic trajectory to a preliminary elliptical orbit. To limit the initial period error to 45 min, an orbit determination accuracy of 50-km 1-σ uncertainty in the magnitude of the **B** vector of the approach trajectory must be available at the time of the orbit insertion computations.[1] Certain limiting orbit determination error sources and the effect of charged particles in the space plasma on meeting the encounter accuracy requirement are examined in this article.

b. Effect of charged particles on radio tracking data. Charged particles in the ionosphere of the earth and in the interplanetary space plasma affect the passage of an electromagnetic wave such that the group velocity is retarded and the phase velocity is advanced. This charged-particle effect is proportional to the total electron content (for range data) or the time rate of change of the total electron content (for doppler data) along the ray path. An error is introduced into the DSIF doppler data if it is not calibrated for time variations in the electron content along the ray path. During the *Mariner* Mars 1971 encounter a uniform electron density of 5 electrons/cm³ along the ray path through the interplanetary medium from earth to Mars would produce a range error of approximately 8 m at S-band frequencies (SPS 37-41, Vol. III, pp. 3–11). The corresponding doppler error would depend on the rate of change of the electron content.

Electron content along the ray path in the interplanetary medium is a function of solar activity, sun–earth–probe angle, and sun–probe distance. Table 1 shows average values of electron content measured from several different spacecraft. Figure 1 shows the solar activity cycle over this period of time and the time of the *Mariner* Mars 1971 arrival. It must be emphasized that the electron content is not a smooth function of time. Over two 6-mo intervals the *Pioneer VI* and *VII* measurements of electron density showed an rms variation of ±4 electrons/cm³. Further, three large and sudden increases in electron content were observed which raised the density 30 to 50 electrons/cm³ above the average value. These large increases lasted about one day and were caused by dense plasma pulses traveling out from the sun (Ref. 1). So while the *Mariner* Mars 1971 arrival date appears to be at a medium point in the solar activity cycle, it is quite possible that the variation in electron content may be

[1]O'Neil, W. J., *Basis of M '71 Transit O.D. Accuracy Requirements*, Sept. 1969 (JPL internal document).

Table 1. Measured electron density

Spacecraft	Time interval	Average density, electrons/cm³
Mariner II	Sept. to Dec. 1962	10 (local)
Pioneer VI	Dec. 1965 to May 1966	4.3
Pioneer VII	Aug. 1966 to Mar. 1967	8.7
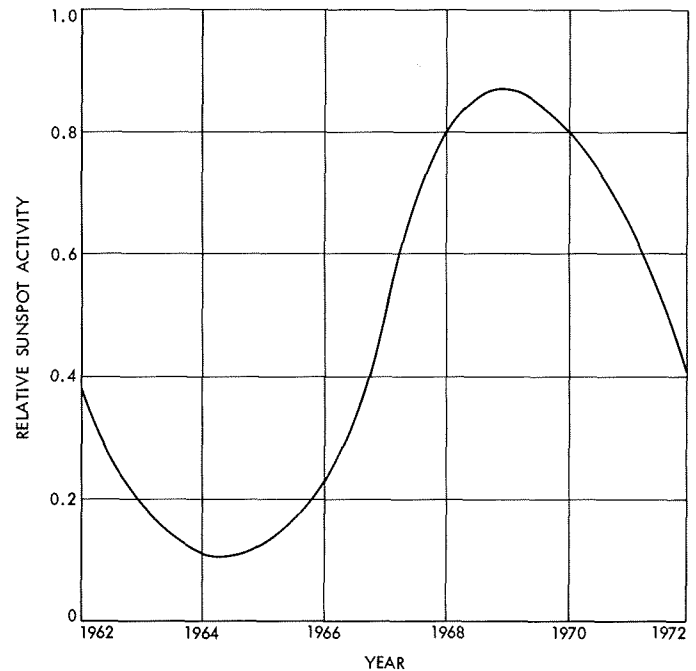
Fig. 1. Solar activity cycle

higher than expected. Also, one cannot rule out the occurrence of a solar flare generating a solar emission of charged particles sometime during the encounter phase of *Mariner* Mars 1971 mission. Without some means of calibration for charged-particle effects, such a solar flare as experienced by *Pioneers VI* and *VII* could cause orbit determination errors greater than 50 km.

c. Method of simulating charged-particle effect. Data from the *Mariner V* dual frequency experiment was used to obtain a time history of space plasma total electron content between the tracking station and spacecraft over a period of several months. Since *Mariner V* was a Venus probe, this electron content profile was then modified to account for the $1/r^2$ variation in density with distance from the sun and also a factor was applied to account for the difference in earth–sun–probe angle so that the *Mariner V* data now represented an equivalent electron

content profile for the *Mariner* Mars 1971 mission. Since the *Mariner* V and *Mariner* Mars 1971 encounters occur at about the same level in the solar activity cycle, the total space plasma electron content for the modified *Mariner* V data could be considered as a representative sample for the *Mariner* Mars 1971 mission.

The program ION developed by B. D. Mulhall and R. N. Wimberly was then used to convert the electron content profile to a change in the measured range rate (SPS 37-56, Vol. II, pp. 58–61). These modifications to range rate were then added to a set of observables generated for a nominal trajectory that assumed no range rate errors. In this manner a data tape of observables corrupted by errors due to variations in space plasma electron content similar to that experienced on *Mariner* V could be generated for a nominal *Mariner* Mars 1971 trajectory. Three tapes were generated. The first tape had the modified *Mariner* V data time shifted so that the largest change in electron density experienced during *Mariner* V occurred at 6 days before the simulated *Mariner* Mars 1971 encounter. Simulations run using this tape are labeled Profile I cases. A second tape had the modified *Mariner* V data time shifted such that the largest change in electron density occurred on the day of encounter. Simulations run using this tape are labeled Profile II cases. The third tape was the same as the second, except that no range rate modifications were made to the DSS 14 data. This third tape was used in simulation for cases where it was assumed the DSS 14 data could be perfectly calibrated for charged particles using differenced range versus integrated doppler techniques (SPS 37-58, Vol. II, pp. 73–77). Simulations run using this tape are labeled Profile III cases. Range rate data was generated with a count time of 600 s and at a rate of 1 point every 20 min. An effective data weight of 2.0 mm/s for a 60-s count time data was used.

d. Discussion and results. The double precision orbit determination program (DPODP) was used to fit the data corrupted by variations in space plasma density and the resulting B-plane dispersions noted. Various subsets of a 32-day span with three-station tracking coverage from DSSs 14, 41, and 62 were examined. Table 2 shows the contribution of various individual error sources to the $1\text{-}\sigma$ uncertainty in **B** magnitude. This table shows that a 40-km rss sigma is available for all error sources not included in the table before the 50-km $1\text{-}\sigma$ uncertainty requirement is exceeded. Table 3 shows the assumptions made to arrive at the equivalent DSS station locations. Table 4 is a summary of the B-plane dispersions obtained using subsets of the available 32-day data span and as-

Table 2. Contribution of individual error sources to the 1σ uncertainty in B-magnitude

Error sources considered	$1\text{-}\sigma$ uncertainty	Contribution to uncertainty in **B** magnitude, km	
		Data from E − 32 days to E − 6 h	Data from E − 12 days to E − 6 h
Equivalent DSS locations	$\sigma_{r_s} = 1.3$ m $\sigma_\lambda = 1.6$ m	16	22
Mass of Mars	$\sigma_{GM} = 0.4$ km^3/s^2	18	18
Astronomical unit	$\sigma_{AU} = 5$ km	5	5
Spacecraft solar radiation coefficients	Coefficients known to 5 %	10	5
Spacecraft propulsion system leak	Unmodeled leak of 10^{-12} km/s^2 in sun direction	10	5
Earth–Mars ephemeris[a]	5-km uncertainty in earth–Mars radial direction	10	10
	50-km uncertainty in direction perpendicular to earth–Mars radial direction and Mars velocity		
	10-km uncertainty in cross-track direction and in direction of Mars velocity		
Rss total of above error sources		30	31
Available rss sigma for remaining error sources		40	39

[a] Ephemeris errors are more significant in predicting time of closest approach.

suming the three different electron content profiles existed during the *Mariner* Mars 1971 encounter.

A 40-km rss sigma is available for all error sources not included in Table 2 before the accuracy requirement is exceeded. The largest perturbation in **B** magnitude from Table 4 is less than 40 km even when just 6 days of data was available. If the space plasma effects for *Mariner*

Table 3. Parameters contributing to equivalent DSS station location

Parameter	1-σ uncertainty
Charged-particle calibration (in terms of range change over a pass)	0.5 m (bias) $\}$ over 0.6 m (random) $\}$ pass
Troposphere calibrations	$\sigma_R = 7N$ units
Transmitter frequency stability	2×10^{-12} (bias) $\}$ over 4×10^{-12} (random) $\}$ pass
Variation in electrical phase path	0.2 m (bias) $\}$ over 0.3 m (random) $\}$ pass
Time synchronization	20 μs
DSS location	$\sigma_{r_S} = 0.5$ m $\sigma_\lambda = 1.0$ m
Earth pole location	$\sigma_x = 0.7$ m $\sigma_y = 0.7$ m
Universal Time with respect to Atomic Time	$\sigma_{\text{UTC-A.1}} = 2.5$ ms

R = refractivity = (index of refraction -1) $\times 10^6$.

Mars 1971 are no worse than the space plasma effects seen during the *Mariner V* mission, then it should be possible to meet the encounter accuracy requirements. This is provided that any other sources present (not listed in Table 2) when root sum squared with the solar plasma contribution do not exceed 40 km. The error sources in Table 2 assume an accurate method of calibration of doppler data for charged particle effects in the ionosphere, and station weather measurements will be available.

The Profile II electron content time history is identical to the Profile I time history except it has been time-shifted toward encounter by 6 days. Profile I has the largest variation 6 days before encounter, while Profile II has the largest variation on the day of encounter. From Table 4 it is seen that the largest perturbations in **B** are associated with the cases using Profile II. Thus, the most undesirable time for large variations in electron content is right before encounter rather than several days before encounter.

By comparing the perturbations in **B** as a function of length of data span, it is seen that the longer the data span the smaller the perturbation in **B** due to space plasma effects. The perturbation in **B** for 4 wk of tracking is about half the perturbation for only 1 wk of tracking. Since space plasma effects tend to average out, this suggests that one can take advantage of the randomness of variations in electron content by using a long data span.

The electron content time history for Profile III is the same as Profile II except that no charged particle effects have been added to the DSS 14 data. In other words, Profile III represents DSS 14 data perfectly calibrated for charged particle effects in both the ionosphere and space plasma and data from the two 85-ft-diam antennas uncalibrated for charged particle effects. The perturbations in **B** for the Profile III results are smaller than the Profile II perturbations. Even if data from only one station can be calibrated for space plasma effects, there is 10% to 25% reduction in the perturbation of **B**.

Range and doppler data could be used to calibrate the DSS 14 data for charged-particle effects using differenced range versus integrated doppler (DRVID) techniques. Two cases were run assuming that the DSS 14 data was perfectly calibrated for all charged particle

Table 4. B-Magnitude perturbations due to space plasma effects

Tracking coverage (2-way doppler)	Data		$\Delta \mid \mathbf{B} \mid$, km		
	from	to	No calibrations case I	No calibrations case IIA	DSS 14 perfectly calibrated case IIA
Continuous three-station tracking	E − 32 days	E − 6 h	5	18	16
Twelve 8-h passes/wk	E − 12 days	E − 6 h	7	30	23
Continuous DSS 14 (no other tracking)	E − 12 days	E − 20 h			0 ($\sigma_B = 53$)
Continuous three-station tracking	E − 6 days	E − 6 h	12	36	26
Continuous DSS 14 (no other tracking)	E − 6 days	E − 20 h			0 ($\sigma_B = 100$)

effects and no other tracking data was used. With 6 days of DSS 14 only tracking, the uncertainty in **B** magnitude was 100 km (twice the mission requirement); with 12 days the uncertainty was 53 km. Due to the mission constraint that the orbit insertion must occur over DSS 14, the last data point from DSS 14 prior to encounter is at encounter -20 h. From these results it is evident that at this time the spacecraft is too far from Mars for the doppler data to be powerful enough to reduce the 1-σ uncertainty in **B** magnitude significantly below the 50-km requirement. In order to increase the probability of meeting the mission accuracy requirements, the DSS 14 range and doppler data should be supplemented with additional tracking data.

e. Conclusion. Simulations were run to examine the error in **B** magnitude caused by space plasma effects for the *Mariner* Mars 1971 mission. The randomness of the variation in electron content is advantageous in reducing the orbit determination error if long data spans are used. An error of 16 km with 4 wk of tracking data, including DRVID data, is approximately half the error with just 1 wk of data. Provided the space plasma effects are no worse than anything experienced during the *Mariner V* mission, and DRVID data from DSS 14 is available, it should be possible to limit the encounter orbit determination error due to space plasma effects to less than 25 km.

Reference

1. Koehler, R. L., *Interplanetary Electron Content Measured Between Earth and the Pioneer VI and VII Spacecraft Using Radio Propagation Effects*, Stanford Electronics Laboratory, Stanford University, Calif., May 1967.

3. A First-Principles Derivation of the Differenced Range Versus Integrated Doppler (DRVID) Charged-Particle Calibration Method, *P. F. MacDoran*

a. Introduction. This article presents the foundations of the DRVID charged-particle measurement/calibration method in as complete a manner as is practical. Although these equations have appeared elsewhere (Ref. 1 and SPS 37-41, Vol. III, pp. 3–11) the derivations have been either generalized or excessively brief. This article offers a consistent notation, making it easier to study how group and phase velocity differences in a charged-particle medium may be exploited to reveal charged-particle dynamical effects.

The idea for exploiting range and doppler data for charged-particle measurement was first independently

proposed by G. S. Levy in 1961 in the context of radar reflections from Venus. However, data resolution and equipment stability prevented positive results until 1969 (SPS 37-58, Vol. II, pp. 73–77), despite attempts to use range and doppler data from the *Lunar Orbiters* and *Mariner V* (Footnote 2 and SPS 37-48, Vol. II, pp. 30–37).

The earliest mention of the group/phase velocity method for charged-particle measurement in the general published literature was by Muhleman and Johnston (Ref. 2) in 1966.

b. Derivation. As a starting point, consider Maxwell's time-dependent equations for a conducting medium, in gaussian units:

$$\nabla \times \mathbf{E} + \frac{\mu}{c} \frac{\partial \mathbf{H}}{\partial t} = 0 \tag{1}$$

and

$$\nabla \times \mathbf{H} - \frac{\xi}{c} \frac{\partial \mathbf{E}}{\partial t} - \frac{4\pi\sigma}{c} \mathbf{E} = 0 \tag{2}$$

where the conductivity σ is given by Ohm's Law $\bar{J} = \sigma \bar{E}$; μ is the permeability; ξ is the dielectric constant; and c is the vacuum speed of electromagnetic propagation.

It is well known that transverse oscillating electric and magnetic fields are solutions to Eqs. (1) and (2) and can be represented by

$$\mathbf{E} = \mathbf{E}_0 \exp\left[j(\mathbf{k} \cdot \mathbf{x} - \omega t)\right] \tag{3}$$

$$\mathbf{H} = \mathbf{H}_0 \exp j(\mathbf{k} \cdot \mathbf{x} - \omega t) \tag{4}$$

As has been shown in Jackson "classical electrodynamics" (Ref. 3) and many other texts on electricity and magnetism, in order that Eqs. (3) and (4) be solutions to Maxwell's equations, the wave number k, must satisfy the following relationship:

$$k^2 = \mu\xi \frac{\omega^2}{c^2} \left(1 + j \frac{4\pi\sigma}{\omega\xi}\right) \tag{5}$$

where $\omega = 2\pi f$.

σ now needs to be interpreted in the context of a tenuous plasma. Consider n_0 electrons per unit volume

free to move under the action of an applied electric field and allow this electron gas to be sufficiently rarefied so that damping forces due to collisions may be neglected. The electron's equation of motion is then

$$m \frac{d\mathbf{v}}{dt} = e\,\mathbf{E}\,(\mathbf{x}, t) \qquad (6)$$

For a rapidly oscillating field the electron's displacement will be small compared to a wavelength, so that

$$m \frac{d}{dt}\mathbf{v} = e\,\mathbf{E}_0 \exp\,(-j\,\omega t) \qquad (7)$$

where

$$\mathbf{E}_0 = \mathbf{E}_0 \exp\,(j\mathbf{k} \cdot \mathbf{x})$$

is the electric field at the average electron position.

The velocity is then

$$\mathbf{v} = \frac{je}{\omega m}\,\mathbf{E}_0 \exp\,(-j\,\omega t)$$

From the definition of current density and Ohm's Law

$$\sigma = j\,\frac{n_0\,e^2}{\omega m} \qquad (8)$$

Inserting Eq. (8) into Eq. (5) and making the approximation that for a tenuous medium $\mu \sim \xi \sim 1$, the wave number k is

$$k^2 = \frac{\omega^2}{c^2}\left(1 - \frac{\omega_p^2}{\omega^2}\right) \qquad (9)$$

where ω_p is referred to as the "plasma frequency" and is given as

$$\omega_p^2 = \frac{4\pi\,n_0\,e^2}{m}$$

and k is directly proportional to the index of refraction $n = ck/\omega$.

It is of interest to compute what electron density is required in order to prevent S-band (2 GHz) wave propagation through the electron gas. The problem is to find what n_0 is required so that k or n become zero or imaginary. Direct substitution gives $n_0 = 1.6 \times 10^9$ electrons/

cm³ as the required density. Solar corona electron density models (Refs. 4, 5) indicate densities of 10^8 electrons/cm³ at 1.2 solar radii and allowing for an order of magnitude increase in localized regions, one could expect S-band propagation to within 1.5 solar radii if having a positive index of refraction were the only radio system limitation.

Therefore, for the majority of situations to be dealt with, $\omega \gg \omega_p$, the index of refraction is real, and the wave is propagated; however, the wave is affected by the charged-particle medium in a rather strange manner, which is about to be derived.

The phase velocity is defined as

$$v_p = \frac{\omega}{k}$$

By using Eq. (9)

$$v_p = \frac{c}{\left(1 - \frac{\omega_p^2}{\omega^2}\right)^{1/2}}$$

which, for $\omega \gg \omega_p$, becomes

$$v_p = c\left(1 + \frac{1}{2}\frac{\omega_p^2}{\omega^2}\right) \qquad (10)$$

The group velocity is defined as

$$v_g = \frac{d\omega}{dk}$$

By using Eq. (9)

$$v_g = \frac{c^2}{v_p}$$

For $\omega \gg \omega_p$

$$v_g = c\left(1 - \frac{1}{2}\frac{\omega_p^2}{\omega^2}\right) \qquad (11)$$

The effect of the charged particles is now evident. The phase velocity is increased by a certain quantity, and the group velocity is decreased by exactly the same quantity. For $\omega \gg \omega_p$ that quantity is

$$\frac{c}{2}\left(\frac{\omega_p}{\omega}\right)^2$$

It now remains to ascribe these velocity shifts to the specific situation of tracking a spacecraft with range and doppler observations. From the standpoint of the range observable, the charged particles have the effect of making the spacecraft appear further away than it actually is. The station spacecraft distance is inferred by multiplying the measured round-trip light time in seconds by an assumed constant speed of electromagnetic propagation, $c = 2.997926 \times 10^8$ m/s. Therein lies the difficulty. The range code, which travels at the group velocity, spends part of its flight time moving at speed c when it is in a vacuum, and the other part of its flight moving at a speed less than c whenever the index of refraction differs from unity.

The round-trip light time T is

$$T = \int_{\text{ray path}} \frac{ds}{v_g}$$

and the apparent range

$$\rho = \frac{c}{2} T = \frac{1}{2} \int_{\text{path}} \frac{ds}{1 - \frac{1}{2}\frac{\omega_p^2}{\omega^2}}$$

$$= \frac{1}{2} \int_{\text{path}} ds + \frac{1}{4\omega^2} \int_{\text{path}} \omega_p^2 (s)\, ds$$

or

$$\rho(t) = \frac{1}{2} \int_{\text{path}} ds + \frac{A}{f^2} I(t) \tag{12}$$

where

$$f = \frac{\omega}{2\pi}$$

$$A = \frac{e^2}{4\pi m} \quad \text{(see Footnote 3)}$$

$$I(t) = \int_{\text{path}} n_0 (s,t)\, ds$$

$I(t)$ is physically the combined uplink and downlink columnar electron content with dimensions of electrons

³$A(\text{cgs}) = 2.02 \times 10^7$
$A(\text{mks}) = 20.15$

per unit cross-sectional area. Since it is both uplink and downlink columns, it is twice the static column usually dealt with; this factor of two is accounted for in A (usually 40.3).

Conceptually, one could also determine the station spacecraft range by measuring the elapsed time for a given phase point within a carrier to accomplish a round-trip flight:

$$\rho = \frac{c}{2} \int_{\text{path}} \frac{ds}{v_p}$$

$$\rho(t) = \frac{1}{2} \int_{\text{path}} ds - \frac{A}{f^2} I(t) \tag{13}$$

The method of doppler tracking is one of accumulating the phase of a received carrier relative to a reference source as a function of time. It is by time-differentiating this phase information that a frequency is determined and a relative station-spacecraft velocity is inferred through the doppler relation. Therefore, charged-particle effects on the phase velocity will be carried over into effects on spacecraft velocity determinations by doppler. So, by differentiating Eq. (13), the charged-particle effect on doppler is seen to come about by a time-varying columnar electron content I.

$$\dot{\rho}(t) = \frac{1}{2} \frac{d}{dt} \int_{\text{path}} ds - \frac{A}{f^2} \dot{I}(t) \tag{14}$$

A convenient quantity for the evaluation of an error source's effect on doppler tracking is to investigate the influence on the range change. This length quantity is called the range-change error $\Delta\rho_\epsilon$ and can be inferred only by assuming that the wave travels at c, but is acted upon by the particular error source in such a manner as to give the appearance of having physically lengthened or decreased the electromagnetic path between the tracking station and spacecraft.

The range at time t is given by Eq. (12), and so the range rate is

$$\dot{\rho}_R(t) = \frac{1}{2} \frac{d}{dt} \int_{\text{path}} ds + \frac{A}{f^2} \dot{I}(t) \tag{15}$$

The R or D subscript denotes whether this information has been derived from range or doppler data. The range

change $\Delta \rho$ over a time interval $(t - t_0)$ is then

$$\Delta \rho_R = \int_{t_0}^{t} \dot{\rho}(t') \, dt'$$

$$\Delta \rho_R(t) = \Delta \rho_a(t) + \frac{A}{f^2} \int_{t_0}^{t} I(t') \, dt' \qquad (16)$$

where $\Delta \rho_a$ is the actual physical change in the range.

An equation similar to Eq. (16) can be derived from the doppler data expression for the velocity in Eq. (14):

$$\Delta \rho_D(t) = \Delta \rho_a(t) - \frac{A}{f^2} \int_{t_0}^{t} \dot{I}(t') \, dt' \qquad (17)$$

Forming the differenced range minus integrated doppler gives

$$DRVID(t) = \Delta \rho_R(t) - \Delta \rho_D(t)$$

$$= 2 \frac{A}{f^2} \int_{t_0}^{t} \dot{I}(t) \, dt$$

In Eqs. (16) and (17) we see that the charged-particle effect on the range change is just $1/2 \, DRVID(t)$:

$$\Delta \rho_\epsilon = \frac{A}{f^2} \int_{t_0}^{t} \dot{I}(t) \, dt = \frac{1}{2} DRVID(t) \qquad (18)$$

Differentiating the negative of Eq. (18) gives exactly the quantity needed to correct charged-particle effects in the velocity (doppler) data.

$$\dot{\rho}_\epsilon = -\frac{1}{2} \frac{d}{dt} DRVID(t) = -\frac{A}{f^2} \dot{I}(t) \qquad (19)$$

c. *Properties of the DRVID method.* The utility of the DRVID artifice is now clear—it has the effect of canceling out the actual tracking station/spacecraft motion $\Delta \rho_a$, and preserving only the time-integrated $\dot{I}(t)$ effect. This intrinsic cancelation of $\Delta \rho_a$ is more general than one may at first think. Take, for example, the situation of a spacecraft undergoing a limit cycling. Such oscillating motions are common to both the doppler and range data and are thus eliminated in DRVID. $\Delta \rho_a$ might more accurately be termed a common-mode element. As another example of this common-mode rejection, consider the situation of the earth's troposphere. The effect in this case is to cause both the group and phase velocities to be

retarded by equal amounts, thus making the effect common and intrinsically rejected. To the extent that the tracking station's frequency system[4] is common to both the range and doppler data subsystems, any excursion in the frequency system will be rejected.

As Eq. (18) indicates, the time integration of charged-particle columnar dynamics extends only over the time interval $t–t_0$, typically the length of a tracking pass (5 to 12 h). Therefore, DRVID is sensitive to only the charged particles which enter or leave the ray path during the observation interval $t–t_0$, and there is no information on total columnar particle content whatever. This lack of total content information prevents DRVID from making absolute range corrections, except under special circumstances when spatial charge density may be modeled from $\dot{I}(t)$ information.

Since $I(t)$ is defined as arising from an integration along the entire radio-signal ray path, DRVID is sensitive to charged-particle dynamics along that path and, therefore, appears capable of calibrating the entire uplink and downlink effects. This aspect will be explored more carefully in the following section.

d. *Effects of differing uplink and downlink frequencies.* The fact that the uplink and downlink frequencies are not identical causes a slight complication to the analysis, and its effects need to be calculated. The charged-particle effect on the signal propagation is assumed to be a frequency effect. This is not, of course, physically correct, since a propagation velocity change is actually manifested as a wavelength change; but since we are dealing with a phenomenon that is proportional to the inverse frequency squared, it is convenient to deal with frequencies.

As was explained previously, the DRVID method preserves only the $\dot{I}(t)$ and cancels out common mode elements such as station/spacecraft motion; therefore, only the charged-particle effects to range and doppler need be specifically accounted for.

From Eq. (12) the range error is seen to be

$$\rho_\epsilon = \frac{A}{f^2} I(t)$$

[4]The attempt at performing a DRVID-type measurement during the *Mariner V* mission did not succeed because the range coding and decoding circuitry were not firmly phase-locked to the station frequency system.

and from Eq. (14) the doppler error is

$$\dot{\rho}_\epsilon = -\frac{A}{f^2}\,\dot{I}(t)$$

Referring to Fig. 2, we find that the signal apparently changes frequency as it propagates through a variable charged-particle medium such that when it arrives at the spacecraft, it is f' instead of f:

$$f' = f + \frac{A}{\lambda f^2}\,\dot{I}_u(t)$$

where

$$\lambda = \frac{c}{f}$$

The spacecraft then coherently retransmits this frequency f' at a slightly higher frequency by the ratio $b = 240/221$.

$$bf' = bf + \frac{bA}{\lambda f^2}\,\dot{I}_u(t)$$

The I subscripts u and d denote uplink and downlink, respectively. On the downlink path the frequency undergoes another shift such that at the tracking station the received frequency is

$$f_r = bf' + \frac{A}{\lambda_r(bf')^2}\,\dot{I}_d(t)$$

$$= bf + \frac{bA}{\lambda f^2}\,\dot{I}_u(t) + \frac{A\,\dot{I}_d(t)}{\lambda_r\left[b\left(f + \frac{A}{\lambda f^2}\,\dot{I}_u\right)\right]^2}$$

where

$$\lambda_r = \frac{c}{bf} = \frac{\lambda}{b}$$

Assuming

$$\frac{A}{\lambda f^3}\,\dot{I}_u \ll 1$$

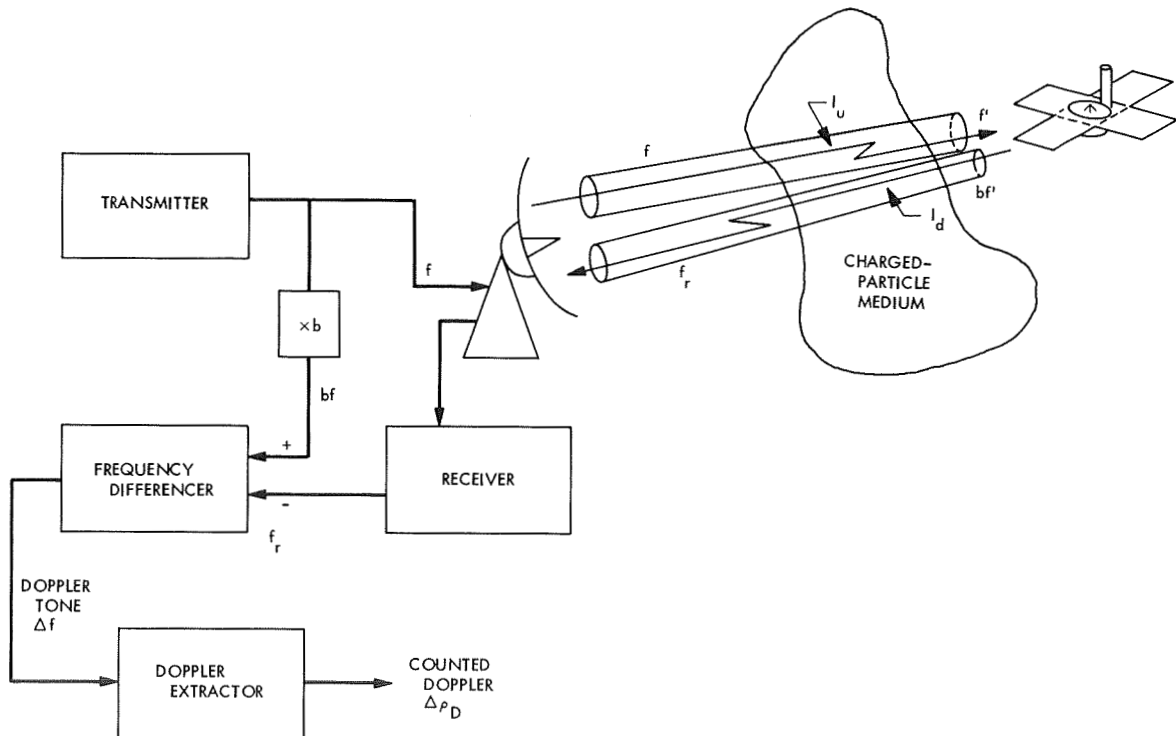$$f_r = bf + \frac{bA}{\lambda f^2}\,\dot{I}_u + \frac{A\,\dot{I}_d}{\lambda bf^2}$$

Fig. 2. Doppler radio tracking in the presence of a charged-particle medium

The received frequency is then differenced against a reference frequency bf, and a doppler tone Δf results:

$$\Delta f = bf - f_r$$

$$= \frac{bA}{\lambda f^2}\left(\dot{I}_u + \frac{1}{b^2}\dot{I}_d\right)$$

It is from the counted doppler tone that a range change is inferred by assuming a constant received wavelength λ_r.

$$\Delta \rho_D = \lambda_r \int_{t_0}^{t} \Delta f(t')\,dt'$$

$$= \frac{A}{f^2}\int_{t_0}^{t}\left(\dot{I}_u + \frac{1}{b^2}\dot{I}_d\right)dt' \qquad (20)$$

The range-rate error then appears as

$$\dot{\rho}_{\epsilon_D} = -\frac{A}{f^2}\left(\dot{I}_u + \frac{1}{b^2}\dot{I}_d\right) \qquad (21)$$

Referring to Eq. (12) and ignoring the actual physical displacement contribution to the range change, the charged-particle effect on the one-way range is

$$\rho_\epsilon = \frac{A}{f^2}I_u + \frac{A}{b^2 f^2}I_d$$

The velocity error inferred from range data is then

$$\dot{\rho}_{\epsilon_R} = \frac{A}{f^2}\left(\dot{I}_u + \frac{\dot{I}_d}{b^2}\right)$$

and the range change in $(t - t_0)$ is

$$\Delta \rho_R = \frac{A}{f^2}\int_{t_0}^{t}\left(\dot{I}_u + \frac{\dot{I}_d}{b^2}\right)dt \qquad (22)$$

Forming DRVID from Eqs. (20) and (22) gives

$$DRVID = \Delta \rho_R - \Delta \rho_D$$

$$DRVID(t) = \frac{2A}{f^2}\int_{t_0}^{t}\left(\dot{I}_u + \frac{1}{b^2}\dot{I}_d\right)dt' \qquad (23)$$

As before, DRVID is directly related the doppler error through one half the negative derivatives of Eq. (23):

$$\dot{\rho}_\epsilon = -\frac{1}{2}\frac{d}{dt}DRVID(t) = -\frac{A}{f^2}\left(\dot{I}_u + \frac{1}{b^2}\dot{I}_d\right) \qquad (24)$$

DRVID also offers the possibility of determining columnar charged-particle dynamics. However, the uplink and downlink dynamics are inseparable, as Eq. (24) indicates. For round-trip light times less than 15 min it is reasonable to expect that $\dot{I}_u \sim \dot{I}_d \sim \dot{I}$, so that

$$\dot{I} = \left(\frac{b^2}{1 + b^2}\right)\frac{f^2}{2A}\frac{d}{dt}DRVID(t) \qquad (25)$$

where f is the uplink frequency, nominally 2115 MHz.

$$\dot{I} = 6.007 \times 10^{16}\frac{d}{dt}DRVID(t), \text{electrons/(m}^2\text{/s)}$$

For long round-trip light times, ½ h or more, there can be significant differences between uplink and downlink dynamics. For instance, the uplink path could be through a nighttime ionosphere where $\dot{I}_u \sim 0$. With a light time of perhaps 1 h, the downlink could be returning to earth during sunrise, where $\dot{I}_d \sim 1 \times 10^{14}$ electron/(m²/s). Therefore, one must be careful when interpreting DRVID data as being a direct measure of columnar charged-particle dynamics. In the absence of *a priori* knowledge of the relationship between uplink and downlink paths, it is probably best to assume the link dynamics equal and use Eq. (25).

From Eqs. (22) and (23) the range-change error is given as

$$\Delta \rho_\epsilon = \frac{1}{2}DRVID(t) = \frac{A}{f^2}\int_{t_0}^{t}\left(\dot{I}_u + \frac{1}{b^2}\dot{I}_d\right)dt' \qquad (26)$$

Therefore, for each 1 m of DRVID change, the charged-particle effect changes just 0.5 m. In most cases DRVID raw data is in the form of a light-time change in nanoseconds. Usually, round-trip light time is converted to range by the factor 0.15 m/ns; however, as Eq. (26) indicates, the charged-particle effect is equivalent to 0.075 m/ns.

References

1. Stratton, J. A., *Electromagnetic Theory*, McGraw-Hill Book Co., Inc., New York, 1941.

2. Muhleman, D. O., and Johnston, I. D., "Radio Propagation in the Solar Gravitational Field," *Phys. Rev. Let.*, Vol. 17, p. L455, August 1966.

3. Jackson, J. D., *Classical Electrodynamics*, John Wiley & Sons, Inc., New York, 1963.

4. Whang, V. C., Liu, C. K., and Chang, C. C., "A Viscous Model of the Solar Wind," *Astrophys. J.,* Vol. 145, p. 255, 1966.

5. van de Hulst, H. C., *Bull. Astrom. Inst. Neth.,* Vol. 11, p. 135, 1950.

4. DRVID Charged-Particle Measurement With a Binary-Coded Sequential Acquisition Ranging System, P. F. MacDoran and W. L. Martin

a. Introduction. During the pre-encounter tracking of the *Mariner* Mars 1969 mission, several passes of doppler and planetary ranging system data were evaluated relative to their potential for charged-particle calibrations of doppler tracking data. The results were encouraging (SPS 37-58, Vol. II, pp. 73–77) when compared with previous attempts at exploiting group and phase velocities for charged-particle effect measurements, although they fell short of desired calibration goals for 1971. The planetary ranging system of the *Mariner* Mars 1969 mission (SPS 37-50, Vol. II, pp. 54–69) was not designed for the differenced-range-versus-integrated-doppler (DRVID) type of application, and it is considered fortuitous that its internal stability was sufficiently high to demonstrate the feasibility of the DRVID method.

With the advent of the *Mariner* Mars 1969 Extended Mission operations came a primary objective to demonstrate the utility and accuracy of the DRVID method of charged-particle calibration of metric radio tracking.[5] In early October 1969, a recently developed binary-coded sequential acquisition ranging system (mu-ranging system) also became available to the *Mariner* Mars 1969 Extended Mission operations. The mu-ranging system differs in several respects from the planetary ranging system used earlier with *Mariner* Mars 1969. For DRVID application the most important difference in the mu-ranging system is the method used to account for the time rate of change of the received range code. The mu-ranging system employs RF doppler rate aiding for range decoder shifting, and it is this method that automatically produces DRVID information.

On November 24 and December 11, 1969, the mu-ranging system was used with the *Mariner VI* spacecraft specifically for the purpose of detecting charged-particle dynamical behavior. The ranging data clearly showed columnar charged-particle dynamics that were identified as being ionospheric in origin, as confirmed by an independent measurement.

b. Operational description. Unlike previous ranging methods, the mu-ranging system measures the phase of received binary-coded components to accomplish an initial acquisition. Once the full set of components are acquired, the phase of the highest-frequency component ($\sim$0.5 MHz) is repeatedly measured to increase the precision of the initial acquisition.

The basic philosophy of this phase-measuring approach is that a model of the received code can be synthesized by employing the RF doppler to shift a replica of the range code originally transmitted. In other words, the doppler effect upon the received carrier frequency is assumed to be a true representation of the time rate of range change. However, the effects of charged-particle dynamics in the radio path prevent such an assumption from being strictly true.

In a changing charged-particle environment the group and phase velocities of a radio wave are not constants. Consider a situation where charged particles are entering the radio path to a receding spacecraft. The group velocity would then be decreasing, and the phase velocity would be increasing. Since the range code is propagated at the group velocity, the range data would give the spacecraft the appearance of having moved further away than its actual physical displacement, in a given time increment. If doppler cycles were added over the same time interval, the spacecraft displacement so derived would be smaller than actual. Thus, a dynamic phase error results when an RF doppler synthesized range code model is used for making a phase comparison against an actual received range code. In the supposed situation of an increasing columnar content, the modeled code will lag further and further behind the received range code. While such a dynamic phase error may be a nuisance in an electronics sense, it is of considerable utility for charged-particle dynamics measurement.

The doppler rate-aiding scheme utilized in the mu-ranging system deserves a more quantitative description.[6] Figure 3 is a simplified block diagram of a binary-coded sequential acquisition ranging system. A frequency synthesizer generates f_s (nominally 22 MHz) which is multiplied by three and phase modulated by the transmitter
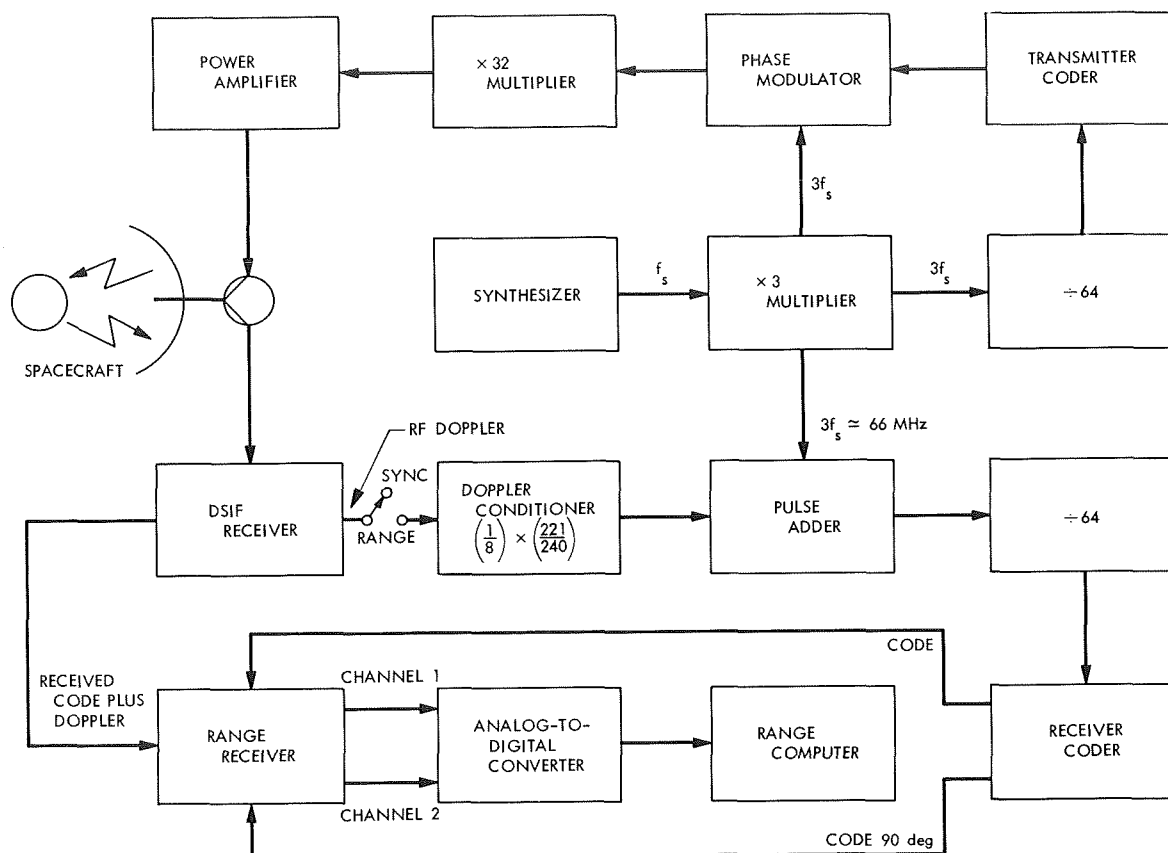

Fig. 3. Binary-coded sequential acquisition ranging (mu-ranging) system

coder. The code is generated by dividing the ×3 multiplier output by 64 and applying the result to an 18-stage binary counter. Each of the eighteen binary counter outputs is individually selectable for modulating the transmitter. The period t_n of the nth component is given by

$$t_n = \frac{64 \times 2^n}{3 f_s} \qquad (1)$$

and the code's period is irrevocably tied to the transmitter's frequency. Changing the transmitter's frequency, as is done from time to time to assure optimum reception at the spacecraft, also changes the coder's frequency in direct proportion.

A virtually identical set of hardware exists in the receiver; however, the ÷ 64 stage is preceded by a doppler pulse-adder circuit. The pulse adder accepts the 66-MHz output of the ×3 multiplier from the transmitter chain. The second pulse adder input is the RF doppler, properly scaled, from the DSIF receiver. In the ranging mode, the pulse-adder output frequency is the algebraic sum of the two input frequencies.

The receiver coder is a duplicate of its counterpart in the transmitter, except for a second code output which is phase delayed by $\pi/2$. These two receiver coder outputs are then combined to establish the amplitude of the returning signal prior to measuring its phase.

When the range sync switch is in sync position, the two coders operate synchronously. Because of the topocentric range rate of the spacecraft the received code slips in phase with respect to the transmitted code. If at time t_0 the switch is changed to the range position, the receiver coder frequency is modified by the RF doppler and becomes coherent with the signal being received from the spacecraft. Assuming that the two coders were synchronized prior to the changeover, the phase difference between the receiver coder and the incoming signal is a measure of the range. This phase difference will remain essentially constant by virtue of the doppler rate aiding, allowing the range measurement to be made at leisure.

Thus, a coherent model of the received range code can be generated by modifying the frequency of the transmitted code by the spacecraft's doppler. Note that the

tracking operation is open loop, eliminating any settling time and greatly simplifying the hardware design. Two conditions are necessary to make the scheme workable. First, before RF doppler can be used as a rate-aiding signal, the code must bear some simple fixed relationship to the transmitted carrier frequency. This is apparent from Eq. (1), which can be conveniently rewritten in terms of the transmitted frequency f:

$$t_n = 2^n \frac{2048}{f} \qquad (2)$$

Second, the implementation requires that high-speed digital logic be available to handle the 66 MHz. Since the pulse adder serves to add or delete cycles from the 66-MHz reference, the logic must have a switching speed well in excess of 66 MHz.

As shown in Fig. 3, a carrier frequency $96f_s$ with modulation frequency $3f_s/64$ is transmitted from the tracking station. Upon arrival at the spacecraft both the carrier and range-modulation frequencies will have undergone shifts due to the relative station/spacecraft motion and the effects of a changing charged-particle content in the radio path, causing these frequencies to appear as

$$f_1 = f\left(1 + \frac{V}{c}\right) + \frac{B}{\lambda f^2}\dot{I}_{up} \qquad (3)$$

and

$$f_{m_1} = f_m\left(1 + \frac{V}{c}\right) - \frac{B}{\lambda_m f^2}\dot{I}_{up} \qquad (4)$$

where

f = transmitted carrier frequency $96f_s$

f_m = modulation frequency $3f_s/64 = f/32 \cdot 64$

V = relative station/spacecraft velocity, m/sec

$\lambda = c/f$

$\lambda_m = c/f_m$

c = vacuum speed of electromagnetic propagation

$B = 40.3$ in MKS units

$\dot{I}_{up}$ = uplink columnar charged-particle dynamics, electrons/(m²/s)

In this derivation the parameter B is twice the corresponding A parameter defined in the preceding article,[7] because we must deal with two-way doppler and range effects.

The spacecraft phase locks its transmitter such that its downlink carrier is 240/221 times the received uplink carrier frequency. The spacecraft receiver also detects the range modulation and uses it to modulate the downlink carrier. When received at the tracking station the carrier frequency is

$$f_r = bf\left[\left(1 + \frac{V}{c}\right)^2 + \frac{B}{cf^2}\left(\dot{I}_{up} + \frac{1}{b^2}\dot{I}_{down}\right)\right] \qquad (5)$$

and the received modulation frequency

$$f_{m_r} = f_m\left[\left(1 + \frac{V}{c}\right)^2 - \frac{B}{cf^2}\left(\dot{I}_{up} + \frac{1}{b^2}\dot{I}_{down}\right)\right]$$

where

$b = 240/221$

$\dot{I}_{down}$ = downlink columnar charged-particle dynamics

Thus, the entire received signal appears as

$$v_r = \cos\left[2\pi\int_{t_0}^{t} f_r\,dt' + \phi'_m \, \mathbf{cos}\left(2\pi\int_{t_0}^{t} f_{m_r}\,dt' - \theta_0\right)\right]$$

where

t_0 = initial time of acquisition

t = arbitrary time of observation

ϕ'_m = spacecraft modulation index

$\mathbf{cos}\,()$ = square-wave approximation of cos ( ), + 1 if cos ( ) > 0 or −1 if cos ( ) < 0.

θ_0 = phase shift in modulation due to spacecraft range

As shown in Fig. 4, the first local oscillator of the DSIF receiver is

$$v_{LO1} = \cos\left(2\pi\int_{t_0}^{t} f_r\,dt' - 10^8\pi t\right)$$

[7]MacDoran, P. F., *A First-Principles Derivation of the Differenced Range Versus Integrated Doppler (DRVID) Charged-Particle Calibration Method*, in Subsection 3.
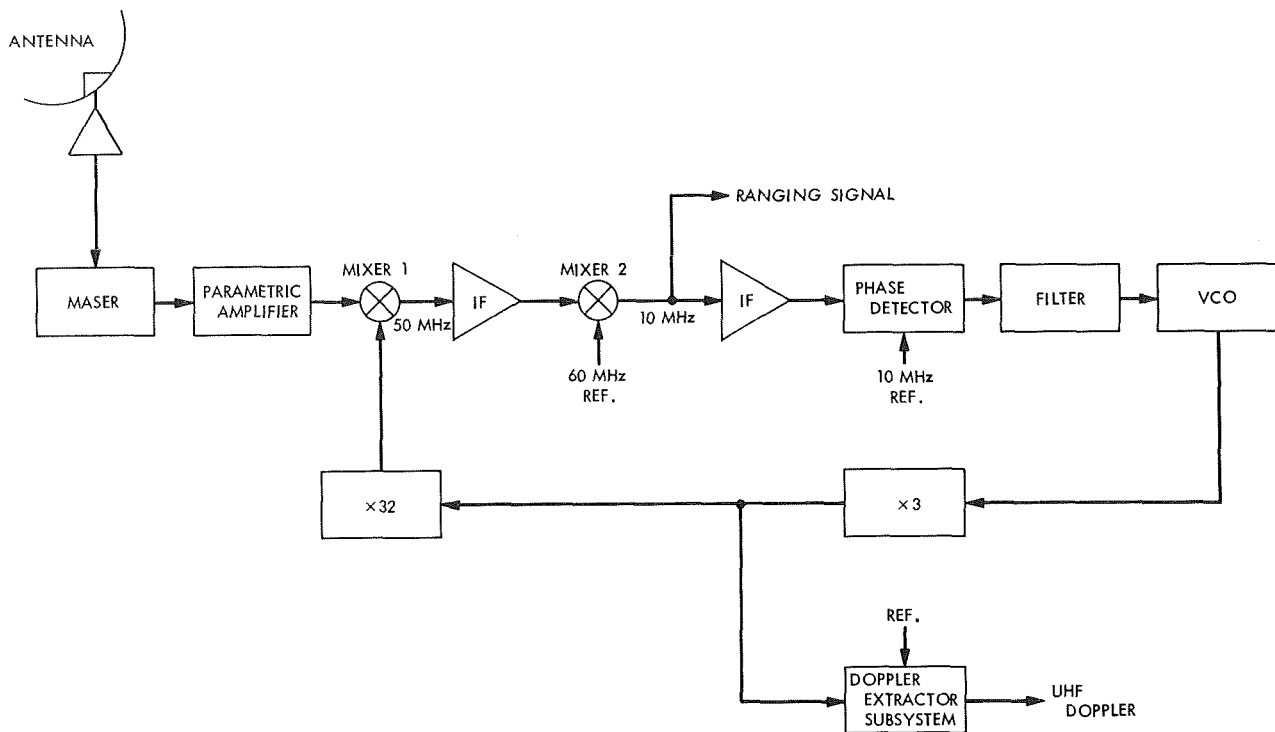
Fig. 4. DSIF receiver block diagram

The output of the first mixer is then

$$v_{m1} = \cos\left(10^8\pi t + \phi'_m \textbf{cos } 2\pi \int_{t_0}^{t} f_{m_r}\, dt'\right) \quad (6)$$

At the second mixer of Fig. 4, the local oscillator is a constant 60 MHz, resulting in a mixer output of the received range code on a 10-MHz carrier.

$$v_{m2} = \cos\left[2\pi\, 10^7\, t + \phi'_m \textbf{cos } (\gamma^- - \theta_0)\right] \quad (7)$$

where

$$\omega_m = 2\pi f_m$$

$$\gamma^- = \omega_m \int_{t_0}^{t} \left[\left(1 + \frac{V}{c}\right)^2 - \alpha\right] dt'$$

$$\alpha = \frac{B}{cf^2}\left(\dot{i}_{\text{up}} + \frac{1}{b^2}\,\dot{i}_{\text{down}}\right)$$

Equation (7) forms one input to the range receiver of Fig. 5.

It now remains to simulate the received code's time rate of change by operating on the received doppler.

The DSIF receiver contains a doppler extraction subsystem (Fig. 4) which provides

$$v_{\text{ext}} = \cos\left[\frac{2\pi bf}{4}\int_{t_0}^{t}\left(\frac{2V}{c} + \frac{V^2}{c^2} + \alpha\right) dt'\right] \quad (8)$$

This extractor signal, known as UHF or unbiased doppler, is scaled to simulate the time rate of change of the received range modulation. This scaling is accomplished digitally in the doppler conditioner stage of Fig. 3 by multiplying by 1/8b, giving a square-wave output of

$$v_{\text{scaled}} = \textbf{cos}\left[\frac{2\pi f}{32}\int_{t_0}^{t}\left(\frac{2V}{c} + \frac{V^2}{c^2} + \alpha\right) dt'\right] \quad (9)$$

This signal is then input to the pulse adder and serves to add or delete cycles of the second input $3\, f_s$ (66 MHz). Performing this pulse addition at a 66-MHz rate rather than the code frequency f_m (~ 1 MHz), minimizes the jitter in the rate aiding. Following the pulse-adder circuit is a $\div 64$ stage and the receiver coder. The receiver-coder output is then

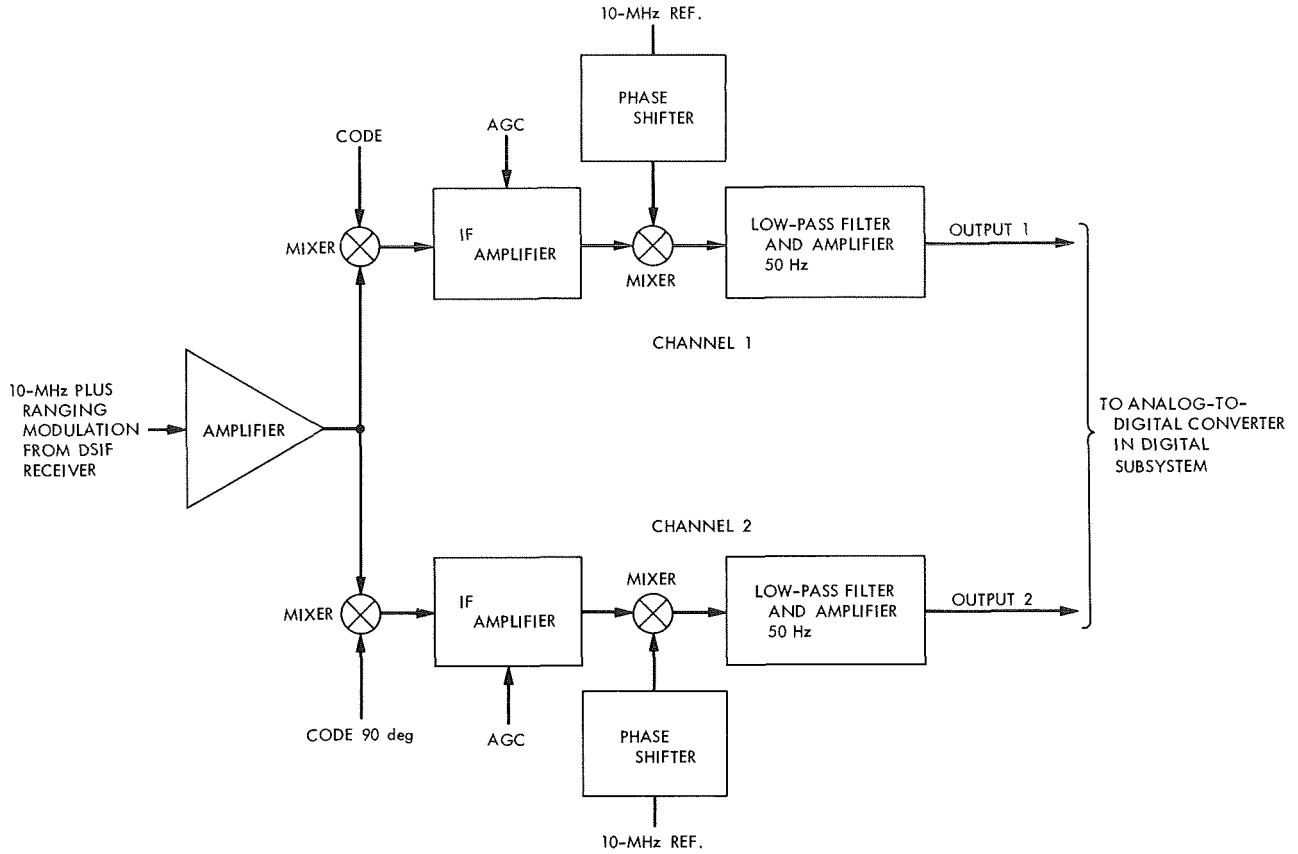$$v_{\text{r-c}} = \textbf{cos } \gamma^+ \quad (10)$$

Fig. 5. Ranging receiver block diagram

where

$$\gamma^+ = \omega_m \int_{t_0}^{t} \left[\left(1 + \frac{V}{c}\right)^2 + \alpha \right] dt'$$

Figure 5 shows the ranging receiver. Conceptually, the first and second mixing operations of this receiver can be interchanged such that after the first mixer the 10-MHz carrier is removed, leaving only the received range modulation.

$$v_{\text{range mod}} = \textsf{cos}\,(\gamma^- - \theta_0) \qquad (11)$$

The range modulation is then mixed with the range code simulated from the RF doppler (Eq. 10), to yield the product of the two square-wave cosine signals. To a first approximation $\textsf{cos}\,x \simeq \cos x$ so that the lower response output of the mixer is

$$\cos\gamma^+ \cos(\gamma^- - \theta_0)_{\text{lower}} = \frac{1}{2}\cos(\gamma^+ - \gamma^- + \theta_0) \qquad (12)$$

$$\cos\gamma^+ \cos(\gamma^- - \theta_0) = \frac{1}{2}\cos\left(\omega_m \int_{t_0}^{t} 2\alpha\,dt' + \theta_0\right) \qquad (13)$$

Although Eq. (13) is an approximation, it does contain the essential properties of the rate-aiding scheme. Specifically, the relative velocity terms have been eliminated, leaving the static phase shift due to the spacecraft range at time t_0 and a time-dependent term α that contains the charged-particle dynamical information.

In actual practice the phase difference between the two $\textsf{cos}$ ( ) functions is determined by a voltage measurement of the second mixer output. The resulting voltage is illustrated in Fig. 6 where

$$\theta = \theta_0 + \omega_m \int_{t_0}^{t} 2\alpha\,dt'$$

By time-averaging the output of the mixer over $T = 1/f_m$, a measure of the phase shift between the two codes is obtained. For example, an average of $+1$ would indicate
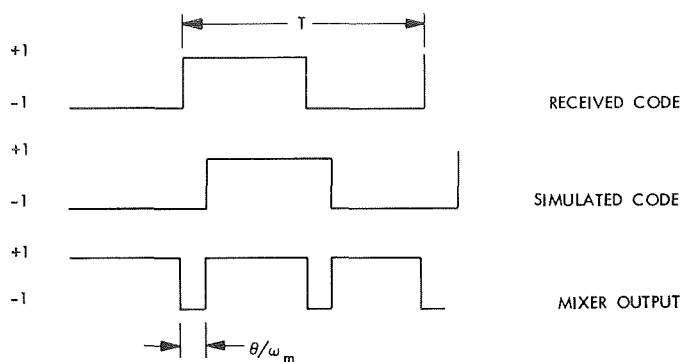
Fig. 6. Phase measurement of received code relative to the simulated code

zero shift; an average of zero would be a 90-deg shift; and an average of -1 would be a 180-deg shift. Units of time can be assigned to the phase, since 2π rad equals $1/f_m$ sec. Thus, from a knowledge of the synthesizer frequency f_s, a time measurement of the phase difference is made, since $f_m = 3\,f_s/64$.

Let τ be the time phase difference

$$\tau = \frac{\theta_0}{\omega_m} + \int_{t_0}^{t} 2\alpha\,dt'$$

Considering just the time-varying portion of τ gives

$$\Delta\tau(t) = \int_{t_0}^{t} 2\alpha\,dt'$$

$$= \int_{t_0}^{t} \frac{2B}{cf^2}\left(\dot{I}_{up} + \frac{1}{b^2}\,\dot{I}_{down}\right)dt' \qquad (14)$$

As shown in the publication cited in Footnote 7, the DRVID function is

$$DRVID = \int_{t_0}^{t} \frac{B}{f^2}\left(\dot{I}_{up} + \frac{1}{b^2}\,\dot{I}_{down}\right)dt'$$

so that

$$DRVID(t) = \frac{c}{2}\,\Delta\tau(t) \qquad (15)$$

The one-way range change error $\Delta\rho_\epsilon$ is just $1/2$ $DRVID$, so a conversion factor of $c/4$ or 0.075 m/ns gives the one-way charged-particle range change effect

$$\Delta\rho_\epsilon = \frac{c}{4}\,\Delta\tau(t) \qquad (16)$$

Thus, the drift away from the initial mu-ranging system acquisition automatically measures the columnar charged-particle dynamics needed for doppler calibrations.

c. Results. Figures 7a and b indicate data obtained with mu-ranging system from *Mariner VI* on November 24 and December 11, 1969, respectively. The range and doppler tracking was performed from the 210-ft-diam antenna station, DSS 14. *Mariner VI* was approximately 2 AU from earth and provided a received ranging power of -183 dBmW. The conditions for tracking on each day were arranged to provide the most favorable circumstances for charged particles to be exhibited in the ranging data—specifically, the largest received ranging power available—constant uplink ranging power and continuous ranging throughout pass.

Also shown in Fig. 7 are the range changes to be attributed to the earth's ionosphere as determined by VHF Faraday rotation monitoring, processed by B. D. Mulhall (SPS 37-58, Vol. II, pp. 66–73). These Faraday rotation measurements were made at DSS 13 by monitoring beacon transmissions of the ATS-1 geostationary
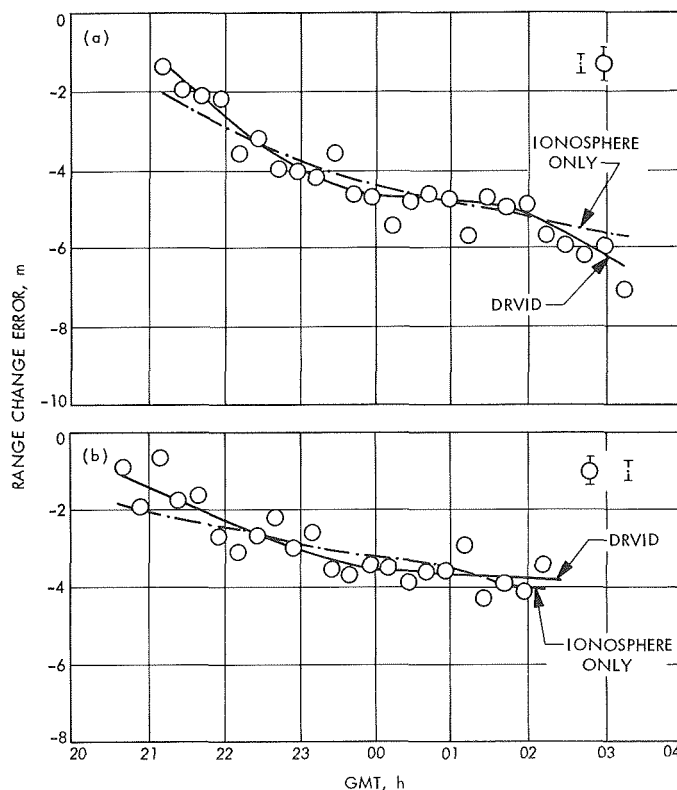

Fig. 7. Differenced range versus integrated doppler for Mariner VI using mu-ranging system: (a) on Nov. 24, 1969, and (b) on Dec. 11, 1969

orbiting satellite. The Faraday rotation method provides a total electron content measurement only along a constant ray path. This ionospheric content must then be mapped in space and time to correspond to the DSS 14 to *Mariner VI* ray path.

d. Discussion. In Fig. 7, the single most important feature is the close agreement (within 1 σ) of the DRVID data with the ionospheric data determined by a VHF Faraday rotation. In other words, despite the approximately 2 AU $(3.0 \times 10^8$ km) of interplanetary space traversed by the radio signals, virtually all the columnar charged-particle dynamics originated in the earth's ionosphere. Such an outcome was indeed fortunate, because it greatly simplifies the evaluation of whether or not the mu-ranging system provides a correct representation of charged-particle dynamics. Had the DRVID results differed significantly from the ionosphere alone, there would have been the necessity of establishing whether the differences were, in fact, space plasma effects or equipmental drifts. However, this close agreement between DRVID and the ionosphere is interpreted to mean that the mu-ranging system does correctly represent the charged-particle effect. To contend otherwise, would be tantamount to conjecturing a conspiratorial universe wherein instrumental variations have canceled out space plasma effects on two separate occasions but left the ionospheric contributions unaltered, to within the data noise of 0.8 m, 1 σ.

The apparent absence of space plasma effects in the DRVID data is, however, not entirely unexpected. The DRVID method is sensitive to only the charged particles which enter or leave the ray path during the observation time; so only an infusion or diffusion of space plasma on a time scale of 1 h or more would have been discernible in these data. The space plasma could contribute to DRVID in at least two ways, through the gradient of the steady-state solar wind and from solar spiral plasma arms transiting the ray path. From models of the solar wind the columnar charged-particle gradient effects[8] are found to be quite small (SPS 37-56, Vol. II, pp. 61–69) for the tracking situations of Fig. 7, amounting to only a few centimeters in 5 h which is substantially below the noise level of this DRVID data (0.8 m, 1 σ). However, gradient effects can become considerable (approximately 3 m of range change in 8 h) when the ray path approaches within 10 deg of the sun.[9] The apparent absence of

spiral plasma arms transiting the ray path has not been independently confirmed on these days, but based on the experience of the *Mariner V* dual-frequency experiment (SPS 37-60, Vol. II, pp. 89–95), had such a transit occurred there would have been a many meter change in DRVID in 5 h.

The two major limitations to the DRVID method are ranging jitter and equipment stability. If the ranging equipment drifts, such excursions will be interpreted as charged-particle dynamical effects. The charged-particle effect calibration goal for the 1971 era is an accuracy of 0.5 m of range change over an 8-h interval. Therefore, the ranging system should be stable to within 7 ns in 8 h. In addition, the ranging jitter should be small enough to discern a 7-ns range change in 20 min with received ranging power ≥ -170 dBmW.

Two closed-loop ranging tests have been made on the mu-ranging system (*Subsection 3*) totalling 12 h. No systematic linear trends are apparent, but rather the drift has a slowly varying character over several hours. An 8-h test showed a maximum excursion of 7.6 ns. With regard to the ranging jitter, the mu-ranging system exhibits a 1-σ value of 1 ns for integration times of 20 min at a received ranging power of -170 dBmW. Such a jitter comfortably meets the 7 ns desired. Also the 7.6 ns drift in 8 h seems commensurate with 7 ns desired; however, the paucity of diurnal drift information leaves the stability issue not completely resolved.

e. Conclusions. A recently developed binary-coded sequential acquisition ranging system has been used with the *Mariner VI* spacecraft specifically for evaluating its ability to automatically compute columnar charged-particle dynamical effects. Results from two tracking passes have clearly shown charged-particle effects which were independently verified as being of ionospheric origin. No space plasma dynamics were detected to within the limits of the data noise (0.8 m of range change); however, no conclusion can be drawn regarding space plasma effects in general.

Measurements of tracking station equipment drift have shown variations sufficiently low to allow charged-particle effects to be determined to within 0.6 m of range change over intervals of 5 to 8 h.

In an overall sense, these tests have shown significant progress toward demonstrating the accuracy of the DRVID charged-particle calibration method as automatically computed by the mu-ranging system. The

[8]Fliegel, H. J., *Charged Particle Effects Expected in DRVID Data From Mariners VI and VII,* Jan. 27, 1970 (JPL internal document).

[9]Muhleman, D. O., *Proposal for a General Relativity Celestial Mechanics Experiment,* May 17, 1970 (JPL internal document).

mu-ranging system artifice of doppler rate-aiding, for charged-particle effect calibration, could make a significant contribution to radio navigation goals for the 1971 era.

5. Status of DSS Location Solutions for Deep Space Probe Missions: Comparison With the SAO Standard Earth 1969 Station Locations, N. A. Mottinger

a. Introduction. This is the fifth article of a series discussing the estimates obtained of the locations of the eight tracking stations in the DSN using the radio tracking data received from numerous deep space probe missions. The current best estimate is compared with the locations derived at the Smithsonian Astrophysical Observatory (SAO) where Baker–Nunn camera optical data and laser data have been used to estimate numerous earth gravitational parameters in addition to station locations. Comparisons with these independently obtained solutions form an important check on current work being done and often prompt investigation into otherwise overlooked areas in order to explain existing differences between solutions. For example, the agreement shown in this comparison has improved by a factor of 2 to 3 with previous comparisons, but there are still systematic differences averaging 21 m in longitude. Comparisons in distance off the spin axis agreement nearly average to zero ±7 m.

If the systematic deviation in longitude is removed, the agreement between solutions is within the bounds of the uncertainties associated with them.

b. Discussion. This series of articles has been written to document the progress being made in determining tracking station locations. To meet the navigation goals of recent and future missions the uncertainties in DSS longitude σ_λ, and distance off the spin axis σ_{r_s}, have had to be known on the order of 1 m and are approaching the fractional meter level. The need for accuracy at this level was shown in an article by Hamilton, Grimes, and Trask (SPS 37-44, Vol. II, pp. 4–11), where an approximate method for determining the navigational accuracy obtainable during the encounter phase of a mission is presented. Other articles (SPS 37-60, Vol. II, pp. 77–89 and SPS 37-56, Vol. II, pp. 45–48) have discussed location solutions obtained from the postflight analysis of various deep space probe missions. These location uncertainties are below the 10-m level and are approaching the 1-m plateau. An important part of achieving accuracies at this level has been the application of corrections

for the charged particles in the earth's ionosphere. The set of station locations (SPS 37-60, Vol. II, p. 83) used in this paper to compare with the latest SAO solutions represents a combination of solutions from several missions. Ionosphere corrections were applied prior to estimating station locations. The combined set is referred to as Location Set (LS) 25, or for the purpose of this paper as the JPL locations.

Among the SAO station location estimates obtained by Gaposchkin and Lambeck (Ref. 1), four are near DSN antennas, such that the relative survey coordinates of each can be used to refer an SAO solution to the antenna. This was done by Lambeck for antennas at DSS 12, DSS 61, DSS 51, and DSS 41. In addition to referring the SAO camera solution to DSS 41 in Woomera, the solution was also extended to DSS 42 at Canberra, about 1200 km away. The comparison at DSS 42 is handled in *Paragraph d.*

The comparison shown in Table 5 indicates that there still is a systematic difference in absolute longitude solutions. Although it has been larger by about a factor of 2 in comparisons made within the last year (SPS 37-56, Vol. II), its reduction may be attributed to changes in both the SAO and JPL solutions. Since 1966 when the first comparisons were made, changes of 32 m have occurred in the JPL longitude solutions (Table 6 and Figs. 8 and 9). Of the 32 m, 20 to 25 m are associated with changing from the lunar missions to the planetary (SPS 37-56, Vol. II), due to the difference in the adopted equinox of the lunar and planetary ephemerides. Within the last year another change averaging about 7 m occurred when changes were made to Universal Time 1

Table 5. SAO 1969[a] station locations minus JPL LS 25

DSS	Δr_s, m	$\Delta\lambda$, deg $\times 10^{-5}$	$\Delta\lambda$, deg $\times 10^{-5}$ (DSS 12 — DSSs in 1st col.)
12	7.1	−25	—
41	−6.7	−16	−9
42	(−8.0)	(−11)	(−14)
51	5.0	−19	−6
61	−4.4	−24	−1
Average excluding DSS 42	0.3	−21	−5.3

[a]From Lambeck (Ref. 1, Table 6).

Table 6. SAO 1969 minus SAO 1966 and JPL 1969 (LS 25) minus JPL 1966 (LS 4)

DSS	$\delta\lambda$, deg $\times 10^{-5}$ ($\sim$1 m)		δr_s, m	
	SAO	JPL	SAO	JPL
12	0	−27	−2.9	14
41	34	−32	9.9	−0.1
51	24	−24	10.7	10.2

(UT1) by the U.S. Naval Observatory and the ionospheric corrections were applied.

It is particularly important to note the reduction in the scatter when comparing the JPL and SAO 1969 longitudes. This is primarily due to the changes in the SAO solutions from 1966 to 1969 when more data became available for the South African and Australian sites. Geometrical and dynamical (SAO) reductions are combined to produce the final location estimate. More detail about these two reductions can be obtained in Refs. 1 and 2. The combination of the two is essential, since the geometrical solution, which is independent of the orbit, determines directions between stations that simultaneously view the satellite. The dynamical solution determines the orbit and absolute station locations. In the previous SAO solution—Standard Earth 1966—the geometric solution was poor in South Africa (DSS 51) and nonexistent in Australia (Ref. 1, p. 9).

One possible error source could be a difference between the SAO star catalog and the JPL planetary ephemeris equinox or inertial reference point. However, the 21 m in longitude which is equivalent to about 0.7 sec of arc is too large to be attributed to an inconsistency of this type. The SAO catalog is reported to be on the FK4 system, and although the planetary ephemeris is actually based upon several catalogs, the probability that it differs from the FK4 by this much is small. How catalog errors are affecting both the JPL and SAO solutions is not known.

Another item to be investigated is the Universal Time 1 (UT1) used to process the data. Differences do exist between the U.S. Naval Observatory UT1 and that of the BIH[10] of Paris, France. Converting the JPL locations to the BIH UT1 puts these locations on the same timing system as SAO, but serves to make the longitude com-

---

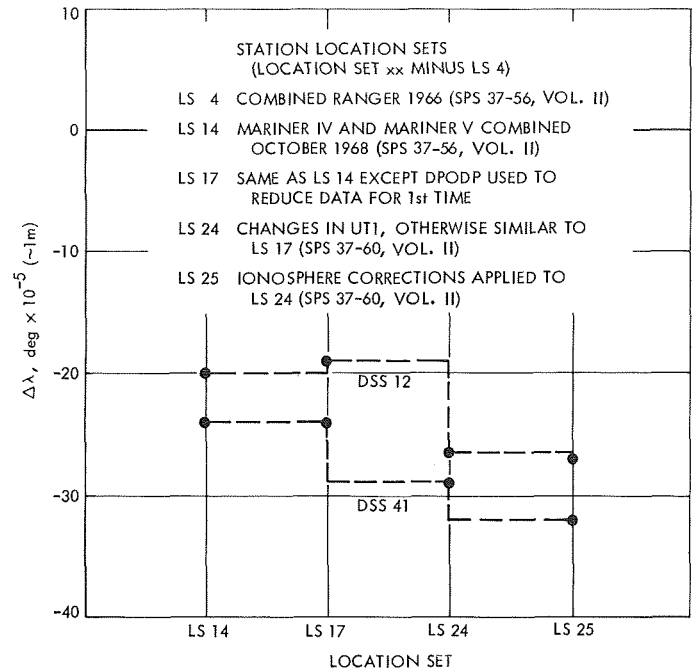[10] BIH = Bureau International de l'Heure (Paris).

Fig. 8. Changes in JPL longitude solutions since LS 4 (1966)
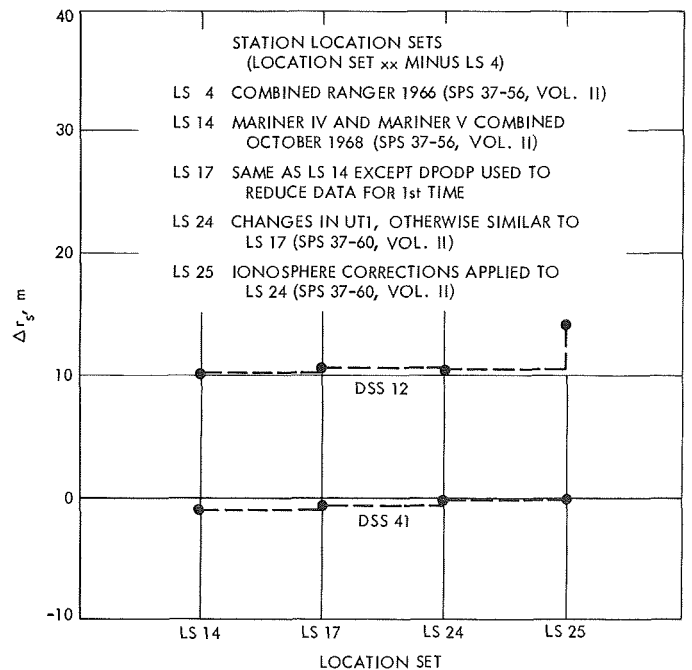

Fig. 9. Changes in JPL spin axis solutions since 1966

parison worse by about 2 m and also has other interesting effects on the JPL independent mission longitude solutions, as will be discussed later in the article and also in *Subsection 6.*

The differences in spin axis, r_s, solutions obtained appear random in that the average disagreement is ⅓ m in spite of the 14-m scatter (Table 5). In Table 6, large changes in both SAO and JPL r_s solutions have occurred since 1966. A primary cause for the JPL location changes is the charged-particle effects in the earth's atmosphere. The 1966 solutions were obtained using L-band doppler data, and the 1969 solutions by using S-band data and correcting for ionospheric effects. The L-band data is about six times as sensitive to the ionosphere. The 10- to 14-m bias may be attributed directly to this. It is probably merely coincidental that the solution at DSS 41 agrees so closely with the 1969 solutions. It is expected that there is some error remaining in the JPL spin-axis solutions, due to the uncalibrated space plasma charged-particle effects. Changes greater than 1 or 2 m are not expected, however, when this calibration is made. The change in the JPL longitude and r_s are also graphically presented in Figs. 8 and 9 for two stations common to the 1966 and 1969 solutions.

Aside from the large increase of data for the SAO solutions the other significant change which might affect the agreement is the decrease in distance between the SAO and JPL California sites from 1966 to 1969. Survey ties are necessary to transfer locations from either agency's site to the other. In 1966 the nearest Baker–Nunn camera to DSS 12 was nearly 1000 km away; in 1969, one only about 10 km away was used. This would aid in diminishing any possible error in the geodetic survey connecting the sites. Separation at the other sites, except DSS 42, is on the same order.

c. Longitude uncertainties. To be explicit in assigning uncertainties for the longitude solutions, Table 7 was prepared listing nine contributing error sources, which were then root-mean-squared. Note that several items are larger for *Mariner VI* than for *Mariners IV* and *V*. This is because the final measurements for these quantities are not available at this time. UT1 uncertainties[11] are shown for the Naval Observatory data and for BIH. Ephemeris errors[12] are in terms of the target body with respect to the earth. Ionosphere errors[13] were expressed in terms of changes which may occur when the data is reprocessed, using improved fitting techniques and more data than was previously available. The troposphere estimate[14] is an upper bound and is probably a factor

[11]Estimated by P. Muller and H. Fliegel.
[12]Prepared by W. Melbourne, J. Lieske, and S. Chesne.
[13]Estimated by B. Mulhall.
[14]Estimated by V. J. Ondrasik.

Table 7. Contributing error sources for Goldstone DSS longitude solutions

Source	Mariner IV[a]	Mariner V[a]	Mariner VI[a]
White noise	0.8	0.9	0.8
Pole motion	0.5	0.5	0.5
UT1	2.5 (1.5)[b]	2.5 (1.5)[b]	3.0
Ephemeris[c]	2.0	1.9	3.0
Ionosphere	2.0	2.0	3.0
Space plasma	0.5	0.5	0.5
Troposphere	0.5	0.5	0.5
Frequency system	0.2	0.2	0.2
Other	0.2	0.2	0.2
Miscellaneous forces	—	—	1.0
rms	4.2 (3.4)	4.1 (3.4)	5.4

[a]Measurements in deg × 10⁻⁵ (~ 1 m).
[b]U.S. Naval Observatory data; BIH UT1 in ( ).
[c]Error in position of target body with respect to earth.

of 2 greater than any changes to be expected. The frequency system concerns itself with the stability of the transmitter and associated equipment at the station and on board the spacecraft. Others refer to possible errors due to electrical path-length variations in station hardware. Miscellaneous forces apply to *Mariners VI* and *VII* where quantities of gas were expelled randomly a few minutes before encounter. The entries in the table should not be taken as final. In certain instances an educated guess has been made. This is particularly true for the last two items. Studies are under way using simulated data to determine how much longitude information may be recovered from the *Mariner* Mars 1969 spacecraft where the discharge of gas accompanied the fly-by of the planet. Perturbations will be injected upon the nominal spacecraft trajectory to test the ability of the program to recover the known solution. Station locations will also be estimated as a part of this process to determine the effects of these perturbations on this part of postflight analysis.

Several root-mean-squared sums were taken to show the contribution of the larger error sources and the effects of the smaller uncertainty on the BIH UT1. It can be noted that the ionosphere, UT1, and ephemeris uncertainty are the primary contributors to the sum. It is important to note that the ionosphere correction procedures are still being developed and the error

implied is more indicative of possible changes in future reductions.

If the systematic longitude difference is removed or relative longitudes are compared, the resulting disagreement is within the uncertainties associated with the solutions. The SAO values are reported accurate around the 10-m level, the JPL approaching the 1 to 2-m level in r_s and 2.5 m based upon the combined *Mariner IV* and V solution uncertainties for absolute longitude. The *Mariner VI* estimates have not been included in any combination.

Relative longitudes are also compared in Table 5. These comparisons may be more meaningful than any other, since numerous error sources associated with the absolute longitude solutions cancel when the relative longitudes are examined. Conditions peculiar to each site are important. Clock synchronization is one; atmospheric effects are another. In the JPL solutions, remaining errors in the ionosphere corrections could affect the solutions. In some cases approximations to these corrections had to be made by mapping from sometimes distant locations where the data was available. The ionosphere calibrations are going to be redone; in doing so, these temporary corrections can be replaced on-site where data is now available. When the values in Table 5 are compared with those in Table 8, an improvement by a factor of 4 can be noted. The changes in the JPL relative longitudes from the previous comparison vary from 2 to 6 m. Based upon the observed scatter among the reductions used to produce LS 25, an estimate of

Table 8. Comparison of SAO Standard Earth 1966 DSN locations with combined JPL LS 4 1966 results

DSS parameter	SAO	SAO — LS4, m
$r_{s_{12}}$	5212.0635	23.5
$r_{s_{41}}$	5450.1820	−17.7
$r_{s_{51}}$	5742.9360	4.0
λ_{12}	243.19431	−51
λ_{41}	136.88701	−80
λ_{51}	27.68500	−71
$\Delta\lambda_{12-41}$	106.30730	29
$\Delta\lambda_{41-51}$	109.20201	−9
$\Delta\lambda_{12-51}$	215.50931	20

about 1½ m appears reasonable for the uncertainty on the relative longitudes.

d. Survey comparison in Australia. The comparison at DSS 42 was omitted from the previous discussion because the same SAO camera solution was used to infer the location for DSS 41 and DSS 42, which requires a long geodetic tie in order to include the second station. After Lambeck completed this tie, it was interesting to note that the longitude solutions obtained at DSS 42 agreed better with LS 25 than did the value for DSS 41. His work was not all geodetic. He reports in Ref. 3, p. 5, that by using solutions from doppler tracking performed by Anderle of the U.S. Naval Weapons Laboratory, distortions were removed in the Australian Geodetic survey net. It has been assumed for some time that distortions did exist. An example of this is shown in Table 9, where the classical geodetic survey relative locations are compared with LS 25 and with those of Lambeck. Very significant differences exist. The classical results differ by 28 and 11 m, respectively, in relative r_s and longitude. Lambeck's disagree with LS 25 by only 1.2 and 5.2 m in the same order. An accuracy assessment of this work is not available. The comparison with LS 25 indicates that it would certainly be at or below the 5-m level.

e. UT1 investigations. At the time LS 25 was produced and used to support the *Mariner* Mars 1969 inflight data reduction with the associated ephemerides and timing data, the agreement noted between predicted encounter parameters from cruise data versus the derived parameters obtained after the probe passed the planet indicated that the locations were accurate below the 5-m level. Soon after encounter a preliminary longitude estimate was obtained from *Mariner VI* and later corrected for

Table 9. Survey comparison in Australia at DSSs 41 and 42

Geodetic	$\Delta\lambda$, deg	Δr_s
SAO[a]	−12.093846	244.8495 km
JPL[b]	−12.093912	244.8767 km
SAO & JPL	6.6×10^{-5}	−27.2 m
LS 25	−12.093794	244.8483 km
SAO — 25	-5.2×10^{-5}	1.2 m

[a]Combination of geodetic and doppler tracking (Ref. 3, p. 5, and private communication with Lambeck).
[b]Geodetic survey only.

differences between the UT1 used at that time and the value available several months after the mission. Available ionosphere corrections were also applied. This solution was plotted along with the *Mariner IV* and *V* solutions for DSS 12. A trend appears between these three solutions, indicating that DSS 12 may be moving westward at about 1 m/yr. An item of immediate concern was the UT1 used to process the data: polynomials prepared for data processing have been based upon the U.S. Naval Observatory at Richmond. Other sources, such as the BIH, also distribute UT1. Their data was prepared in polynomial form (SPS 37-57, Vol. II, pp. 42–51) and used in reductions with the orbit determination program to recompute for station locations using the *Mariner IV* and *V* data. Hand calculations for the expected longitude shift due to differences between BIH and USNO UT1 were prepared and noted to agree with the shifts obtained in the orbit determination program. An approximate slope of 1¼ m/yr can be inferred from either the Richmond or BIH data. These solutions are shown in Fig. 10. A very important part of establishing this drift involves the uncertainty associated with each longitude estimate. When two Goldstone deep space stations were in the reduction together, the survey locations have been used to transfer each solution to station 12. These have not agreed exactly, and hence have established a lower bound for the quality of the longitude solution. This could only be done for *Mariners V* and *VI*, since only one Goldstone DSCC station was tracking *Mariner IV* at encounter. Estimates of the total uncertainty were prepared in Table 7.

Fliegel and Lieske[15] have studied numerous sources for the drift in terms of timing and associated star catalog errors. Their initial conclusions have been that the timing data could not be responsible for the apparent constant westward drift in station locations. The drift may turn out to have been merely coincidental and not due to perturbations in UT1. Investigations into this and other error sources, such as the ephemeris, may produce the solution to this problem.

f. Conclusion. The comparison between the SAO standard earth 1969 and the JPL Location Set 25 station locations shows the least scatter of all previous comparisons made. Changes have occurred in both the SAO and JPL locations between 1966 and 1969 as a result of improved data packages and data handling. The relative

---

[15]Fliegel, H. F., and Lieske, J. H., *Error Analysis of U.S. Naval Observatory Timing Data*, Jan. 6, 1970 (JPL internal document) and *Subsection 6*.
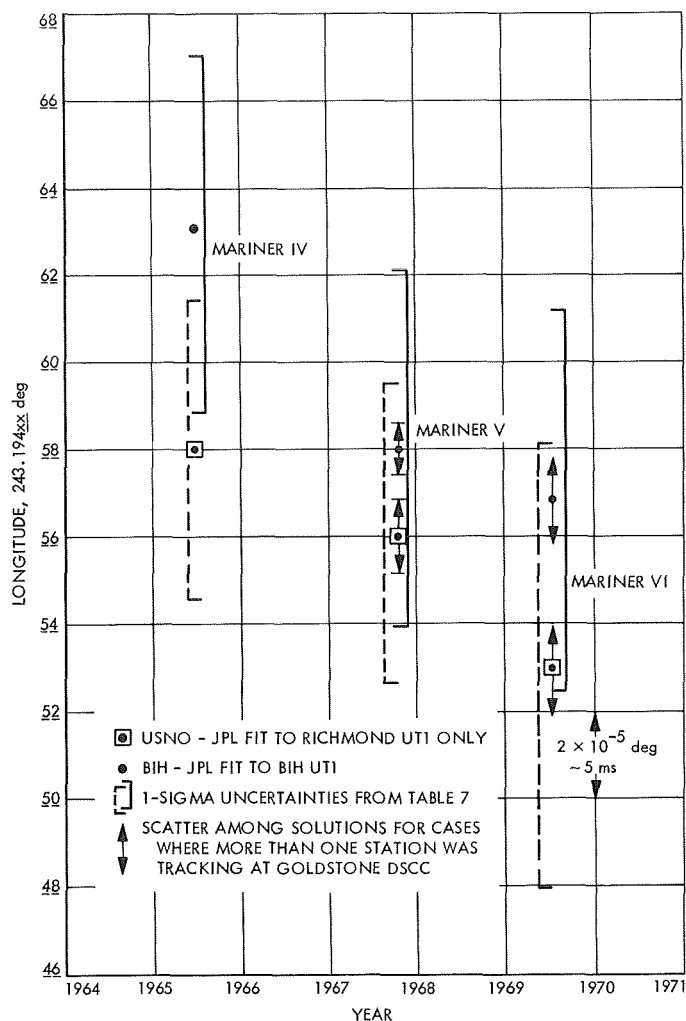

Fig. 10. Longitude solutions for DSS 12 using USNO and BIH UT1

agreement between JPL and SAO has improved by factors of 2 to 3. Realization of fundamental differences between lunar and planetary ephemerides was a big factor in improving longitude agreement. The problem of the variation in longitude as a function of UT1 remains to be resolved.

References

1. Gaposchkin, E. M., and Lambeck, K., *New Geodetic Parameters Standard Earth*, Smithsonian Astrophysical Observatory, Cambridge, Mass., Dec. 1969.

2. *Geodetic Parameters for a 1966 Smithsonian Institution Standard Earth: Vol. I.* Edited by C. A. Lundquist and G. Veis. Smithsonian Astrophysical Observatory, Cambridge, Mass., 1966.

3. Lambeck, K., "Comparisons and Combinations of Geodetic Parameters Estimated From Dynamic and Geometric Satellite Solutions and From *Mariner* Flights," paper prepared for Twelfth Plenary Meeting of COSPAR, Prague, May 1969.

6. Inherent Limits of Accuracy of Existing UT1 Data,

H. F. Fliegel and J. H. Lieske

a. Introduction. In order to determine the orbit of a spacecraft from stations on the surface of the earth, the instantaneous position of each station must be known in an inertial coordinate system. An error of 1.00 ms in time is equivalent to an error of 0.379 m in the longitude of the DSS 14 antenna in the coordinate system in which time is determined.

One may distinguish two kinds of timing errors of importance to JPL missions: (1) random or periodic errors familiar in every branch of astrometry; and (2) a slow rotation of the system of coordinates in which time is determined—due, for example, to an error in the adopted value of precession or in the values of proper motions of timing stars—which would cause an apparent secular drift of all stations with respect to Greenwich. Mottinger has reported (SPS 37-60, Vol. II, pp. 77–88) evidence for such a secular drift. All the known sources of error in timing data which might produce the reported effect are examined here. We shall conclude that the known sources of error in timing would produce an effect with sign opposite to the reported drift and that the evidence cannot be explained in terms of timing error.

We describe the sources of error in the values of UT1 − A.1 supplied by the U. S. Naval Observatory and used in the timing polynomial (TPOLY) program (SPS 37-57, Vol. II, pp. 42–51). These values are derived from two virtually identical photographic zenith tubes (PZT)—a device for measuring the time of zenith transit of stars—one at the U. S. Naval Observatory in Washington, D.C. and one at the Naval Observatory substation in Richmond, Fla. Although only data from the Richmond PZT, which is less frequently clouded out than that at Washington, is currently used by TPOLY, data from either or both can be used. Data from both will be discussed here. The best estimate of the true value of UT1 is provided by *Circular D* of the Bureau International de l'Heure (BIH), which supplies a weighted and corrected mean of measurements from 68 instruments throughout the world. These data are not suitable for JPL mission requirements because they are not available until 4 to 6 wk after observations are made, but they provide a standard against which the errors of observation of any one instrument can be measured.

b. Long-term secular errors. Long-term systematic timing errors, which produce the illusion of a longitude drift of one time observatory with respect to another,

were reported at the IAU–IUGG Symposium held in Stresa, Italy, in March, 1967. Stoyko (Ref. 1) reported that observatories in North America appeared to have approached those in Europe by 0.6 ms/year from 1925 to 1965. Torao, Okazaki, and Fujii (Ref. 2) found, however, that this rate was highly variable. For the period 1933 to 1962, they obtained average results in fair agreement with Stoyko's, but for the period 1956.8 to 1965.9, they discovered a westward drift of the mean of Washington and Richmond of 1.23 ±0.29 ms/year ($1\rlap{.}''84$ ±$0\rlap{.}''42$/ century) with respect to the unweighted average of five European observatories included in the study. This effect is presumably caused by the net error of the proper motions in right ascension ascribed to the PZT stars of Washington and Richmond.

c. Precession and equinoctial motion. A systematic bias in the proper motions in right ascension of a star catalog is commonly called an "equinoctial" motion. It is believed to be caused by changes in the techniques of observation, since any observational error between two observations of a given star at two greatly differing epochs will result in an incorrect proper motion for the star.

The *raison d'être* for astronomers accepting the existence of an equinoctial motion stems from difficulties commonly encountered in discussions of precession errors. Ideally, an error in precession is compensated by a catalog proper motion error having the opposite sign (SPS 37-55, Vol. III, pp. 13–16, Feb. 28, 1969). However, it has been found that if one analyzes the proper motions of a given star catalog, one finds that the estimate for the precession error as computed from proper motions in right ascension differs from the precession error estimated from proper motions in declination (Ref. 3). The equinoctial motion Δe (arc seconds per century) has then been introduced as a parameter which affects the right ascensions but not the declinations. The net effect is that estimates for the precession error as computed from proper motions in right ascension will then be consistent with the estimate computed from the declination proper motions. Physical justification for the introduction of the equinoctial motion Δe is based on the supposition that changes in observational techniques (eye-and-ear, traveling wire, chronograph, etc.) have introduced time-like discontinuities which are absorbed in catalog proper motions.

All star catalogs contain proper motion errors due to equinoctial motion. The best current star catalog system, the FK4, is believed to contain a proper motion error due to the equinoctial motion given by $\Delta e + \Delta\lambda = + 1\rlap{.}''20$

±0″.11 per century, according to Fricke (Ref. 4), where Δλ represents an error in planetary precession.

Since the equinoctial motion was introduced because of its entanglement with precession-like effects, one logically also should consider precession errors when discussing errors due to equinoctial motion. The effect of precession errors on radar data has been discussed by Lieske (SPS 37-54, Vol. II, pp. 7–11), and its similarity with longitude or UT1 errors is apparent.

d. Random and periodic errors. In addition to the random errors of measurement common to all astrometry, two special error sources—catalog error and zenith refraction—are believed to be responsible for a large part of the final residuals in timing data. The purely random errors of measurement may be expected to be small. The "seeing disk" of a single star image is usually 1 to 2 arc sec in diameter and has positional uncertainty of 0″.1 to 0″.4, that is, 6 to 25 ms. Since each star produces four usable images, and since the average number of stars observed is large (for example, 16 for the Washington and 16 for the Richmond PZT during the first six months of 1969), the purely random error of a single night's time determination should be less than 3 ms. The actual error, however, is somewhat larger. Because the PZTs used for time determination have a narrow field of view, the number of stars that can be observed on a given night is not large (in practice not more than 30), and catalog errors are most troublesome. The standard deviation calculated for a single night's time determination has increased for the Richmond PZT from $\sigma = 15$ ms in 1962 to $\sigma = 21$ ms in 1968, and had been increasing at Washington from $\sigma = 15$ ms in 1962 to $\sigma = 22$ ms in 1968. Such behavior is most reasonably attributed to errors in the previous catalog's star positions. If the ideal could be attained of assimilating all PZT star positions to the reference frame of the FK4, then, of course, there would still be systematic errors in timing due to the systematic error in right ascension of the FK4; and the values of this error, of course, are unknown, since there is no other fundamental catalog of equal accuracy to which the FK4 may be compared. However, the systematic differences between the FK3 and the N30[16] average 6 ms at declination + 40 deg (Ref. 5). It is reasonable to suppose that a systematic error, varying with right ascension, of perhaps 2 or 3 ms amplitude exists in the FK4 and, therefore, in both BIH data and the most recent Washington data.

---

[16]Morgan's *Catalog of 5268 Standard Stars* (not strictly a fundamental catalog).

To state the mean periodic error in right ascension of the Washington catalog would be meaningless, since that catalog has recently been smoothed. The mean annual periodic error of Richmond, measured against BIH for 1962 to 1968, is 4 ms. A significant amount of this is due to Group 6 (a group of stars observed in summer) which in 1968 gave values 9.5 ms in excess of other groups. Thus, in May and June of 1966 to 1968 the size–frequency distribution of residuals from the JPL TPOLY functions was significantly bimodal, which is reasonably explained as the effect of Group 6, which, because of changing weather conditions, was observed on some nights but not others. On the other hand, there is no significant correlation of standard deviations for individual nights with lunar phase, and no significant harmonic of monthly period in the time data, which shows that loss of faint stars during the bright of the moon does not detectably bias the results.

Short-term quasiperiodic differences between the final values of UT1 − A.1 supplied by the U.S. Naval Observatory and the values of UT1−A.1 published by the BIH over an interval of about 1800 days are illustrated in Fig. 11. To a crude approximation, for a date selected at random one may compute the probability of the occurrence of a residual of given size by supposing that the U.S. Naval Observatory final data obeys a gaussian distribution with $\sigma = 3\frac{1}{2}$ ms. This implies that the instantaneous positions of the DSS 14 antenna, for example, will be in error by more than 1 m on about 45% of randomly selected dates and in error by more than 2 m on about 13% of randomly selected dates from short-term errors alone (assuming that U.S. Naval Observatory final data is used). To this must be added a possible drift of ½ m/yr or so from net catalog error in right ascension. The errors in BIH data are presumably smaller, but are completely unknown.

The most likely source of short-term timing error is zenith refraction. An error of 6 ms would be produced (Ref. 6) by an east–west temperature gradient of 0.05°C/km on an isobaric surface—a not unreasonable value for the U.S. Naval Observatory, which is located on the slope of the Wisconsin Avenue ridge at the outskirts of downtown Washington. The Richmond staff has reportedly found a significant correlation of systematic error with the passage of weather fronts, and the whole problem is receiving careful attention.

e. Discussion. Expressed in terms of apparent changes in station location, expected timing errors would be as follows: Assuming no error in the fit of TPOLY functions
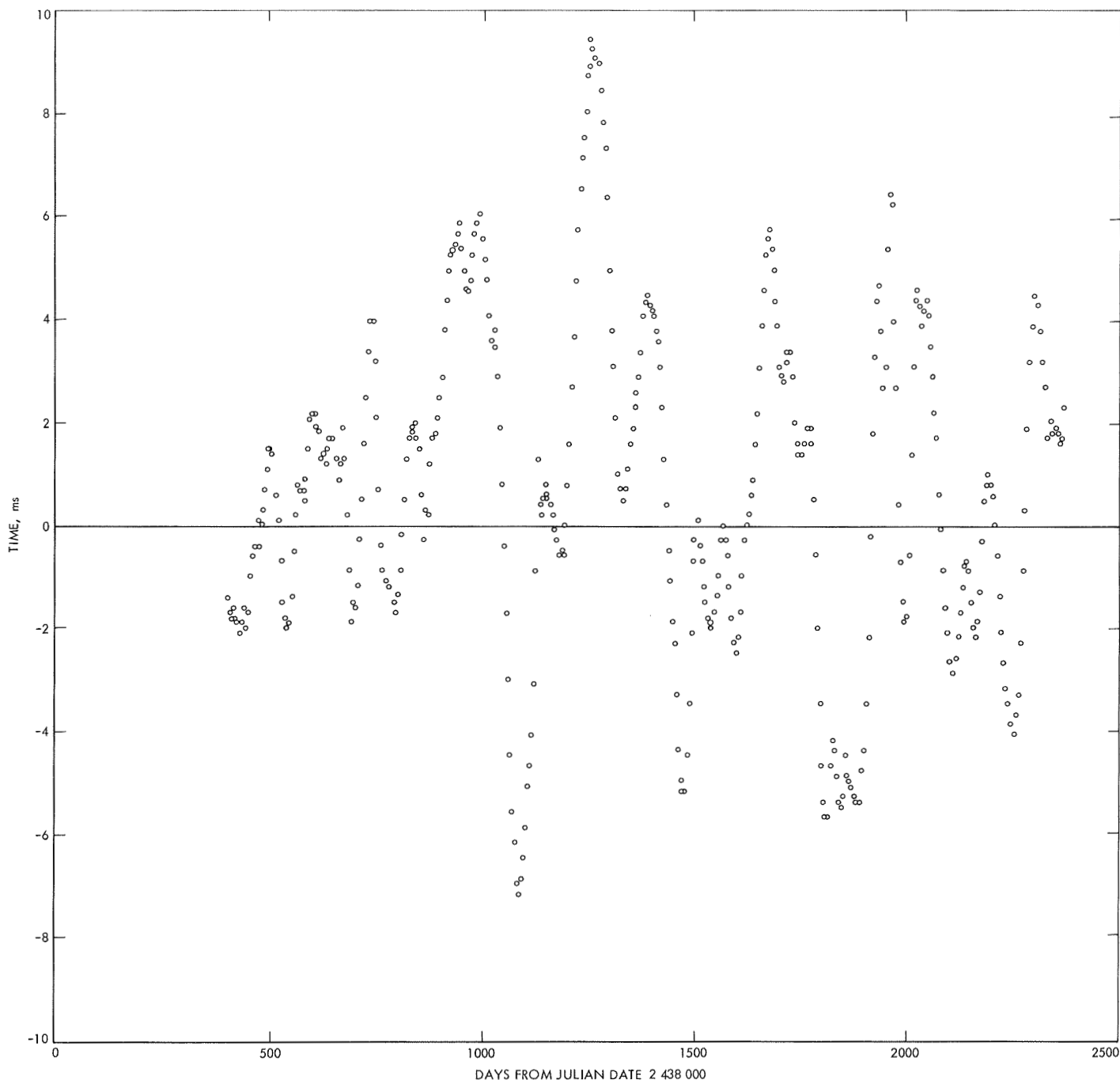
Fig. 11. USNO final values [UT1 — WWV] minus [BIH (UT1 — UTC)]

to U.S. Naval Observatory data, one expects a random error of $\sigma = 1\frac{1}{2}$ m. The results of Torao, et al., imply that Washington and Richmond appeared to drift westward by 0.6 m/yr with respect to BIH. This would be equivalent to an eastward drift of DSN stations with respect to Washington and Richmond, opposite to the effect found by Mottinger. The officially adopted BIH system of coordinates—that is, the frame of reference of the FK4—

is rotating westward by 0.4 m/yr, according to Fricke; however, this effect is nearly canceled by the error in the adopted value of precession, which enters the DPODP directly in its computation of the orientation of the earth in space. This precession error maps into an apparent eastward drift of 0.3 m/yr. If a new value of the constant of precession is adopted by JPL, then some compensation for the equinoctial motion of the FK4 will be required

either in TPOLY or in the double precision orbit determination program (DPODP). We know of no systematic error in timing data which could produce a constant apparent westward drift of station locations.

Mission requirements for *Mariner* Mars 1971 include timing and polar position data—that is, information specifying the orientation of the earth in space in an inertial system of coordinates—to an accuracy of 2.5 ms. Since the random residual of USNO final data exceeds this value about half the time, we conclude that data from additional sources—for example, from BIH—will be necessary. The limit to the accuracy of BIH data is set by the FK4, and is about 2 or 3 ms. Therefore, to meet more stringent requirements of post-*Mariner* missions, another type of data, such as that provided by very long baseline interferometry (VLBI) or laser-ranging operations, will be required.

References

1. Stoyko, N., "Variation Séculaire des Longitudes," in *Symposium on Continental Drift, Secular Motion of the Pole, and Rotation of the Earth*, pp. 57–62, IAU Symposium No. 32, held in Stresa, Italy, 1967. Edited by W. Markowitz and B. Guinot. Springer-Verlag, New York, 1968.

2. Torao, M., Okazaki, S., and Fujii, S., "Secular Variation of Longitude and Related Problems," in *Symposium on Continental Drift, Secular Motion of the Pole, and Rotation of the Earth*, pp. 45–51, IAU Symposium No. 32, held in Stresa, Italy, 1967. Edited by W. Markowitz and B. Guinot. Springer-Verlag, New York, 1968.

3. Böhme, S., and Fricke, W., "Astronomical Constants: A Survey of Determined Values," in *Symposium on the System of Astronomical Constants*, p. 285, IAU Symposium No. 21, held in Paris, 1963. Edited by J. Kovalevsky. Gautier-Villars, Paris, 1965.

4. Fricke, W., *Astron. J.*, Vol. 72, p. 1368, 1967.

5. Scott, F. P., "The System of Fundamental Proper Motions," in *Basic Astronomical Data*, p. 15. Edited by K. A. Strand. University of Chicago Press, 1963.

6. Alley, C. C., and Bender, P. L., "Information Obtainable From Laser Range Measurements," in *Symposium on Continental Drift, Secular Motion of the Pole and Rotation of the Earth*, p. 89, IAU Symposium No. 32, held in Stresa, Italy, 1967. Edited by W. Markowitz and B. Guinot. Springer-Verlag, New York, 1968.

7. Very Long Baseline Interferometry and Its Sensitivity to Geophysical and Astronomical Effects, J. G. Williams

a. Introduction. This is the first of several articles which will investigate very long baseline interferometry (VLBI). These studies will be directed toward the suitability of the DSN as a VLBI network, tracking of space-

craft by VLBI, and determination of additional data such as polar motion, UT1, and station locations that are needed in orbit determination. The first part of this paper will outline the technique of VLBI. The second part will investigate the sensitivity of VLBI data to various astronomical and geophysical effects.

b. Technique. Figure 12 shows a schematic diagram of an interferometer. Two antennas labeled 1 and 2 receive a signal from some extraterrestrial source. Figure 13 shows the geometry of the situation. The two antennas are separated by a distance D, and the vector from the first to the second antenna will be called the baseline vector. The direction of the radio source makes an angle ψ to the baseline vector. There will be a difference in the time of reception of the signal at the two
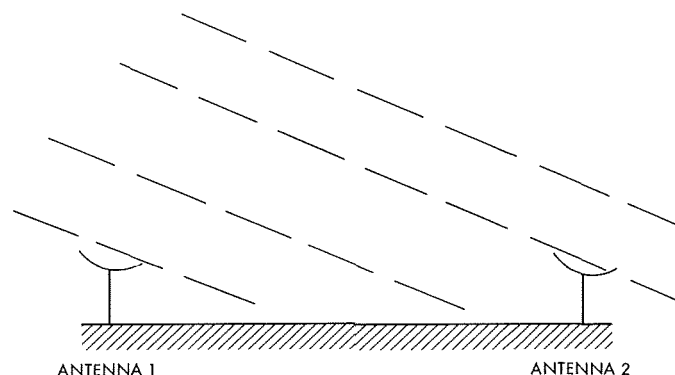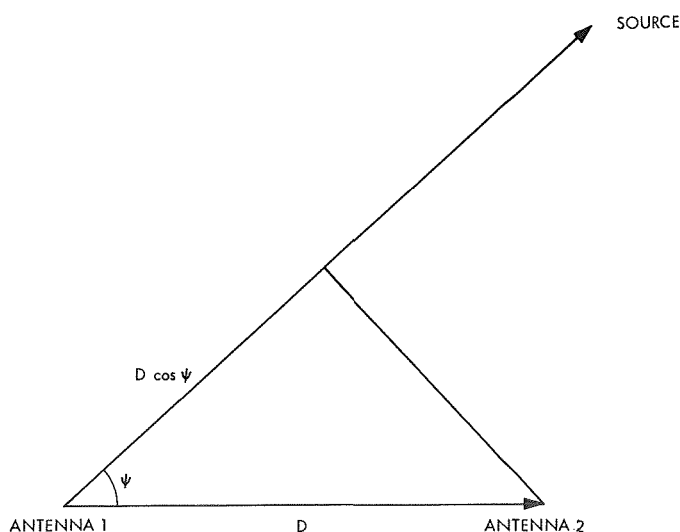

Fig. 12. Interferometer pair

Fig. 13. Interferometer geometry

antennas, and this time delay τ_g is given by

$$\tau_g = \frac{D}{c} \cos \psi \qquad (1)$$

where c is the speed of light. This time delay is an observable quantity. It has a maximum possible value of the earth's radius/c, or 0.021 s.

For the purpose of illustration, consider the signal to be monochromatic so that the electric field at antenna 1 may be represented as

$$A \cos \omega t \qquad (2)$$

where A is the amplitude, ω the frequency, and t the time. The electric field at the second antenna is

$$A \cos [\omega (t - \tau_g)] \qquad (3)$$

In a conventional interferometer the output of the two antennas is brought together and beat against one another to recover τ_g. In the case of VLBI, however, the output of the two antennas is recorded separately on magnetic tapes, and the tapes are later brought together for processing.

At S-band frequencies (2.3 GHz), the frequency is too high to record, but this can be overcome by mixing the signal from the two antennas with signals from two local oscillators with frequencies ω_1 and ω_2. This results in signals composed of frequencies $\omega + \omega_1$ and $\omega - \omega_1$ at the first site and $\omega + \omega_2$ and $\omega - \omega_2$ at the second. The local oscillators have S-band frequencies so that one frequency is about 4.6 GHz, and the other is low enough to record. The high-frequency part is then filtered out so that the voltage recorded at antenna 1 is

$$V_1(t) = A \cos [(\omega - \omega_1) t + \phi_1] \qquad (4)$$

and that recorded at antenna 2 is

$$V_2(t) = A \cos [(\omega - \omega_2) t - \omega \tau_g + \phi_2] \qquad (5)$$

Unknown phase shifts ϕ_1 and ϕ_2 are introduced by the receivers and the local oscillators. The frequency of Eq. (5) is

$$\omega - \omega_2 - \omega \frac{d\tau_g}{dt}$$

and the quantity

$$v_F = \omega \frac{d\tau_g}{dt} \qquad (6)$$

is known as the fringe rate. It is just the negative doppler shift between the two sites. Cross correlation of the two records allows the time delay τ_g and fringe rate v_F to be measured. For the purposes of this article these two quantities will be considered the fundamental data types.

From Eq. (1) the effect of a small change $\delta\tau_g$ in τ_g can be related to a change in angle $\delta\psi$.

$$\delta\tau_g = -\frac{D}{c} \sin \psi \delta\psi \qquad (7)$$

If the time delay is varied by one wavelength, it will cause the cross correlation to undergo one cycle of a sinusoidal variation (referred to as a one-fringe change), an easily detectable effect. The corresponding shift in ψ would be

$$\delta\psi = -\frac{\Lambda}{D \sin \psi} \qquad (8)$$

where Λ is the wavelength (13 cm at S-band frequencies). Using a baseline of 10,000 km the fringe spacing is 1.3×10^{-8} rad/sin ψ or 0.0027 arc sec/sin ψ. This illustrates the potential of VLBI: a change in position of 10^{-3} arc sec causes detectable changes in the cross correlation. At the present, though, there is an ambiguity in determining which fringe the source is on. This ambiguity has restricted absolute position measurements to the 0.1 to 1.0 arc sec level of accuracy.

If a radio source has a size comparable to, or greater than, the fringe spacing, the cross correlation will be reduced. A good way to visualize the fringe phenomena is to think of a grid of parallel lines in the sky with spacing Λ/D sin ψ. Changing the time delay τ causes the fringes to move. As the grid moves in front of a point source, the source is alternately covered and uncovered, which causes the detectable variation in the cross correlation. An extended source, however, will be partly covered and partly uncovered so that the variation in the cross correlation is reduced. Small point sources are available. The quasar 3C 273, for example, has four known components of which one is about 0.0025 arc sec in diameter and another is ≤ 0.0006 arc sec in diameter.

To be useful, the angle ψ between the interferometer direction and the source direction must be related to the right ascension and declination of the source. Figure 14 shows the spherical triangle which relates the right ascension and declination of the source α, δ to the right ascension and declination of the direction of the baseline vector α_b, δ_b. From spherical trigonometry the law of cosines gives

$$\cos \psi = \sin \delta \sin \delta_b + \cos \delta \cos \delta_b \cos (\alpha_b - \alpha) \tag{9}$$

The baseline is fixed in the earth so that its right ascension α_b can be related to its constant longitude λ_b and the right ascension of Greenwich $\alpha_G(t)$ by

$$\alpha_b = \lambda_b + \alpha_G(t) \tag{10}$$

Substituting Eq. (9) in Eq. (1) gives

$$\tau_g = \frac{D}{c} [\sin \delta \sin \delta_b + \cos \delta \cos \delta_b \cos (\alpha_b - \alpha)] \tag{11}$$

The fringe rate from Eq. (6) is given by

$$v_F = - \frac{\omega D}{c} \omega_e \cos \delta \cos \delta_b \sin (\alpha_b - \alpha) \tag{12}$$

where ω_e is the rotation rate of the earth, 0.73×10^{-4} rad/s. If v_F is expressed in hertz, then

$$v_F = - \frac{D \omega_e}{\Lambda} \cos \delta \cos \delta_b \sin (\alpha_b - \alpha) \tag{13}$$

The equatorial projection of D will be

$$r_b = D \cos \delta_b \tag{14}$$

so that the fringe rate becomes

$$v_F = - \frac{\omega_e r_b}{\Lambda} \cos \delta \sin (\alpha_b - \alpha) \tag{15}$$

For $r_b \approx 9000$ km and $\Lambda = 13$ cm, the coefficient $\omega_e r_b / \Lambda \approx 5000$ Hz. Since the fringe rate has already been referred to as the difference in the doppler shift between the two sites, it should not be too surprising that the fringe rate equation looks like the doppler equation for a spacecraft without the geocentric component. The phase term $\alpha_b - \alpha$ is no longer symmetrical about the pass center, though.
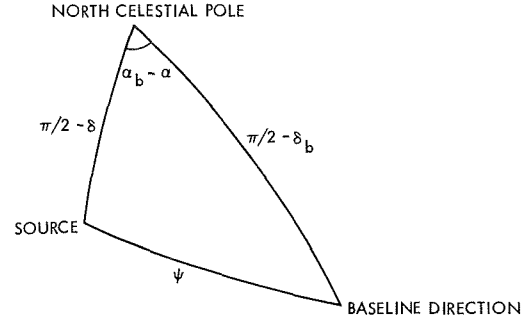

Fig. 14. Spherical triangle for ψ

The similarity of the fringe rate equation to the conventional doppler equation means that much of our intuition built on experience with doppler tracking can be applied to VLBI fringe rate data. The great advantage of VLBI is that not only can it be applied to spacecraft, but it can be used on natural radio point sources as well. The extragalactic distances of these natural sources means that they define a nearly inertial coordinate system. By observing these sources, VLBI has the potential to measure such quantities as polar motion, UT1, precession and nutation constants, and relative station locations to a high degree of accuracy. Each of these quantities is an important error source at the level of accuracy of present tracking.

Before the partials with respect to the geophysical and astronomical quantities are developed, it is convenient to write out the time delay in Eq. (11) in terms of the vector components of the baseline. The x and y components of the baseline are defined in the equatorial plane at longitudes 0 and 90 deg E, while the z component is in the direction of the north pole. Then in terms of the baseline declination (or latitude) δ_b and longitude λ_b one has

$$\left.\begin{array}{l} x = D \cos \delta_b \cos \lambda_b \\ y = D \cos \delta_b \sin \lambda_b \\ z = D \sin \delta_b \end{array}\right\} \tag{16}$$

The time delay becomes

$$\tau_g = \frac{1}{c} [z \sin \delta + r_b \cos \delta \cos (\alpha_b - \alpha)] \tag{17}$$

or, using Eq. (17)

$$\tau_g = \frac{1}{c} [z \sin \delta + \cos \delta (x \cos \lambda + y \sin \lambda)] \tag{18}$$

where

$$\lambda = \alpha - \alpha_G(t) \qquad (19)$$

is the longitude of the source as a function of time. Equation (13) for the fringe rate may be similarly written

$$v_F = \frac{\omega_e}{\Lambda} \cos \delta \, (x \sin \lambda - y \cos \lambda) \qquad (20)$$

The fringe rate has no dependence on the z-component of the baseline.

In summary, Eqs. (11), (17), or (18) give the time delay τ_g, and Eqs. (13), (15), or (20) may be used to calculate the fringe rates. In practice it would be necessary to modify these equations with small corrections for ionosphere, troposphere. and light time.

c. DSN parameters. Since it is part of the aim of this article to evaluate the suitability of the DSN as a VLBI network, the tabulation of some parameters is in order. Table 10 lists some data from the ten station pairs which result from combining DSSs 11, 41, 42, 51, and 61. Short baseline combinations from the other stations were not considered. The first column indicates the two stations involved; for example, the first line indicates a baseline vector from DSS 11 to DSS 61. Subsequent columns indicate the baseline length, minimum fringe spacing, equatorial and polar components of the baseline, the longitude and latitude (or declination) of the baseline vector direction, and the great circle arc length between the two sites.

d. Partials of time delay and fringe rate. This section will present the partials of τ_g and v_F with respect to station locations, source position, UT1, polar motion, and precession and nutation effects. Order-of-magnitude values will be given for the partials. To meaningfully consider these order-of-magnitude calculations, some typical accuracies are needed. Cohen, et al. (1969), with an interferometer using DSSs 14 and 42, cite accuracies of 0.3 μs in time delay and 0.003 Hz in fringe rate.

First consider the dependence of τ_g and v_F on the components of the baseline vector. From Eq. (18)

$$\left. \begin{array}{l} \dfrac{\partial \tau_g}{\partial x} = \cos \delta \cos \lambda / c \\[2mm] \dfrac{\partial \tau_g}{\partial y} = \cos \delta \sin \lambda / c \\[2mm] \dfrac{\partial \tau_g}{\partial z} = \sin \delta / c \end{array} \right\} \qquad (21)$$

This has an order of magnitude value of $1/c$ or 3 ns/m. The fringe rate partials come from Eq. (20):

$$\left. \begin{array}{l} \dfrac{\partial v_F}{\partial x} = \omega_e \cos \delta \sin \lambda / \Lambda \\[2mm] \dfrac{\partial v_F}{\partial y} = - \omega_e \cos \delta \cos \lambda / \Lambda \\[2mm] \dfrac{\partial v_F}{\partial z} = 0 \end{array} \right\} \qquad (22)$$

Table 10. DSN baseline data

DSS	D, km	Fringe spacing, arc sec	r_b, km	z, km	λ_b, °E	δ_b, deg	Great circle arc, deg
11 and 61	8391	0.0032	8379	441	30.8	3.0	82.4
11 and 51	12260	0.0022	10430	−6443	44.5	−31.7	148.2
11 and 41	11017	0.0024	8527	−6976	101.0	−39.3	119.6
11 and 42	10590	0.0025	7625	−7348	106.1	−43.9	112.4
61 and 51	7524	0.0036	3038	−6884	85.8	−66.2	72.4
61 and 41	12233	0.0022	9727	−7417	155.2	−37.3	147.5
61 and 42	12515	0.0021	9795	−7790	161.9	−38.5	158.3
51 and 41	9141	0.0029	9126	−533	173.4	− 3.3	91.6
51 and 42	9589	0.0028	9546	−906	179.9	− 5.4	97.6
41 and 42	1207	0.0222	1149	−372	245.2	−18.0	10.9

The fringe rate is sensitive to the x and y components by about 5×10^{-4} Hz/m.

Using Eq. (17) to get the partials of τ_g with respect to the right ascension and declination of the source

$$
\left.\begin{aligned}
\frac{\partial \tau_g}{\partial \alpha} &= r_b \cos \delta \sin (\alpha_b - \alpha)/c \\[2mm]
\frac{\partial \tau_g}{\partial \delta} &= \frac{1}{c} \left[z \cos \delta - r_b \sin \delta \cos (\alpha_b - \alpha) \right]
\end{aligned}\right\} \quad (23)
$$

Order-of-magnitude calculations give partials of about 100 ns/arc sec. The fringe rate from Eq. (15) yields

$$
\left.\begin{aligned}
\frac{\partial \nu_F}{\partial \alpha} &= \omega_e r_b \cos \delta \cos (\alpha_b - \alpha)/\Lambda \\[2mm]
\frac{\partial \nu_F}{\partial \delta} &= \omega_e r_b \sin \delta \sin (\alpha_b - \alpha)/\Lambda
\end{aligned}\right\} \quad (24)
$$

for which an order of magnitude calculation gives 0.01 Hz/arc sec.

For UT1 Eqs. (17) and (15) are differentiated with respect to the right ascension of Greenwich α_G so that

$$
\left.\begin{aligned}
\frac{\partial \tau_g}{\partial \alpha_G} &= - r_b \cos \delta \sin (\alpha_b - \alpha)/c \\[2mm]
\frac{\partial \nu_F}{\partial \alpha_G} &= - \omega_e r_b \cos \delta (\alpha_b - \alpha)/\Lambda
\end{aligned}\right\} \quad (25)
$$

It should be noted that

$$
\frac{\partial \tau_g}{\partial \alpha_G} = - \frac{\partial \tau_g}{\partial \alpha}
$$

and

$$
\frac{\partial \nu_F}{\partial \alpha_G} = - \frac{\partial \nu_F}{\partial \alpha}
$$

so that α_G and α are not linearly independent. In practice this means that the origin of the right-ascension coordinate system cannot be determined from VLBI. Since this origin is defined by the apparent position of the sun, it can only be determined by observations of the sun. It is sufficient to define the right ascension of one of the radio sources as perfectly known. The order-of-magnitude estimates become 2 μs/s and 0.2 Hz/s.

In deriving the equations for the time delay and fringe rate, the coordinates of the source and baseline were taken with respect to the instantaneous spin axis of the earth. The spin axis moves with respect to an inertial reference frame and the position of the spin axis moves with respect to the crust of the earth. The former effect is called precession and nutation, the latter polar motion. It is necessary to refer the coordinates to fixed systems, such as equinox of 1950 and mean pole of 1903, and transform to the moving system. The transformation of the right ascension and declination uses the precession and nutation constants, while polar motion is specified by the X and Y coordinates of the spin axis. For a more specific discussion, see Ref. 2. The notation of that document is used here.

There are five parameters, $\delta\psi$, z, ζ_0, θ, and $\delta\epsilon$, used to describe precession and nutation. The first three describe rotations about the spin axis. VLBI is insensitive to them, since the right ascension always enters as a difference $\alpha_b - \alpha$. A rotation about the spin axis leaves the difference unchanged. $\delta\epsilon$ describes changes in the obliquity, which are rotations about an axis in the equator at right ascensions of 0 and 180 deg. θ describes rotations about an axis in the equator with right ascension of 90 and 270 deg. Since we are considering small changes in small parameters, it is sufficient to write the rotation matrix in terms of a first-order expansion

$$
R = \begin{pmatrix}
1 & -z - \zeta_0 - \delta\psi \cos \bar{\epsilon} & -\theta - \delta\psi \sin \bar{\epsilon} \\
z + \zeta_0 + \delta\psi \cos \bar{\epsilon} & 1 & -\delta\epsilon \\
\theta + \delta\psi \sin \bar{\epsilon} & \delta\epsilon & 1
\end{pmatrix} \quad (26)
$$

where $\bar{\epsilon}$ is the obliquity.

A position vector

$$\mathbf{U} = \begin{pmatrix} \cos \delta \cos \alpha \\ \cos \delta \sin \alpha \\ \sin \delta \end{pmatrix} \qquad (27)$$

for a fixed equinox is rotated into the coordinates of date by multiplying by the rotation matrix. If $\mathbf{U}_F$ is in the fixed system and $\mathbf{U}_D$ is in the system of date then

$$\mathbf{U}_D = R\,\mathbf{U}_F \qquad (28)$$

and the partials with respect to $\delta\epsilon$ and θ are

$$\left. \begin{aligned} \frac{\partial \mathbf{U}_D}{\partial(\delta\epsilon)} &= \frac{\partial R}{\partial(\delta\epsilon)}\,\mathbf{U}_F = \begin{pmatrix} 0 \\ -\sin\delta \\ \cos\delta\sin\alpha \end{pmatrix} \\[2mm] \frac{\partial \mathbf{U}_D}{\partial\theta} &= \frac{\partial R}{\partial\theta}\,\mathbf{U}_F = \begin{pmatrix} -\sin\delta \\ 0 \\ \cos\delta\cos\alpha \end{pmatrix} \end{aligned} \right\} \qquad (29)$$

Writing Eqs. (17) and (15) so that the components of $\mathbf{U}_D$ appear explicitly

$$\left. \begin{aligned} \tau_g &= \frac{1}{c}\,(z\sin\delta + r_b\cos\alpha_b\cos\delta\cos\alpha \\ &\qquad + r_b\sin\alpha_b\cos\delta\sin\alpha) \\[2mm] \nu_F &= -\frac{\omega_e r_b}{\Lambda}\,(\cos\delta\cos\alpha\sin\alpha_b - \cos\delta\sin\alpha\cos\alpha_b) \end{aligned} \right\} \qquad (30)$$

The partials are now simply

$$\left. \begin{aligned} \frac{\partial \tau_g}{\partial(\delta\epsilon)} &= \frac{1}{c}\,(z\cos\delta\sin\alpha - r_b\sin\alpha_b\sin\delta) \\[2mm] \frac{\partial \tau_g}{\partial\theta} &= \frac{1}{c}\,(z\cos\delta\cos\alpha - r_b\cos\alpha_b\sin\delta) \\[2mm] \frac{\partial \nu_F}{\partial(\delta\epsilon)} &= \frac{-\omega_e r_b}{\Lambda}\cos\alpha_b\sin\delta \\[2mm] \frac{\partial \nu_F}{\partial\theta} &= \frac{\omega_e r_b}{\Lambda}\sin\alpha_b\sin\delta \end{aligned} \right\} \qquad (31)$$

The α and δ in the above are now understood to be in a fixed system such as that of the 1950 equinox. The order-of-magnitude values are the same as for the partials with respect to α and δ, 100 ns/arc sec and 0.01 Hz/arc sec.

Actually, for the quantities $\delta\epsilon$ and θ, it is their rates which are most uncertain; the quantities themselves are defined zero for 1950.0. The relevant partials are then

$$\left. \begin{aligned} \frac{\partial \tau_g}{\partial(\delta\dot\epsilon)} &= \frac{\partial \tau_g}{\partial(\delta\epsilon)}\,t \\[2mm] \frac{\partial \tau_g}{\partial\dot\theta} &= \frac{\partial \tau_g}{\partial\theta}\,t \\[2mm] \frac{\partial \nu_F}{\partial(\delta\dot\epsilon)} &= \frac{\partial \nu_F}{\partial(\delta\epsilon)}\,t \\[2mm] \frac{\partial \nu_F}{\partial\dot\theta} &= \frac{\partial \nu_F}{\partial\theta}\,t \end{aligned} \right\} \qquad (32)$$

The sensitivity to the rates $\delta\dot\epsilon$ and $\dot\theta$ increases linearly with the time span covered by the data. For a time span T yr one would expect order-of-magnitude sensitivities of $100\ T$ ns/arc sec/yr and $0.01\ T$ Hz/arc sec/yr.

For small rotations of the station coordinates due to polar motion

$$R' = \begin{pmatrix} 1 & 0 & -X/a \\ 0 & 1 & Y/a \\ X/a & -Y/a & 1 \end{pmatrix} \qquad (33)$$

where X and Y are the coordinates of the spin axis, and a is the polar radius of the earth. The X axis is at 0 deg longitude, while the Y axis is at 270° E. As before the

Table 11. Order-of-magnitude values for partials

Partial with respect to	τ_g	ν_F
x, y	3 ns/m	5×10^{-4} Hz/m
z	3 ns/m	0
α, δ	100 ns/arc sec	10^{-2} Hz/arc sec
UT1	2 μs/s	0.2 Hz/s
$\delta\epsilon$, θ	100 ns/arc sec	10^{-2} Hz/arc sec
X, Y	3 ns/m	5×10^{-4} Hz/m

coordinates of date (D) are derived from the fixed coordinates (F) by

$$\begin{pmatrix} x \\ y \\ z \end{pmatrix}_D = R' \begin{pmatrix} x \\ y \\ z \end{pmatrix}_F \qquad (34)$$

The partials depend only on the partials of R', so that Eqs. (18) and (20) give

$$\left. \begin{aligned} \frac{\partial \tau_g}{\partial X} &= \frac{1}{c} \left[-\cos \delta \cos \lambda \, z/a + \sin \delta \, x/a \right] \\ \frac{\partial \tau_g}{\partial Y} &= -\frac{1}{c} \left[-\cos \delta \sin \lambda \, z/a + \sin \delta \, y/a \right] \\ \frac{\partial v_F}{\partial X} &= -\left(\frac{z \, \omega_e \cos \delta}{a \, \Lambda} \right) \sin \lambda \\ \frac{\partial v_F}{\partial Y} &= -\left(\frac{z \, \omega_e \cos \delta}{a \, \Lambda} \right) \cos \lambda \end{aligned} \right\} \qquad (35)$$

It is to be understood that the x, y, z which appear in Eqs. (35) are in the fixed system. Order-of-magnitude calculations give 3 ns/m and 5×10^{-4} Hz/m the same as for the partials with respect to $\dot{x}$, $\dot{y}$, $\dot{z}$.

Comparing the above order-of-magnitude calculations in Table 11 with the quoted accuracies of 300 ns and 0.003 Hz for a single run shows that the variables x, y, X, and Y are sensitive at the 5-m level, while α, δ, $\delta\epsilon$, and θ are sensitive at the 0.3 arc sec level and UT1 at the 20-ms level. Processing a number of runs together should allow reduction of these numbers, but it must be cautioned that simulations of the separability of the effects have not been carried out. No useful information is available on the z component of the baseline. Virtually all of the useful information comes out of the fringe rate. The key to more accurate time delays are wide bandwidths, while more accurate fringe rates will come from improved frequency standards.

By restricting consideration to fringe rate data only, it can be seen that maximum sensitivity to the baseline (or station position) comes at zero declination. Source position, precession and nutation constants, and UT1 improve with increasing equatorial projection of the baseline, while polar motion effects are most detectable with large polar-axis components of the baseline. The source right ascension, UT1, and polar motion are most accurately determined for sources at 0-deg declination, while the source declination and the precession and nutation

constants θ and $\delta\epsilon$ are best determined for sources in the polar regions. The separation of the effects will require baselines with a variety of declinations and longitudes and sources with a variety of right ascensions and declinations.

References

1. Cohen, M. H., et al., "Compact Radio Source in the Nucleus of M87," *Astrophys. J. Letters*, p L83, 1969.

2. Melbourne, W. G., et al., *Constants and Related Information for Astrodynamic Calculations*, Technical Report 32-1306, Jet Propulsion Laboratory, Pasadena, Calif., Nov. 5, 1968.

B. Communications Systems Research

1. Information Systems: Performance of the Binary-Coded Sequential Acquisition Ranging System of DSS 14, W. L. Martin

a. Introduction. During September 1969 the Binary-Coded Sequential Acquisition Ranging System, described in SPS 37-52, Vol. II, pp. 46–49, and SPS 37-57, Vol. II, pp. 72–81, was installed at DSS 14. Through January 1970, when the station's operation was suspended for installation of the tri-cone, 46 separate ranging acquisitions had been made with *Mariners VI* and *VII*. Throughout the intervening 4 mo, several tests were conducted to accurately assess the performance of the ranging system in a DSS environment. This article summarizes the results of the tests performed and forms some conclusions regarding the potential of the tracking network.

b. System delay. Range is determined by accurately measuring the elapsed time between the transmission of a signal and its return to the tracking station. Delays inherent in the ground equipment and in the spacecraft's transponder are indistinguishable from those due to distance and must be subtracted from the measured range to yield its true value. Obviously, transponder calibration must be completed prior to launch since this act precludes any further testing. Fortunately, this is not true of the ground equipment, which is readily accessible and therefore can be examined quite thoroughly.

A unique property of this ranging system results from its use of RF doppler to simulate code doppler (see MacDoran and Martin, *Section A-4*, this chapter). The presence of charged particles along the signal ray path causes the code and clock dopplers to be shifted in frequency by nearly equal but opposite amounts. This results in a slow drift in the apparent range, which in

turn can be used to calibrate the charged-particle activity. Since a charged-particle calibration may require several hours, during which time the apparent range may change by only a few nanoseconds, it is important to know how much of this variation might be contributed by the equipment.

c. Ranging system delay stability. Prior to shipping the ranging system to Goldstone, a test was conducted to measure its internal delay and its delay stability. Figure 15 illustrates how the system was configured for this evaluation. A highly stable reference was supplied to two frequency synthesizers, which in turn acted as references for the RF and digital subsystems. A portion of the 10-MHz signal was bi-phase modulated, using a double balanced mixer, to provide the requisite input to the RF subsystem. An attenuator, placed between the modulator and the RF unit, was used to set the input level to approximately −100 dBmW. This relatively strong signal was employed so that any dc drift or delay variation would be readily discernible. Thus, the system was connected to literally range itself, providing not only a measure of its internal delay but also of its delay stability. It is important to understand that only the RF and digital subsystems described in SPS 37-57, Vol. II, were under test at this time. The equipment was allowed to warm up for 6 h prior to the calibration which commenced at 3 p.m. and lasted for a period of just under 2 h. All measurements were made in a laboratory environment.

Results of the test are shown in Fig. 16. The average delay was found to be 4.876 ns for the 102 sample points collected with a standard deviation of 13.9 ps. Drift rate was obtained by using least-squares criteria to fit a third-degree polynomial to the data. When completed, the average drift over the test period was found to be only 9.6 ps/h. This corresponds to a drift in range of about 0.05 in./h.

One of the more obvious conclusions to be reached from this test is that delay stability of the ranging system will not be a limitation to accuracy in the foreseeable future. Moreover, it has been suggested that the system may have some value as a calibration tool for spacecraft ranging transponders. To be useful in this capacity, additional interfacing hardware would be required to translate the signal to the proper S-band frequency.

d. Ranging at DSS 14. Performance of the ranging equipment in a DSS environment, which includes the associated transmitting, receiving, and antenna equipment, is of greater concern to the experimenter. Important parameters include total system delay, long- and short-term delay stability, delay dependence upon signal level, and reacquisition integrity.

System delay. Prior to each ranging pass, the entire ground system is calibrated to determine its delay. The
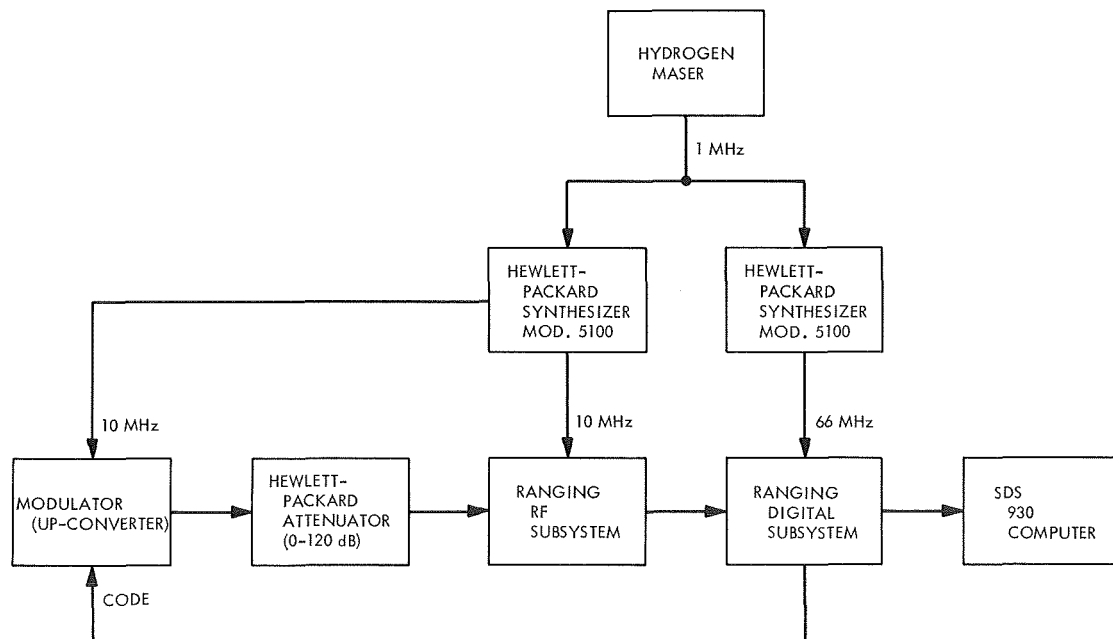

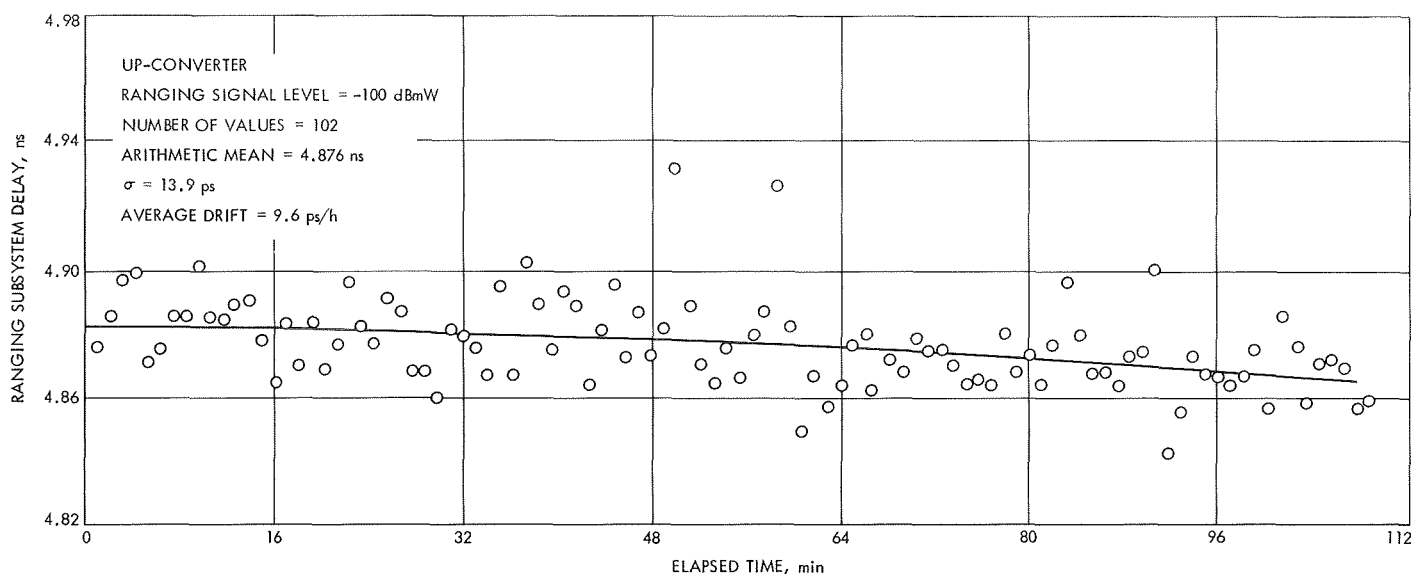**Fig. 15. Ranging system laboratory test configuration**

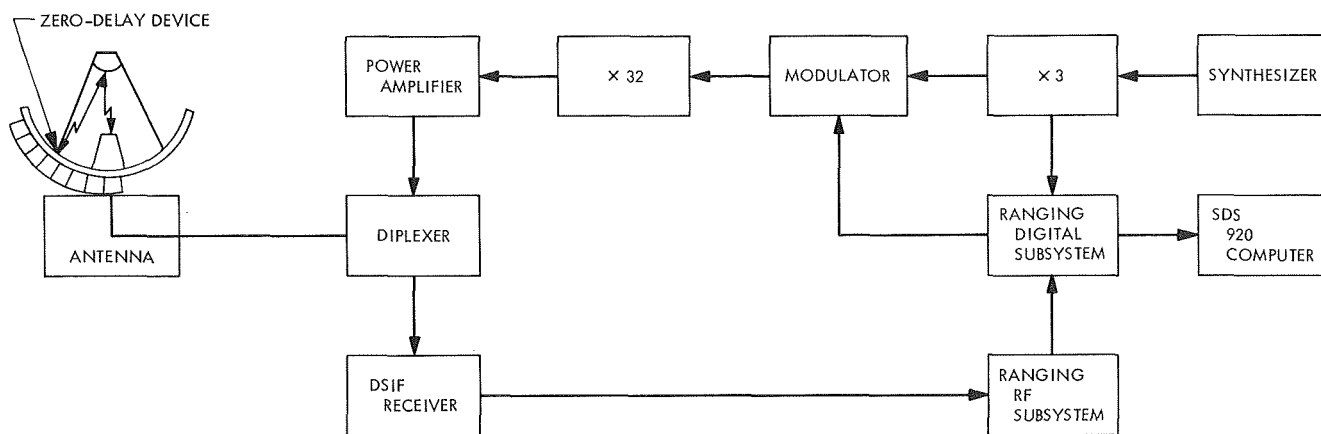**Fig. 16. Ranging subsystem drift (Jul 31, 1969)**

Fig. 17. DSS 14 ranging test configuration

system is configured with the antenna at zenith and the transmitter operating at full power, modulated by the ranging code (Fig. 17). A small crystal mixer (termed a zero-delay device) is located on the antenna surface near one of the quadrupods. Its purpose is to convert a portion of the transmitted signal to the receiver frequency $[\omega_R = (240/221)\omega_T]$ without introducing a significant delay. This translated frequency re-enters the horn and is processed by the DSIF receiver. The magnitude of the received signal is adjustable via an attenuator from above -100 dBmW to well below the receiver's threshold. Thus, it is possible to calibrate the delay of the ground equipment normally used with a spacecraft, and under virtually identical conditions. This delay, measured in microseconds, must be subtracted from the calculated range to yield its true value.

Long-term stability. Long-term delay stability can be assessed by comparing calibration numbers over several weeks. A 2-mo period from November 22, 1969 through January 24, 1970 was selected which included 12 data points (Fig. 18). The mean value for the total system delay throughout the period was found to be 3.34 μs (501 range meters) while the standard deviation was computed at 26 ns (3.9 range meters). A least-squares linear fit to the data shows a slope of -15 ns/mo (-2.2 range meters per month).

Long-term stability is mainly of academic interest since variations can be removed by daily calibration. However, it does provide some information about the inherent stability of a typical DSN station. It demonstrates, for example, that the delay drift is less than 0.5% per
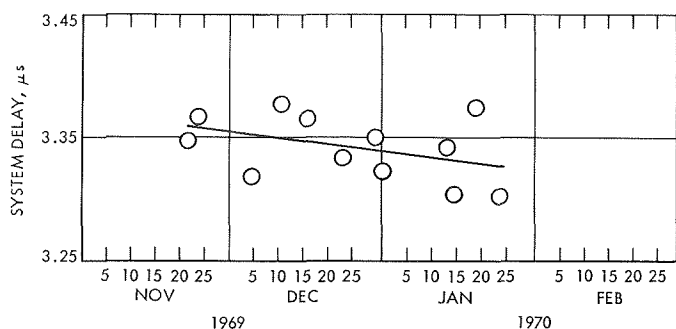
Fig. 18. Long term stability

month, which is a remarkable achievement for a system of that size and complexity. Moreover, the small value for σ suggests that one could forego range calibrations, using instead a standard value of 3.34 μs, and still be within the 5-m error budget.

Short-term stability. Short-term delay stability extending throughout a single pass is of more direct concern to the experimenter. As previously noted, during a charged-particle experiment, it is important to know how much of the range signature is attributable to system drift. Two investigations at different signal levels were conducted. The first on November 4, 1969 was made at −185 dBmW and covered an 8-h period (Fig. 19), while the second on December 6, 1969 at −170 dBmW had a duration of approximately 5 h (Fig. 20).

Results of the first test show an average delay of 3.26 μs over the 8-h period with a $\sigma = 20.2$ ns (Fig. 19). Observe that the average delay is somewhat less than that indicated on Fig. 18. The explanation is that the measurement was made shortly after the equipment was installed at Goldstone. Subsequent equipment and cabling modifications caused a slight increase in the total delay.
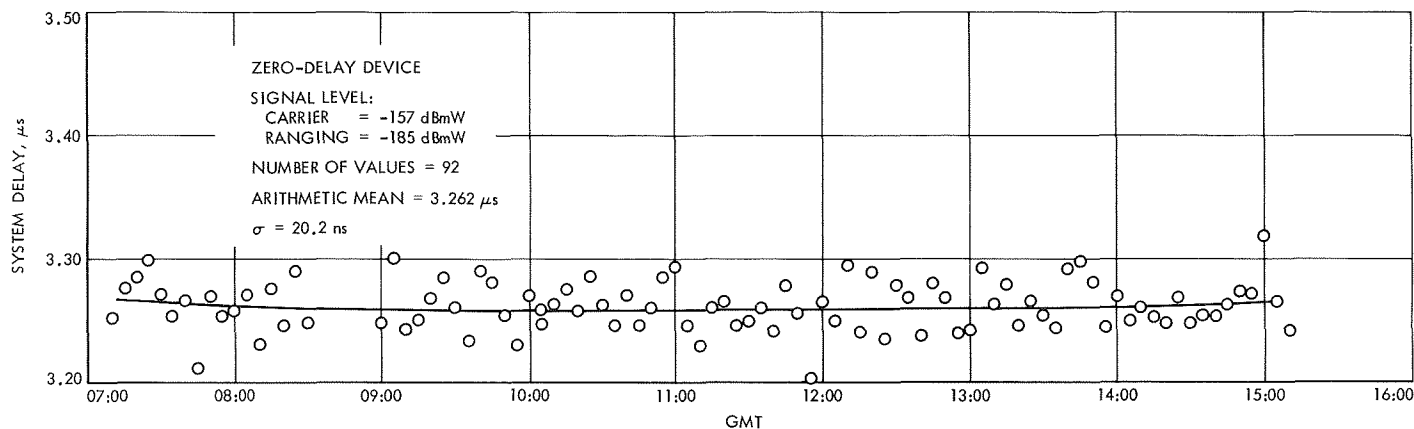
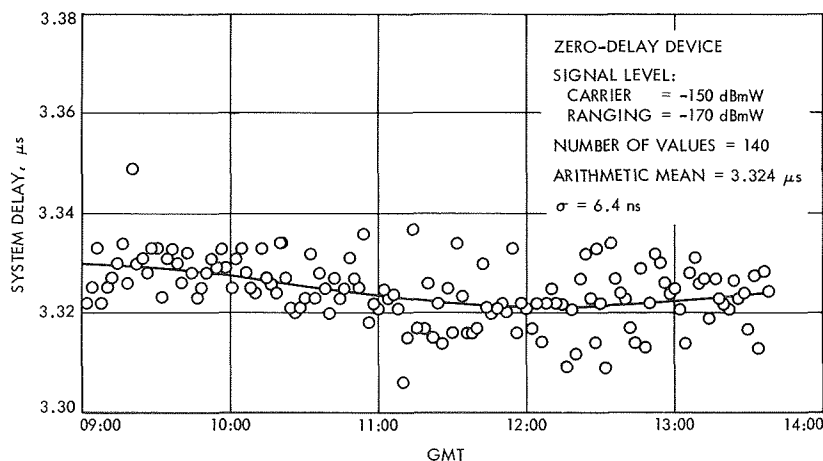

Fig. 19. Ranging system drift (Nov 4, 1969)

Fig. 20. Ranging system drift (Dec 6, 1969)

By using least-squares criteria to fit a third-degree polynomial through the data, the peak change was found to be 7.6 ns (1.1 range meters) over the 8-h period. This corresponds to an average change of 1.9 ns/h (0.285 range meter per hour) since the minimum appears to occur about midpass at 11:00 GMT. The maximum rate of change appears near the end of the test where it increases to 2.9 ns/h (0.43 range meter per hour).

This data is largely corroborated by the second test one month later when the average delay was found to be 3.324 μs. A decline in σ to 6.4 ns can be attributed to the relatively stronger signal and to a difference in the integration time. Fitting a third-degree polynomial to the data, the peak variation was measured at 9.2 ns (1.3 range meters) over the 3.5-h period. Average drift was computed to be 2.6 ns/h (0.39 range meter per hour) with a maximum slope of 3.7 ns/h (0.5 range meter per hour) occurring at 10:30 GMT.

Several remarks can be made regarding these investigations. Note that the minimum delay appears in both tests at approximately the same time (11:00–12:00 GMT). This suggests that the drift may have a diurnal character. An explanatory model is difficult to formulate since the reversal takes place between 3:00 and 4:00 a.m. PST. The obvious supposition of a thermal stimulus is awkward to justify since nearly 9 h have elapsed since there were any important thermal inputs. Variations in the plenum temperature are either too small to be measured or are not correlated with the observed excursions. Coaxial cables, the most likely point of thermal influence because of the quantity involved, can be discarded since measurements indicate a change of only 10 ps per degree of temperature rise per 100 ft. The maxima and minima in the delay, particularly evident in the December 6 run, together with almost identical excursions for the two tests, imply a limit cycle process of a massive system— massive because the time constant is clearly several hours. Power line variations, plausible from a timing consideration, become impractical as an explanation because of the excellent voltage regulation employed. Summarizing, additional testing over considerably longer time periods will be required to isolate the source of the drift.

In any event, the data indicates that the maximum drift to be experienced over a pass will be less than 1.5 m. Fortunately, a variation of this magnitude is within the error budget for *Mariner* Mars 1971. Similarly, maximum short-term drift rates of 0.5 m/h are believed to be adequate for charged-particle investigations provided that the limit of 1.5 m per pass is not exceeded.

Signal level dependency. System delay variations resulting from changes in the received signal level are another source of error. Phase shifts in the ground receiver's IF amplifiers vary slightly with automatic gain control voltage, causing the system delay to be dependent upon signal level. This problem is particularly acute in the spacecraft's transponder where changes as great as 1 m of range per dB of signal level have been observed.

An investigation was conducted on November 12, 1969 to ascertain the extent of the delay variation in the ground equipment. The system was configured as shown in Fig. 17 with the transmitter operating at 20 kW. Ranging and carrier power were set for −100 dBmW and an acquisition was initiated. After collecting a suitable number of range points, the power was reset to −130 dBmW without breaking lock. This procedure was repeated once more to reduce the level to −160 dBmW.

Results of the test appear in Fig. 21 and indicate that the change in system delay is less than 1 ns (0.15 range meter) over the 60-dB range. Some uncertainty arises in the last set of points due to the large value of σ. However, evidence obtained in a later test, in which reacquisition
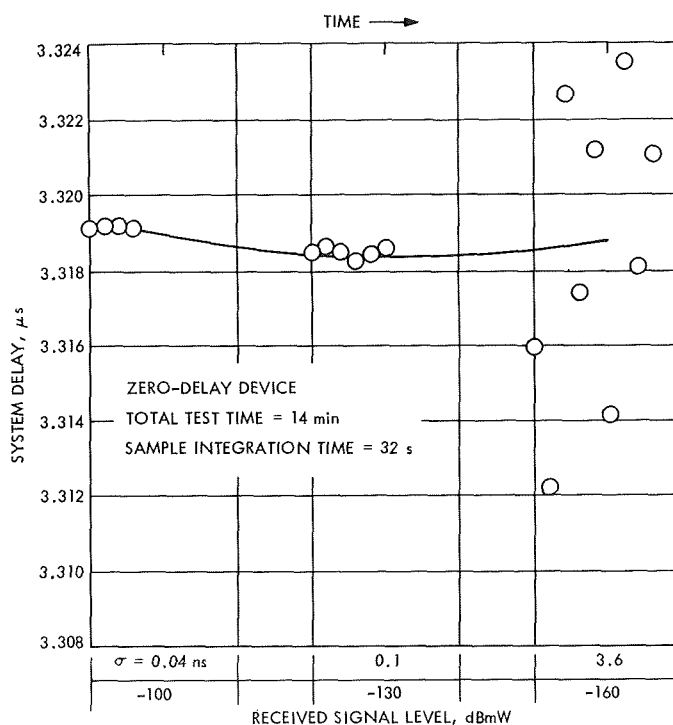

Fig. 21. Signal level stability

follows each signal level change, substantiates the independence of system delay and signal strength. The data of Fig. 21 also includes any drift that may have taken place during the 14-min test period but this should not exceed 1–2 ns.

It can be concluded from this experiment that the received signal level does not grossly influence the system delay, unlike the behavior of the spacecraft's transponder. When drift is accounted for, the delay should not change by more than 2 ns (0.3 range meter) over a 60-dB signal range. In most situations, even for long data arcs, the error due to signal strength fluctuations should be well below 1 ns (0.15 range meter).

Acquisition integrity. Consider a stationary target at a known distance. Each acquisition should produce an identical number representing the correct range. The extent to which this is true is a measure of the system's acquisition integrity. Reasons for poor integrity would be delay drift, insufficient resolving power, and poor noise performance.

An experiment was conducted on November 12, 1969 to measure the acquisition integrity of the ranging equipment. System configuration was identical to that employed in the previous signal level dependency test. Seven acquisitions were obtained, each at a different received signal strength. The first set of measurements was made at −100 dBmW. The signal level was then reduced by 10 dBmW and a reacquisition initiated. The

purpose of this test was to explore the acquisition integrity and its dependence upon received signal power.

Results of the investigation are plotted in Fig. 22. A 3-ns variation was found to exist throughout the test period which lasted slightly less than 1 h. Careful examination of the points, particularly at strong signal levels, reveals a very definite trend. The points within a given set clearly describe an arc with very little scatter. Therefore, it is reasonable to assign the nonlinearity of the data to delay drift and not to the reacquisition process. Spaces that represent the reacquisition process have been left between the sets of points and an average curve has been fitted to the data.

Two conclusions to be reached from this investigation are:

(1) Reacquisition introduces no major discontinuities. Had the lock not been broken the data would continuously follow the average curve in Fig. 22.

(2) The data also confirms the previous finding that there are no significant variations in delay resulting from signal level changes.

The magnitude and period of the drift are of some concern. Quite possibly the drift is due to temperature variations within the cone located on the antenna structure. During this test an operator was present in the cone to adjust the signal level, and temperature fluctuations could have resulted from his opening and
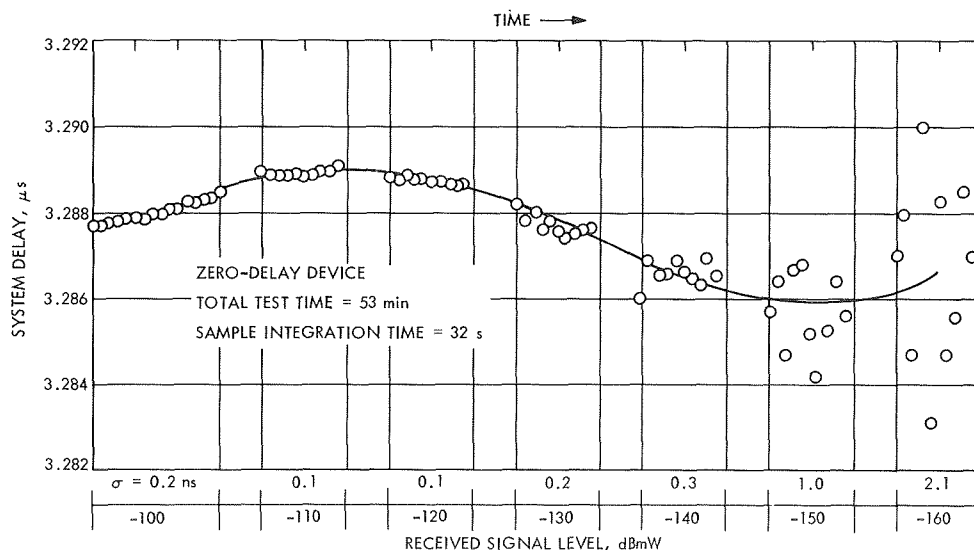

Fig. 22. Reacquisition and signal level test

closing the door and the equipment cabinets. Additional tests will be necessary to isolate the source.

e. **Conclusions.** These investigations have provided experimenters with the following information regarding the DSN ranging capability:

(1) The ranging system introduces no significant delay or delay drift.

(2) The long-term stability of DSS 14 is excellent since the delay changes by only 2.2 m (0.5%) per month.

(3) The short-term drift extending over one pass is less than 1.5 m although slopes as great as 0.5 m/h have been observed.

(4) No significant change in the delay of the ground equipment was found by varying the input signal over a 60-dB range.

(5) Reacquisition introduces no observable discontinuities in the ranging data.

Two additional tests are required for clarification of the system's performance. First, a closed-loop ranging calibration covering a continuous 24-h period should be obtained to determine whether the drift has a diurnal character. Second, the system should be calibrated at several different antenna angles to discover if the antenna's position influences the delay. This information, together with that previously obtained, should provide a complete understanding of DSN ranging.

2. Information Systems: Buffer Parameters and Output Computation in an Optimum Convolutional Decoder, *J. W. Layland*

a. **Introduction.** The impressive results obtained by Heller (SPS 37-54, Vol. III, pp. 171–177) for the decoding of short constraint length convolutional codes by the Viterbi algorithm have motivated work aimed at the design of special-purpose equipment to implement this type of decoding. Heller's results showed the need for a buffer of 3 to 5 constraint lengths (K) for each of the 2^{K-1} states of the convolutional encoder. Since this is the largest single identifiable item in the decoder, and may, in fact, be the limiting factor for decoding speed, a more precise knowledge of the behavior of this buffer is needed. This article reports the results of a series of simulations which were performed to obtain that knowledge. The initial part of this series was performed using modified versions of Heller's program; the remainder was performed using the faster decoding program described in the following article, *Subsection 3.*

b. **Problem statement.** A convolutional code of constraint length K and rate $1/V$ may be thought of as a finite state machine with one input bit and V output bits per cycle, and 2^{K-1} possible states. For each state of the encoder, the optimum convolutional decoder must remember the most-likely bit stream (the *survivor*) leading to that state, and the likelihood of that survivor. Theoretically, the length of the survivors is infinite, since there is no finite length at which all of them must converge (Ref. 1). However, convergence may be forced by the inclusion of K or more known bits periodically into the data, as was suggested in the original description of the algorithm (Ref. 2). As a practical matter, however, convergence is rapid enough so that truncation of the survivor memory at a few constraint lengths will introduce only slight degradation in performance. The degradation suffered is a function not only of the length of the survivors but also of the method by which the output data stream is constructed from the 2^{K-1} survivors.

c. **Decoder output construction.** In previous simulations of this decoding algorithm, the output bit at each step was selected to be the oldest bit associated with the most-likely state. Depending upon the organization of the decoder, the selection of the most-likely state may be almost trivial, or it may be a rather large portion of the decoder. In the latter case, other methods of constructing the output data stream may be preferable. Another reasonable choice for selection of the data output is the majority function of the oldest bits of each of the 2^{K-1} survivors. Intuitively, it would seem that in most cases, where not all of the survivors were identical at their trailing ends, more would agree with the correct bit than would disagree. This has been borne out by simulation. The third output method that appears reasonable is the selection of the oldest bit in some arbitrarily chosen survivor.

These three techniques are compared in Figs. 23a, b, and c for $K = 4$, 6, and 8. The arbitrary state was, in each case, the all 1's state, the complement of the correct data. The curves are shown for an error probability close to 5×10^{-3}, a design point typical of deep-space missions. Each curve represents 10^5 decoded bits. The design trade-offs can be easily specified for these three output techniques: if the arbitrarily selected survivor is used as a standard, a majority function output is approximately equal in value to an additional one and one-half constraint lengths in every survivor, and selection of the most-
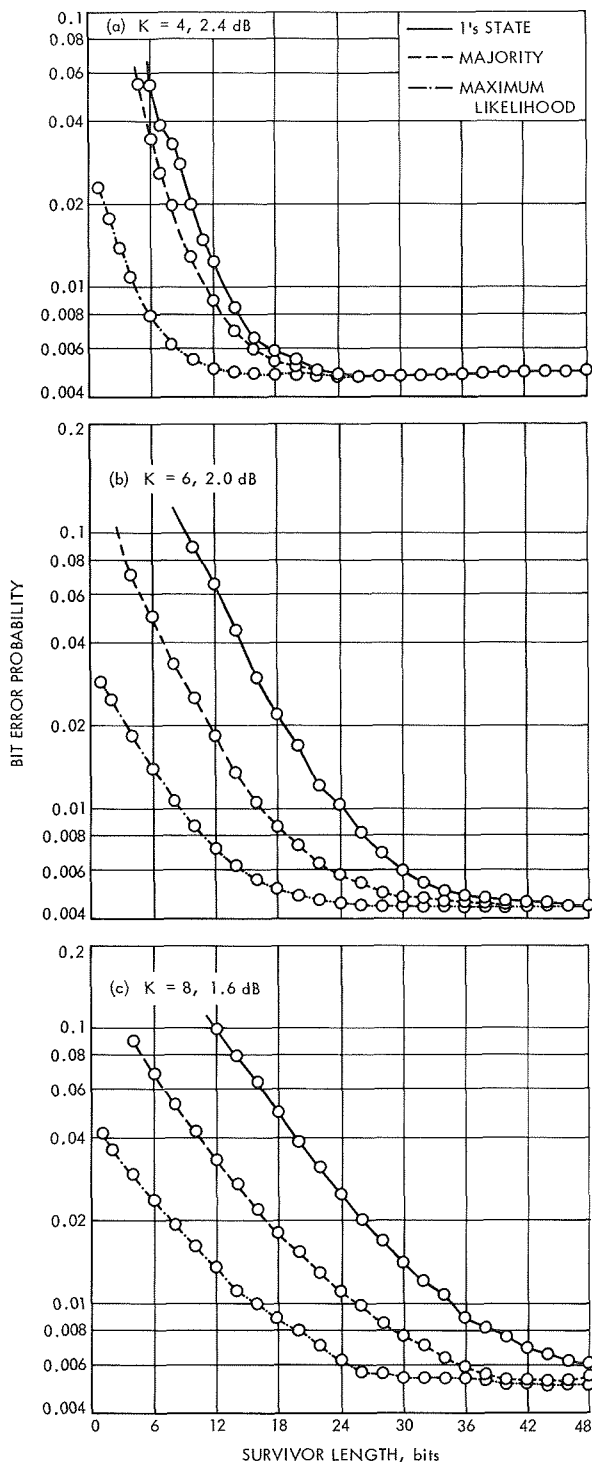
Fig. 23. Bit error probability vs survivor length

show the same relative value for the output construction methods at error probabilities of 5×10^{-4} or lower.

Numerous other methods of output construction have been given at least a partial evaluation. None have appeared to have practical values. One can, for example, create a family of curves that fall between the majority output and the full maximum likelihood output in the following manner: the survivors are grouped in sets which contain approximately M each. The most-likely survivor in each of these groups is selected, and the majority function on these selected survivors is the output data. Unfortunately, this output is little better than straight majority unless M is a significant fraction of 2^{K-1}. Another family of curves can be obtained by the truncation of the M least-significant bits of the likelihood metrics in the selection of the most-likely survivor. Performance deteriorates rapidly with M toward that of the arbitrarily selected survivor. A hill-climbing technique can be used to provide a sophisticated guess at the most-likely survivor. An arbitrary survivor is flagged initially. At each step, the flag moves to the more likely of the two successors to the presently flagged survivor. The output bit is the trailing bit of the flagged survivor. Performance is approximately that of the majority at $K = 6$, but becomes poorer as K increases. The task of updating the flag should be about as complex as the majority function if means to prevent a catastrophic failure in the flag memory is included.

d. Survivor structure. The processing options discussed above have all assumed that each survivor is contained in a fixed number of bits. Since the survivors converge within one or two constraint lengths to only a few distinct bit streams, such an even distribution of the survivor storage might be wasteful, and dynamic storage allocation should at least be evaluated. Figures 24a, b, and c show experimental probability distributions for the number of distinct bit streams at varying distance into the survivor buffer. The data is again presented for a design point of 5×10^{-3} bit error rate, and the sample size is 10^5 bits. The figures indicate that roughly half of the storage required for output from an arbitrary survivor can be eliminated if dynamic storage allocation were used. Amusingly enough, most, if not all, of the methods for dynamic storage result in a two-fold increase in the needed storage; i.e., the same number of bits are needed to link the storage elements together as are contained in the storage elements themselves. Dynamic storage is thus a "break even" alternative with respect to total hardware volume, but a considerable increase in design and maintenance complexity.
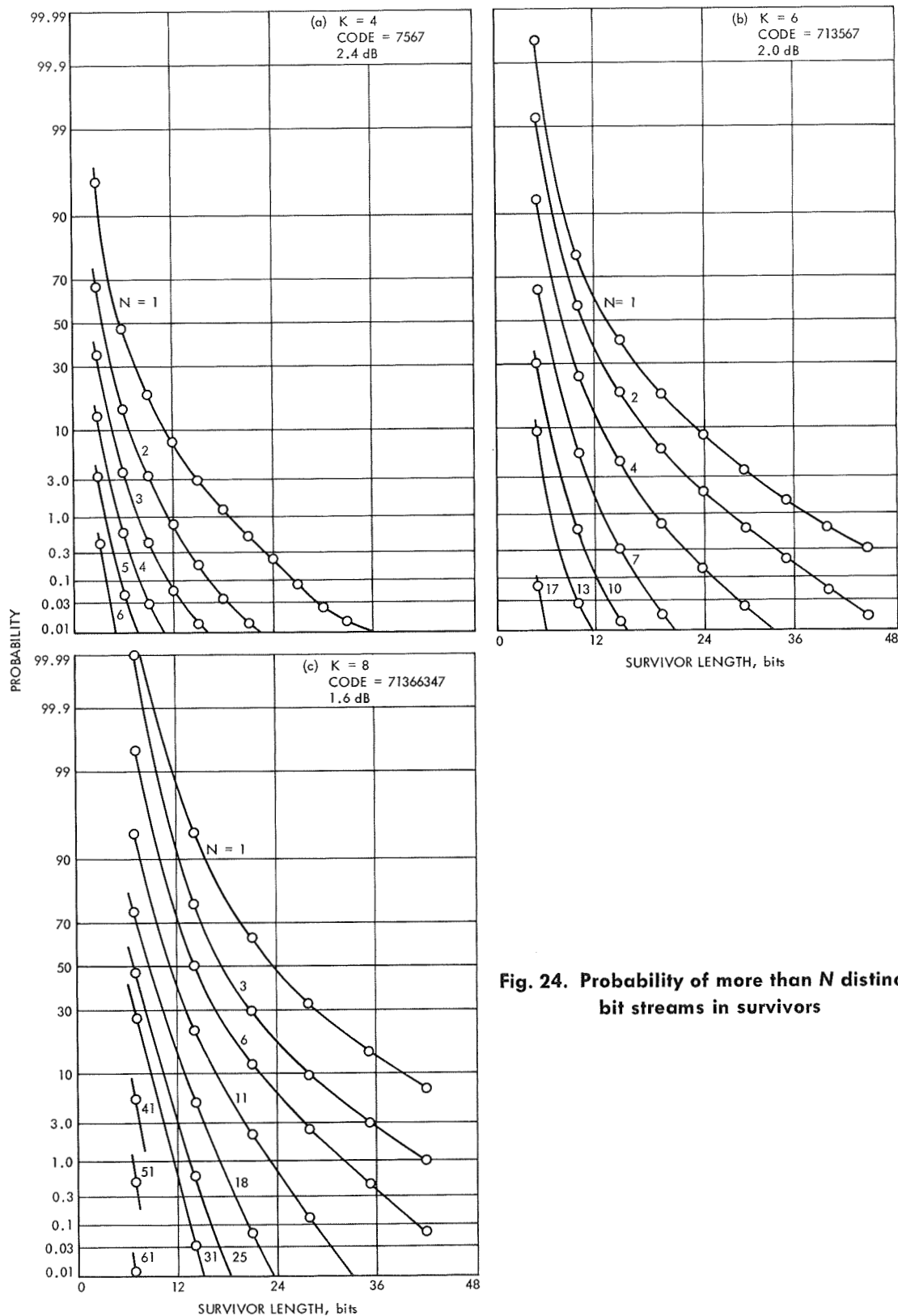
likely survivor is approximately equal in value to an additional three constraint lengths in each survivor. The form of this result is not strongly a function of error probability, and similar curves could be drawn which

Fig. 24. Probability of more than N distinct bit streams in survivors

e. Design implications. A number of factors in addition to those discussed in this article will affect the overall organization of an optimum convolutional decoder. Most important among these is the required decoding speed. Once the decoder organization is established, the results presented here can be used to complete the definition of decoder parameters. If a design is chosen which contains a single, high speed, arithmetic unit that computes all of the 2^{K-1} survivor likelihoods, overall maximum likelihood selection is a small addition which is well worth the attendant reduction in survivor buffer length. If, however, a design is chosen which has a serial arithmetic unit for each survivor, overall maximum likelihood selection is a very expensive addition that does not appear justifiable. The amount of equipment involved in the majority function on 2^{K-1} variables is roughly equivalent to 2 or 3 bits of storage per survivor, significantly less than the survivor length which the majority function can replace if constraint length is more than six. However, for constraint lengths of six or less, the compactness of commercially available integrated circuit arrays makes the longer survivor with arbitrary survivor selection the preferable configuration.

References

1. Morrissey, T. N., *A Unified Markovian Analysis of Decoders for Convolutional Codes,* Technical Report EE-687, p. 76. University of Notre Dame, Indiana, Oct. 24, 1968.

2. Viterbi, A. J., "Error Bounds for Convolutional Codes and an Asymptotically Optimum Decoding Algorithm," *IEEE Trans. Inform. Theory,* Vol. IT-13, pp. 260–269, Apr. 1967.

3. Information Systems: Capabilities of an All-Software Optimum Convolutional Decoder, *J. W. Layland*

a. Introduction. The simulation results obtained by Heller (SPS 37-54, Vol. III, pp. 171–177) for the decoding of short constraint length convolutional codes using the Viterbi decoding algorithms have created considerable interest in the practical application of the algorithm at JPL and elsewhere. The probable implementations are either in special-purpose digital hardware or in a general-purpose computer with software. This article describes a software convolutional decoder written for the SDS 900-series computers which operate at a speed very close to the maximum possible in these machines. The program was written to extend Heller's simulation results, and to provide design parameters for a hardware implementation; however, with almost no modification, it could also be used to decode live telemetry.

b. Convolutional codes and the optimum convolutional decoding algorithm. A convolutional encoder for a code of constraint length K and rate $1/V$ consists, typically, of a shift register of length $K-1$, coupled with V parity-check adders. For each new bit to be encoded, the V linear combinations (Mod-2) of the $K-1$ bits in the shift register, and the new data bit, are computed and transmitted. The new data bit is then shifted into the coder register and the oldest bit therein shifted out. Clearly, the encoder can be viewed as a finite-state machine with 2^{K-1} states. The optimum convolutional decoder contains a buffer which holds the most-likely bit stream leading to each of the possible states of the encoder, and the likelihood or metric of each state and bit-stream combination. These bit-stream and metric combinations will be called the *states* of the decoder. The bit streams associated with each state are termed the survivors. Proof of the optimality of this decoder may be found in many places. Heller's results showed that near-optimal performance could be obtained with a practical-sized buffer for the survivors.

c. Program organization. The maximum likelihood decoding program described here is a METASYMBOL subroutine for a Fortran II program. One call is made to the subroutine for each step of the decoding algorithm, i.e., for each bit, and one call is made by the subroutine to another data-source subroutine for each symbol of the coded data stream. If the code constraint length is large ($K = 8$ to 10 for this kind of decoding) and efficiency important, the overhead added by the subroutine interface is negligible compared to the overall decoding time. Furthermore, these interfaces make the addition of instrumentation for the decoder parameters relatively easy, and would make the modification of the program for use with live data sources equally easy. All decoder parameters, the survivors and the state metrics are stored in the Fortran common area. Their location is established by an EQU directive in the subroutine, which must be maintained compatible with the absolute common locations of the main program.

The computations of the Viterbi decoding algorithm are performed "in place." The states of the convolutional decoder are modified in pairs that differ only in their oldest or most significant bit. From each pair of states the four branches to the two successor states that differ only in the newest bits are computed and the best metrics corresponding to the two successor states are stored in the same locations as the metrics of the original pair of states. The survivors are updated by shifting the oldest bit of the state name to which the survivor was originally

attached into the newest position of that survivor, and storing the updated winning survivor(s) in the same locations as the survivors of the original pair of states. As a result, the states of the convolutional decoder are not stationary in the memory but move with time, with a period of $K-1$.

This apparent complication of the decoding provides two benefits. The required memory is half what would be required if the states were fixed in memory, since in that case an intermediate buffer would be needed to hold the metrics and survivors until each decoding step were completed on all 2^{K-1} states. Also, since the computer being used has only one index register, some time is saved by having one, rather than two index pointers that must be repeatedly exchanged, as is the case for a decoder with stationary state assignments. The cyclic movement of the states through memory is accomplished by the modification of 15 instructions at the start of each decoding step, which represents more than 90% of the overhead associated with entering the subroutine.

The Fortran main program is nothing but a sequence of calls to Fortran and METASYMBOL subroutines. The set up subroutine allows specification of the code, code constraint length, number of 1000-bit blocks to decode before summarizing, and the signal-to-noise ratio at which data is to be generated. It also allows (optionally) the setting of the value of the pseudorandom noise kernel for the continuation of a long experiment. The code rate in the decoding subroutine is parameterized and this routine could therefore be assembled for any rate. The input program, however, is limited to rates $\frac{1}{2}$ to $\frac{1}{4}$, as the code is input in standard hexadecimal notation (0–9, A–F). A set of subroutines performs the initialization chores, such as computing from the requested code a table of branch values for each state, establishing thresholds for the uniform to quantized-gaussian transformation of the pseudorandom noise, and initializing all of the modifiable instructions in the decoding subroutine to a fixed and consistent status. Other subroutines act as instrumentation on the decoder, tabulating such things as the output error statistics and the probability distribution of the number of distinct decoder states at some fixed but arbitrary depth into the survivor stream. The set of instrumentation subroutines called will vary considerably with the statistics that are being collected on the decoder at any particular time.

d. Decoding speed. The decoding speed of the convolutional decoder can best be described with reference to the operation and timing flow chart of Fig. 25. The
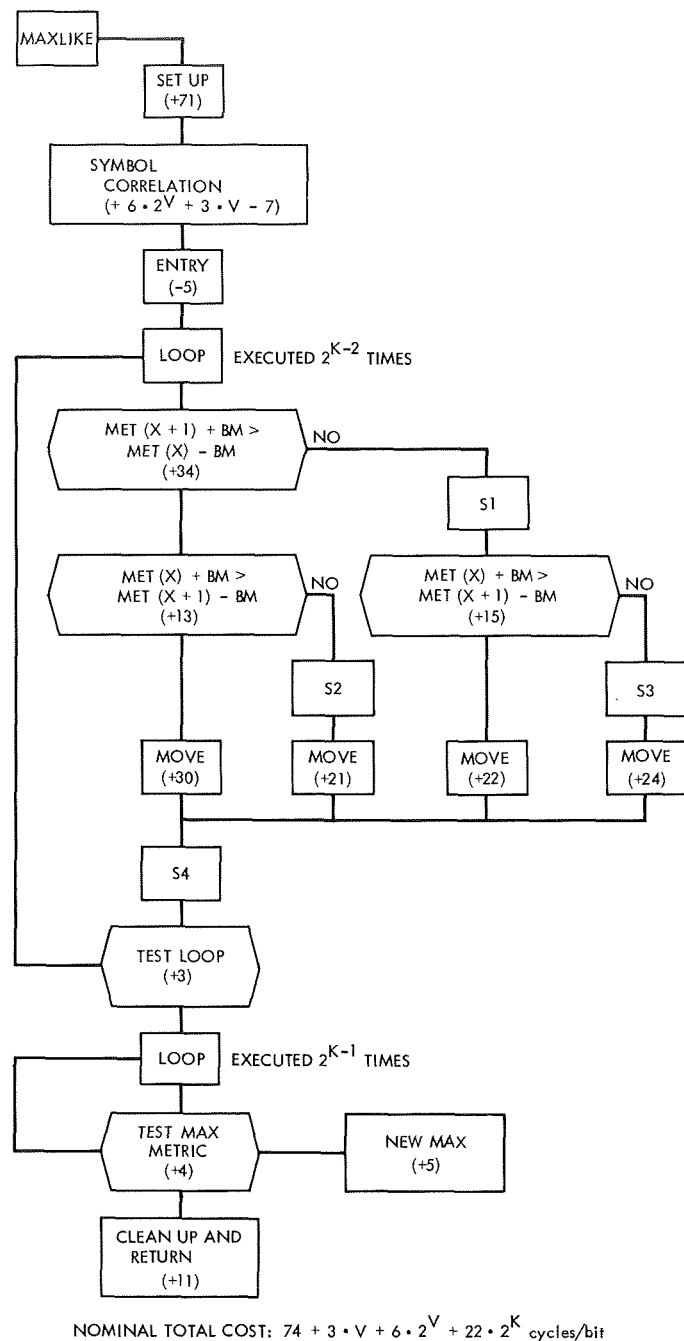
numbers inside each box represent the number of machine cycles (1.75 μs on an SDS 930, 8 μs on an SDS 920) required to perform that operation. As noted earlier, the majority of the overhead for initial entry into the decoder corresponds to modification of instructions for indexing through the survivor array. The 2^V possible branch metric values are computed and stored immediately following subroutine entry to reduce the computation in the main loop.

```
MAXLIKE

SET UP
(+71)

SYMBOL
CORRELATION
(+ 6·2^V + 3·V − 7)

ENTRY
(−5)

LOOP     EXECUTED 2^(K−2) TIMES

MET (X + 1) + BM >
MET (X) − BM          NO
(+34)
                                         S1

MET (X) + BM >          MET (X) + BM >
MET (X + 1) − BM   NO   MET (X + 1) − BM   NO
(+13)                  (+15)

              S2                    S3

MOVE    MOVE    MOVE    MOVE
(+30)   (+21)   (+22)   (+24)

S4

TEST LOOP
(+3)

LOOP     EXECUTED 2^(K−1) TIMES

TEST MAX
METRIC            NEW MAX
(+4)              (+5)

CLEAN UP AND
RETURN
(+11)
```

NOMINAL TOTAL COST: $74 + 3·V + 6·2^V + 22·2^K$ cycles/bit

Fig. 25. Operation and timing flow chart

The branches that correspond to the four possible alternative decisions for each pair of states within the main program loop are each performed in separate instruction sequences. In the flow chart, the symbol X represents the name of the state with a most-significant zero bit, MET(X) the accumulated metric value for that state, and BM the associated zero-branch metric. The boxes labeled "MOVE" represent the storing of the new state metric values and the updating of the survivors. Their costs vary because in some cases only one of the two survivors had to be updated, and in some cases other instruction simplifications could be made because of favorable arrangement of the data. The final operation is the selection of the most-likely state. The overall computation time for one decoding step is approximately

$$74 + 3 \cdot V + 6 \cdot 2^V + 22 \cdot 2^K \text{ cycles/bit} \tag{1}$$

where V is the number of symbols per branch and K is the code constraint length. This represents a decoding rate of about 25 bits/s at $K = 10$, $V = 3$; 370 bits/s at $K = 6$, $V = 3$; and 1.1 kbits/s at $K = 4$, $V = 3$ on the SDS 930.

At the smaller values of K, however, other programming techniques could be used to provide increased speed at the expense of massive increases in the memory requirement. Specifically, what must be done is to duplicate the instructions for each state pair in the decoder, to "ping-pong" between two sets of instructions and two different buffer areas, and to reduce the length of the survivor bit streams to one computer word instead of two. The duplication of instructions and buffer area eliminates all indexing through the survivor and metric storage since each reference to this area is made by an instruction that only references one specific cell. In this form, the overall computation time is then approximately

$$4 + 3 \cdot V + 3 \cdot 2^V + 11 \cdot 2^K \text{ cycles/bit} \tag{2}$$

This represents, on the SDS 930, a decoding rate of about 2.6 kbits/s for $K = 4$, $V = 3$; and 5.0 kbits/s for $K = 3$, $V = 2$. Use of this faster technique for K larger than 4 is probably impractical since approximately $15 \cdot 2^K$ words of program and data storage are required.

4. Communication Statistics: The Distribution of the Order Statistics of Discrete Distributions, I. Eisenberger

a. Introduction. If a set of n independent sample values $y_1, y_2, \cdots, y_n$, taken from a population with density function $f(y)$ and distribution function $F(y)$, is arranged in ascending order of magnitude

$$y_{(1)} \leq y_{(2)} \leq \cdots \leq y_{(n)} \tag{1}$$

then $y_{(k)}$ is usually referred to as the kth order statistic. For our purposes, however, we will denote by X_ν the νth value from the top in relation (1), that is, $X_\nu = y_{(n-\nu+1)}$, $\nu = 1, 2, \cdots, n$. Thus, for $\nu = 1$ and $\nu = n$, X_ν denotes the maximum and minimum values, respectively, of the sample. When $f(y)$ is continuous, the density function associated with the random variable X_ν is well known and given by (Ref. 1)

$$g_\nu(x) = n \binom{n-1}{\nu-1} [F(x)]^{n-\nu} [1 - F(x)]^{\nu-1} f(x) \tag{2}$$

However, when $f(y)$ is discrete, that is,

$$f(y) = \begin{cases} \text{Prob}\,(Y = y), & y = a_1, a_2, \cdots, a_n \\ 0, & \text{otherwise} \end{cases}$$

the density $g_\nu(x)$ is not of the relatively simple form given by Eq. (2). Familiar examples of this type of distribution are the Poisson and binomial distributions. For the Poisson, the range of Y is the set of all non-negative integers, while for the binomial the range is, for finite m, the set of integers $0, 1, \cdots, m$. The purpose of this report is to derive the density function of the νth value from the top of an ordered set of n sample values taken from a population with a discrete distribution, since the number of failures of DSIF subsystems in a given time has a discrete rather than a continuous distribution.

b. Derivation of the Distribution of X_ν. We will first assume that, as in the case of the Poisson distribution, Y takes on only the values $0, 1, 2, \cdots$ with positive probability and consider the distribution of X_ν for $\nu = 1$. The density of X_1, the maximum of the sample, is of the form

$$g_1(x) = \begin{cases} \text{Prob}\,(X_1 = x), & x = 0, 1, 2, \cdots \\ 0, & \text{otherwise} \end{cases}$$

For $x > 0$, $X_1 = x$ if k of the samples equal x and $n - k$ of the samples are less than x, for $k = 1, 2, \cdots, n$. For a

given value of k, the number of permutations of the sample values that meet this condition is

$$\binom{n}{k}$$

Thus,

$$g_1(x) = \sum_{k=1}^{n} \binom{n}{k} [F(x-1)]^{n-k} f^k(x), \qquad x = 1, 2, \cdots \tag{3}$$

For $x = 0$, all the sample values must equal zero, so that

$$g_1(0) = f^n(0)$$

This value of $g_1(0)$ can also be derived from Eq. (3) if when $x = 0$ one defines

$$[F(x-1)]^{n-k} = \begin{cases} 0, & k \neq n \\ 1, & k = n \end{cases}$$

For $\nu > 1$, $X_\nu = x$ if j of the sample values are greater than x, for $j = 0, 1, \cdots, \nu - 1$; k of the sample values are less than x, for $k = 0, 1, \cdots, n - \nu$ and the remaining $n - k - j$ of the sample values equal x. The number of permutations of the sample values for given j and k that meets these conditions is

$$\binom{n}{n-k-j} \binom{k+j}{j}$$

Thus,

$$g_\nu(x) = \sum_{j=0}^{\nu-1} \sum_{k=0}^{n-\nu} \binom{n}{k+j} \binom{k+j}{j} [F(x-1)]^k [1 - F(x)]^j [f(x)]^{n-k-j} \tag{4}$$

An alternate form of Eq. (4) is given by

$$g_\nu(x) = \sum_{j=1}^{\nu} \sum_{k=j}^{n-\nu+j} \binom{n}{n-\nu+j} \binom{n-\nu+j}{k} [F(x-1)]^{n-\nu+j-k} [1 - F(x)]^{\nu-j} f^k(x)$$

By putting $k = 0$ in Eq. (4), one obtains for $x = 0$

$$g_\nu(0) = \sum_{j=0}^{\nu-1} \binom{n}{j} [1 - F(0)]^j [f(0)]^{n-j}$$

which reduces to $f^n(0)$ when $\nu = 1$. It is also evident that

$$g_n(0) = 1 - [1 - f(0)]^n$$

When Y takes on only the values $x = 0, 1, 2, \cdots, m$, by putting $j = 0$ in Eq. (4), one obtains for $x = m$

$$g_\nu(m) = \sum_{k=0}^{n-\nu} \binom{n}{k} [F(m-1)]^k [f(m)]^{n-k}$$

which becomes $f^n(m)$ for $\nu = n$.

For computational purposes, the following recursion formula may be used for $\nu > 1, x > 0$:

$$g_\nu(x) = g_{\nu-1}(x) + \sum_{k=1}^{n-\nu+1} \binom{n}{\nu-1} \binom{n-\nu+1}{k} [F(x-1)]^{n-\nu+1-k} [1-F(x)]^{\nu-1} f^k(x)$$

$$- [F(x-1)]^{n-\nu+1} \sum_{j=1}^{\nu-1} \binom{n}{j} \binom{n-j}{\nu-j+1} [1-F(x)]^{\nu-j-1} f^j(x)$$

When Y takes on the values $x = a_1 < a_2 < \cdots < a_m$, then

$$g_\nu(a_1) = \sum_{j=0}^{\nu=1} \binom{n}{j} [1-F(a_1)]^j [f(a_1)]^{n-j}$$

$$g_1(a_1) = f^n(a_1)$$

$$g_\nu(a_m) = \sum_{k=0}^{n-\nu} \binom{n}{k} [F(a_{m-1})]^k [f(a_m)]^{n-k}$$

$$g_n(a_m) = f^n(a_m)$$

The distribution function, $G_\nu(x)$, for both continuous and discrete distributions, is given by

$$G_\nu(x) \sum_{j=0}^{\nu-1} \binom{n}{j} [F(x)]^{n-j} [1-F(x)]^j \qquad (5)$$

In the continuous case, differentiation of Eq. (5) gives Eq. (2). In the discrete case, if a_m is the largest value that Y can assume,

$$G_\nu(a_m) = [F(a_m)]^n$$

for all ν.

Table 12. Expected value and sample mean of the order statistics from a Poisson distribution*

| | $n = 10$ | | | | | | | | $n = 20$ | | | |
| ν | $\lambda = 1$ | | $\lambda = 3$ | | $\lambda = 5$ | | $\lambda = 10$ | | $\lambda = 1$ | | $\lambda = 10$ | |
	$E(X_\nu)$	$\bar{X}_\nu$	$E(X_\nu)$	$\bar{X}_\nu$	$E(X_\nu)$	$\bar{X}_\nu$	$E(X_\nu)$	$\bar{X}_\nu$	$E(X_\nu)$	$\bar{X}_\nu$	$E(X_\nu)$	$\bar{X}_\nu$
1	2.738	2.72	5.895	5.96	8.681	8.60	15.12	15.46	3.213	3.22	16.32	16.28
2	1.990	2.00	4.742	4.80	7.253	7.28	13.19	13.42	2.525	2.58	14.62	14.58
3	1.551	1.56	4.052	4.22	6.387	6.40	12.00	12.12	2.149	2.08	13.63	13.52
4	1.230	1.14	3.521	3.42	5.714	5.78	11.07	11.04	1.887	1.82	12.89	13.00
5	0.979	0.96	3.065	3.06	5.130	5.14	10.25	10.28	1.660	1.66	12.29	12.28
6	0.737	0.74	2.644	2.60	4.585	4.58	9.47	9.38	1.444	1.42	11.77	11.78
7	0.471	0.46	2.233	2.14	4.045	3.94	8.70	8.62	1.259	1.16	11.29	11.42
8	0.225	0.20	1.807	1.84	3.476	3.42	7.87	7.68	1.122	1.10	10.85	11.00
9	0.0695	0.12	1.327	1.38	2.819	2.72	6.89	6.78	1.027	0.96	10.44	10.46
10	0.0102	0.02	0.713	0.72	1.910	1.86	5.46	5.24	0.946	0.90	10.04	9.92
11									0.846	0.84	9.65	9.60
12									0.708	0.70	9.26	9.18
13									0.535	0.54	8.87	8.74
14									0.353	0.30	8.47	8.26
15									0.196	0.12	8.04	7.86
16									0.089	0.08	7.59	7.52
17									0.031	0.04	7.09	7.04
18									0.0080	0	6.51	6.46
19									0.0013	0	5.77	5.62
20									0.0001	0	4.62	4.60

* $f_1(y) = \dfrac{e^{-\lambda} \lambda^y}{y!}$, $y = 0, 1, 2, \cdots$

c. Examples. Very often the information that is of greatest interest with respect to order statistics is the mean, or expected value $E(X_\nu)$, of X_ν. Since the distribution of the order statistics of a discrete distribution is also discrete, $E(X_\nu)$ is given by

$$E(X_\nu) = \sum_x x_i\, g_\nu(x_i)$$

where x_i runs over all values of x in the range of X_ν.

Three examples of discrete distributions are considered.

(1) *Poisson:* $f_1(y) = \dfrac{\lambda^y e^{-\lambda}}{y!}$, $y = 0, 1, 2, \cdots$.

(2) *Binomial:* $f_2(y) = \dbinom{m}{y} p^y (1-p)^{m-y}$,

$\quad y = 0, 1, 2, \cdots, m$.

(3) *Uniform:* $f_3(y) = 1/m$, $y = 0, 1, 2, \cdots, m-1$.

For each example, $E(X_\nu)$ was computed for several values of the parameters involved for $n = 10$, and for some of the values for $n = 20$. Then, using random numbers, for each case 50 sets of samples (each of size n) were drawn from a density $f(y)$. The order statistics were determined for each of the 50 sets and then averaged to obtain $\overline{X}_\nu$, $\nu = 1, 2, \cdots, n$. Tables 12–14 give the results. In Table 13, $E(X_\nu; p) = m - E(X_{n-\nu+1}; 1-p)$, so that $E(X_\nu; p)$ can be computed for $p = 0.2$, 0.4, 0.7, and 0.9 from the results given in the table for $p = 0.8$, 0.6, 0.3, and 0.1, respectively. For the uniform example (Table 14), it can be seen that $E(X_\nu; m) = (m-1) - E(X_{n-\nu+1}; m)$.

It should perhaps be noted that, since the data given in the tables under the headings $\overline{X}_\nu$ are the means of samples of size 50, Var $(\overline{X}_\nu) = $ Var $(X_\nu)/50$.

Reference

1. Cramér, H., *Mathematical Methods of Statistics,* p. 370. Princeton University Press, Princeton, N.J., 1946.

Table 13. Expected value and sample mean of the order statistics from a binomial distribution*

| ν | n = 10, m = 10 | | | | | | | | | | n = 20, m = 10 | | n = 20, m = 20 | |
| | p = 0.1 | | p = 0.3 | | p = 0.5 | | p = 0.6 | | p = 0.8 | | p = 0.5 | | p = 0.5 | |
	$E(X_\nu)$	$\overline{X}_\nu$	$E(X_\nu)$	$\overline{X}_\nu$	$E(X_\nu)$	$\overline{X}_\nu$	$E(X_\nu)$	$\overline{X}_\nu$	$E(X_\nu)$	$\overline{X}_\nu$	$E(X_\nu)$	$\overline{X}_\nu$	$E(X_\nu)$	$\overline{X}_\nu$
1	2.609	2.58	5.293	5.18	7.382	7.48	8.268	8.32	9.670	9.76	7.866	7.86	14.12	14.22
2	1.945	1.86	4.453	4.46	6.576	6.46	7.536	7.44	9.229	9.34	7.199	7.22	13.13	13.28
3	1.540	1.48	3.921	3.88	6.039	5.99	7.032	7.08	8.871	8.88	6.781	6.78	12.52	12.52
4	1.236	1.32	3.495	3.40	5.597	5.56	6.609	6.50	8.556	8.50	6.454	6.52	12.06	12.10
5	1.002	1.00	3.119	3.00	5.195	5.20	6.220	6.02	8.244	8.24	6.179	6.16	11.67	11.62
6	0.780	0.82	2.763	2.68	4.805	4.82	5.839	5.72	7.934	7.84	5.940	5.88	11.32	11.40
7	0.522	0.52	2.403	2.40	4.403	4.32	5.441	5.38	7.604	7.58	5.718	5.74	11.01	11.00
8	0.265	0.32	2.021	1.96	3.961	3.88	4.997	4.92	7.220	7.18	5.501	5.52	10.71	10.76
9	0.0873	0.08	1.574	1.62	3.424	3.30	4.450	4.42	6.731	6.60	5.291	5.26	10.42	10.50
10	0.0137	0.02	0.957	1.00	2.618	2.480	3.608	3.62	5.941	5.78	5.095	5.08	10.14	10.28
11											4.905	4.84	9.86	9.94
12											4.709	4.52	9.58	9.72
13											4.499	4.36	9.29	9.52
14											4.282	4.18	9.00	9.18
15											4.060	3.96	8.68	8.84
16											3.821	3.72	8.33	8.48
17											3.456	3.50	7.94	8.10
18											3.219	3.18	7.48	7.64
19											2.801	2.84	6.87	7.08
20											2.134	2.18	5.88	5.96

* $f_2(y) = \dbinom{m}{y} p^y (1-p)^{m-y}$, $y = 0, 1, 2, \cdots, m$

Table 14. Expected value and sample mean of the order statistics from a discrete uniform distribution*

ν	n = 10				n = 20			
	m = 10		m = 20		m = 10		m = 20	
	$E(X_\nu)$	$\overline{X}_\nu$	$E(X_\nu)$	$\overline{X}_\nu$	$E(X_\nu)$	$\overline{X}_\nu$	$E(X_\nu)$	$\overline{X}_\nu$
1	8.509	8.62	17.64	17.64	8.866	8.94	18.47	18.32
2	7.680	7.64	15.86	15.94	8.531	8.56	17.59	17.72
3	6.774	6.66	14.05	14.58	8.078	8.06	16.64	16.84
4	5.864	5.68	12.23	13.00	7.597	7.52	15.69	15.92
5	4.955	5.02	10.41	11.04	7.119	7.10	14.74	15.08
6	4.045	4.08	8.59	9.20	6.643	6.56	13.79	14.10
7	3.136	3.24	6.77	7.26	6.167	5.94	12.83	13.04
8	2.226	2.38	4.95	5.46	5.690	5.46	11.88	12.08
9	1.320	1.26	3.14	3.30	5.214	4.82	10.93	11.10
10	0.491	0.40	1.36	1.24	4.738	4.48	9.98	10.12
11					4.262	4.04	9.02	9.44
12					3.786	3.50	8.07	8.28
13					3.310	3.10	7.12	7.36
14					2.833	2.66	6.17	6.38
15					2.357	2.30	5.21	5.14
16					1.881	1.74	4.26	4.08
17					1.403	1.28	3.31	3.12
18					0.922	0.86	2.36	2.10
19					0.469	0.38	1.41	1.24
20					0.134	0.06	0.54	0.54

*$f_3(y) = 1/m, y = 0, 1, 2, \cdots, m - 1$

5. Frequency Generation and Control: A Method for Temperature Stabilization of Cables Transmitting Standard Frequencies, P. Clements

a. Introduction. The hydrogen maser output frequency is sensitive to small disturbances in the external magnetic field (SPS 37-59, Vol. II, pp. 40–43). It is necessary to locate the maser away from these disturbances in order to obtain maximum frequency stability. In order to achieve this isolation, a temporary facility was constructed approximately 450 ft south of the control building at DSS 14. Cables were placed underground from the facility to the control room to investigate the feasibility of maintaining frequency stability over this distance.

b. Factors determining temperature stability. The greatest influence that degrades frequency stability in a cable is changes in the temperature of the cable. The ground is a good thermal insulator and its effectiveness can be investigated as follows. The amplitude of a surface originated sinusoidal temperature oscillation at a depth X in the ground, considered here as a semi-infinite solid, decreases as (Ref. 1)

$$y = \exp\left(\frac{-2\pi X}{\lambda}\right) \qquad (1)$$

where λ is the wavelength given by

$$\lambda = \left(\frac{4\pi k}{\nu}\right)^{1/2} \qquad (2)$$

$k \approx 0.01$ for rock-like material and ν is the radian frequency of the temperature oscillation.

For typical rock-like material:

λ	ν
2.7 cm	1 cycle/min
1 m	1 cycle/day
20 m	1 cycle/yr

Consider a diurnal periodic wave with amplitude A. At the surface of the ground, the first harmonic is 1 cycle/day. At a depth into the ground of $X = \lambda$,

$$y = \exp\left(\frac{-2\pi X}{\lambda}\right) = \exp\left(-2\pi\right) \approx 0.0019 \tag{3}$$

so that at 1 m

$$a = Ay = 0.0019A \tag{4}$$

and, with $A = 50°\text{C}$ peak to peak (p–p),

$$a = (50)(0.0019) = 0.0950°\text{C p–p} \tag{5}$$

c. Cable installation at DSS 14. For this particular installation at DSS 14, where the cable length is approximately 450 ft, a frequency stability can be calculated. Assuming the value of a given by Eq. (5) and considering the cable as being phase-modulated with temperature, calculations show a frequency stability of approximately 2.4×10^{-16} at 1 MHz using a cable with a stability of 10 ppm/°F (Times Wire and Cable Co. semi-rigid 50 Ω PCM-5014 PX-10).

To protect the cables from mechanical damage, as well as providing additional thermal protection, a layer of rigid urethane foam was applied around a duct in which the cable was placed (Fig. 26). The additional thermal protection provided by the approximately 10-cm thickness of foam can be calculated as follows: With a particular urethane having a value of $k \approx 0.0001$,

$$\lambda = \left(\frac{4\pi k}{\nu}\right)^{1/2}\Bigg|_{1\,\text{cycle/day}} \approx 10\,\text{cm} \tag{6}$$
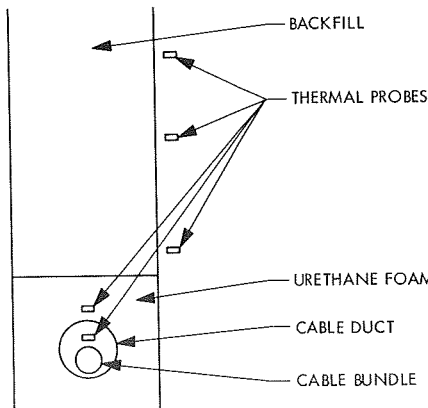
Fig. 26. Cross-sectional view of cable run at test point

which means 10 cm of foam is roughly equivalent to 1 m of earth.

Thermal probes were installed approximately 100 ft from any structure (Fig. 26). These probes will provide data on true temperature variations in the ground for more precise design information for future applications.

d. Conclusion. It has been shown to be feasible to locate hydrogen maser frequency standards as far as 1000 ft from the area in which the standard frequencies will be used without degrading their performance. Since it is not presently feasible to locate hydrogen masers in DSN control buildings because of magnetic fields, the ability shown here to isolate the masers without degrading phase and frequency stability is necessary to equip the DSN with hydrogen maser frequency standards.

Reference

1. Carslaw, H. F., and Jaeger, J. C., *Conduction of Heat in Solids*, Second Edition. The Macmillan Co., New York, 1959.

6. Digital Telemetry and Command: An Improved Noise Estimator for Biorthogonal Block Codes, *J. K. Holmes*

a. Introduction. Recently Posner (SPS 37-58, Vol. II, pp. 37–39) proposed a new method of estimating the standard deviation of the noise for a first-order Reed–Muller $(2^n, n + 1)$ biorthogonal code. This estimate, when used with a signal estimate, produces a monitor on the signal-to-noise ratio (SNR), and thereby a monitor of the system. This method modified the previously existing technique in that it utilized both the largest and second largest correlation values of the code words, whereas the previous method (SPS 37-49, Vol. III, pp. 306–310) used the largest correlation and one picked at random. Posner's method decreased the variance of the estimate substantially [12.25 dB for the (32,6) code]. Both of these methods utilize only one correlation per word time for the noise estimate.

The estimator to be described here utilizes all the noise-only word correlations per word time, and provides an additional improvement over Posner's estimate that increases with n [3 dB for a (32,6) code]. Furthermore, it appears to be essentially no more difficult to implement and would be nearly compatible with the existing software for the noise estimate. Finally, this estimator is only 0.5 dB worse in variance than the maximum likelihood estimate (MLE) for all n, whereas Posner's estimate decreases in efficiency as n increases.

b. The estimator. If we let $|C_i^j|$ denote the magnitude of the word correlations of the jth word at time iT, then the estimate of σ, the standard deviation of the noise, is of the form

$$\hat{\sigma} = \frac{(\pi/}{M(2^n - 1)} \sum_{i=1}^{M} \left(\sum_{j=1}^{2^n} |C_i^j| - |C_i^J| \right) \quad (1)$$

where 2^n is the number of code words in one word time and $|C_i^J|$ is the largest correlation at word time iT. In other words, for each word time all $2^n - 1$ noise-only correlations are added (the largest is excluded since it contains signal with high probability) so that after M word times there are $M(2^n - 1)$ correlations that have been added.

It is not difficult to obtain the division by $2^n - 1$ in the binary number system either in the hardware prior to the software or in the software itself.

c. Performance. It can be shown for a single sample of the magnitude of a gaussian, zero-mean random variable, $|C_i^j|$, with variance σ^2 that

$$E[|C_i^j|] = \left(\frac{2}{\pi}\right)^{1/2} \sigma \quad (2)$$

$$\text{Var}(|C_i^j|) = \left(1 - \frac{2}{\pi}\right) \sigma^2 \quad (3)$$

Hence, the per sample variance, of our estimate, is

$$\text{Var}(\hat{\sigma}) = 0.571 \, \sigma^2 \quad (4)$$

and for $2^n - 1$ samples per word the variance is

$$\text{Var}(\hat{\sigma}_n) = \frac{0.571}{2^n - 1} \sigma^2 \quad (5)$$

In comparing the estimate described here with that presented in SPS 37-58, Vol. II, the following improvements were noted:

Code	n	Variance decrease, dB
(16,5)	4	1.72
(32,6)	5	3.06
(64,7)	6	4.14

Of course, for M word times, the estimate has a variance given by

$$\text{Var}\,\hat{\sigma}_{Mn} = \frac{0.571}{M(2^n - 1)} \sigma^2 \quad (6)$$

It can be shown (Ref. 1) that the MLE of σ, that is, $\hat{\hat{\sigma}}$, has a large-sample variance given by

$$\text{Var}\left(\hat{\hat{\sigma}}\right) = \frac{0.5}{M(2^n - 1)} \sigma^2 \quad (7)$$

and hence the estimate proposed here is only 0.5 dB worse than the MLE.

d. The SNR estimate. The SNR estimator, employing the noise estimator discussed here, can be expressed as

$$\widehat{\text{SNR}} = \frac{\frac{1}{M} \sum_{i=1}^{M} |C_i^J|}{\frac{(\pi/2)^{1/2}}{M(2^n - 1)} \sum_{i=1}^{M} \sum_{\substack{j=1 \\ j \neq J}}^{2^n - 1} |C_i^j|} \quad (8)$$

This is a voltage SNR estimate and will be used to show the relative effect of the noise part of the SNR estimate. In order to compute Var $(\widehat{\text{SNR}})$, let

$$\frac{1}{M} \sum_{1}^{M} |C_i^J| = AT_w + \delta_M \quad (9)$$

and

$$\frac{(\pi/2)^{1/2}}{Mn} \sum_{i=1}^{M} \sum_{\substack{j=1 \\ j \neq J}}^{2^n - 1} |C_i^j| = \sigma + \gamma_{Mn} \quad (10)$$

where AT_w is the mean value of the correlation containing the transmitted word with amplitude A and word time T_w. To facilitate the following computation, it is assumed that the largest word correlation corresponds to the transmitted word. The error in this assumption can be shown to be negligible. Since M is quite large (4096), γ_{Mn} is small compared to σ and δ_M is small compared to AT_w so that we may write

$$\text{SNR} = \frac{AT_w}{\sigma} \left(1 + \frac{\delta_M}{AT_w} - \frac{\gamma_{Mn}}{\sigma}\right) + R \quad (11)$$

with the remainder R being negligible in comparison to the terms retained. Upon computing the variance of

Eq. (11) with R assumed to be zero, we obtain

$$\text{Var}\,(\widehat{\text{SNR}}) = \frac{1}{M}\left(\frac{AT_w}{\sigma}\right)^2 \left[\frac{\sigma^2}{(AT_w)^2} + \frac{\left(\frac{\pi}{2}-1\right)}{(2^n-1)}\right]$$

(12)

We see from Eq. (12) that at high SNR the second term dominates, and this is the term due to the noise estimate. Hence, although the signal estimate cannot be improved significantly for fixed M, an improvement in the noise estimate, which this article proposes, translates into almost a direct improvement in the SNR estimate at high SNR. For a (32,6) code, the variance due to the noise estimate dominates whenever SNR > 18 dB.

Reference

1. Mood, A. M., *Introduction to the Theory of Statistics.* McGraw-Hill Book Co., Inc., New York, 1950.

7. Digital Telemetry and Command: Coding Efficiency and Decoder Complexity, *J. E. Savage*[17]

a. Introduction. In this article it is shown that coding efficiency is limited by the amount of computational work allowed by a decoder. Coding efficiency is the rate, as a fraction of channel capacity, at which coded data is transmitted. The computational work X, done by a decoder consisting of L sequential machines S_1, S_2, $\cdots$, S_L is defined by

$$X = \sum_{i=1}^{L} X_i T_i$$

(1)

where T_i is the number of cycles executed by S_i and X_i is the number of two-input, binary logic elements it contains (assuming that storage in each machine consists of individually accessed binary cells).

b. Bounds on coding efficiency. It has been shown[18] that

$$X \geq \frac{n}{2}$$

(2)

where n is the total number of decoder inputs to a completely connected discrete memoryless channel (DMC) and the average probability of error P_e is less than $P_{\min}$, the smallest channel transition probability. There is reason to believe that this bound is weak at non-zero code rates and that it should, rather, grow as n^2.

Let us now look at M-orthogonal signaling on the additive gaussian noise (AGN) channel. The decoder inputs will be the outputs of M matched filters quantized to Q bits, say. Then $n = MQ$ and

$$2X \geq MQ = e^{RT}Q$$

(3)

where R is the rate in bits/s and T is the duration of each orthogonal signal. Since $Q < \infty$, the channel that has been created by cascading the modulator (the AGN channel) and quantized matched filter output is a DMC to which we can apply lower bounds to P_e. We have

$$P_e \geq \exp\{-T[E_Q(R) + o(T)]\}$$

(4)

where $o(T) \to 0$ as $T \to \infty$.

Let reliability $\mathcal{E}$ be defined by

$$\mathcal{E} = -\log_2 P_e$$

(5)

Then, for large $\mathcal{E}$, we have for T from inequality (4)

$$T \geq \frac{\mathcal{E}}{E_Q(R)}$$

(6)

or from inequality (3)

$$2X \geq Q\exp\left[\frac{\mathcal{E}R}{E_Q(R)}\right]$$

(7)

From this basic inequality we see that *we do not want to increase the quantization Q indefinitely* since $E_Q(R)$ approaches a non-zero limit.

In the limit of large Q, P_e is well known (Ref. 1) and Gallager (Ref. 2) has shown that

$$E_\infty(R) = \begin{cases} \dfrac{C_\infty}{2} - R, & 0 < R \leq \dfrac{C_\infty}{4} \\ (C_\infty^{1/2} - R^{1/2})^2, & \dfrac{C_\infty}{4} \leq R \leq C_\infty \end{cases}$$

(8)

where $C_\infty = \frac{1}{2}\,S/N$ is the capacity of the infinite band-width AGN channel. Assume that Q is sufficiently large, such that $E_Q(R) \cong E_\infty(R)$. Then, with coding efficiency λ given by

$$\lambda = \frac{R}{C_\infty} \tag{9}$$

we have from inequality (7) for $C_\infty/4 \le R \le C_\infty$ and large $\mathcal{E}$

$$\lambda \le \left[1 - \frac{1}{1 + \left[\frac{1}{\mathcal{E}}\ln\left(\frac{2x}{Q}\right)\right]^{1/2}} \right]^2 \tag{10}$$

This quantifies the following for the white gaussian channel with infinite bandwidth: *to increase coding efficiency, $\mathcal{E}$ or Q must be decreased (or x increased).*

Example. Suppose that an efficiency of 0.81 is desired. Suppose also that $Q = 3$, $\mathcal{E} = 7$ ($P_e \sim 10^{-3}$) and that the large $\mathcal{E}$ approximations hold. Then inequality (10) implies that

$$x \ge e^{567} \tag{11}$$

which is too large an amount of computational work.

Consider next a (narrowband) channel of bandwidth W where each output is quantized to Q bits. Then, if T is the duration of the $M = e^{TR}$ signals, we have

$$2x \ge n = 2WTQ \tag{12}$$

so that the computational work required by the decoder grows at least linearly (and very likely faster) with the time–bandwidth product.

The bandlimited AGN channel is an example of a very noisy channel when the signal-to-noise ratio (S/N) is small. On such channels, the bounds of inequalities (4) and (6) with $E_\infty(R)$ given by Eq. (8) apply.

Making the appropriate substitutions into inequality (12), we have for large $\mathcal{E}$

$$2x \ge \frac{2WQ\,\mathcal{E}}{E_Q(R)} \tag{13}$$

from which it is clear that the size of Q should be limited. Now solving for λ we have

$$\lambda \le \left[1 - \left(\frac{\mathcal{E}\,Q}{2x(C/2W)}\right)^{1/2} \right]^2 \tag{14}$$

where

$$\frac{C}{2W} = \frac{1}{2}\ln\left(1 + \frac{S}{N}\right) \tag{15}$$

We recall that the bandlimited AGN channel is very noisy for small S/N and that the bound of inequality (14) holds for large $\mathcal{E}$.

We see that efficiency is increased by reducing $\mathcal{E}\,Q$ [or increasing $2x\,(C/2W)$]. Again, suppose that $\lambda = 0.81$ is desired and that $\mathcal{E} = 7$, $Q = 3$ and $C/2W = 1$. Then, if the approximation of large $\mathcal{E}$ holds,

$$x \ge 1050$$

and if the lower bound of inequality (2) grows as the square of n, this bound will be near 10^6, which is within the realm of implementability.

c. Conclusions. The empirical fact that it is difficult to approach channel capacity is supported by the results of this article. It is decidedly more difficult to approach capacity in the large bandwidth case as can be seen by comparing the bounds on coding efficiency given by inequalities (10) and (14).

References

1. Viterbi, A. J., "On Coded Phase-Coherent Communications," *IRE Trans. Space Electron. Telemetry*, Vol. SET-7, pp. 3–14, 1961.

2. Gallager, R. G., *Information Theory and Reliable Communication*, p. 383. John Wiley & Sons, Inc., New York, 1968.

C. Communications Elements Research

1. Low Noise Receivers: Microwave Maser Development, R. C. Clauss, H. F. Reilly, Jr., and M. S. Reid

a. Introduction. An X-band maser has been tested to determine phase and amplitude stability characteristics. The maser covers a wide tuning range with reasonably high gain (30 to 40 dB). No attempt has been made to increase the instantaneous bandwidth beyond that achieved by operation in a uniform magnetic field.
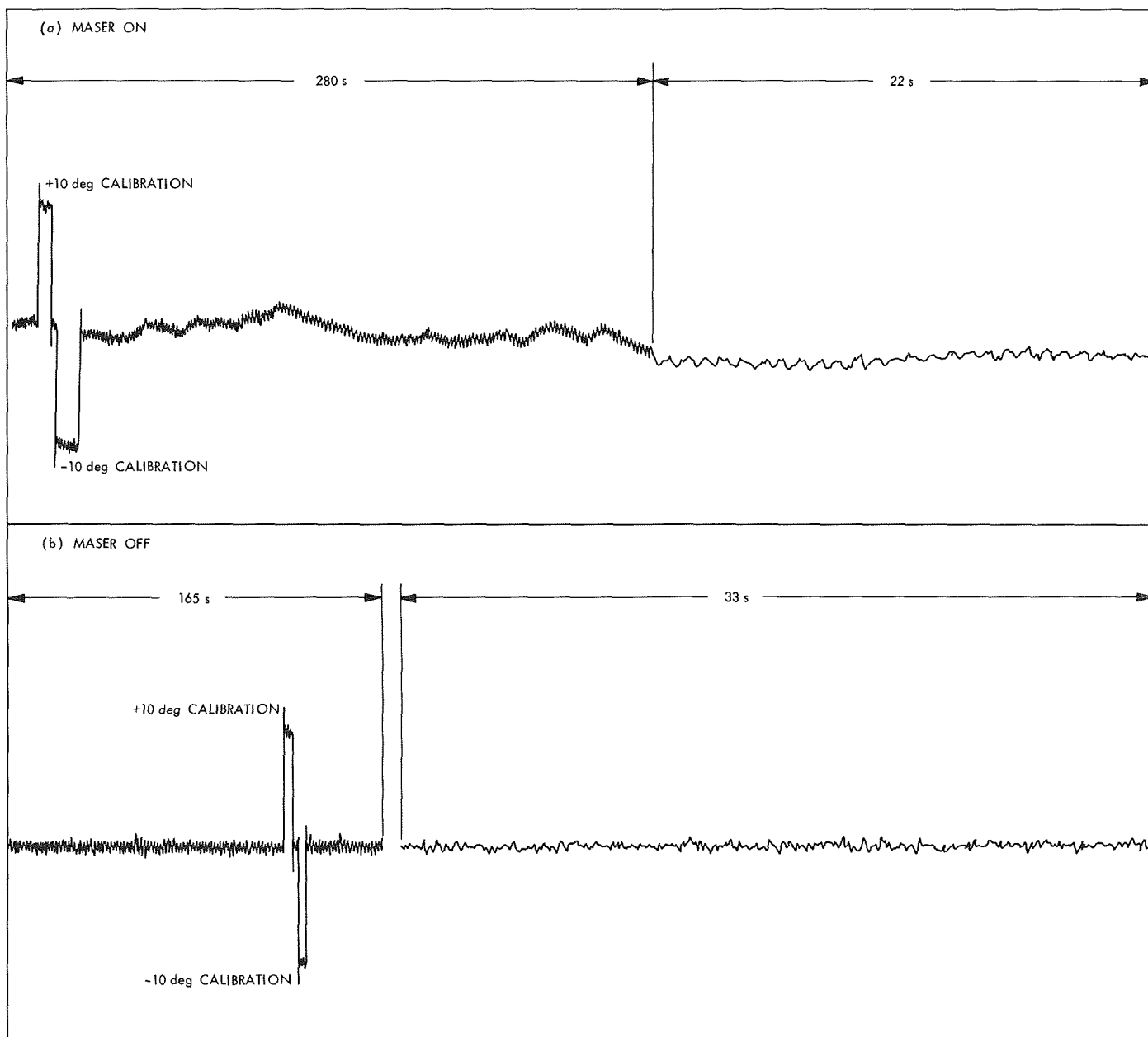
Fig. 27. Phase stability recordings at two different chart speeds

Noise temperature measurements have been made using both ambient and cryogenic terminations and waveguide horns facing the cold sky. The equivalent input noise temperature of the maser is 10°K at 7840 MHz and 7°K at 8448 MHz. Optimized input match and waveguide components selected for best performance at 8448 MHz cause improved performance at the higher frequency. Operation of the maser at reduced refrigerator temperature (4.0°K) and a minimum of waveguide components resulted in a total system temperature of 13°K.

b. Stability. Two parameters that affect the phase and amplitude of a signal amplified by the maser are pump frequency and magnetic field strength. The magnetic field required for maser operation between 7600 and 8900 MHz ranges from 4630 to 5120 G. A temperature-compensated, 4500-G permanent magnet is used. Electrical adjustment of the field is obtained with trim coils (on the pole pieces) and an adjustable power supply. Phase and amplitude changes with magnetic field changes are summarized in Table 15.

Table 15. Phase and amplitude changes caused by magnetic field changes

Trim current change		Magnetic field change		Signal change	
Amperes	Percent	Gauss	Percent	Amplitude, dB	Phase, deg
±0.005[a]	±0.61	±2.74[b]	0.055	−3.7[a]	±77[a]
±0.003[a]	±0.37	±1.64[b]	0.033	−1.5[a]	±50[a]
±0.001[a]	±0.12	±0.55[b]	0.011	−0.2[b]	±17[a]
±0.00006[b]	±0.007	±0.034[b]	0.00065	Not measurable	±1[b]

[a]Direct measurement.
[b]Extrapolation of measured data.

A Hewlett-Packard 8410A network analyzer was used to make phase stability measurements. Figure 27a shows short-term phase changes caused by the maser. Drift rates up to 4 deg/min were correlated with magnet power supply output changes. A 1.2-Hz phase modulation of approximately 1 deg peak-to-peak was caused by the refrigerator drive unit. The trace in Fig. 27b shows the resolution of the measurement system.

A klystron with 100-mW power output at 43.34 GHz is used to pump the maser (for a signal frequency of 8448 MHz). Signal phase and amplitude changes were measured while changing pump frequency with continuous-wave and frequency-modulated pumping techniques. Maximum maser gain and best stability are obtained when the pump frequency is modulated with a sine wave producing ±40 MHz frequency modulation. Spin-relaxation times in ruby are sufficiently long so that pump modulation rates above 20 kHz produce no measurable signal frequency modulation. Signal phase changes and maser gain changes caused by pump frequency changes are shown in Fig. 28.
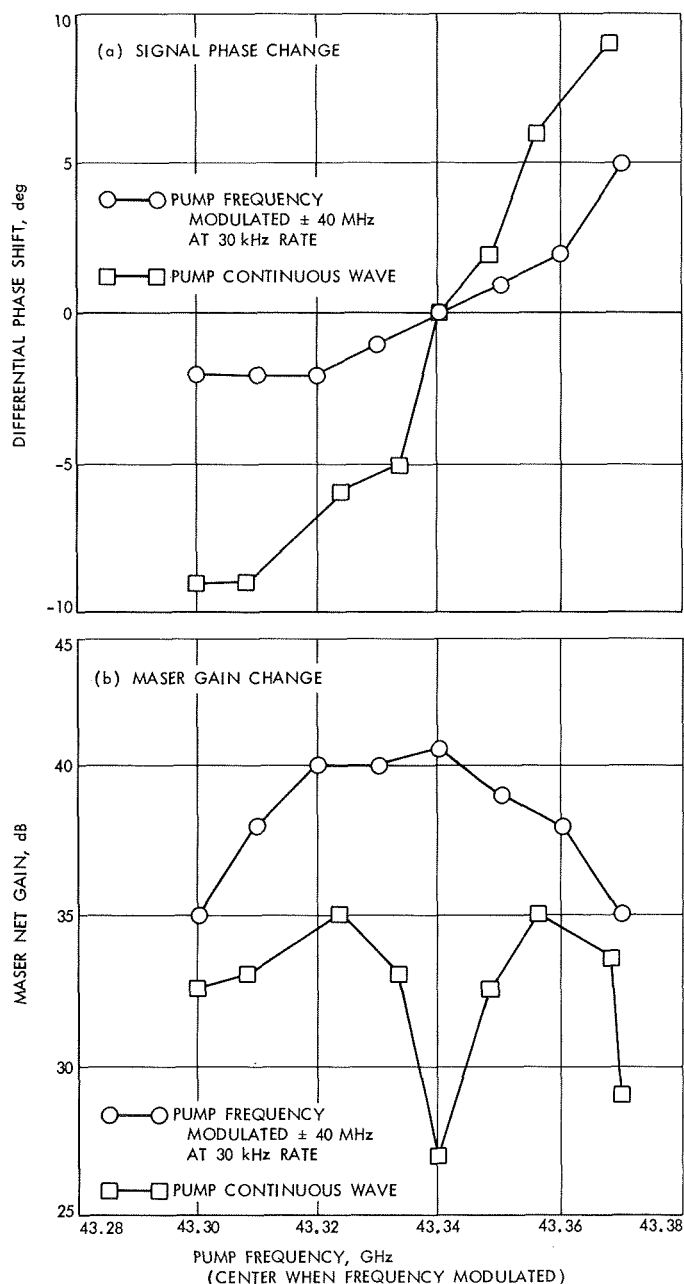
Fig. 28. Signal phase shift and maser gain versus pump frequency

c. Noise measurements. The equivalent input noise temperature of the maser has been measured using waveguide terminations at ambient and liquid nitrogen temperatures. At 8448 MHz, the predicted noise temperature (6.5°K) is in close agreement with measured values (~ 7°K). System temperature data indicate an approximate temperature of 10°K for the maser at 7840 MHz. Input waveguide components selected for best performance at 8448 MHz and optimized input match cause improved performance at the higher frequency.

The maser has been used to evaluate waveguide and feed system components. A block diagram of the very simple system used is shown in Fig. 29 and a photograph of the system is shown in Fig. 30. Power ratios measured when switching input terminations are used to calculate total system temperature. Microwave absorber material was placed above the horns to ensure validity of the measurements. Total system power recorded for either horn with absorber was equal to power from the ambient termination. Movement of the absorber, away from the horns for a distance of several inches, produced no measurable system power changes. Total system temperature was measured for several configurations. Comparison of the noise performance of a corrugated horn and a smooth horn was of particular interest (the corrugated horn has been described in SPS 37-58, Vol. II, pp. 61–64). A summary of system noise measurements is shown in Table 16. All measurements were made during excellent weather conditions (clear sky and low humidity). Variations in the follow-up receiver contribution were caused by several different maser gain settings (a

result of change in refrigerator temperature or maser tuning adjustment). A total power measurement resolution of 0.02 dB during the tests enabled the measurement of system temperature changes to 0.1°K.

The lowest system temperature (13°K) was measured by using microwave absorber above the horn as an ambient reference termination. Removal of the absorber (ambient temperature = 16°C), allowing the horn to

Fig. 30. Maser with feed horns for comparison

Fig. 29. System temperature evaluation block diagram

Table 16. System noise temperature measurements

Configuration	Temperature contribution at 8448 MHz			Total system temperature, °K
	Maser and horn, °K	Follow-up receiver, °K	Other feed components, °K	
1. Corrugated horn, maser, receiver (refrigerator temperature = 4.0°K)[a]	12.8	0.2	0	13.0
2. Corrugated horn, maser, receiver	13.1	0.7	0	13.8
3. Corrugated horn, 90-deg bend, waveguide switch, 4-in. waveguide (7–10 GHz), maser, receiver	13.1	0.7	2.5	16.3
4. Smooth horn, 90-deg bend, waveguide switch, 4-in. waveguide (7–10 GHz), maser, receiver	13.2	0.7	2.5	16.4
5. Corrugated horn, polarizer, 90-deg bend, waveguide switch, 4-in. waveguide (7–10 GHz), maser, receiver	13.1	0.4	3.7	17.2
6. 0.003-in. mylar horn cover, corrugated horn, polarizer, 90-deg bend, waveguide switch, 4-in. waveguide (7–10 GHz), maser, receiver	13.1	0.4	3.9	17.4
7. 0.005-in. kapton horn cover, corrugated horn, polarizer, 90-deg bend, waveguide switch, 4-in. waveguide (7–10 GHz), maser, receiver	13.1	0.4	3.9	17.4
8. Assembled cassegrain cone including all components listed for Configuration 7 plus a calibration coupler	13.1	0.4	5.2	18.7
9. Same as Configuration 8 (measured at 7840 MHz)	16.1	1.1	5.5	22.7

[a]The refrigerator temperature = 4.4°K for Configurations 2–9.

"see" cold sky, caused a total system noise power reduction of 13.58 dB (±0.02 dB peak-to-peak measurement spread). The maser was operated at a reduced refrigerator temperature (4.0°K) and the corrugated horn was bolted directly to the maser input connection. The minimum configuration system temperature was 13.8°K at the normal operating refrigerator temperature of 4.4°K.

2. Improved RF Calibration Techniques: MXK Cone (Mod 0) Waveguide and Noise Temperature Calibrations, P. D. Batelaan and M. S. Reid

a. Introduction. This article presents noise temperature, reflection coefficient, and waveguide loss data for the new JPL MXK antenna cone. Measurement of spacecraft received signal strength and radio star flux density requires accurate knowledge of the RF losses, both dissipative and reactive, in the cone. Knowledge of the system-contributed noise is important for spacecraft performance, predictions, and measurements, and as a monitor of the cone microwave system stability and performance.

Figure 31 is a block diagram of the MXK cone waveguide system. For the insertion loss and reflection coefficient measurements, ports A and B were terminated in waveguide loads each with a voltage standing wave ratio (VSWR) of better than 1.01. For the noise temperature measurements, these ports were connected to the cone noise box having a VSWR of about 1.03.

The loss measurements were made by a contractor using precision techniques developed at JPL. The remaining measurements were made by JPL personnel when the cone was in its final assembly and test stages.

b. Waveguide calibration results. The insertion losses of the MXK cone were measured with a precision laboratory dc insertion loss test set (SPS 37-25, Vol. IV, pp. 132–133). Reflection coefficients were measured with a precision tuned reflectometer. Table 17 shows the results of reflection coefficient measurements for the feed horn and Table 18 shows the attenuation data.

c. Noise temperature calibration results. After completion of the waveguide insertion loss and reflection coefficient measurements, the traveling wave maser was installed in the cone and noise temperature calibrations were made.

A WR-112 liquid nitrogen load was connected to port 2 (Fig. 31), and, by use of the Y-factor method, the various noise temperatures were calibrated. These data were

Table 17. Voltage reflection coefficients for antenna feed horn versus polarization measured at port 1

Frequency, MHz	Polarization	Voltage reflection coefficient
8448	Right-circular	0.0675
	Left-circular	0.0692
	Linear	0.0793
8115	Right-circular	0.0237
	Left-circular	0.0316
	Linear	0.0700
7840	Right-circular	0.0211
	Left-circular	0.0188
	Linear	0.0562

taken at 7840 and 8448 MHz. The results are presented in Table 19.

The impedance matching of the various waveguide components is an important factor in all microwave measurements and is especially important here. The ambient load, which is used for on-the-antenna performance monitoring, had been tuned to 8448 MHz. It was determined that the mismatch at 7840 MHz was so bad as to cause large errors in noise measurement. Further, attempts to broadband-tune the ambient load failed. As a result, the original ambient load was replaced with a commercial broadband waveguide load. The reflection coefficient of this load had not been measured in the laboratory but measurements made with the
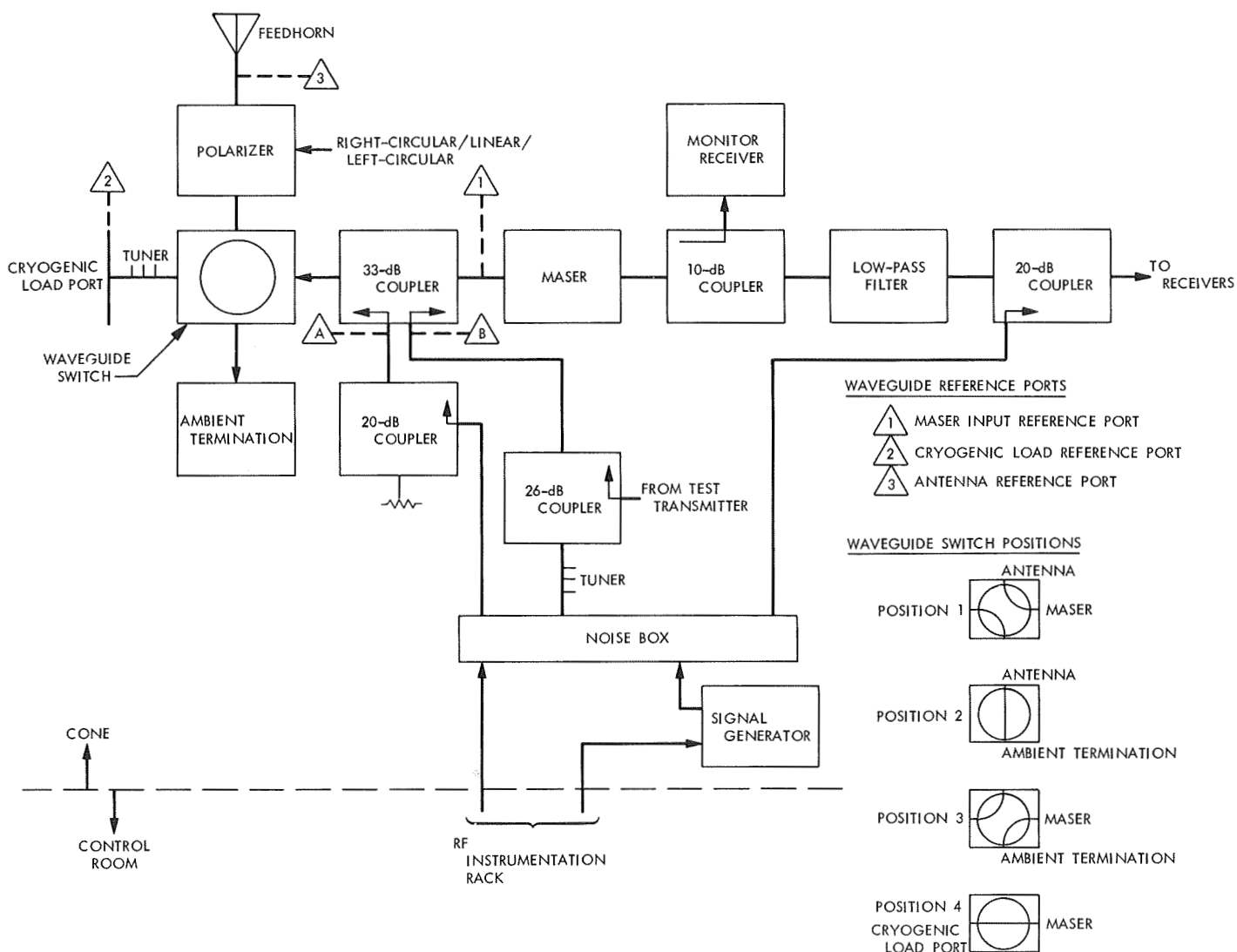
Fig. 31. MXK cone (SN 1, Mod 0) block diagram

Table 18. Attenuation data for waveguide paths in MXK cone

Frequency, MHz	Path[a]	Line attenuation			
		Total, dB	Total probable error,[b] dB	Dissipative, dB	Total probable error,[b] dB
8448	Cryoload to maser, port 2 to port 1	0.0681	±0.0004	0.0681	±0.0043
	Antenna to maser, port 3 to port 1	0.0481	±0.0005	0.0466	±0.0006
8115	Cryoload to maser, port 2 to port 1	0.0902	±0.0008	0.0814	±0.0013
	Antenna to maser, port 3 to port 1	0.0595	±0.0007	0.0539	±0.0010
7840	Cryoload to maser, port 2 to port 1	0.0787	±0.0014	0.0482	±0.0029
	Antenna to maser, port 3 to port 1	0.0617	±0.0008	0.0572	±0.0010

[a]See Fig. 31.

[b]The total probable error listed for each attenuation value includes the probable errors for (1) measurement dispersion, (2) imperfections in the sliding load, (3) mismatch errors, and (4) measurement system nonlinearity and resettability.

Table 19. Noise temperature calibrations of MXK cone measured at maser port (port 1, Fig. 31)

Source	Temperature, °K	
	7840 MHz	8448 MHz
System operating noise temperature (neglecting follow-up contribution)	22.3	18.6
Low-noise diode	3.42	1.30
High-noise diode	43.34	42.65

internal cone reflectometer indicated that its VSWR was 1.015 at 8448 MHz. Similar units have since been measured in the laboratory and show VSWR of 1.014 at 8448 MHz and 1.04 at 7840 MHz.

3. X-Band Cassegrain Cone Modification, D. E. Neff

a. Introduction. The X-band cone (MXK) is a low-noise antenna feed system designed primarily for use with the DSS 14 210-ft-diam antenna tricone system. It has been used previously to evaluate the 210-ft antenna structure at higher frequencies for the DSN. Since that time, substantial improvements have been implemented.

b. Recent work. The current MXK cone configuration (Fig. 32) is a logical step from the X-band cone (SPS 37-57, Vol. II, pp. 103–104) used for the first high-frequency gain measurements on the DSS 14 antenna.

The tricone structure has three main feedcone assemblies; (SPS 37-57, Vol. II, pp. 160–165, Figs. 24 and 25)

however, during the design stage, it was found to be possible to stop the subreflector in two additional positions over the R&D cone if the individual feedhorns could be mounted on an arc with 18-in. centers. At X-band (7000 MHz) or above, it is now possible to mount three separate antenna systems in the one cone.

The cone which is now complete, consists of a single-channel X-band feed system, maser, and associated receiver and calibration equipment (Fig. 31). Eventual use of this cone possibly may include other receivers for use on radio science experiments. Floor space has also been reserved in the cone for a possible future X-band transmitter installation.

4. S-Band Cassegrain Ultracone Modifications, D. E. Neff

a. Introduction. The ultracone (SCU) is a low-noise antenna feed system designed primarily for use with the DSS 14 210-ft-diam antenna system. Its use offers the best performance for the existing DSN tracking missions.

b. Recent work. The SCU antenna cone (SPS 37-58, Vol. II, pp. 59–61) has required several minor alterations to allow use on the DSS 14 tricone-equipped antenna. One alteration consisted of a new interlock system, designed by the JPL RF Systems Development Section, to protect equipment and personnel from the new 400-kW transmitter. This required fabrication of a new switch control panel and junction box for the cone. A second alteration included the construction of a new power supply with synchro indicator to operate the received linear polarization angle system for use with the *Pioneer* spacecraft. A third alteration was the addition of a
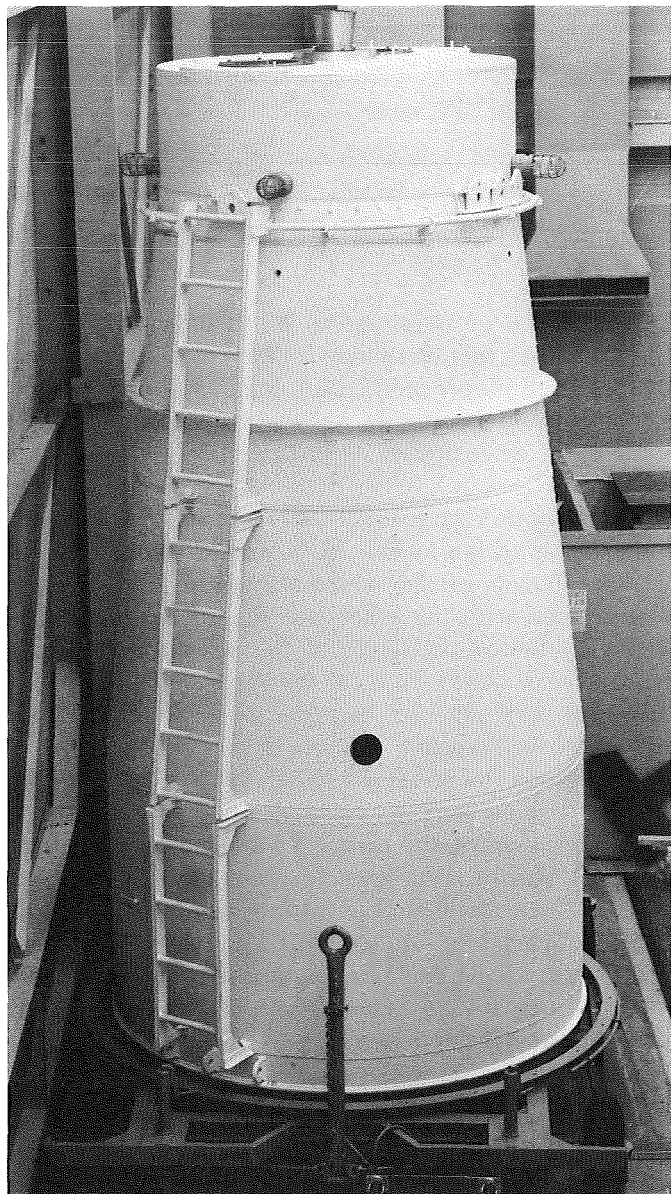
Fig. 32. X-band cone

polarization indicator to display the transmitted–received signal condition, i.e., right-circular, left-circular, or linear polarization. This work has been completed and the SCU cone is awaiting the new tricone configuration for final testing and ultimate operation.

A great effort has been made to guard against any change in the electrical performance of the SCU during the tricone construction since several very accurate gain calibrations have been made. It is anticipated that a direct gain test will be made to determine the exact tricone performance with respect to the old system.

5. RF Calibration Techniques: A Precision Compact Rotary Vane Attenuator, *T. Y. Otoshi*

a. Introduction. It has been demonstrated (SPS 37-60, Vol. II, pp. 41–43) that a modified attenuation law could be used to extend the useful dynamic attenuation range of a precision S-band rotary vane attenuator. The S-band attenuator is of the conventional design where the rotor is long, i.e., at least 3 or 4 waveguide wavelengths long at the lowest operating frequency.

Another application of the modified law is in the development of accurate compact rotary vane attenuators that have very short rotor sections. A shortening of the rotor section will cause a corresponding reduction of the total dynamic attenuation range; however, in theory, these compact attenuators will obey the modified law over the entire dynamic range.

To verify the modified law theory for attenuators with shortened rotors, a compact H-band rotary vane attenuator was fabricated and tested. This article presents a review of the theoretical equations and also the results of attenuation and phase shift calibrations made at 8448 MHz.

b. Theoretical equations. As derived in SPS 37-46, Vol. III, p. 73, the modified attenuation law for rotary vane attenuators is

$$A_{dB} = -10 \log_{10} [\cos^4 \theta$$
$$+ 10^{-L_{dB}/20} (2 \cos \phi \cos^2 \theta \sin^2 \theta) + 10^{-L_{dB}/10} \sin^4 \theta]$$

$$(1)$$

where

$\theta =$ the true rotary vane angle measured relative to the plane of the vanes in the stators. (It is assumed that there is no misalignment between the vanes in the stators.)

$L_{dB} =$ attenuation (in decibels) of the tangential component relative to the normal component at the rotor output. (It is related to the power loss ratio L by $L_{dB} = 10 \log_{10} L$.)

$\phi =$ phase shift difference between the tangential and normal electric field components at the rotor output.

From Eq. (2) of the referenced SPS article, the differential phase shift at any vane angle setting relative to the

0-deg vane angle setting can be derived as

$$\Delta\psi_{21} = \psi_{21}(\theta) - \psi_{21}(0)$$

$$= \arg\left[\frac{E_y(\theta)}{E_y(0)}\right]$$

$$= \tan^{-1}\left[\frac{-10^{-L_{dB}/20}\sin\phi\sin^2\theta}{\cos^2\theta + 10^{-L_{dB}/20}\cos\phi\sin^2\theta}\right] \quad (2)$$

where

$E_y(\theta), E_y(0)$ = total vertical component of the voltage wave at the rotor output when the vane angle is at the θ- and 0-deg settings, respectively

$\psi_{21}(\theta), \psi_{21}(0)$ = phase angles (in radians) of $E_y(\theta)$ and $E_y(0)$, respectively

It is interesting to note that when L_{dB} approaches infinity, Eq. (1) will reduce to the familiar unmodified law. It is also of interest to note that when $\theta = 90$ deg is substituted into Eqs. (1) and (2), A_{dB} becomes L_{dB} and $\Delta\psi_{21}$ becomes $-\phi$. Therefore, these two parameters can be experimentally determined by measuring the incremental attenuation and differential phase shift when the vane angle is set at 90 deg.

For most attenuators, there will be some deviations between the indicated and true vane angle due to boresight and other readout errors. The true vane angle can be expressed as

$$\theta = \theta_I + \alpha_1 + \alpha_2(\theta_I) \quad (3)$$

where

θ_I = indicated vane angle

α_1 = boresight error

$\alpha_2(\theta_I)$ = angle runout error calibrated relative to $\theta_I = 0$ deg setting. (It is a function of θ_I and is due to gearing errors, bearing runout, eccentricities, etc.)

The vane angle errors α_1 and $\alpha_2(\theta_I)$ should be calibrated to ensure that the attenuator follows the law given by Eq. (1). With proper mechanical design and use of high-precision components, the angular errors α_1 and $\alpha_2(\theta_I)$ can often be made negligibly small.

c. Description of compact attenuator. The compact attenuator is shown in Fig. 33. A pair of stepped transitions are shown installed on the attenuator. These can be interchanged with the other pair of tapered transitions shown to the left and right of the attenuator. The attenuator was tested in both the stepped and tapered transition configurations in order to determine if any differences would result from use of shortened transitions as well as a shortened rotor section.

A comparison of the compact attenuator and a conventional H-band rotary vane attenuator is shown in Fig. 34. (Both attenuators were fabricated by the Measurement Specialties Laboratory of Van Nuys, Calif.) The rotor length of the compact attenuator is approximately 3.4 in. as compared to a rotor length of about 10.9 in. for the conventional attenuator. Based on the rotor section
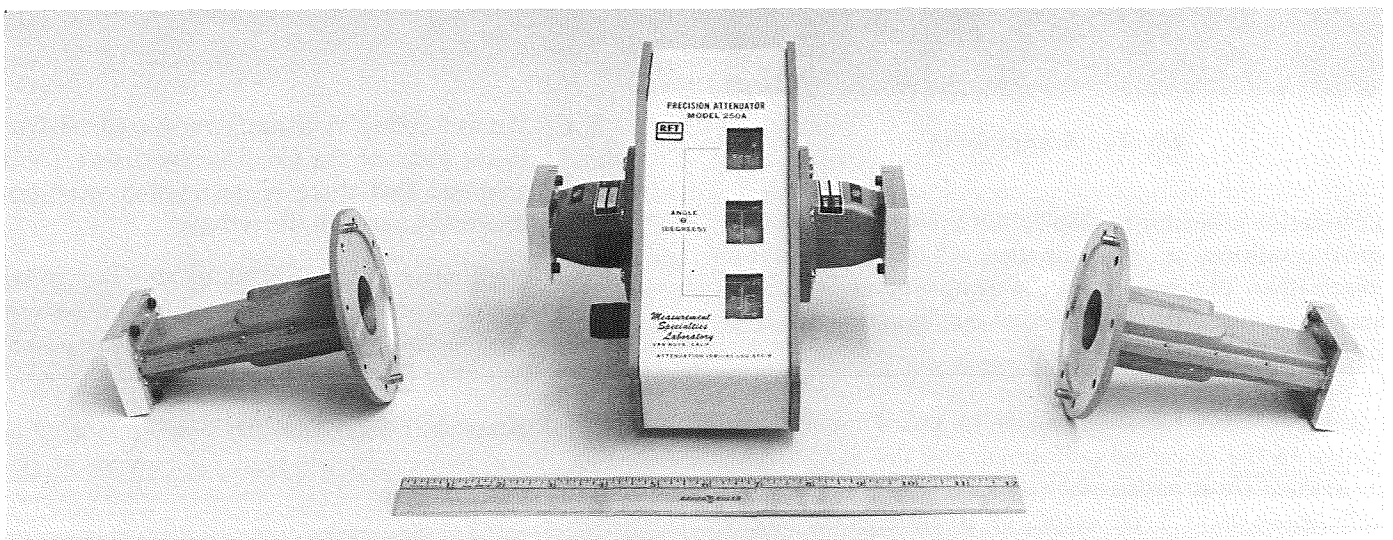
Fig. 33. Compact rotary vane attenuator shown with interchangeable transitions
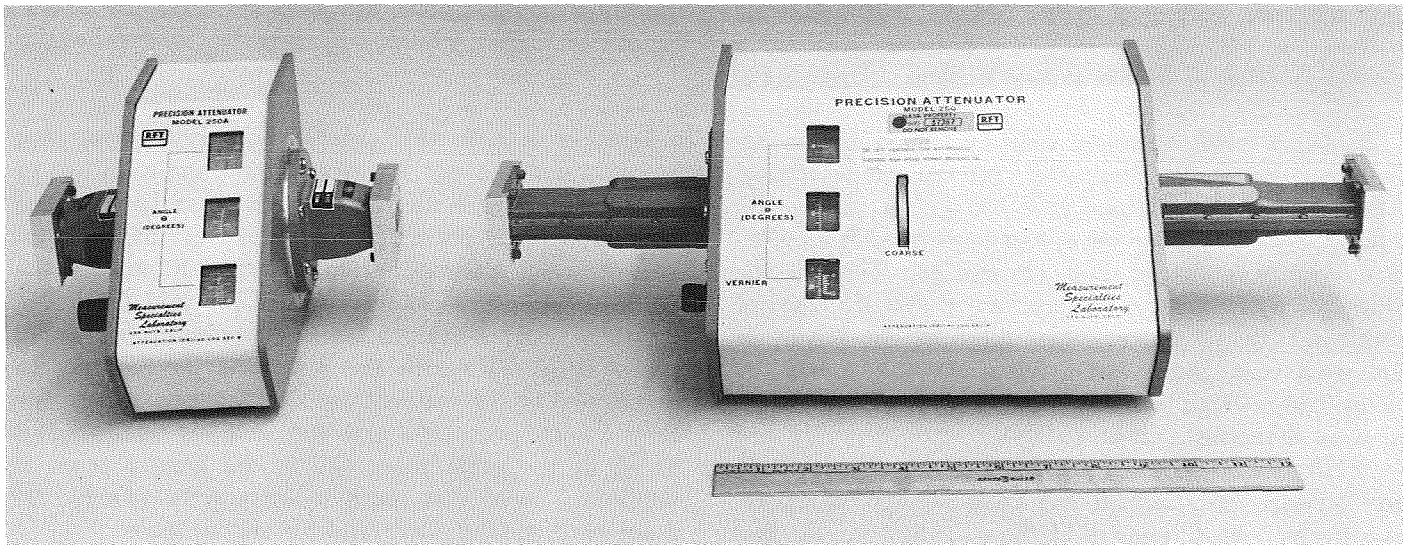
Fig. 34. Compact and conventional H-band rotary vane attenuators

diameter of 1.250 in. for both the conventional and compact attenuators, the waveguide wavelength λ_g for the TE_{11} mode in the rotor will be 1.852 in. at an operating frequency of 8448 MHz. (Note that the electrical length of the short rotor section is only 1.8 λ_g at this frequency.) When the stepped transitions are installed on the compact attenuator, the overall length is 8.1 in. as compared to an overall length of 21.6 in. for the conventional attenuator.

The compact attenuator is fabricated to have a very precise vane angle readout; the resolution of the readout of the vane angle position is 0.0001 deg, backlash appears to be less than 0.001 deg, and the readout error caused by gearing eccentricities and bearing runout is stated by the manufacturer to be less than 0.005 deg.

d. Electrical tests. All calibrations of the compact attenuator were performed at an operating frequency of 8448 MHz. The results presented in the remainder of this article are those of (1) reflection coefficient, (2) boresight error, (3) residual loss, (4) incremental attenuation, and (5) differential phase shift. Identical calibrations were made of the compact attenuator in the two different transition configurations.

Reflection coefficients. Figure 35 shows plots of measured reflection coefficients versus indicated vane angle settings. The maximum reflection coefficients measured for tapered and stepped transition configurations were, respectively, 0.050 at $\theta_I = 90$ deg and 0.046 at $\theta_I = 0$ deg.
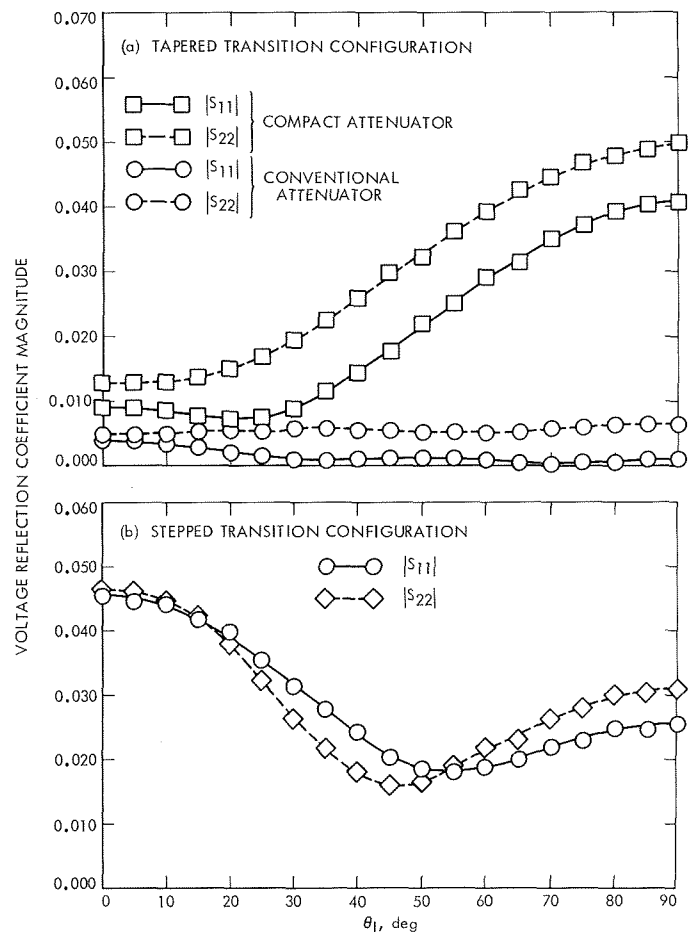
Fig. 35. Compact attenuator reflection coefficient versus θ_I setting

The reflection coefficient of the conventional attenuator is shown in Fig. 35a for reference purposes and has a maximum value of 0.0065 at $\theta_I = 90$ deg.

Boresight error. Boresight error is defined as the difference between the indicated and the true electrical 0-deg vane angle positions. It is the term α_1 in Eq. (3). An explicit relationship for α_1 can be derived from algebraic manipulations of Eqs. (1) and (3). Then, if the values of L_{dB}, ϕ, and $\alpha_2(\theta_I)$ are known and if values of measured attenuations are substituted for A_{dB} at various indicated vane angles, an average value of α_1 can be determined. Using this technique, the average values of α_1 were determined to be $(0.0064 \pm 0.0018\sigma_{\bar{x}})$ deg and $(-0.178 \pm 0.004\sigma_{\bar{x}})$ deg for the compact attenuator in the tapered and stepped transition configurations, respectively. The differences of the α_1 values for the two

transition configurations are believed to be due to differences in the mechanical alignments of the stator vanes.

Residual loss. In this article, the residual loss of a rotary vane attenuator is defined as the insertion loss of the attenuator when the vane angle is set at the indicated 0-deg vane angle setting. Residual losses of the compact attenuator for the tapered and stepped transition configurations were measured to be 0.111 and 0.115 dB, respectively. These values can be compared to a residual loss of 0.096 dB, which was measured for the conventional attenuator shown in Fig. 34. Although the conventional attenuator has the smallest residual loss while, at the same time, having the longest rotor, it should be noted that residual loss can be affected by stator card misalignment and mismatch losses.

Table 20. Incremental attenuation and differential phase shift for compact rotary vane attenuator in tapered transition configuration

θ_I, deg	Incremental attenuation, dB		Differential phase shift, deg			θ_I deg	Incremental attenuation, dB		Differential phase shift, deg	
	Theoretical value	Measured minus theoretical value	Theoretical value	Measured minus theoretical value			Theoretical value	Measured minus theoretical value	Theoretical value	Measured minus theoretical value
2.787	0.0202	−0.0001				48.752	7.006	0.002		
3.937	0.0403	−0.0005				51.646	8.007	0.004		
4.819	0.0604	−0.0008				54.286	9.008	−0.002		
5.562	0.0805	−0.0011				55.782	9.615	−0.004		
6.142	0.0982	−0.0014				56.710	10.008	−0.005		
6.216	0.1005	−0.0013				59.921	11.468	−0.002		
8.779	0.201	−0.002				60.000	11.506	−0.003	−4.0	−0.1
12.248	0.392	−0.001				61.028	12.010	−0.003		
12.388	0.401	−0.001				64.779	14.012	−0.008		
15.142	0.601	−0.001				68.089	16.014	−0.003		
17.451	0.802	0.000				71.051	18.016	0.002		
19.255	0.979	0.001				71.565	18.384	0.003		
19.474	1.002	0.001				73.749	20.019	−0.007		
20.000	1.058	0.001	−0.2	−0.1		76.259	22.021	−0.006		
27.284	2.003	0.000				78.677	24.025	0.009		
32.712	2.928	−0.003				80.000	25.114	0.013	−25.9	0.0
33.109	3.003	−0.002				81.146	26.027	0.013		
37.880	4.004	−0.001				84.019	28.030	0.003		
40.000	4.506	0.001	−1.0	−0.1		85.000	28.569	0.000	−41.6	−0.2
41.964	5.005	0.002				86.012	29.029	−0.003		
44.932	5.824	0.002				88.497	29.714	−0.003		
45.550	6.006	0.001				89.994	29.825[a]	—	−50.7[a]	—

[a]These are measured values used in the theoretical Eqs. (1) and (2).

Incremental attenuation and differential phase shift. Incremental attenuation is defined as the difference between the attenuation at the given vane angle setting and the attenuation at the 0-deg indicated vane angle setting (Ref. 1). Differential phase shift is defined as the difference of the phase angles of the output signals when the rotary vane is set to θ and 0 deg (Eq. 2). Incremental attenuations were calibrated at various indicated vane angles through the use of the ac ratio transformer test set described in Ref. 2. The differential phase shift measurements were made by the Microwave Standards Laboratory at the Hughes Aircraft Company (Culver City, Calif.). The overall accuracy of the phase shift measurements is estimated to be better than ± 0.5 deg.

A comparison of theoretical and measured attenuations and phase shifts are given in Tables 20 and 21, respec-

tively, for the compact rotary vane attenuator in the two transition configurations. Theoretical attenuations and differential phase shifts were computed through the use of Eqs. (1) and (2) and the following measured parameters:

Tapered transition configuration

$$L_{dB} = 29.825 \text{ dB}$$

$$\phi = 50.7 \text{ deg}$$

$$\alpha_1 = +0.0064 \text{ deg}$$

Stepped transition configuration

$$L_{dB} = 29.800 \text{ dB}$$

$$\phi = 50.1 \text{ deg}$$

$$\alpha_1 = -0.178 \text{ deg}$$

Table 21. Incremental attenuation and differential phase shift for compact rotary vane attenuator in stepped transition configuration

θ_I, deg	Incremental attenuation, dB		Differential phase shift, deg		θ_I, deg	Incremental attenuation, dB		Differential phase shift, deg	
	Theoretical value	Measured minus theoretical value	Theoretical value	Measured minus theoretical value		Theoretical value	Measured minus theoretical value	Theoretical value	Measured minus theoretical value
2.787	0.0176	0.0005			48.752	6.942	−0.003		
3.937	0.0366	0.0009			51.646	7.936	0.009		
4.819	0.0559	0.0011			54.286	8.930	0.005		
5.562	0.0752	0.0010			55.782	9.533	0.001		
6.142	0.0923	0.0011			56.710	9.923	0.004		
6.216	0.0946	0.0006			59.921	11.372	0.007		
8.779	0.192	0.002			60.000	11.410	0.009	−4.0	−0.6
12.248	0.380	0.002			61.028	11.910	0.005		
12.388	0.389	0.001			64.779	13.896	−0.004		
15.142	0.586	0.000			68.089	15.882	−0.003		
17.451	0.784	−0.001			71.051	17.868	−0.004		
19.255	0.960	0.002			71.565	18.233	−0.004		
19.474	0.982	0.002			73.749	19.855	−0.020		
20.000	1.038	0.003	−0.2	−0.2	76.259	21.844	−0.034		
27.284	1.974	0.000			78.677	23.840	−0.037		
32.712	2.892	−0.003			80.000	24.930	−0.043	−25.1	−1.2
33.109	2.967	−0.003			81.146	25.848	−0.052		
37.880	3.961	0.000			84.019	27.883	−0.073		
40.000	4.459	0.002	−1.0	−0.5	85.000	28.441	−0.076	−40.6	−0.9
41.964	4.954	0.004			86.012	28.922	−0.075		
44.932	5.768	0.004			88.497	29.659	−0.041		
45.550	5.948	0.006			90.000	29.798	−0.009		
					90.18	29.800[a]	—	−50.1[a]	—

[a]These are measured values used in the theoretical Eqs. (1) and (2).

Table 22. Calibration parameter summary of JPL research cones

Cone Model	Cone SN	Cone Mod	Construction date	Frequency, MHz	Maser SN	Maser Temperature, °K	Noise box correction,[a] dB C_1 (gain)	Noise box correction,[a] dB C_2 (VSWR)	VSWR[b] S_A	VSWR[b] S_P	VSWR[b] S_e	Approximate zenith low-noise path operating noise temperature, °K Ground located	Approximate zenith low-noise path operating noise temperature, °K Antenna mounted	Comments
SRO	01	00	7/69	2295	02	5.3	33.0	33.0	1.020	1.174	1.128		18.8	SPS 37-59, Vol. II, pp. 57–59
				2388		5.0	33.0	33.0	1.040	1.463	1.010		17.1	
SCU	01	02	6/69	2297	05	4.2	33.0	33.0	1.061	1.135	1.001	13.1	16.9	SPS 37-58, Vol. II, pp. 55–56
				2388		4.2	33.0	33.0	1.130	1.300[c]	1.081		22.6	
SCU (3A)	01			2297	03	5.5	33.0	33.0	1.004	1.135	1.003		22.1	
				2388		5.5	33.0	33.0	1.284	1.300[c]	1.292			

[a] C_1 = path loss to maser input reference to maser output; C_2 = path loss to maser input to termination or antenna under evaluation.
[b] S_A, S_P, S_e = VSWR (defined at maser input) of antenna (right-circular polarization), ambient termination, and maser input, respectively.
[c] Estimated.

The runout error $\alpha_2(\theta_t)$ was assumed to be zero at all vane angle settings. It can be seen from Tables 20 and 21 that excellent agreement between theoretical and measured values was obtained over about a 20-dB dynamic attenuation range. Although the errors of the attenuation calibrations have not been fully analyzed as yet, the deviations are believed to be due mainly to mismatch and runout errors.

e. Conclusion. It has been demonstrated that precision rotary vane attenuators will obey the modified law even when the rotor is very short. Although the compact attenuator has a smaller dynamic attenuation range (30 dB) than that of a conventional rotary vane attenuator, a compact attenuator can be very useful in the noise temperature calibrations of low-noise antenna systems.

References

1. Beatty, R. W., "Insertion Loss Concepts," *Proc. IEEE,* pp. 663–671, June 1964.

2. Finnie, C. J., Schuster, D., and Otoshi, T. Y., *AC Ratio Transformer Technique for Precision Insertion Loss Measurements,* Technical Report 32-690. Jet Propulsion Laboratory, Pasadena, Calif., Nov. 30, 1964.

6. Improved RF Calibration Techniques: System Operating Noise Temperature Calibrations of the JPL Research Cones, M. S. Reid and C. T. Stelzried

This article discusses the system operating noise temperature performance of the low-noise research cones. The operating noise temperature calibrations are performed with the ambient termination technique (SPS 37-42, Vol. III, pp. 25–32). The principal advantage of this method is the stability and reliability of the ambient termination.

The JPL research cones using this technique during this reporting period (October 1, 1969 through February 1, 1970) are:

(1) S-Band Research Operational (SRO) Cone.

(2) S-Band Cassegrain Ultra (SCU) Cone.

These cones are operated on the DSS 13 and DSS 14 antennas in a Cassegrain configuration. (The calibration data were taken by the personnel of the DSSs.) The calibration parameters of the JPL research cones are summarized in Table 22.

The averaged operating noise temperature calibrations of the various research cone configurations for this reporting period are presented in Table 23. The data taken at DSS 14 with Maser 2 used an aperture load placed by hand in position over the horn opening.

The operating noise temperature data were reduced with JPL computer program ID 5841000, CTS 20B. The indicated errors in Table 23 are the standard deviation of the individual measurements and of the means, respectively, and do not include instrumentation systematic errors. The averages were computed using only data with:

(1) Antenna at zenith.

(2) Clear weather.

(3) No RF spur in receiving passband.

(4) $PE_{T_{op}/D}$ less than 0.1°K (from computer program).

Table 23. Averaged system operating noise temperature calibrations of the various research cones

DSS	Frequency, MHz	Cone	Maser	Configu- ration	Maser gain, dB	Follow-up noise temperature contribution, °K	System operating noise temperature, °K
13	2388	SRO SN1 Mod 0	—	—	36.9 ± 0.52/0.10 (25 measurements)	0.80 ± 0.06/0.02 (13 measurements)	15.9 ± 0.28/0.08 (13 measurements)
13	2388	SRO SN1 Mod 0	—	Cone on ground	35.2 ± 0.92/0.38 (6 measurements)	1.12 ± 0.23/0.09 (6 measurements)	14.0 ± 0.39/0.17 (5 measurements)
14	2295	SCU SN1 Mod 2	2	Diplexed operation	50.4 ± 0.16/0.07 (8 measurements)	0.14 ± 0.02/0.01 (8 measurements)	22.5 ± 0.25/0.10 (8 measurements)

7. Received Signal Polarization Tracking Using an HA–dec Antenna, C. T. Stelzried, T. Sato, D. D. Hubiak, and A. Abreu

The polarization of a spacecraft signal received on an HA–dec antenna can be predicted by incorporating a slight modification into an existing computer program. The program (JPL ID 5879000) was originally written for the received signal polarization tracking of the *Pioneer VI* spacecraft during the 1968 Superior Conjunction (SPS 37-59, Vol. II, pp. 64–67) on the DSS 14 az–el antenna. This modification will provide operating personnel with the optimum setting for the DSN polarization converter used on the 85-ft-diam HA–dec antennas when tracking spacecraft with linearly polarized signals. Although the DSN polarization converter setting does not change (essentially) during a day's track, the setting will change slightly from day to day. Also, the setting can vary considerably with various spacecraft tracked from the same antenna on the same day.

The original polarization program transforms the polarization reading of an az–el antenna from the local horizon to the plane of the ecliptic. The signal polarization referred to the plane of the local horizon is (SPS 37-59, Vol. II with previous nomenclature).

$$\tau = \theta_p - p \qquad (1)$$

where

τ = signal polarization referred to plane of the ecliptic, deg

θ_p = signal polarization referred to local horizon, deg

p = angle between the plane of the ecliptic and the local horizon defined by the line of sight between the DSS and the probe, deg

An antenna polarization prediction is computed by assuming an initial signal polarization of 90 deg with reference to the plane of the ecliptic and transforming back to the DSS. This is given by

$$\theta_p = 90 + p \qquad (2)$$

During meridian transit, az–el and HA–dec antennas are similarly aligned. Therefore, the computer program can be easily modified to provide polarization prediction for an HA–dec antenna simply by interpolation of the polarization at meridian transit (azimuth = 180 or 360 deg). The criteria for using an azimuth of 180 or 360 deg is determined by the polarity of the zenith angle (Fig. 36) of the probe at meridian transit (Ref. 1 solving for Z_m)

$$Z_m = \delta - \phi \qquad (3)$$

where

Z_m = zenith angle of probe at meridian transit (positive when probe is north with an azimuth of 360 deg and negative when probe is south with an azimuth of 180 deg)

δ = probe declination

ϕ = DSS station latitude

This is appropriate for upper culmination (the meridian transit nearest to zenith) with the DSS in either the northern (ϕ positive) or southern hemisphere (ϕ negative). Specifically, the program interpolates the polarization to 180 deg azimuth when Z_m is negative and to 360 deg azimuth when Z_m is positive.

The DSN polarization converter consists of parallel vanes mounted on the face of the feed horn (Fig. 37). These vanes transform a linearly polarized signal (nominally at 45 deg with respect to the vanes) into a circularly polarized signal by the differential phase velocity of the signal components parallel and perpendicular to the vanes. This adapts the linearly polarized signal to the DSN right-circular polarized feed system.

Due to the non-IEEE standard readout of the DSN polarization converter (clockwise angle readout looking out antenna referred to the local vertical),

$$\theta_p' = 90 - (\theta_p)_{MT} \qquad (4)$$

where

θ_p' = polarization prediction for 85-ft antenna DSN polarization converter during meridian transit, deg

$(\theta_p)_{MT}$ = polarization prediction for az–el antenna interpolated at meridian transit (from Eq. 2, IEEE standard), deg

A sample printout for *Pioneer VIII* computed for DSS 12 is shown in Fig. 38. This provides a prediction for the

(a) NORTHERN HEMISPHERE DSS
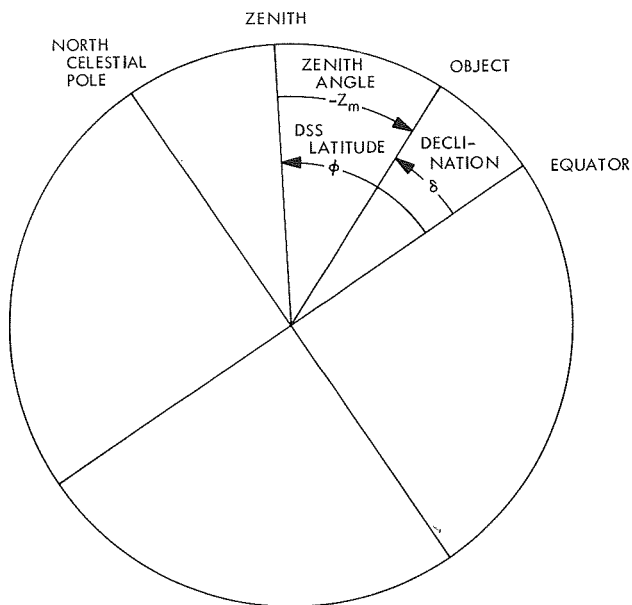
(b) SOUTHERN HEMISPHERE DSS
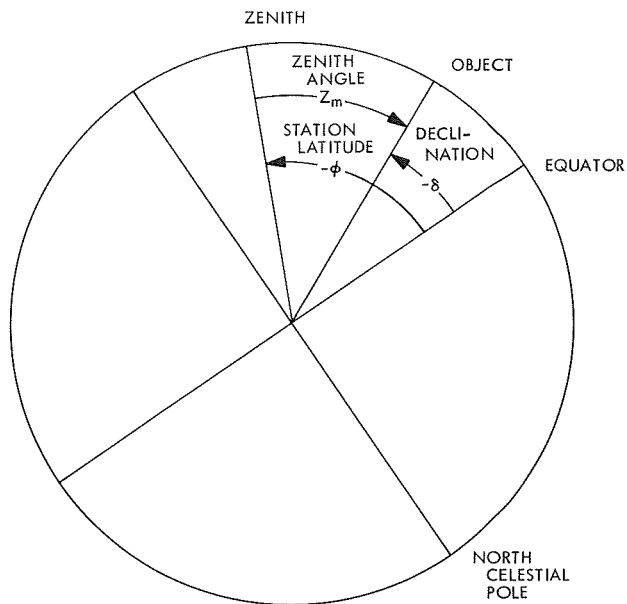
Fig. 36. Relation between declination, DSS latitude, and zenith angle at meridian transit during upper culmination
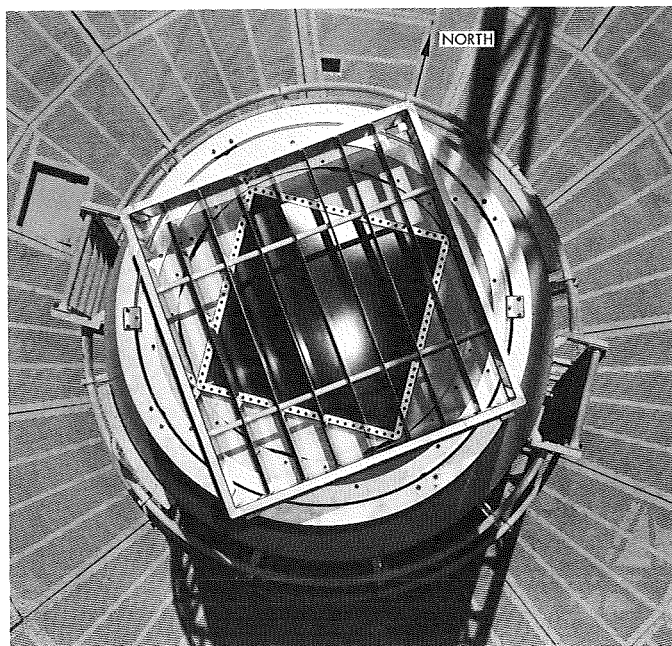
Fig. 37. DSN polarization converter mounted on DSS 11 85-ft-diam antenna feed horn

DATE   11570

DEC1	.960	RA1	2.297	TIME	0	LAT	35.118689
DEC2	1.364	RA2	3.227	TIME	2400	LONG	243.194560

INTERPOLATE AT AZ=180.0

DAY NO.	TRANSIT TIME	POL (IEEE)	POL (DSN)	G.H.A. ARIES
15.0141	.339	66.570	23.430	119.117
16.0139	.335	66.590	23.410	120.046
17.0138	.331	66.616	23.384	120.976
18.0136	.327	66.649	23.351	121.907
19.0135	.324	66.688	23.312	122.839
20.0133	.320	66.734	23.266	123.772
21.0132	.317	66.785	23.214	124.706
22.0131	.313	66.845	23.155	125.641
23.0129	.310	66.911	23.089	126.577
24.0128	.307	66.983	23.017	127.515
25.0127	.304	67.061	22.939	128.454
26.0125	.301	67.147	22.853	129.394
27.0124	.298	67.238	22.762	130.336
28.0123	.295	67.337	22.663	131.280
29.0122	.292	67.442	22.558	132.225
30.0121	.290	67.554	22.446	133.173
31.0120	.287	67.672	22.329	134.122
32.0119	.285	67.797	22.203	135.073
33.0118	.283	67.929	22.071	136.026
34.0117	.281	68.067	21.933	136.981
35.0116	.279	68.212	21.789	137.939
36.0115	.277	68.363	21.637	138.899
37.0115	.276	68.521	21.479	139.861
38.0114	.274	68.686	21.314	140.826
39.0114	.273	68.857	21.143	141.792
40.0113	.272	69.035	20.965	142.762
41.0113	.271	69.219	20.781	143.734
42.0113	.270	69.410	20.590	144.709
43.0112	.270	69.607	20.393	145.686
44.0112	.269	69.811	20.189	146.666
45.0112	.269	70.022	19.978	147.648
46.0112	.269	70.239	19.761	148.634
47.0112	.269	70.462	19.538	149.621
48.0112	.270	70.691	19.309	150.612
49.0113	.270	70.927	19.073	151.605
50.0113	.271	71.169	18.831	152.601
51.0113	.272	71.418	18.582	153.600
52.0114	.273	71.672	18.328	154.602

Fig. 38. Sample polarization predictions

HA–dec antenna using either a DSN polarization converter or for the new SPU cone (see *Subsection 8*) with IEEE readout at the time of the meridian transit.

Reference

1. Kraus, J. D., *Radio Astronomy*, p. 39. McGraw-Hill Book Co., Inc., New York, 1966.

8. Efficient Antenna Systems: S-Band Polar Ultra Cone,
F. E. McCrea

a. Introduction. To extend the threshold level and, therefore, the time period during which an 85-ft-diam-antenna station can deliver usable data from extended missions such as *Pioneers VI* and *VII*, a new low-noise front end for the DSIF HA–dec reflectors was constructed. Several novel features are employed and discussed here. The new front end has been designated SPU (S-band polar ultra) cone and provides ultra low-noise listen-only or low-noise diplexed modes with right circular polarization (RCP), left circular polarization (LCP), or linear polarization (LIN). Preliminary zenith

system temperatures of 17.2 and 25.8°K were demonstrated on January 28, 1970 at DSS 12.

b. Description. The SPU-cone block diagram (Fig. 39) shows the feedhorn, mode generator, polarizer, and rotary joints as identically used in the S-band cassegrain ultra (SCU) cone (SPS 37-49, Vol. II, pp. 58–59, and SPS 37-51, Vol. II, pp. 78–82). A minimal cost was a primary objective; therefore, a sheet metal feedhorn was used. Also, the quarterwave plate is made from a single extruded tubing with integral transformers, further reducing costs. Finally, the motor-driven rotating linear polarization mechanism is not needed on a polar-mounted reflector. A daily manual setting is entirely sufficient to prevent polarization loss during a pass (SPS 37-59, Vol. II, pp. 64–67).

Figure 40 is a view of the SPU-cone interior, looking upwards toward the feedhorn. The quarterwave plate weldment is seen; also shown is the manual RCP/LCP/LIN setting handle. Rotating parts are contained within a basket assembly, which was selected to be a bolted assembly. Previous welded assemblies are somewhat
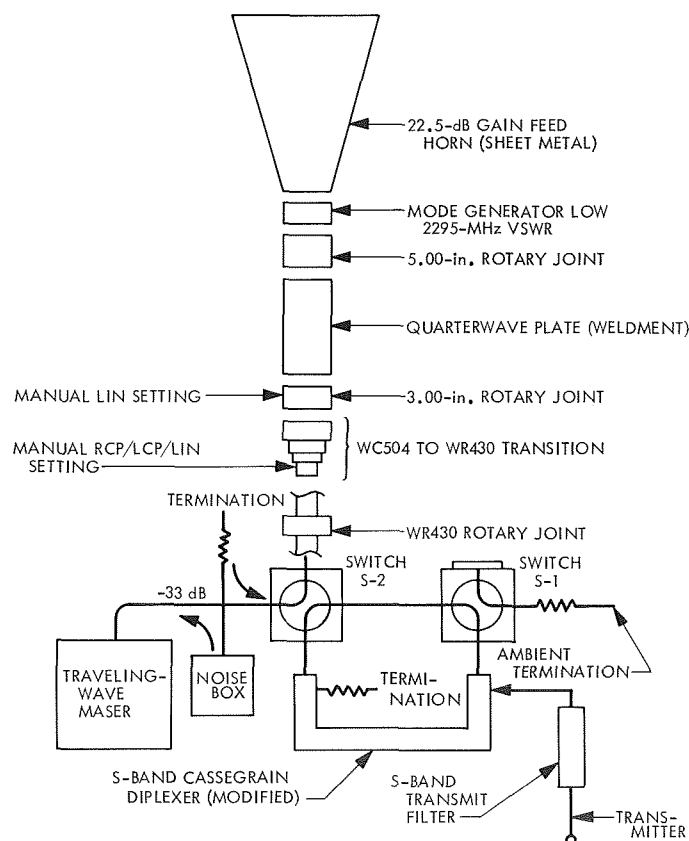
Fig. 39. SPU-cone block diagram
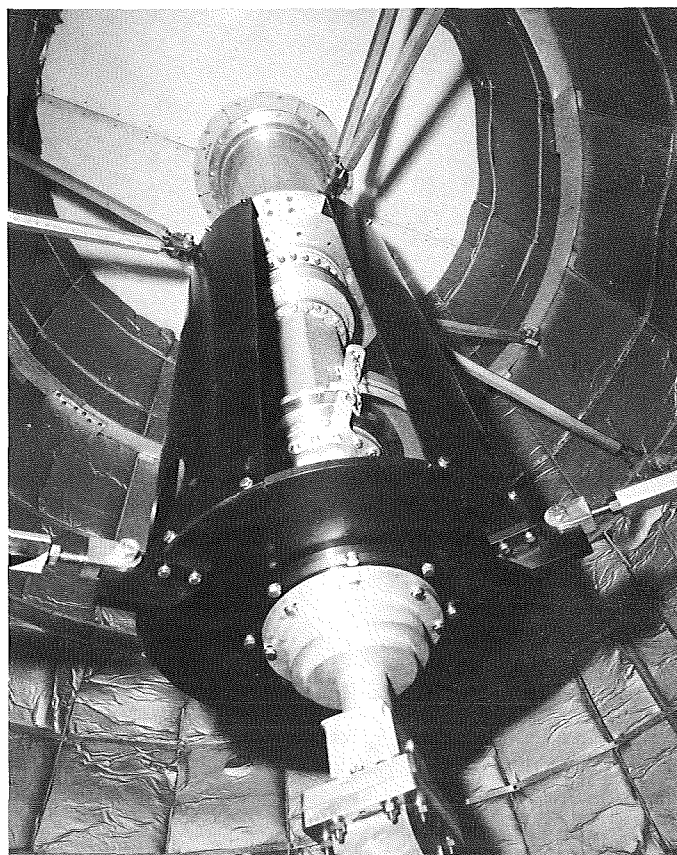
Fig. 40. SPU polarization basket assembly

more expensive and require lead time unavailable for this construction.

Figure 41 is a view of the SPU-cone interior, looking downwards toward the floor. The manual linear polarization setting vernier (Ref. 1) is seen at the bottom of the basket.

Several means were used to provide the minimum dissipative loss possible. Standard DSIF two-position waveguide switches were reworked for reduced loss and increased isolation. Losses obtained were 0.016 and 0.018 dB at 2295 MHz. Switch isolation was 75 dB at 2110 MHz. Good isolation, beyond being an indicator of efficient switch design for low loss, is also mandatory in the SPU-cone block diagram used (Fig. 39). In Fig. 39, it is noted that the transmitter-to-receiver isolation is not a function of diplexer rejection but rather solely dependent on switch S-2 isolation. An independent measured value of transmitter-to-receiver leakage was made at 10-kW output. The maser is irradiated with −2 dBm
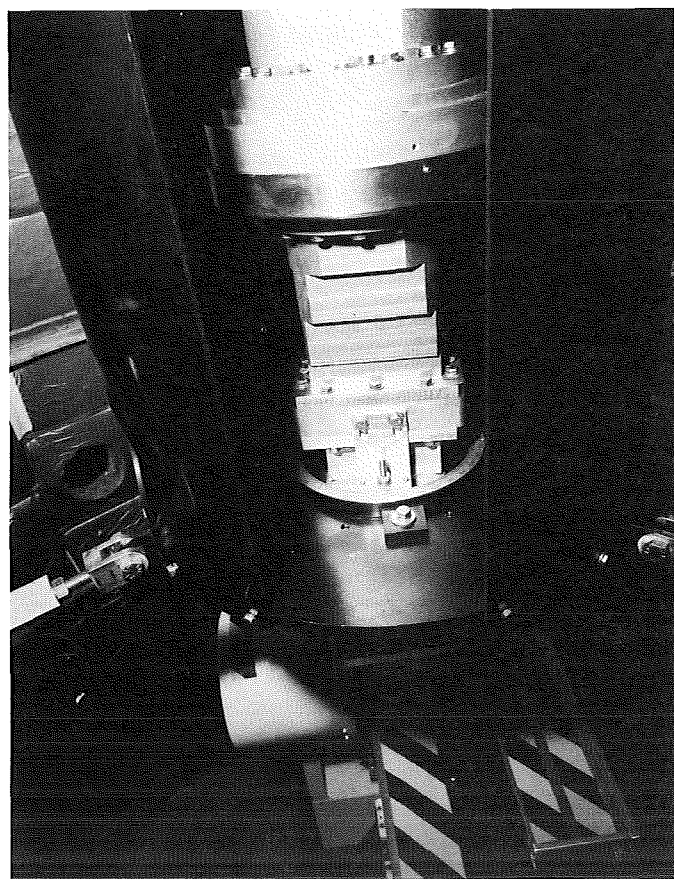
Fig. 41. Polarization vernier

at 2115 MHz after a 2-h system warmup. This value (72 dB of switch isolation following warmup) is consistent with the laboratory measured 75 dB. The point is, that noisy oscillations have been observed in the laboratory (SPS 37-52, Vol. II, pp. 58–61), with +10-dBm signals at 2115 MHz irradiating the maser. This design pushes this limit within a 10-dB margin. 50:1 bronze reduction gears were added to improve reliability; 30:1 micarta gears are standard within the switches.

A 33-dB directional coupler is used to inject test signals to the maser input. Standard units are 26 dB, resulting in approximately 0.75°K more noise. Copper waveguide was used wherever practical.

The standard S-band cassegrain diplexer is characterized by a rather long (79 in.) dimension between antenna and receiver ports. This dimension generally controls feedcone layouts, most often resulting in undue losses because of additional waveguides. In the case of the SCU cone, the solution was to permit the diplexed maser to be housed within module III of the 210-ft cassegrain assembly. This is not possible on the 85-ft polar antennas. The solution for the SPU-cone system was to fold the diplexer into a "U" shape without destroying the critical phasing within the 3-dB hybrid couplers and cutoff waveguides. This was accomplished by inserting doubled 90-deg mitered bends between the diplexer matching sections and the hybrids. Individual bends were electrically matched, by selection, to be within 0.25 electrical degrees prior to subassembly welding. The slight additional dissipative loss (approximately 0.006 dB at 2295 MHz) was more than compensated by the shorter waveguide runs permitted by ease of feedcone layout. Figure 42 shows the modified diplexer installed in the SPU cone prior to installation of a protective cover. The short connection from the diplexer receiver port to the maser is obvious. A stepladder shown in Fig. 42 is for operator convenience in setting the polarization setting vernier seen in Fig. 41.

An overriding constraint in the planning for the SPU-cone system was minimal, if indeed any, changes to the standard systems beyond the front end itself. To meet this objective, a simulator box was designed to take advantage of the DSIF switch controller. The simulator, housed within the feedcone, reacts as though the DSIF standard S-band cassegrain monopulse feed is in place while operating the two required switches. Switching from low-noise listen to diplex is accomplished at the mode control panel. All safety interlocks used in the standard system are retained.
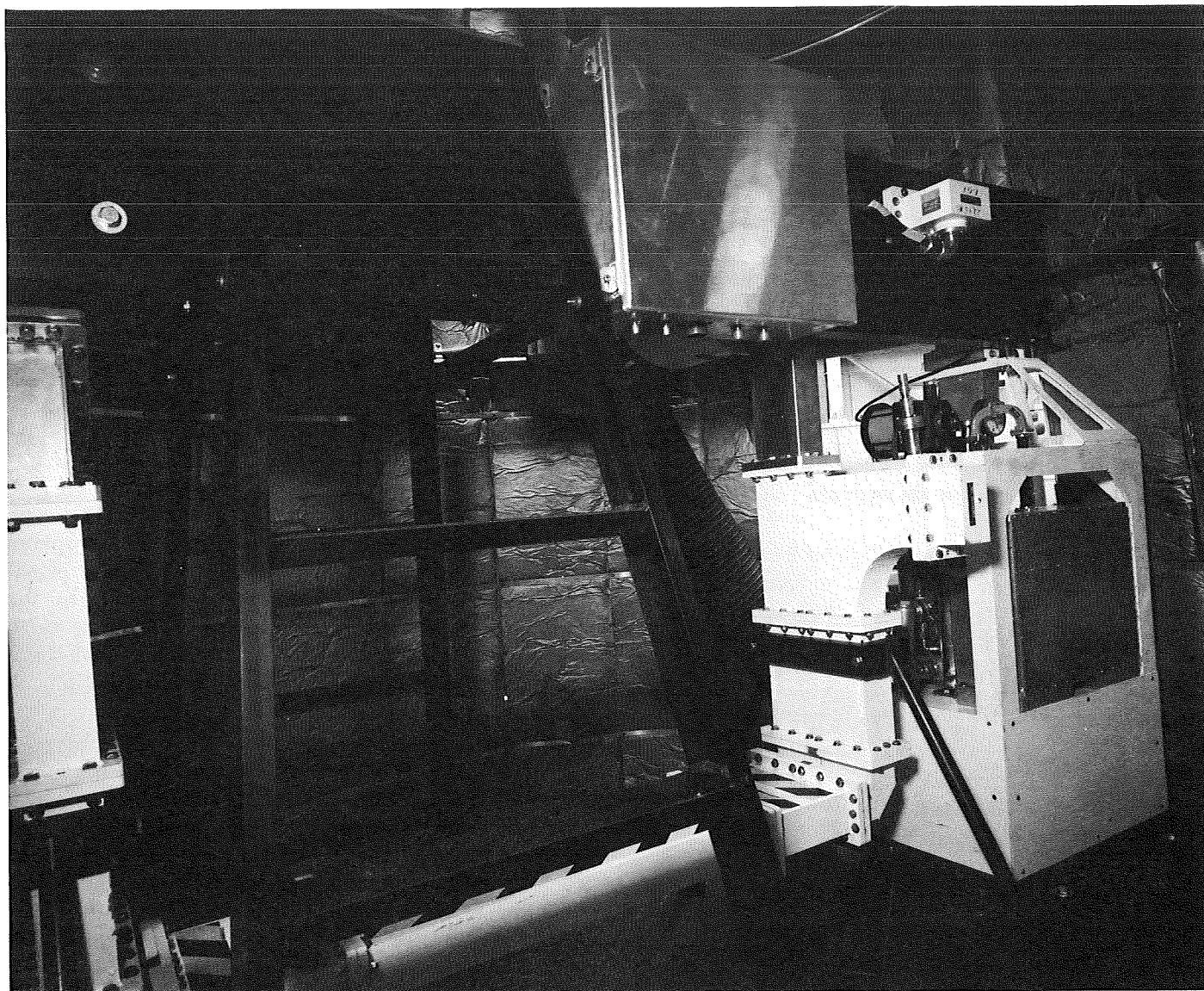
Fig. 42. Folded diplexer

The traveling-wave maser used (SPS 37-58, Vol. II, pp. 50–52) utilizes a new solid-state pump for the first time. The synchronous-tuned bandwidth is 13.5 MHz at the 3-dB points. Synchronous-tuned gain is 47–49 dB, with a calculated equivalent noise temperature of less than 4°K. A noise box, in conjunction with the 33-dB coupler, provides an approximate 9°K calibration signal, as well as maser gain measurement facilities.

The primary noise standard is a well-matched ambient termination. For both operating modes, the ambient load radiates through the diplexer to reach the maser. For this reason, that transmission line was well matched.

Figure 43 shows measured total operating system temperature T_{op} as a function of pointing. With the hour angle set to 360.00 deg (south), the declination axis was tipped and T_{op} was obtained by the Y-factor technique. Initial radio star tests show the system gain is unchanged; further tests should show a slight gain improvement (order of 0.2 dB).

c. Conclusion. By use of existing spares, improved components, and minimal cost hardware, coupled with an R&D maser, an SPU operating system with approximately 17 and 26°K at zenith for low-noise listen and diplexed modes, respectively, has been demonstrated.
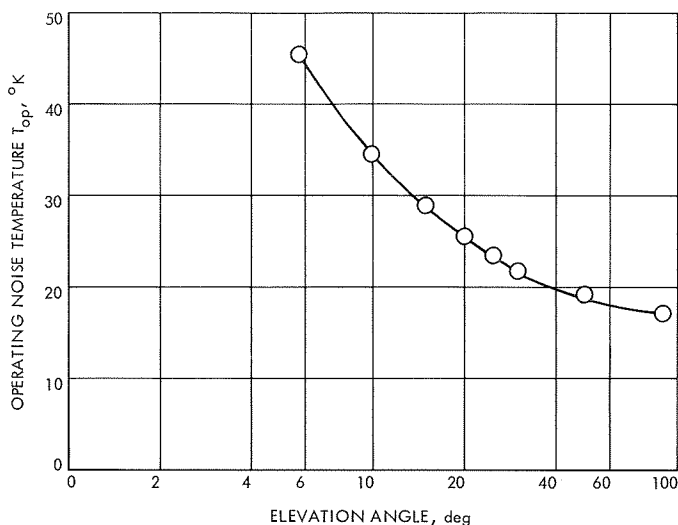
Fig. 43. DSS 12 low-noise listen path, system temperature vs angle

With the exception of somewhat high back power on linear polarized transmission (which was reduced by using a standard isolator in the 10-kW line), the system performed as predicted. In the first two weeks of operations, *Pioneers VI, VII, VIII*, and *IX*, as well as *Mariners VI* and *VII*, were tracked from DSS 12.

Reference

1. Kraus, J. D., *Radio Astronomy*, pp. 110–111. McGraw-Hill Book Co., Inc., New York, N.Y., 1966.

9. Ground Instrumentation for the *Mariner VI* and *VII* Occultation Experiment, B. L. Seidel and D. L. Nixon

a. Introduction. As in the *Mariner IV* occultation experiment, the determination of the Martian atmospheric perimeters was the objective of the *Mariner VI* and *VII* occultation experiment. This was accomplished by the measurement of the doppler frequency perturbations to the S-band telemetry link produced by the refractive index of the planetary atmosphere. The methods of obtaining and analyzing the data were described previously (Ref. 1). The following is an abbreviated description of *Mariner* Mars 1969 occultation and of the ground instrumentation used during the experiment.

b. Occultation. *Mariner VI* made its closest approach to Mars at 5:19:06 UT on July 31, 1969. Approximately 20 min later it disappeared from the view of the earth and its radio beam was interrupted by the surface of Mars at a point near Maridiani Sinus (4°N lat, 350°E lon). At the moment of occultation, the spacecraft was

about 9800 km from the limb. After remaining in occultation for about 20 min, the spacecraft emerged in the vicinity of the north pole at 79°N lat and 84°E lon. At this time, the spacecraft was approximately 17,400 km from the limb.

Mariner VII arrived in the vicinity of Mars approximately 5 days later, making its closest approach at 05:00:49 UT on August 5, 1969. Some 19 min later, the spacecraft S-band radio beam was cut by the surface of Mars in the area of Hellespontus at 58°S lat and 30°E lon. At that time, the *Mariner VII* spacecraft was about 9050 km from the limb. About 30 min later, the spacecraft's radio signal emerged from behind Mars in the vicinity of Amazonis and Arcadia at 38°N lat and 211°E lon. At the time of emergence, the spacecraft was about 20,180 km from the limb.

c. Instrumentation and data acquisition. During each entry and exit of the radio beam through the atmosphere of Mars, the frequency and amplitude of the signal received afterwards at the earth were changed by the effects of refraction upon the propagation of the radio signal. These effects are treated in more detail in descriptions of previous radio occultation experiments (Refs. 2, 3, and 4).

For both *Mariner VI* and *VII*, the entry into occultation was performed in a two-way mode of operation, in which a frequency referenced to a rubidium standard at the DSN station is transmitted to the spacecraft, where it is coherently retransmitted. The exit data, however, were obtained in the one-way mode of operation in which the spacecraft's transmitter is referenced to its on-board crystal oscillator. The received signal was passed through the standard phase-locked-loop receiver, and the record of non-destructively counted doppler was recorded by the Tracking Data Handling System. This constituted the closed-loop data. Simultaneously, the signal was passed through a special open-loop receiver having an audio passband of approximately 5 kHz. This produced a frequency-translated version of the received signal, which was recorded on an analog tape recorder, as well as being digitized in real time and recorded on digital magnetic tape. These data are referred to as the open-loop data.

For the *Mariner VI* and *VII* occultation experiment, DSSs 14 and 12 at the Goldstone DSCC were instrumented with open-loop receivers, and the open-loop data from DSS 14 were transmitted over a microwave link to DSS 13, where they were digitized in real time and

recorded. Closed-loop doppler data were also taken at DSSs 14 and 12, as well as at DSS 41. A simplified block diagram of the data recovery system is shown in Fig. 44. Two major differences exist between the system that was used for the 1969 mission and that used for the previous occultation experiments. First, the open-loop receivers were equipped with local oscillators that were completely independent of those used by the phase-locked-loop receivers. This, though not improving the data directly, certainly simplified operations and improved the reliability of the total receiving subsystem. The second major difference was that for the first time the open-loop occultation data were digitally recorded in real time. This directly improves the quality of the received data by not introducing time base instabilities in the recorded data.

The open-loop receiver is necessary to insure instantaneous reception of the data as the spacecraft reemerges from behind the planet. This is difficult to accomplish with the phase-locked-loop receiver because of its finite lockup time. Another purpose of the open-loop receiver is to obtain amplitude data that are difficult to obtain from the locked-loop receiver because of the long time constant of the receiver automatic gain control circuit. The bandwidth of the open-loop receiver was selected

on the basis of the projected doppler frequency rates due to the motion of the spacecraft. These rates, together with the fact that it was undesirable to retune the receiver within 3 min of occultation, led to an open-loop passband selection of approximately 5 kHz. To insure precise tuning of the open-loop receivers, as well as to preserve their frequency-translation integrity, all the local oscillator frequencies were synthesized from a rubidium standard. An audio phase-locked-loop receiver, as well as a spectrum analyzer and other test equipment, were provided in the open-loop system to give a real-time indication of the signal being received and recorded (Fig. 45). This test equipment could be switched between the output of the open-loop receiver and the various reproducing units of the analog tape recorders. A 20-kHz test tone reference to a rubidium standard was added to the data channel prior to recording to insure that the frequency recorded by the analog recorders was not distorted by more than a fraction of a hertz. Later, this test tone was used as a time base for keying the digitizer sampling the data. The analog recordings were used primarily as back-ups to the real-time digital recordings, which, because of system constraints, had to be obtained over a microwave link. A description of the digital frequency measurement technique can be found in Ref. 5.
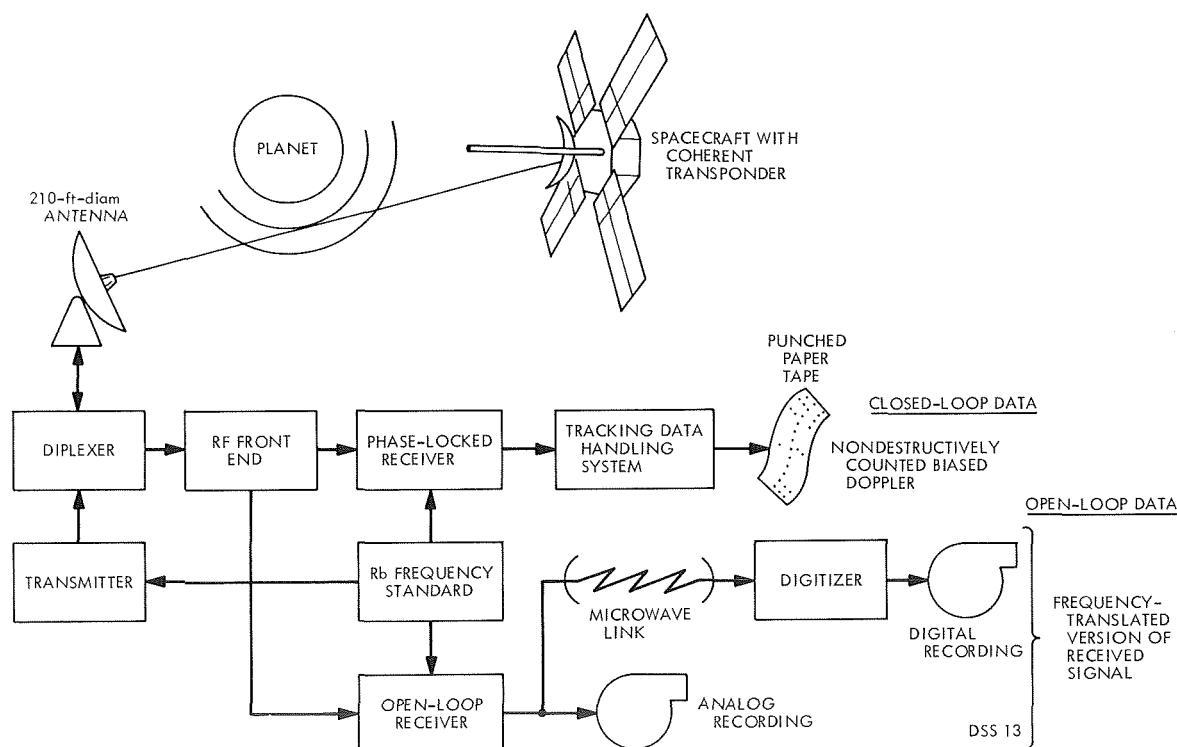
Fig. 44. Occultation data acquisition system
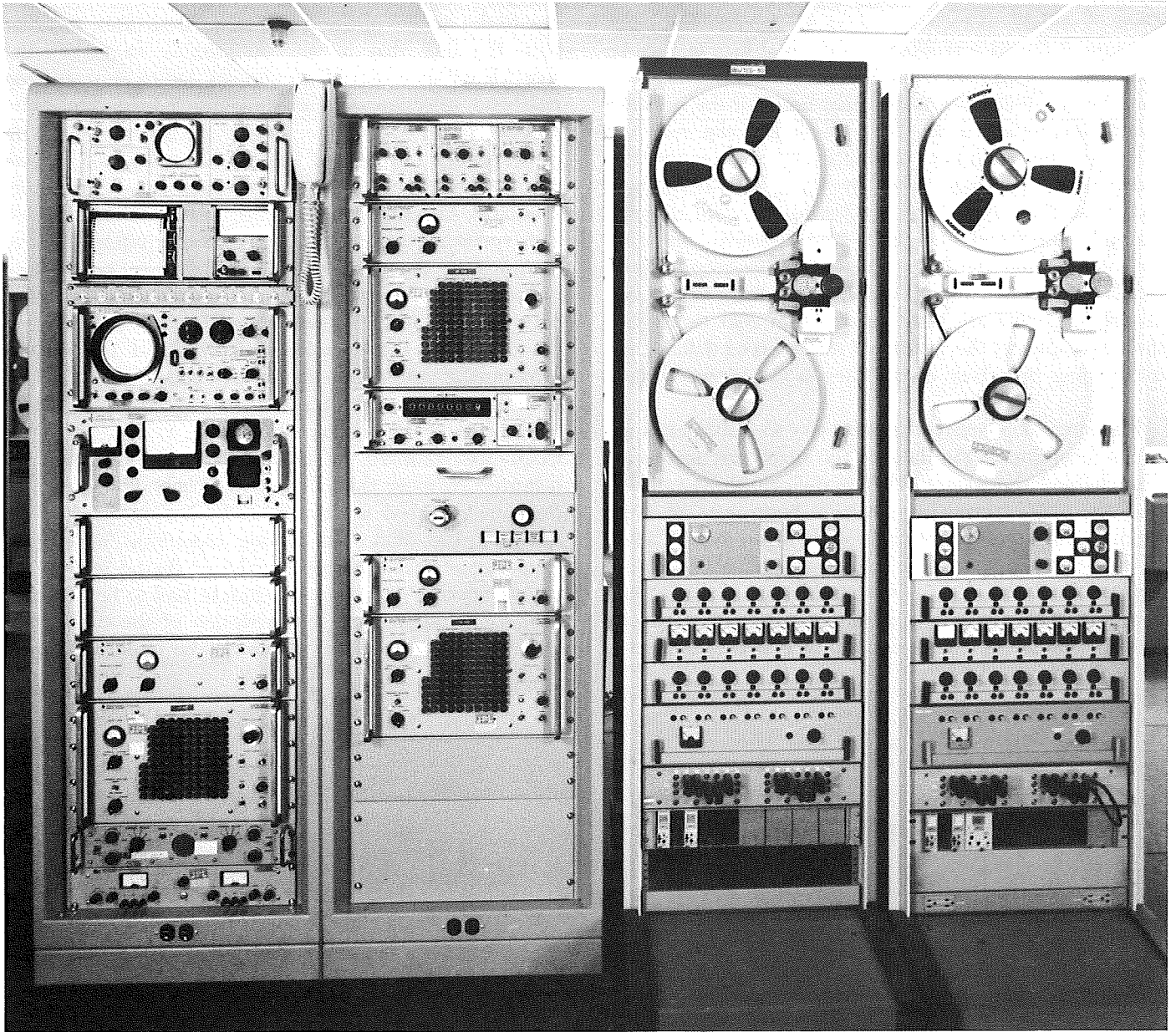
Fig. 45. Open-loop receiver and analog recorder racks for the *Mariner* Mars 1969 occultation experiment

Though the occultation data are still being analyzed, some of the early results of the experiment have been compiled (Ref. 6).[19],[20]

[19]Kliore, A., Fjeldbo, G., and Seidel, B., "First Results of the *Mariner VI* Radio Occultation Measurement of the Lower Atmosphere of Mars," *Radio Science* (in print).

[20]Fjeldbo, G., Kliore, A., Seidel, B., "The *Mariner* 1969 Occultation Measurements of the Upper Atmosphere of Mars," *Radio Science* (in print).

c. Conclusion. Experience gained from past occultation experiments indicates that real-time digital recording of open-loop data not only improves the quality of the data, but should also prove to be cost effective. The cost effectiveness is accomplished by eliminating the intermediate step of digitizing analog tape prior to data reduction, while quality is improved by not introducing the time base instabilities inherent in analog recording. Also, relative to the required ground instrumentation, for operational simplicity it is a must to have a local

oscillator chain for the open-loop receiver that is operationally independent of the locked-loop receiver.

References

1. Levy, G. S., Otoshi, T., and Seidel, B. L., *IEEE Trans. Instrumen. Meas.*, Vol. IM-16, No. 2, Jun. 1967.

2. Kliore, A., et al., *Science*, Vol. 149, p. 3689, 1965.

3. Kliore, A., Cain, D. L., and Levy, G. S., *Space Research VI— Moon and Planets*, pp. 226–239. North Holland Publishing Co., Amsterdam, Holland, 1967.

4. Fjeldbo, G., and Eshleman, V. R., *Planet. Space Sci.*, Vol. 16, pp. 1035–1059, 1968.

5. Kendall, W. B., and Parsons, P. L., "A Precision Frequency Measurement Technique for a Moving Signal with a Low Signal to Noise Ratio," *IEEE Trans. Instrumen. Meas.*, Vol. IM-17, No. 4, pp. 358–365, Dec. 1968.

6. Kliore, A., et al., "*Mariners VI and VII*: Radio Occultation Measurements of the Atmosphere of Mars," *Science*, Vol. 166, pp. 1393–1397, Dec. 12, 1969.

D. Supporting Research and Technology

1. A Newton Method for the Complex Eigenvalue Problem, T. J. Cullen

a. Introduction. The generalized eigenvalue problem can be written as

$$AX = \lambda BX \qquad (1)$$

where A and B are $n \times n$ matrices, X is an $n \times 1$ non-zero vector, and λ is a scalar (any scalar or entry is allowed to be complex). Given an estimate λ_0 to an eigenvalue λ, we shall describe a method for improving on this estimate. The purpose of this article is to generalize the method described in SPS 37-59, Vol. II, pp. 68–69. Desiring to transform the complex case into the real case, we rewrite Eq. (1) as

$$(C + Di)(Z + Wi) = (a + bi)(E + Fi)(Z + Wi) \qquad (2)$$

where $A = C + Di$, $X = Z + Wi$, etc., and now all entries are considered to be real.

b. Theory. Performing the indicated multiplication in Eq. (2), we obtain

$$(CZ - DW) + i(DZ + CW) = [a(EZ - FW) - b(FZ + EW)] + i[b(EZ - FW) + a(FZ + EW)] \qquad (3)$$

and equating real and imaginary parts:

$$\left. \begin{array}{l} CZ - DW = a(EZ - FW) - b(FZ + EW) \\ DZ + CW = b(EZ - FW) + a(FZ + EW) \end{array} \right\} \qquad (4)$$

These equations can be written as the matrix equation

$$\begin{pmatrix} C & -D \\ D & C \end{pmatrix} \begin{pmatrix} Z \\ W \end{pmatrix} = \begin{pmatrix} E & -F \\ F & E \end{pmatrix} \begin{pmatrix} aZ - bW \\ aW + bZ \end{pmatrix} \qquad (5)$$

Since $X \neq 0$, for definiteness we can assume that the first component $z_1 = 1$. Making this substitution into Eq. (5), we obtain

$$\left. \begin{array}{l} c_{i1} + \sum_{j=2}^{n} c_{ij} z_j - \sum_{j=1}^{n} d_{ij} w_j = ae_{i1} - be_{i1} w_1 + \sum_{j=2}^{n} e_{ij}(az_j - bw_j) - af_{i1} w_1 - bf_{i1} - \sum_{j=2}^{n} f_{ij}(aw_j + bz_j) \\ d_{i1} + \sum_{j=2}^{n} d_{ij} z_j + \sum_{j=1}^{n} c_{ij} w_j = af_{i1} - bf_{i1} w_1 + \sum_{j=2}^{n} f_{ij}(az_j - bw_j) + ae_{i1} w_1 + be_{i1} + \sum_{j=2}^{n} e_{ij}(aw_j + bz_j) \end{array} \right\} \qquad (6)$$

for $1 \leq i \leq n$. We write this as the $2n \times (2n - 1)$ overdetermined system

$$PV = Q \qquad (7)$$

where

$$v_j = \begin{cases} z_{j+1}, & 1 \leq j \leq n-1 \\ w_{j-n+1}, & n \leq j \leq 2n-1 \end{cases} \qquad (8)$$

$$p_{ij} = \begin{cases} c_{i,j+1} - ae_{i,j+1} + bf_{i,j+1}, & 1 \le j \le n-1 \\ af_{i,j-n+1} + be_{i,j-n+1} - d_{i,j-n+1}, & n \le j \le 2n-1 \end{cases} \quad (9)$$

for $1 \le i \le n$,

$$p_{ij} = \begin{cases} d_{i-n,j+1} - af_{i-n,j+1} - be_{i-n,j+1}, & 1 \le j \le n-1 \\ c_{i-n,j-n+1} + bf_{i-n,j-n+1} - ae_{i-n,j-n+1}, & n \le j \le 2n-1 \end{cases} \quad (10)$$

for $n+1 \le i \le 2n$, and

$$q_i = \begin{cases} ae_{i1} - bf_{i1} - c_{i1}, & 1 \le i \le n \\ af_{i-n,1} + be_{i-n,1} - d_{i-n,1}, & n+1 \le i \le 2n \end{cases} \quad (11)$$

Let H be the least-squares solution to Eq. (7) so that the residuals are

$$\epsilon_i = \sum_{j=1}^{2n-1} p_{ij} h_j - q_i, \qquad 1 \le i \le 2n \quad (12)$$

We define the following functions in terms of these residuals:

$$\left. \begin{array}{l} T(a,b) = \text{sgn}(\epsilon_1) \left(\dfrac{\sum\limits_{i=1}^{n} \epsilon_i^2}{\sum\limits_{i=1}^{n} |\epsilon_i|} \right) \\[6ex] U(a,b) = \text{sgn}(\epsilon_{n+1}) \left(\dfrac{\sum\limits_{i=n+1}^{2n} \epsilon_i^2}{\sum\limits_{i=n+1}^{2n} |\epsilon_i|} \right) \end{array} \right\} \quad (13)$$

The final step in the algorithm is to perform the usual Newton iteration on the system

$$\left. \begin{array}{l} T(a,b) = 0 \\ U(a,b) = 0 \end{array} \right\} \quad (14)$$

A motivation for the Functions (13) is that Cheney (Ref. 1) has shown that the Chebyshev (or minimax) solution to Eq. (7) is obtained by solving the consistent system

$$\sum_{j=1}^{2n-1} p_{ij} v_j = q_i + s_i, \qquad 1 \le i \le 2n \quad (15)$$

where

$$s_i = \text{sgn}(\epsilon_i) \left(\dfrac{\sum\limits_{j=1}^{2n} \epsilon_j^2}{\sum\limits_{j=1}^{2n} |\epsilon_j|} \right), \qquad 1 \le i \le 2n \quad (16)$$

so that the s_i are the Chebyshev residuals.

c. Example. We take as an example

$$\begin{pmatrix} 1 & i & 3 \\ 2+i & 1-i & 1+2i \\ 2 & 2i & 1+i \end{pmatrix} X =$$

$$\begin{pmatrix} i & -i & 1 \\ 1+i & -\frac{1}{2} - \frac{5}{2}i & 1+2i \\ -i & 1 & -2i \end{pmatrix} X \quad (17)$$

with $\lambda_0 = 0.8 + 1.3i$ taken as the initial estimate to an eigenvalue $\lambda = 1 + i$. The results are as follows:

i	a^i	b^i	z_1^i	w_1^i	z_2^i	w_2^i	z_3^i	w_3^i
0	0.80000000	1.30000000	1.00000000	0.00000000	0.63988419	0.46438966	−0.26812918	0.11480374
1	1.04507580	1.03958260	1.00000000	0.00000000	0.50197479	0.47581523	−0.29920899	0.09782165
2	0.99949010	0.99885267	1.00000000	0.00000000	0.49973339	0.50044458	−0.30003656	0.10003345
3	0.99999892	1.00000007	1.00000000	0.00000000	0.50000048	0.50000020	−0.29999996	0.10000003
4	1.00000000	1.00000000	1.00000000	0.00000000	0.50000000	0.50000000	−0.30000000	0.10000000

Reference

1. Cheney, E. W., *Introduction to Approximation Theory*. McGraw-Hill Book Co., Inc., New York, 1966.

2. Additional Features of the Spacecraft-Simulation Problem-Oriented Language, R. I. Ścibor-Marchocki

a. Introduction. The first seven articles in this series on spacecraft telemetry simulation discussed:

(1) Certain aspects of the supervisory program (SPS 37-57, Vol. II, pp. 117–121).

(2) The user-oriented source language (SPS 37-58, Vol. II, pp. 87–96).

(3) The lines of communication created among the various program components (SPS 37-59, Vol. II, pp. 74–78).

(4) The use of the Hamilton–Cayley–Klein parameters for attitude simulation (SPS 37-59, Vol. II, pp. 84–87).

(5) The modifications to the syntax of the transmogrification (TMG) compiler (SPS 37-60, Vol. II, pp. 51–59).

(6) Further aspects of the supervisory program (SPS 37-60, Vol. II, pp. 46–51).

(7) The modifications to the functions of the TMG compiler (SPS 37-61, Vol. II, pp. 92–98).

With the help of the TMG compiler, a simulation compiler is being written to translate from the user-oriented spacecraft-simulation language to FORTRAN IV. As a result of continuing experience in the use of this simulation compiler, additional features, which were not described in (2) above, have been introduced into the user-oriented language. This article deals with those new features that differ from FORTRAN. Hence, this article is a follow-on to (2) above.

b. The simulation language. The simulation language is a user-oriented dialect of FORTRAN with provisions to couple with the simulation supervisor by means of suitable supervisor-assisted pseudo operations. Thus, the simulation language consists of FORTRAN IV with the modifications described in the second article in this series and the present article. The following features of FORTRAN have been omitted intentionally:

(1) There are no DOUBLE-PRECISION variables or constants.

(2) There are no COMPLEX variables.

(3) There are no LOGICAL variables or constants as a distinct class. Instead, any INTEGER variable or constant may be used as LOGICAL.

(4) Variables may not be declared as either REAL or INTEGER. Instead, they are identified exclusively by their initial letter.

(5) The EQUIVALENCE statement is not allowed.

Only four alternative methods of writing a REAL constant are permitted; i.e.,

⟨optional sign⟩ ⟨one-or-more digits⟩ • ⟨one-or-more digits⟩

⟨sign⟩ ⟨one-or-two digits⟩ |

⟨optional sign⟩ ⟨one-or-more digits⟩ • ⟨one-or-more digits⟩

The supervisor-assisted pseudo operations are available only in the numbered SECTIONs. Thus, the language and its compiler also may be used in situations where the simulation supervisor is not available. The target coding of these pseudo operations consists of either subroutine calls or suitable GO-TO statements and numbered statements so that the supervisor may execute the code at its convenience.

Formally, the simulation language is a collection of all programs, each of which conforms with the grammar of the simulation language. The concise statement of this grammar in the TMG meta-language constitutes the source coding of the simulation compiler and therefore is definitive. The diagnostic capability of the TMG compiler has helped to improve this statement of the grammar of the simulation language.

Since the simulation compiler uses FORTRAN IV as the target language, it is natural for us to quote the translated output as an aid in the description of the simulation; i.e., source, language.

DATA/SAVE. In a real-time simulation of a spacecraft, there are many people and much equipment on-line to the simulation computer. During a long run, it may happen that someone or something makes a wrong response or, for some other reason, the consequences of an alternative response are of interest. In order to obviate the necessity of starting from the beginning, a checkpoint is taken periodically and upon demand. From the dump produced at each checkpoint, it should be possible to restart the simulation with a minimum of effort.

It is apparent that the present value of each variable that has been initialized by means of a DATA statement should be dumped and restored automatically at each checkpoint. Similarly, certain designated additional variables may have to be SAVEd.

For example, the source statement

> DATA IEXSHA IGYRON IPAS/0 1 0/

translates into the target code

> DATA IEXSHA,IGYRON,IPAS/0,1,0/
> GO TO 30702

> 29002 READ(9) IEXSHA,IGYRON,IPAS
> GO TO 29003

> 29502 WRITE(9) IEXSHA,IGYRON,IPAS
> GO TO 29503

> 30702 CONTINUE

and the source statement

> SAVE K

translates into the target code

> GO TO 30703

> 29003 READ(9) K
> GO TO 29004

> 29503 WRITE(9) K
> GO TO 29504

> 30703 CONTINUE

In the foregoing target codes, the statement number sequence commencing with 30700 is for bypassing the checkpoint code. The supervisor transfers control to the sequence commencing with 29500 whenever a checkpoint dump is to be written and to the sequence commencing with 29000 whenever a checkpoint restart is to be performed.

Commas are optional throughout the source code, but a space is required if ambiguity would result otherwise: For example, the subscript 3,J could be written as either 3 J or 3J , in addition to the formal 3,J, while the subscript 3,5 could be written only 3 5 , but not 35 , in addition to the always-acceptable 3,5 .

DO/DO-END. To provide for easy nesting of DO-loops and for various interaction between the DO and the IF structures, it is convenient to avoid the use of statement numbers in the source language. Thus, the scope of a DO terminates at the corresponding DO END.

An actual example from the coding of the temperature subsystem of the spacecraft simulation illustrates the interaction of the DO/DO-END and the IF/OTHERWISE/ANYHOW structures. The source code

> DO I = 1,28
>
> DO END IF(II(I)=IE)
>
> CHAN(YY(I TP X Y12 TK 28) A (I 1) A(I 2) IE)
>
> OTHERWISE GO TO 13

translates into the target code

> DO 27092 I = 1,28
>
> IF(II(I) . EQ . IE) GO TO 27093
>
> 27092 CONTINUE
> GO TO 27094

```
27093   CONTINUE
        CALL  CHAN(YY(I,TP,X,Y12,TK,28),A(I,1),A(I,2),IE)
        GO TO 27095
27094   CONTINUE
        GO TO 3013
27095   CONTINUE
```

The DO-END may not possess a statement number and must be the first expression on its card. If an IF expression immediately follows a DO-END on the same card, then the condition of that IF expression becomes a condition for the satisfaction of the DO alternative to its exhaustion. The code-word CALL must be omitted from the subroutine call in the source language if and only if there is at least one argument present.

A more complicated, contrived example of source code

```
10   DO  I0 = 10 20
 1   DO  I1 = 11,21
 2   DO  I2 = 12 22
 3   DO  I3 = 13 23
 4   DO  I4 = 14,24
 5   IF(A5=B5)
     DO  END  OTHERWISE  IF(A6.GE.B6) I6 = J6.K6
 7   IF(A7=B7)
     DO  END  OTHERWISE
     DO  END  IF(A9=B9)
     DO  END  IF(A0 = B0) C0 = D0
11   ANYHOW
     DO  END  OTHERWISE  IF(A12.GT.B12.I12) J12 = K12 V L12
```

translates into the target code

```
10       DO 27008 I0 = 10,20
1        DO 27009 I1 = 11,21
2        DO 27010 I2 = 12,22
3        DO 27011 I3 = 13,23
4        DO 27012 I4 = 14,24
5        IF(.NOT.(A5.EQ.B5)) GO TO 27013
27012    CONTINUE
         GO TO 27014
```

```
27013   CONTINUE
        Il1000 = 0
        IF(A6.GE.B6) Il1000 = 1
        I6 = Il1000*(J6*K6−I6)+I6
27014   CONTINUE
7       IF(.NOT.(A7.EQ.B7)) GO TO 27015
27011   CONTINUE
        GO TO 27016
27015   CONTINUE
        CONTINUE
        IF(A9.EQ.B9) GO TO 27017
27010   CONTINUE
        GO TO 27018
27017   CONTINUE
        IF(A0.EQ.B0) C0 = D0
27009   CONTINUE
27018   CONTINUE
11      CONTINUE
27008   CONTINUE
        GO TO 27019
27016   CONTINUE
        Il1000 = 0
        IF(A12.GT.B12) Il1000 = 1
        J12 = Il1000*I12*(MIN0(K12+L12,1)−J12)+J12
27019   CONTINUE
```

The source statements ordinarily would not be numbered. They have been numbered here to facilitate the visual correlation of the source and target codes. Because certain FORTRAN target compilers cannot terminate a DO-loop on an IF statement, the simulation compiler separates the associated DO-END and IF statements by generating numbered CONTINUE statements. In the source logical expressions, a period (.) is used for AND, a V for OR, and a $ for NOT.

READ. During a real-time simulation, it is desirable to be able to modify certain variables at will instead of under program control. Consequently, the supervisor may be instructed manually to read in data and to insert it into the simulation at a designated instant of time. This input data is labeled by subsystem name and the source name of the variable within the subsystem. Within the coding of each subsystem, the names of these scalar or array variables have to be listed in a READ statement, which may be placed anywhere (following the dimensioning declaration of the arrays involved) that the names are known. As many such READ statements may be used as are convenient.

For example, if we assume that the variables ACS and TAB5 have been declared in the source as

DIMENSION ACS(41) TAB5(2 50)

prior to the source statement

READ ACS1 G ACS TAB5

which occurs in the attitude control subsystem, whose name is abbreviated as ACS, then the target code

```
              GO TO 30704
      30400   CALL  RD(1,4,4HACS1,ACS1,0,0,1,3,3HACS)
              CALL  RD(2,1,1HG,G,0,0,1,3,3HACS)
              INTEGER A0000X(2)
              DATA A0000X/41,0/
              CALL  RD(3,3,3HACS,ACS,0,A0000X,1,3,3HACS)
              INTEGER T1000X(3)
              DATA T1000X/2,50,0/
              CALL  RD(4,4,4HTAB5,TAB5,0,T1000X,1,3,3HACS)
              CALL  RD(5,3,3HIN,IN,1,0,1,3,3HACS)
              GO TO 30401
      30704   CONTINUE
```

will provide the supervisor with a set of CALL RD statements, each describing one of the variables. The nine arguments of the CALL RD statement are, in order:

(1) Serial number of the CALL RD statement. The supervisor may use this number as a subscript for its own storage arrays.

(2) The length of the real name of the variable.

(3) The real name of the variable (in Hollerith).

(4) The address of the variable. Ordinarily, it would be given by the alias of the variable, rather than by the real name as shown in the foregoing.

(5) 0 for a real variable, 1 for an integer variable.

(6) Dimensioning information which consists of either a zero if and only if the variable is a scalar; or an array, terminated by a zero, listing the dimensions of the array variable.

(7) The serial number of the subsystem.

(8) The length of the real name of the subsystem.

(9) The real name of the subsystem (in Hollerith).

From this description of the variable, the supervisor can associate the input name with the source name of the variable and can construct suitable assembly language read statements of its own for the input value(s) of the variable. The input data may consist of:

(1) Name and subsystem of a scalar followed by its value.

(2) Name and subsystem of an array followed by a list of the value of each element of the array.

(3) Name and subsystem of an array followed, for each element to be modified, by a list of subscripts and the value of the element.

In any case, those scalars, elements of arrays, or arrays for which new values are not read in will retain their respective current values.

DEFINE. For consistency with the FORTRAN V requirement, the usually redundant code-word DEFINE always is required as the first entity on a card with a statement function definition.

For example, the source statement

$$\text{DEFINE USEN(E17 E27 E37)} = \text{ACS37} + (\text{ACS38} - \text{ACS37})$$

$$\text{\$*(USNO(JX E17)} + \text{USNO(JY E27)} + \text{USNO(JZ E37))}$$

translates into the target code

$$\text{USEN(E17,E27,E37)} = \text{ACS37} + (\text{ACS38} - \text{ACS37})*(\text{USNO(JX,E17)} + \text{USNO(JY,E27)} + \text{USNO(JZ,E37))}$$

The $, in column six of each the source code and the target code, indicates a continuation card. Any other non-blank character except a zero may be employed similarly in the source code.

Whenever possible, the computation of the telemetry output should be performed in the numbered SUBSECTIONs. If a particular variable changes continuously as a function of time, it should be computed in SUBSECTION 0; otherwise, it should be recomputed upon demand by a WHEN condition in one of the other SUBSECTIONs. The designation of the telemetry output is performed exclusively in the numbered SUBSECTIONs; SUBSECTION 0 contains little else.

The actual telemetry output is performed under the control of the supervisor. A given variable is output when required by the commutator. The output value of that variable is obtained by interpolation over an interval of continuity using those points that happen to be available in the interior of that interval, as well as the left-hand limit at the left-end of the interval and the right-hand limit at the right-end of the interval. These latter two points are obtained deliberately under control of the supervisor.

Data that a given subsystem wants to have transmitted out on a given telemetry channel number is designated as shown in the example of source code

```
        SUBSECTION 0 STEP-TERMINATION
        SET(01,2,8)
        105 = EP 1.0 10.0
        106 = EY 1.0 10.0
        118 = FLOAT(ISTAT(ICTR(1) ISTR(1) ICTR(2))) 0.0 127.0
        SUBSECTION 1 DC AND CC
```

which translates into the target code

```
        GO TO 30001
24007   GO TO 32700
32000   CONTINUE
        CALL SET3(01,2,8)
        CALL CHAN(EP,1.0,10.0,105)
        CALL CHAN(FLOAT(ISTAT(ICTR(1),ISTR(1),ICTR(2))),0.0,127.0,118)
        GO TO 32001
31001   IF(KSUB.NE.1) GO TO 31002
```

The source statement SUBSECTION 0 generates the first three target cards, the first two of which terminate the preceding (i.e., −1 unnumbered) subsection and the last one initiates the new (i.e., 0 numbered) SUBSECTION. The SET3 effectively transfers control to WHEN 8 of SUBSECTION 2 to execute a block of coding that had to be placed there to be performed upon demand in addition. The telemetry designation source code is similar to an equation followed by two real expressions. The left-hand side of the equation is the integer constant designating the telemetry channel number. The right-hand side of the equation consists of the real variable to be output and its lower and upper bounds, in that order. The variable will be scaled linearly between these bounds; i.e.,

$$AMAX1(AMIN1((X-A)/(B-A),1.0),0.0)$$

for the source expression

$$N = X \ A \ B$$

If the left-hand side of the source equation were an integer variable, one would have to use the alternative source code

$$CHAN(X \ A \ B \ N)$$

instead. The source statement SUBSECTION 1 generates the last two target cards, the first of which terminates the preceding (ie., 0 numbered) SUBSECTION and the second of which initiates the new (ie., 1 numbered) SUBSECTION.

ASSIGN. The ASSIGN source statement consists of the code-word ASSIGN followed by an equation whose left-hand side is an integer variable and whose right-hand side is an integer constant. For example, the source card

$$ASSIGN \ ISTP = 27$$

translates to the target card

$$ASSIGN \ 27 \ TO \ ISTP$$

HEADER card options that affect the source language. The HEADER source statement consists of the code-word HEADER followed by a list of one or more options separated by commas, a blank space, and an optional main-deck name. The absence of any option is indicated by a comma. Each of the foregoing commas is required. Of the various available options, (1) some affect the performance of the compiler, (2) some effect changes in the target language, and (3) some influence the grammar or meaning of the source language. Only those options that belong to the third category will be described here.

The option SUBD allows subscripts to be employed in the right-hand side of a function statement definition in the source language. (This is a FORTRAN V feature.)

The option MIXED MODE allows mixed-mode arithmetic in the source language. (This is a feature of FORTRAN V and FORTRAN IV H.)

The option LOGICAL causes each of the bits of a logical word to be operated upon by the logical operators and . and or V in a computer-dependent manner. Without this option, only the low-order bit is operated upon in a computer-independent manner. In either case, the arithmetic relations yield a word consisting of zeros except in the rightmost bit while the IF operator tests for a non-zero condition. Suitable shifting and masking may be employed to set, clear, or test the other bits. The ability to test the leftmost bit is dependent upon the computer-dependent interaction of the hardware and the target FORTRAN compiler: On the IBM 360 computers, the leftmost bit can be tested easily because there is no negative zero integer; on the IBM 7090 type computers, the leftmost bit cannot be tested because the FORTRAN tests load this bit into the S position but test the P position.

For example, the source HEADER card

$$HEADER \ SUB-DICT,LIST,REF \ SAMPLE$$

translates into the target card

$$\$IBFTC \ SAMPLE$$

and would cause the three non-contiguous source cards

$$IF(\$(IPINE \ V \ IACOFF) \ . \ IEXSHA)$$

$$IF(ICACQ \ \$=(\$KCC(2) \ . \ (LOGA \ V \ IDCOM)))$$

$$IF(IABS(J6)=4 \ V \ J6=0 \ . \ IABS(JJ(6))=4)$$

to be translated into the target code

IF((1-MIN0(IPINE+IACOFF,1))*IEXSHA.EQ.0) GO TO 27035

IF(.NOT.(ICACQ.NE.(1−KCC(2))*MIN0(LOGA+IDCOM,1))) GO TO 27056

and

I11000 = 0

IF(IABS(J6.EQ.4) I11000 = 1

I11001 = 0

IF(J6.EQ.0) I11001 = 1

I11002 = 0

IF(IABS(JJ(6)).EQ.4) I11002 = 1

IF(MIN0(I11000+I11001*I11002,1).EQ.0) GO TO 27047

respectively. Here, the target code employs computer-independent integer arithmetic to operate upon the right-most bit only. The LOGICAL option on the source HEADER card

HEADER SUB-DICT,LIST,REF,LOGICAL3 SAMPLE

translates into the same target card, but would cause the foregoing three source cards to be translated into the target code.

IF(LAND(LCOMPL(LOR(IPINE,IACOFF)),IEXSHA).EQ.0) GO TO 27035

IF(.NOT.(ICACQ.NE.LAND(LCOMPL(KCC(2)),LOR(LOGA,IDCOM)))) GO TO 27056

and

I11000 = 0

IF(IABS(J6.EQ.4) I11000 = 1

I11001 = 0

IF(J6.EQ.0) I11001 = 1

I11002 = 0

IF(IABS(JJ(6)).EQ.4) I11002 = 1

IF(LOR(I11000,LAND(I11001, I11002)).EQ.0) GO TO 27047

respectively. Here, the target code employs computer-dependent logical functions to operate upon each of the corresponding bits of the logical words. It will be the option of the target FORTRAN compiler whether to compile these various logical functions in-line or out-of-line. Additional logical operators or functions may be provided in the future.

c. *Conclusion.* This simulation language has been used successfully and conveniently for coding the simulation of the *Mariner* Mars 1969 spacecraft's attitude control, power, and temperature subsystems. The simulation compiler, written to represent the grammar of the simulation language, has verified that the aforementioned coding conforms with the grammar of the simulation language,

thereby demonstrating that the simulation language is adequate for writing the simulation problem. Experience with this language and its compiler indicates that if one were to delete or ignore the supervisor-assisted pseudo instructions (i.e., those instructions whose execution requires the presence of the simulation supervisor), the balance of the language would be a very pleasant dialect of FORTRAN to use in other applications.

3. DSS 13 Operations, E. B. Jackson and R. B. Kolbly

a. Experimental activities. During the period December 16, 1969 through February 15, 1970, DSS 13 was in limited operation. Clock synchronization transmissions were carried out and a limited number of pulsar observations were made, but basically the station devoted its efforts toward evaluation and modification of the 85-ft-diam antenna and support of the DSS 14 tri-cone construction and testing.

To provide a continuous baseline timing for pulsar observation, the 85-ft antenna was restored to a "receive-only" configuration twice during this period, and data were collected on 19 of the 50 known pulsars.

Clock synchronization transmissions, being made to DSSs 14, 41, 42, 51, and 62, were interrupted by the failure of the rectifier transformer in the high-voltage dc power supply. Later testing revealed the failure to be a shorted primary winding. Operation has been restored by temporary employment of a substitute transformer.

Additional work has been done on the noise adding radiometer discussed in SPS 37-61, Vol. II, p. 102. This radiometer, to be used by DSN stations for observation of weak radio sources, has undergone extensive ground testing at DSS 13 and has been placed into successful operation at DSS 11. The computer program has been carefully optimized to maximize gain stability and resolution, and a version of the program for operation at DSS 14 has also been written.

b. Significant maintenance or modification. The DSS 14 tri-cone support structure (TCSS) was completed and shipped to DSS 14 on February 9, 1970. The S-band megawatt transmitting (SMT) feed cone was completed (see *Paragraph c,* below) and installed for testing. The 400-kW transmitter was installed in the TCSS and successfully operated at 400 kW, in the diplexed mode, for 15 to 20 h. Some difficulty was experienced with the harmonic filter and different waveguide gaskets had to be used along with additional waveguide cooling on

the center section. A nominal diplexed system temperature, with temporary waveguide installed, of 26°K was achieved while radiating 400 kW out of the SMT feedhorn.

c. SMT feed cone for DSS 14 tri-cone. The S-band megawatt transmitting (SMT) feed cone was designed to operate on the DSIF transmit and receive bands, and to be compatible with the tri-cone support structure used on the 210-ft-diam antenna at DSS 14. To achieve wide-band performance, the recently developed corrugated feedhorn (SPS 37-58, Vol. II, pp. 61–64) was employed. The SMT feed cone is single polarization (right-hand circular) only, capable of operating in either diplexed or low-noise listen mode.

The SMT feed cone is designed to be completely compatible with the standard tri-cone interface (SPS 37-56, Vol. II, pp. 121–124; SPS 37-58, Vol. II, pp. 59–61). Due to the high-power level of most of the waveguide runs, it was necessary to provide water cooling to prevent excessive heating. Figure 46 is a block diagram of the SMT feed cone. Switch 1 is a three-position, water-cooled waveguide switch which selects the diplexed (position 1), low-noise listen (position 3) or protect (position 2) mode with the horn shorted.

Right-hand circular polarization is obtained by means of a quarter-wave plate. The length of the quarter-wave plate was selected for best performance at the center of the DSIF receive band (2295 MHz). To assure acceptable ellipticity at the DSIF transmitting band (2110–2120 MHz), a frequency-selective mismatch was installed between the quarter-wave plate and the corrugated feedhorn. Figure 47 illustrates the polarizer assembly.

To reduce the waveguide lengths to a minimum, the high-power diplexer (megawatt cassegrain diplexer) was installed at a 3° 56' angle off normal by means of three wedge-shaped angle spacers which allowed the receiver and antenna ports on the diplexer to align with the maser bypass port and the waveguide switch ports, respectively. This reduced the number of waveguide parts connecting the diplexer to the switch from seven to three, as well as reducing losses and resulting in a lower system temperature.

Since operation of the WR-430 waveguide at 400 kW results in losses of approximately 350 W/ft, it is necessary to cool all transmitting waveguide parts. The waveguide was cooled by soldering four pieces of X-band (WR-90) waveguide to the corners of the WR-430 waveguide.
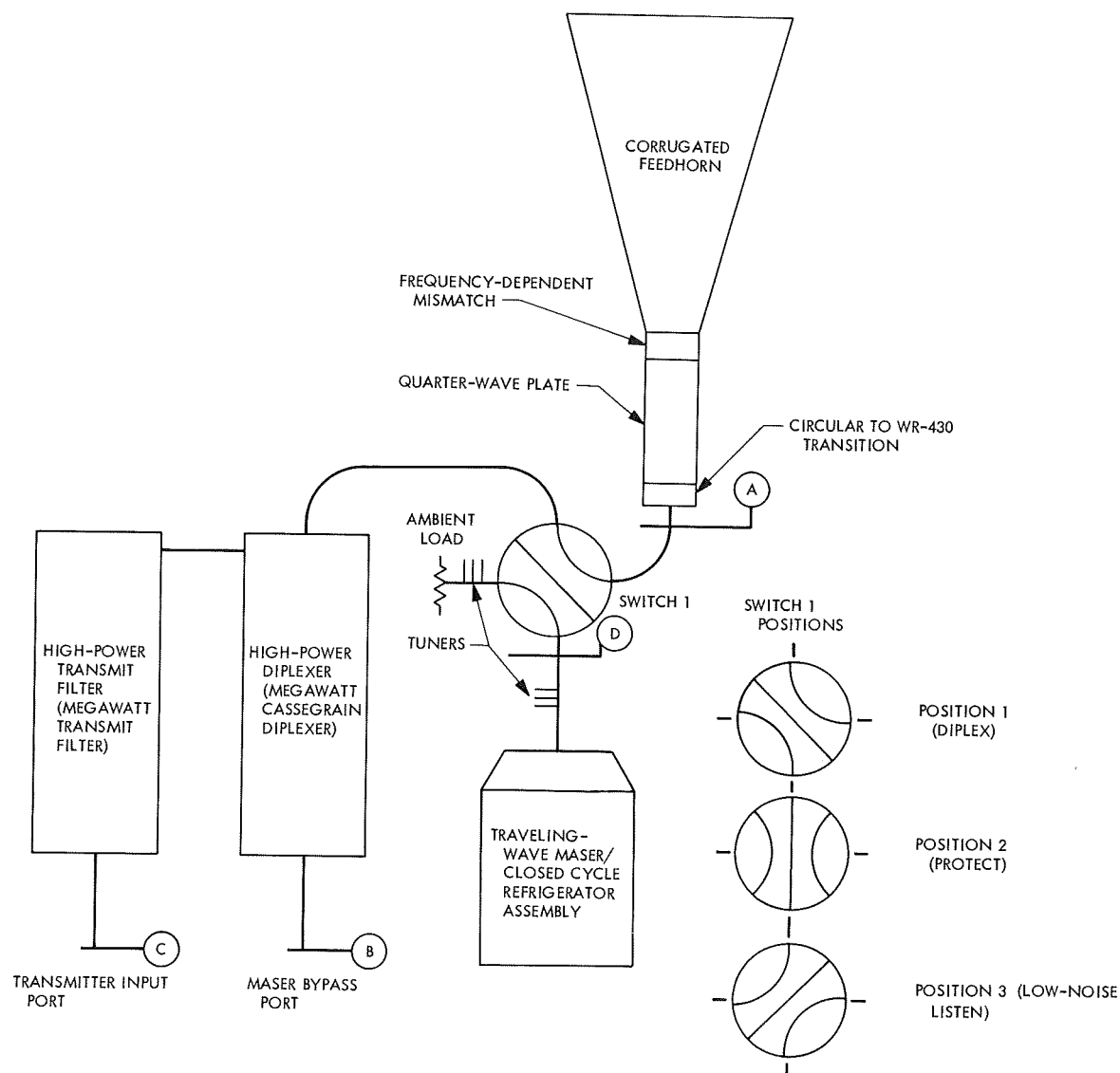
Fig. 46. SMT feed cone block diagram

- CORRUGATED FEEDHORN
- 3.002-in. SPACER[a]
- FREQUENCY-DEPENDENT MISMATCH
- MATCHING TRANSFORMER
- QUARTER-WAVE PLATE
- MATCHING TRANSFORMER
- 4.093-in. SPACER[a]
- WC-504 TO WR-430 CIRCULAR TO RECTANGULAR WAVEGUIDE TRANSITION

[a]SPACERS INCLUDED IN DESIGN TO ALLOW FOR POSSIBLE ADDITION OF ROTARY JOINTS
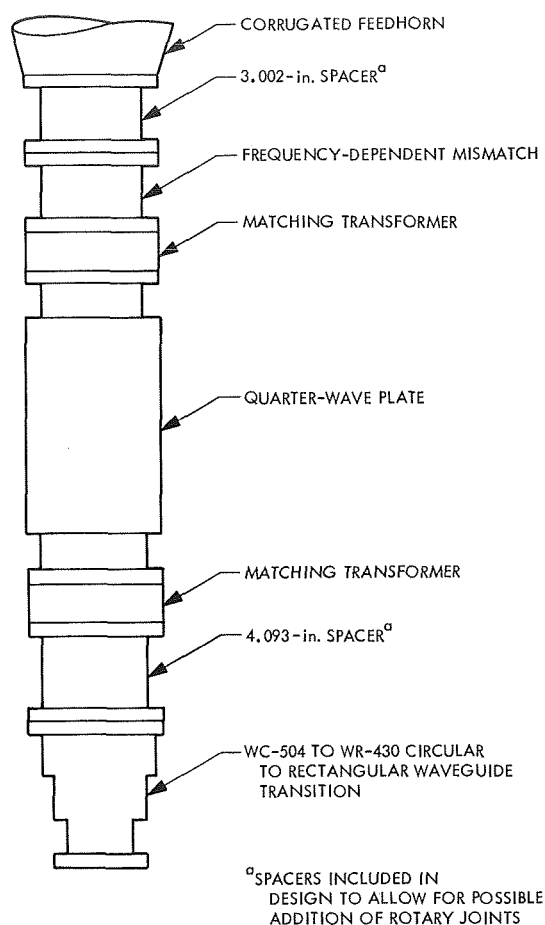
Fig. 47. SMT feed cone polarizer assembly

The waveguide parts were painted flat black to increase heat dissipation by radiation. The cooled waveguide parts as well as the other cooled parts, such as switches, diplexer, and filter, were supplied cooling water from a 2-in. manifold within the cone. For protection against water flow loss, an indicating differential flow switch was installed in the water manifold and was wired to the transmitter interlock circuit. The indicating flow switch has the secondary purpose of allowing an operator to check flow through various parts of the system by means of shutoff valves for each major component in the cone.

Input impedance to the SMT feed cone at various points was measured with a network analyzer calibrated against a sliding load at each frequency. These measurements were made with the feedhorn pointed at the sky. Results are given in Table 24.

Insertion losses of several crucial paths were measured with an insertion loss test set with WR-430 waveguide heads. Results were as follows:

Horn input (point A, Fig. 46) to:	
Maser bypass port (point B) at 2295 MHz	0.0862 dB
Transmitter input port (point C) at 2115 MHz	0.1171 dB
Low-noise listen port (point D) at 2295 MHz	0.0101 dB

4. 210-ft-diam Antenna Reflector Upgrade Study—Phase I, M. S. Katow

a. Introduction. During the evaluation period of distortions of the 210-ft-diam antenna's reflector structure under gravity loadings (SPS 37-52, Vol. II, pp. 86–92), studies could not be made of non-symmetric reflector structures about the elevation axis plane because of the limitations of the assumed quadrant symmetry.

Table 24. VSWR measurements on SMT feed cone

Frequency, MHz	Horn transition (point A)	Maser bypass port (point B)	Transmitter input port (point C)	Low-noise listen port (point D)	
				To feedhorn	To ambient load
2110	1.047	—	1.06	—	—
2115	1.040	—	1.05	—	—
2120	1.030	—	1.062	—	—
2290	1.062	1.10	—	1.083	1.02
2295	1.062	1.084	—	1.083	1.02
2300	1.050	1.063	—	1.083	1.01

(a) ZENITH LOOK ANGLE, rms = 0.059
CONTOUR DEFINITIONS

NORMAL ERROR, in.	LABEL
-0.125	A
-0.100	B
-0.075	C
-0.050	D
-0.025	E
0.000	F
0.025	G
0.050	H
0.075	I
0.100	J
0.125	K
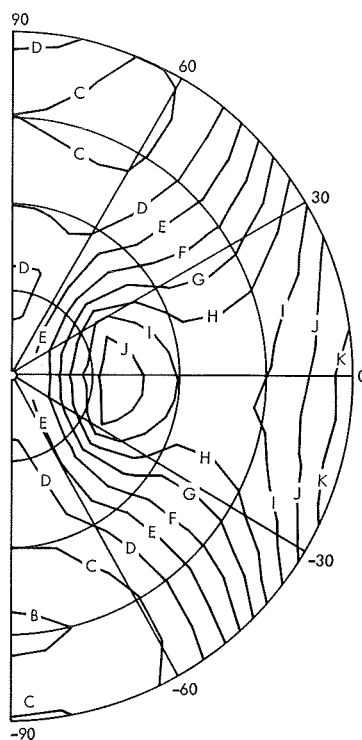
(b) HORIZON LOOK ANGLE, rms = 0.093
CONTOUR DEFINITIONS

NORMAL ERROR, in.	LABEL
-0.225	A
-0.200	B
-0.175	C
-0.150	D
-0.125	E
-0.100	F
-0.075	G
-0.050	H
-0.025	I
0.000	J
0.025	K
0.050	L
0.075	M
0.100	N
0.125	O
0.150	P
0.175	Q
0.200	R
0.225	S
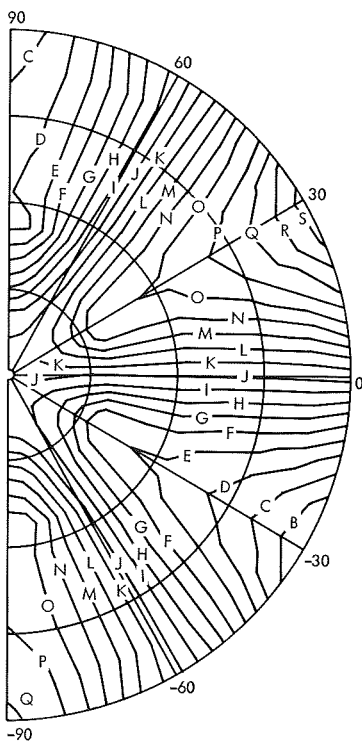
Fig. 48. ½-section reflector deflection patterns after
best-fit with knee bars (gravity off-to-on)

With the implementation of the NASTRAN structural program (Ref. 1) at JPL, it became practically possible to analyze ½-section reflector structure of the 210-ft antenna. It was also possible to study the effects of improved structural modeling by using rigid-joint and shell-type elements available in NASTRAN.

As also described in SPS 37-52, Vol. II, the deflections of the symmetric and the anti-symmetric gravity loading cases are used to compute the distortions at the zenith and horizon look angles of the reflector structure with the surface panels set at 45-deg elevation angle. The two loading cases, resulting in contour level plots for the surface panel support points of the residual distortions after best-fitting of the paraboloid by the RMS Computer Program (SPS 37-40, Vol. IV, pp. 176–184 and Ref. 2), are shown on Fig. 48 for the ½-section or dish NASTRAN analysis.

Changes and improvements in structural modeling were made. The tie-truss assembly was analyzed as rigid-joint bars and triangular-plate members. To reduce the input data, the intermediate ribs were deleted and substituted by equivalent weights.

b. Structural upgrade. Analysis from the structural engineering considerations of ½-section distortion patterns for the anti-symmetric loading case (Fig. 48b) pointed out the possibility that moment reactions in the main girder from the moment arm of the elevation housing could produce excessive deflections in the reflector. The high deflection levels are centered about the ±30-deg radial lines from the horizon and are opposite in directions, that is, the deflection shape is convex above and concave below the horizontal radial line.

By changing the application points of the reaction supports, the distortion level was lowered for this moment reaction. The four existing knee bars, shown in Fig. 49, were removed and two new reaction bars were added (on the top side only) running from the bottom of the elevation housing to the intersection point of the elevation wheel and the wheel girder. For the symmetric loading case, it was necessary to strengthen some diagonals in the main girder because of the removal of the existing knee bars.

c. Results. The structural changes were made in the ½-section model and analyzed with the NASTRAN
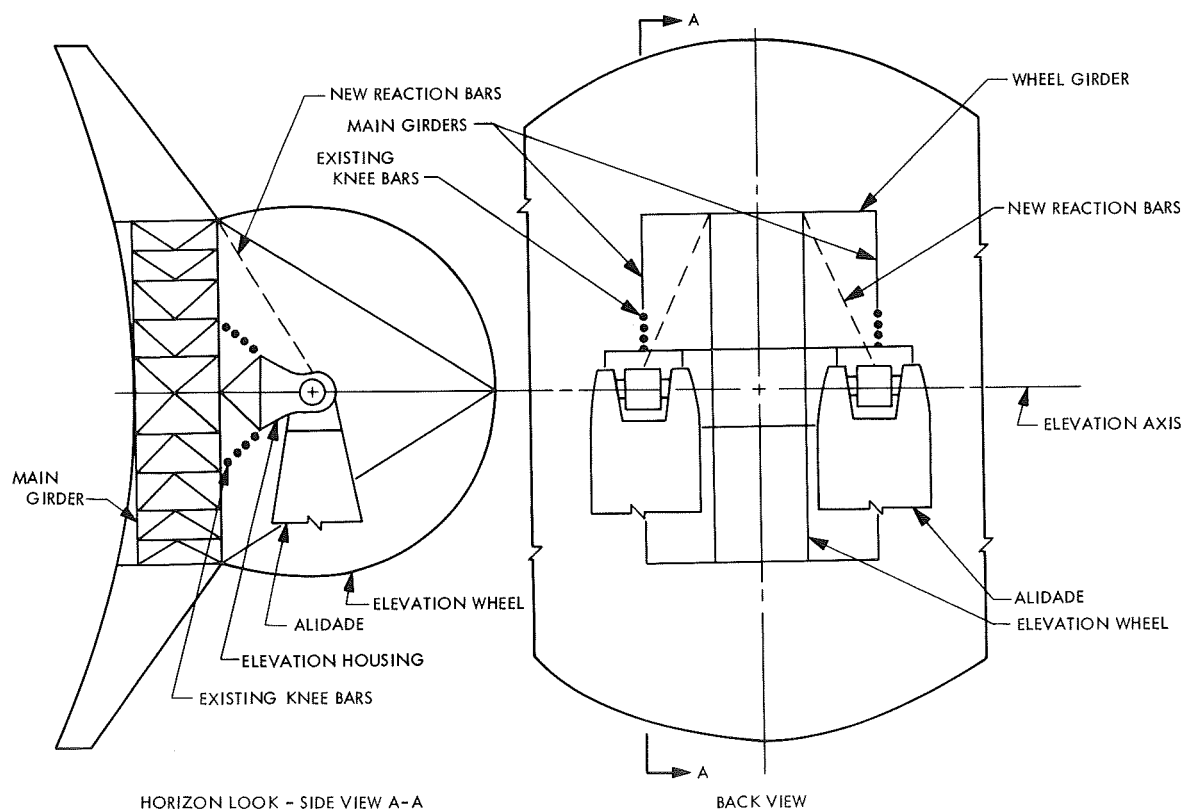
Fig. 49. 210-ft antenna schematic structure

(a) ZENITH LOOK ANGLE, rms = 0.039

CONTOUR DEFINITIONS

1/2 RF PATHLENGTH

ERROR, in.	LABEL
-0.050	A
-0.040	B
-0.030	C
-0.020	D
-0.010	E
0.000	F
0.010	G
0.020	H
0.030	I
0.040	J
0.050	K
0.060	L
0.070	M
0.080	N
0.090	O
0.100	P
0.110	Q
0.120	R
0.130	S
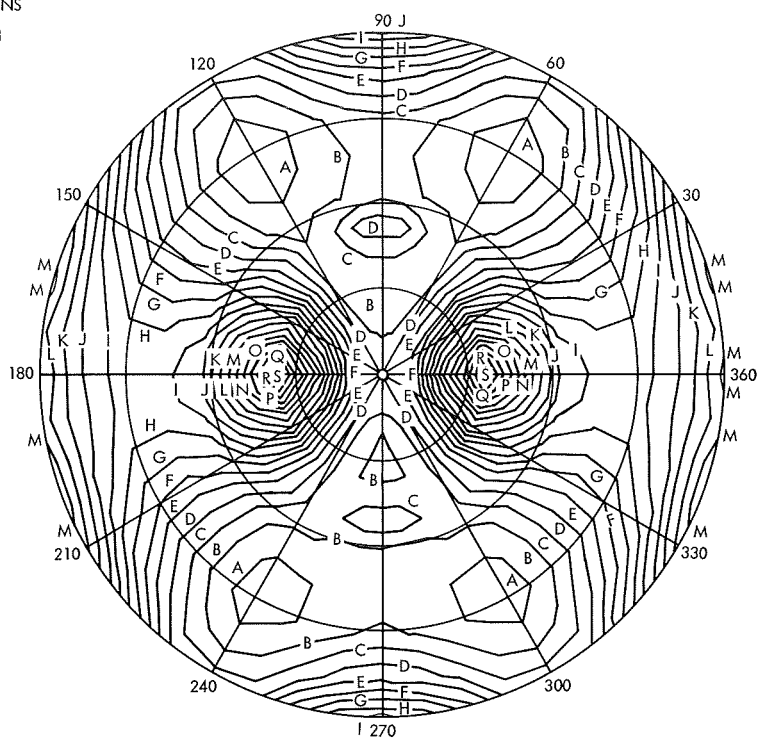
(b) HORIZON LOOK ANGLE, rms = 0.026

CONTOUR DEFINITIONS

1/2 RF PATHLENGTH

ERROR, in.	LABEL
-0.070	A
-0.060	B
-0.050	C
-0.040	D
-0.030	E
-0.020	F
-0.010	G
0.000	H
0.010	I
0.020	J
0.030	K
0.040	L
0.050	M
0.060	N
0.070	O
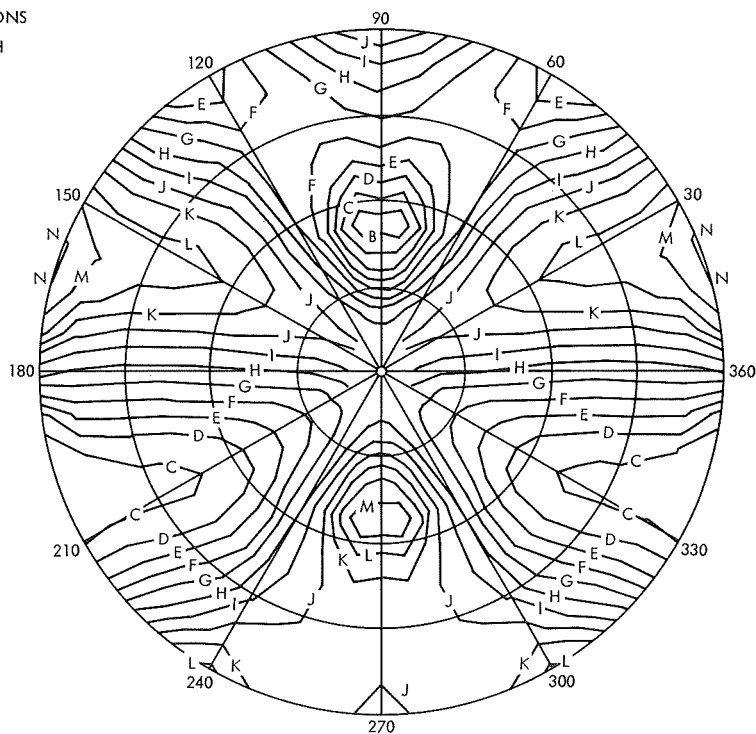
Fig. 50. Reflector deflection patterns after best-fit with new reaction bars (gravity off-to-on)

program. The resulting deflection vectors of the panel-support points were input to the RMS program, and the resulting contour level plots after best-fit are shown in Fig. 50.

The rms reduction in the anti-symmetric and symmetric loading cases is from 0.093 to 0.026 in. and from 0.060 to 0.039 in., respectively.

d. Conclusions. As shown, a large reduction in the anti-symmetric loading case results from the change in the reaction support. A portion of the benefit is from the geometric stance of the added reaction bars. The compressive loads in the bars also produce a bending in the wheel girder in the reverse direction to the bending produced by the normal anti-symmetric loading. At the same time, an improvement of the symmetric loading case results from the more flexible support of the main girder by the elevation bearings. This change in rigidity evidently results in a closer conformity of the deflected shape of the reflector structure to a best-fit paraboloid.

It should be emphasized that only the deflections resulting from gravity "off-to-on" loadings in the symmetric and the anti-symmetric directions are given. This is because the effectiveness of the structural modification can be more clearly forecasted as well as evaluated by the computing process.

References

1. *NASA General Purpose Structural Analysis Program (NASTRAN)*, Computer Software Management and Information Center (COSMIC), Computer Center, University of Georgia, Athens, Ga.

2. Katow, M. S., and Schmele, L., "Utku/Schmele Paraboloid RMS Best-Fit Program," in *Computer Programs for Antenna Feed System Design and Analysis: Volume I. Programs and Sample Cases*, pp. 75–82. Edited by A. Ludwig, Technical Report 32-979. Jet Propulsion Laboratory, Pasadena, Calif., April 15, 1967.

5. Rejection Levels for Outlying Points in Antenna Surface Measurements, R. Levy

The exacting procedures used in the field to obtain precise measurements of antenna surface distortions, plus the conflicting requirement of speed in obtaining a set of readings, result in a significant possibility that typical sets of target readings taken for the antenna are not mistake-free. Although the current measuring procedures tend to ensure a small probability of a mistake in a single reading, the number of readings in a set of surface measurements is sufficient to make the presence of a few mistakes possible. Depending upon manpower availability and the form in which data is recorded in the field, it is sometimes feasible to identify and correct mistakes by noting and re-reading particular targets that tend to exhibit strong departures from the local pattern of the readings for adjacent targets. Although this "field-screening" of the measurements is worthwhile, it is not sufficiently comprehensive and also tends to interfere with progress of the measuring procedure. An approach for supplementary screening proposed here can be employed to reject field measurements that are likely to be spurious.

The method consists of establishing a rejection level, which is a measure that when exceeded will be used to eliminate a particular field reading (called "outlier") from the data set. Heretofore, such rejection levels have been established arbitrarily *a priori*. It is more reasonable to determine the rejection level through a rational-mathematical basis that is derived from information available from the particular configuration and set of measurements.

The standard adopted for developing field-measurements rejection levels is the corresponding point-by-point analytical predictions of these measurements for the antenna in question. Evidently, these predictions are subject to the typical errors resulting from mathematical idealization. Nevertheless, such errors are acceptable for the present purpose, providing that all mistakes of rejection-level magnitude have been eliminated. This usually entails only the routine checking of the analytical model and examination of the results to identify and correct anomalies.

The rejection criterion is formulated in terms of the sample mean μ and standard deviation σ of the vector of point-by-point differences between the field measurements and analytical predictions, and an additional rejection-level constant ρ to be selected for the particular set of measurements. Consequently, the criterion is to reject field readings whenever the difference vector departs by more than $\pm \rho \sigma$ from μ. A rational method to establish ρ will be given subsequently.

Whenever the criteria are invoked to reject an outlier, either the desired result of eliminating a mistake has been achieved or else the undesired effect is to eliminate a valid measurement falling within the tail regions of the governing probability density function. Although it is apparently impossible to determine whether or not an

outlier represents a valid measurement or a mistake, it is simple to determine ρ to be consistent with a specified risk of having valid measurements included within the rejected outliers.

To do this, let

$\phi =$ the risk that a valid point (at least one) is included among the outliers

$\gamma = (1 - \phi)$, the probability that no valid points are excluded

$\alpha =$ the probability that a difference falling within the rejection-level tail of the distribution function of the difference vector is derived from a valid field measurement

Hence, for N points in the measurement set, the binomial probability law yields

$$\gamma = P(0) = (1 - \alpha)^N \tag{1}$$

The solution to Eq. (1) can usually be approximated as

$$\alpha = \frac{-1}{N} \ln \gamma$$

or

$$\alpha = \frac{-1}{N} \ln (1 - \phi) \tag{2}$$

Once α is known, ρ can be chosen from the distribution function of the difference vector $\{d\}$ to satisfy

$$\alpha = P\left[\,|(d_j - \mu)| > \rho\sigma\,\right] \qquad j = 1, 2, \cdots, N \tag{3}$$

Figure 51 gives curves to select ρ for values of ϕ and N, with the assumption that the difference vector is normally distributed. Experience to date indicates that the normal
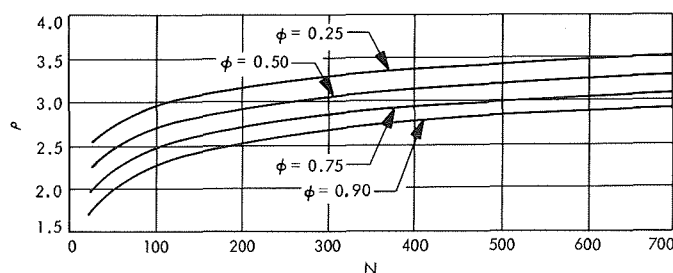
distribution is reasonable, at least for preliminary computations. After the outliers have been rejected, the normal hypothesis for the remaining elements of the difference vector could be tested with α as the level of significance for a Type 1 error.

The choice of a relatively smaller value for the risk ϕ increases ρ and is correspondingly less discriminating. To avoid the loss of capability to reject mistakes, we might consider increasing the risk of rejecting a valid measurement as long as, on the average, the outliers so determined were predominately mistakes. To determine the expected number of valid readings $N\alpha$ that would be included within the outliers, it is convenient to use Fig. 52, which shows the α contours on plots of ϕ vs N. To illustrate, assuming $N = 400$, and for an initial choice of a 25% risk of discarding a valid measurement, then, according to Fig. 51, ρ would be selected as 3.35. Depending upon particular knowledge of the circumstances, this might be considered to be too large to detect certain of the mistakes. As an alternative, using Fig. 52, a selection of ρ as 2.8 would be equivalent to $\alpha = 0.005$ and an 86% risk of rejecting a valid measurement. This might be acceptable if, for example, eight outliers were rejected. That is, since the expected number of valid measurements rejected is equal to 2 ($= 400\alpha$), there is only a 25% chance that any one of the rejected points was a valid measurement.

As a specific example, Figs. 53 and 54 show the distribution function of the difference vector for an actual set

Fig. 51. ρ vs N and ϕ

Fig. 52. ϕ vs N and α
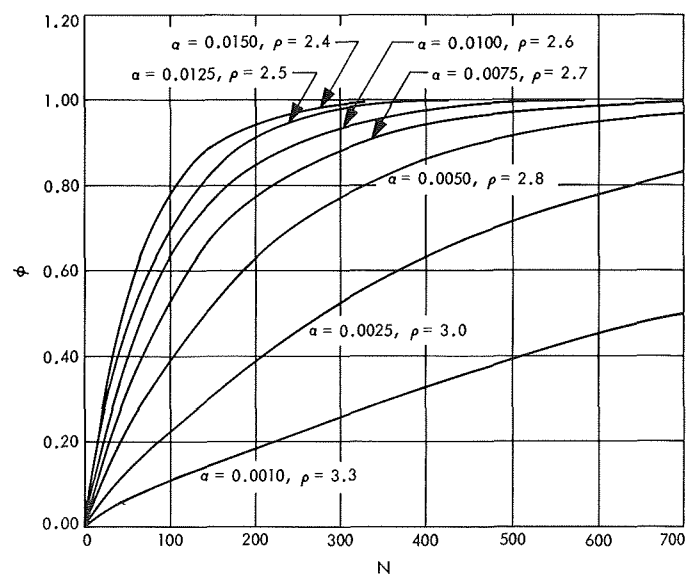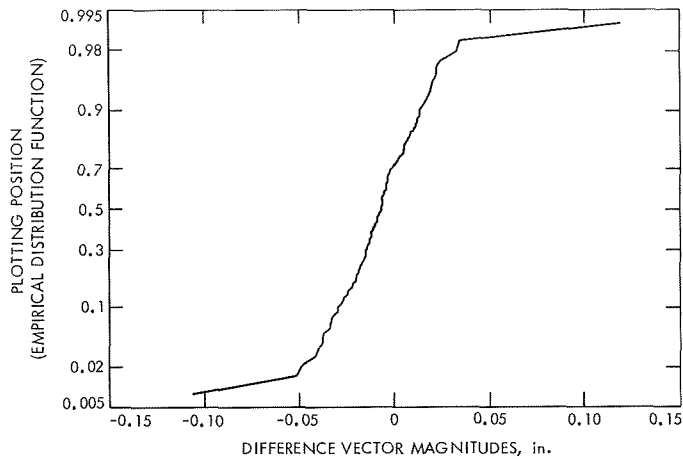
Fig. 53. Difference vector distribution function before outlier rejection
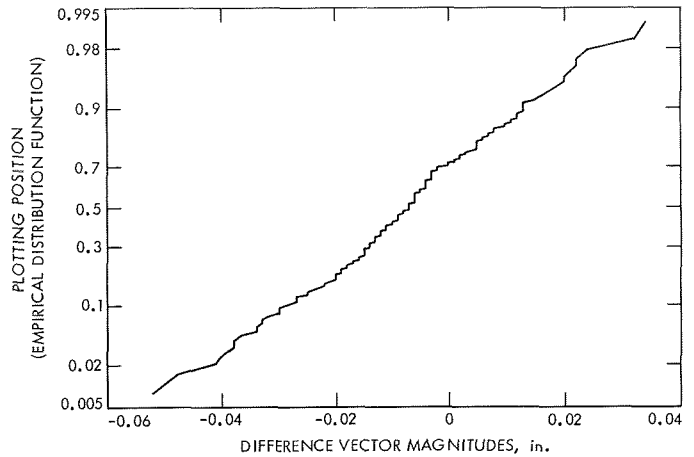
Fig. 54. Difference vector distribution function after outlier rejection

of analytical and measured data. The structure is an 85-ft-diam az–el antenna for which 163 field readings are matched with the corresponding analytical predictions. The difference vector is based upon the deviations of the normals to the theoretical paraboloid. A rejection level of $\rho = 3.3$ was selected and, according to Fig. 52, this amounts to at most a 16% chance that at least one valid measurement would be classified as an outlier and a 0.1% chance for any of individual measurement. Figure 53 shows the distribution function before outlier rejection. Figure 54 shows the distribution function for the remaining points after rejection. Two outliers were rejected at -5.0 and $+6.3$ standard deviations from the mean, indicating a considerably smaller chance than the previously mentioned 16% limit for either outlier being valid. A hypothesis test to verify a normal distribution function for the difference vector indicates acceptance at

significance levels of 0.118 before and 0.458 after rejection. This is extremely strong evidence, particularly after outlier rejection, that the assumption of a normal distribution is valid. Since the graphs are constructed with a normal probability scale on the ordinate, the good fit to a normal distribution is evident from the near-linearity of the plotted functions.

A more comprehensive approach to establishing rejection levels could be developed if statistics for the incidence and magnitude of measurement mistakes were available. Until these statistics are obtained, it is apparently necessary that the levels incorporate a combination of judgment and rationality. Nevertheless, curves such as in Figs. 51 and 52 are of assistance in selecting the rejection levels, and in evaluating possible consequences of these selections.

IV. Development and Implementation

A. DSIF Development

1. Clock Synchronization System Performance, H. W. Baugh

a. Introduction. The Clock Synchronization System consists of a computer-controlled transmitter at DSS 13 and several remote receiving units. The transmitter frequency is controlled according to a precomputed ephemeris to correct for doppler shifts on both up-link and down-link, so that the signals arrive at the fixed-tuned receivers exactly on the designed carrier frequency. The pointing of the transmitting antenna, a 30-ft reflector on an az–el mount, is also ephemeris-controlled, so that the beam is aimed at the center of the reflecting zone, considering the parallax due to the location of the stations, as well as standard-atmosphere refraction corrections. Similarly, predicts that are precomputed and mailed to the remote stations permit them to adjust the four-foot receiving antennas (which use HA–dec mountings) so their beam can track the same subradar point on the moon.

Having established a communication link on an X-band carrier, radiating 20 kW at 8.4501 GHz, the transmitter is in a position to send timing signals. The technique used is to modulate the carrier with a pseudorandom code whose phase is offset according to an ephemeris for round-trip time. The code generation is timed by the DSS 13 station clock (using a combination of cesium and rubidium frequency standards) which is maintained in close synchronization with the National Bureau of Standards by means of microwave link and portable clock measurements.

The remote receivers use correlation detection to determine the phase relationship between the received code and a local code which is controlled by the remote station's clock. This measurement can be made with microsecond resolution over a range of $\pm 25 \ \mu s$. Typically, 20 to 50 measurements are made during the course of a day's operations, and these measurements will usually have a standard deviation of from 2 to 5 μs, so that the probable error of the offset thus determined is no more than 5 μs.

b. Future capability. The present network, consisting of the DSS 13 transmitter and receivers at DSSs 41, 42, 51, and 62, was implemented for the *Mariner* Mars 1969 encounter, with the objective of providing real-time synchronization if possible, and "paper" sync after the fact to within 20 μs between all the stations. Portable

clock visits to the stations have repeatedly shown the system to be operating well within 10 μs.

The station clocks in use at that period could only be corrected in 100-μs steps, so that it was impractical to attempt to keep them closer than ±50 μs in real-time, but their stability permits their data to be adjusted to a fraction of a microsecond within the Orbit Determination Program.

New clocks are being installed in the stations, having much greater reliability, and 1-μs setting capability. The objective for future missions will be to keep these clocks synchronized in real-time, so that the time-tags on tracking data can be used in the Orbit Determination Program directly, without the need for the calibration data which must now be input to the program.

To achieve this type of synchronization, the stations will have to make daily corrections to compensate for the drift rate of their frequency standards as monitored by a suitably weighted combination of VLF data and clock sync data. If time is lost completely at a station, a clock sync measurement may be used to reset the clock; but, in view of the noise on the measurements, it will probably be better to make routine adjustments on the basis of long-term (i.e., several days) averages of clock sync measurements.

An additional receiver is being readied for installation at the U. S. Naval Observatory (USNO) in Washington, D.C. The unit will be installed as soon as practicable (probably in March) and this should permit an extensive evaluation of the system to be made by independent observers.

c. Performance. The system was shut down on November 15, 1969, to permit necessary modifications to be made to the transmitter housing. Successful transmissions were resumed on January 5, 1970. DSSs 41 and 42 received good data. DSS 51 is still awaiting the repair of one of the modules in its receiver, and the quality of the data at DSS 62 was so poor as to be essentially unusable. The difficulty at DSS 62 is possibly due to a mistuned crystal filter in the 100-kHz IF amplifier. They are maintaining their clock by reference to LORAN-C data at DSS 61 via microwave link.

The transmitter went out of service on January 15 when a high-voltage power supply failed; it returned to service on February 2, 1970. Thus, we have data from the two Australian stations for days 5 through 14, and 33 through 41.

Figure 1 shows the data points reported by DSS 41, with a straight-line fit to the data. The straight line is considered to be the best model to use for assessing the data, because the drift rate of a rubidium standard is essentially constant over this period of time. Figure 2 gives the same information for DSS 42.

Figure 3 shows the residuals, i.e., the differences between the observed points and the straight-line fit, of the data for both stations plotted on an expanded scale. It is immediately apparent that the data from both
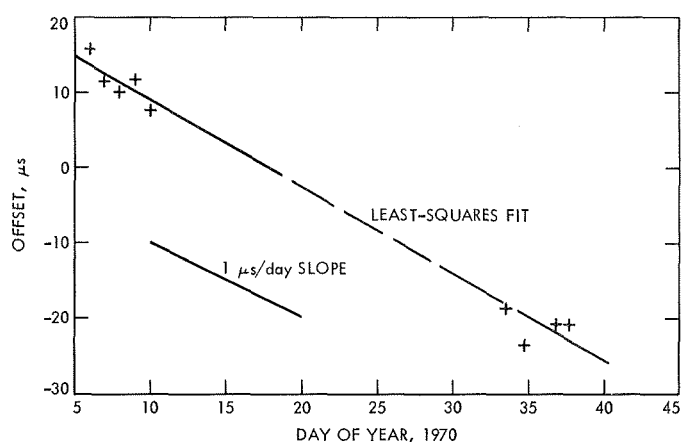
Fig. 1. DSS 41 clock offsets
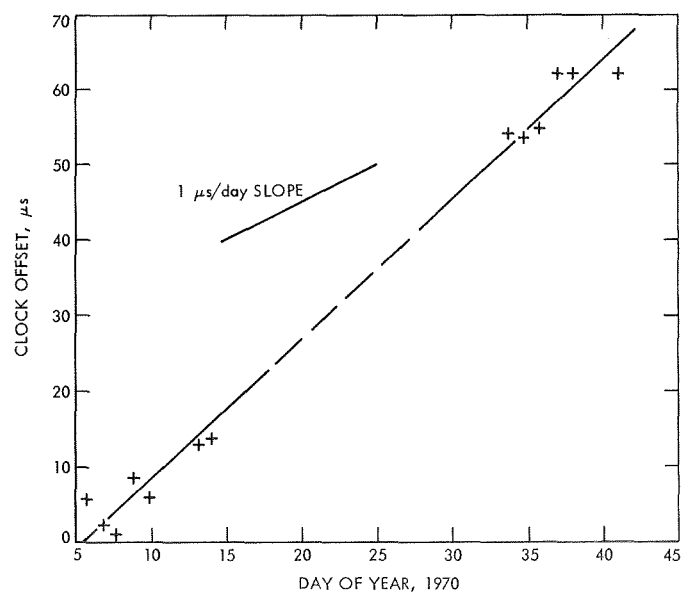
Fig. 2. DSS 42 clock offsets
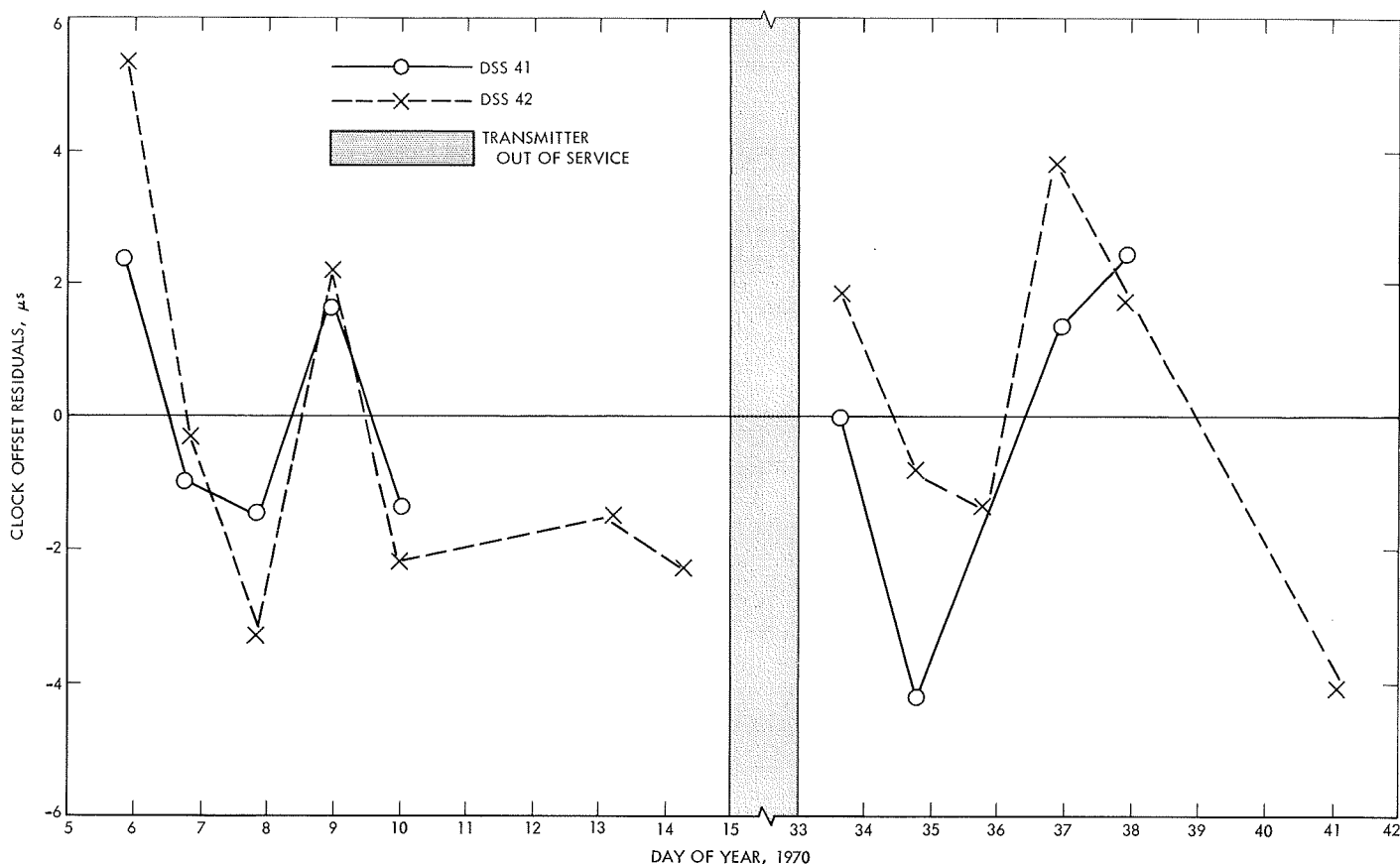
Fig. 3. Residuals of clock sync data

stations have similar trends. While this is only a small data sample, a similar effect was reported in SPS 37-61, Vol. II, pp. 120–121. Such excursions of from 5 to 10 μs could well be the effect of changes of average elevation of the moon's surface; they could, however, be the result of periodic errors in the ephemeris, or many other as yet uncalibrated system errors.

The clock sync system includes a receiver at DSS 14 for the express purpose of measuring the system error. DSS 14 has a timing system which is referenced to NBS nearly as well as that at DSS 13; if the clock sync system gives a different apparent offset from that which DSS 14 can determine by other means, the difference should be a measure of the overall calibration of the system. Unfortunately, DSS 14 has been involved in major reconfiguration work and has not been reporting data during this period, except for two values on days 008 and 009. The application of those values would decrease the amplitude of the change in residuals for those days. When all four overseas stations transmit data, and calibration data is received from DSS 14, a more thorough assessment of this possible effect can be made.

2. Compatibility Test Control Panel, *L. E. Butcher and R. E. Mossinger*

a. Introduction. The SMC control panel as originally described in SPS 37-53, Vol. II, p. 112, has undergone numerous design changes and has been renamed the compatibility test control panel. This article describes the functions of the panel and its utilization at the JPL Compatibility Test Station (CTS) at Cape Kennedy and the Compatibility Test Area (CTA) at JPL.

b. Purpose. The purpose of the compatibility test control panel is to provide a central location for the control and display of the test functions that have been semiautomated. The following semiautomated test functions are controlled and/or displayed from the panel at the station monitor console (SMC):

(1) Computer-controlled attenuators (HP 8731B pin modulator) in the exciter output and both receiver inputs.

(2) Exciter and receiver VCOs and display of the associated S-band frequencies and receiver signal levels.

(3) Call-up of all computer subroutines stored on digital magnetic tape.

(4) Recording of all pertinent data on the line printer for a permanent record.

c. Functional description. The compatibility test control is functionally divided into two distinct control categories—the display control and the computer control. The two control functions are operated in conjunction with the digital instrumentation subsystem (DIS 920 Computer).

Display control. An 11-unit display is mounted above the control panel and is capable of displaying the functions as selected by the following display control switches:

(1) Common. Operating in conjunction with the common selector digiswitch and the mode select switch, any of 600 common core locations in memory can be displayed.

(2) Receiver 1, AGC. The signal level of receiver 1 is displayed in dBmW from the automatic gain control (AGC) versus signal level curve stored in computer memory.

(3) Receiver 2, AGC. The signal level of receiver 2 is displayed in dBmW from the AGC versus signal level curve stored in computer memory.

(4) Exciter XA. A predicted exciter VCO frequency is displayed based upon calculations of the received frequency.

(5) Receiver 1, RF. The receiver 1 S-band frequency is displayed from calculations based upon the VCO frequency $\times$ 96 + 50 MHz.

(6) Receiver 2, RF. The receiver 2 S-band frequency is displayed from calculations based upon the VCO frequency $\times$ 96 + 50 MHz.

(7) Exciter, RF. The exciter S-band frequency is displayed from calculations based upon the exciter VCO frequency $\times$ 96.

(8) Receiver 1, CCA. The amount of attenuation in the receiver computer-controlled attenuator (pin modulator) is displayed in dB. The attenuation is derived from receiver 1 AGC curve when operating in the closed-loop mode, or the attenuation versus voltage curve of the pin modulator stored in memory for the open-loop mode.

(9) Receiver 2, CCA. The amount of attenuation in the receiver computer-controlled attenuator (pin modulator) is displayed in dB. The attenuation is derived from receiver 2 AGC curve when operating in a closed-loop mode, or the attenuation versus voltage curve of the pin modulator stored in memory for the open-loop mode.

(10) Exciter, CCA. The amount of attenuation in the exciter computer-controlled attenuator (pin modulator) is displayed in dB. The attenuation is derived from the test transponder AGC curve when operating in the closed-loop mode, or the attenuation versus voltage curve of the pin modulation stored in memory for the open-loop mode of operation.

Computer control. Control of the computer subroutines is accomplished by utilizing the interrupt system of the DIS. The parameters of the subroutines are entered by the interrupt system by activating the following computer control switches:

(1) Auxiliary I/O. Operating in conjunction with the interrupt switch, allows the SMC operator to select the remote typewriter (DIS Phase II), or the DIS typewriter (DIS Phase I) for control of the DIS computer.

(2) Print. Operating in conjunction with the subsystem select switch and the interrupt switch, outputs on the line printer either the station configuration status (i.e., switch positions) or receiver/exciter data (i.e., frequencies and signal levels).

(3) Zero. Operating in conjunction with the interrupt switch, the Ramp subroutine digital-to-analog (D/A) channel is placed at 0 V.

(4) Rest. Operating in conjunction with the interrupt switch, enters into the Ramp subroutine rest frequency and references the ramp frequencies to this point.

(5) Stop. Operating in conjunction with the interrupt switch, stops the ramp subroutine D/A channel output.

(6) Ramp. Operating in conjunction with the change/rate digiswitch, lock, loop, zero, direction, and interrupt switches, initiates the ramp subject to the parameters entered by the above switches.

(7) Receiver 1, CCA. Operating in conjunction with the change/rate digiswitch, direction and interrupt switches, initiates the pin modulator subroutine subject to the parameters entered by the change/rate digiswitch.

(8) Receiver 2, CCA. Operating in conjunction with the change/rate digiswitch, direction and interrupt switches, initiates the pin modulator subroutine subject to the parameters entered by the change/rate digiswitch.

(9) Exciter, CCA. Operating in conjunction with the change/rate digiswitch, direction, and interrupt switches, initiates the pin modulator subroutine subject to the parameters entered by the change/rate digiswitch.

d. Conclusion. The benefits derived from the implementation and operation of the compatibility test control panel and associated software and hardware at the CTA and CTS are as follows:

(1) A personnel reduction of approximately 50% is accomplished in the performance of some telecommunications tests.

(2) The test time has been reduced one-third to one-half during some compatibility tests.

(3) An improvement in test quality has resulted from being able to automatically establish frequencies, adjust signal levels, and record all pertinent data on the line printer from the SMC by a single operator.

3. DSS 12 Temporary Reconfiguration, C. B. Bricker

The standard DSIF S-band Cassegrain monopulse feed cone (SCM) was removed at DSS 12 and replaced with an R&D S-band polar ultra (SPU) feed cone in order to provide the *Mariner* Mars 1969 Extended Operations Mission and *Pioneer* Projects with an 85-ft tracking system capable of providing data in the Goldstone DSCC longitude during the DSS 14 tri-cone reconfiguration in late January and February of 1970. Reconfiguration of this station was accomplished in approximately three days. During this time period the hardware was modified, and abbreviated system tests were performed.

The SPU cone, maser, and all associated hardware was R&D-type equipment. A detailed description as to design and functional characteristics of the SPU cone can be found in *Subsection III-C-6.*

Modifications to the standard DSIF tracking and communications system consisted of: (1) replacement of the SCM cone, diplexer, and associated waveguide with an SPU cone, modified switches, and a harmonic filter; (2) replacement of the standard DSIF maser with an R&D-type second-generation maser; (3) minor modifications to the standard microwave switch control assembly; and (4) minor reconfiguration of the cone airconditioning system. Subsequent to the installation, star tracks and abbreviated system tests were performed which provided the following data: (1) a maser gain of 47 dB versus the normal gain of 35 dB; (2) a system temperature in the diplex mode of 25.8°K versus a normal system temperature of 42.0°K, and a system temperature in the receive-only mode of 17.6°K versus a normal system temperature in this mode of approximately 30.0°K.

At the conclusion of these tests the station was committed to the *Mariner* Extended Operations Mission and *Pioneer* Projects on a best-efforts basis. Subsequently, successful tracking has been accomplished on the *Mariner* and *Pioneer* spacecraft at the following average signal levels:

Mariner VI	174.5 dB
Mariner VII	174.4 dB
Pioneer VI	169.1 dB
Pioneer VII	171.4 dB
Pioneer VIII	162.1 dB
Pioneer IX	170.4 dB

Installation of the SPU cone and R&D maser has produced a nonstandard 85-ft tracking and communications system with improved system performance characteristics; i.e., a gain increase of approximately 2.3 dB in the diplex mode, permitting the tracking of spacecraft not normally within the capabilities of the standard 85-ft tracking system.

4. Digital Frequency Synthesis, C. E. Johns

a. Introduction. There are many commercial variable-frequency synthesizers available using various techniques to accomplish the synthesis processes. These techniques include both direct synthesis (i.e., mixing and filtering) and phase-locked loops, or combinations of both. Another technique, described in this article, is the synthesis of radio frequencies by the generation of digital waveforms.

b. Digital frequency synthesis technique. Under investigation at the present time is the use of rate multipliers to synthesize radio frequencies. Although the

principle of the rate multiplier is well known, its operation can be briefly described by reference to Fig. 4. The input reference frequency, f_r, is divided by two by a flip-flop (F-F A), whose output terminals are then gated with f_r to provide two anticoincident $f_r/2$ signals, f_1 and f_2. f_2 is used as the timing signal for a binary divider (flip-flops 1 through 4). The divided outputs are gated with f_2 in control gates U, V, W, and X along with a dc control for each gate. When the dc control for gate U is at a high logic level, the gate output is a pulse sequence at a $f_2/2$ rate; similarly, with their dc controls at a logic 1, gates V, W, and X outputs are $f_2/4$, $f_2/8$, and $f_2/16$, respectively. The pulse rates from the control gates are all anticoincident and are applied to the inputs of gate Y, whose output is the summation of the control gates. The output pulse rate from gate Y, therefore, can be controlled to provide from zero to $(15/16) f_2$ in $f_2/16$

increments by application of dc control voltages. The output from gate Y is then recombined with f_1 by means of gate Z; since all the pulses are anticoincident, the output of gate Z is the summation of f_1 and the selected pulse rate from gate Y.

The omission of pulses in the sequence creates unevenly spaced pulses; consequently, the output frequency is the average frequency over a given time period. These omitted pulses actually create 360 phase steps in the output signal. The magnitude of these steps can be reduced by several methods. One such method is to frequency-divide the pulse sequence, which, at the same time, reduces the phase step by the same factor. Another method is to spread the phase step over many cycles with either a passive or tracking filter. Combinations of these techniques can also be used. This article describes
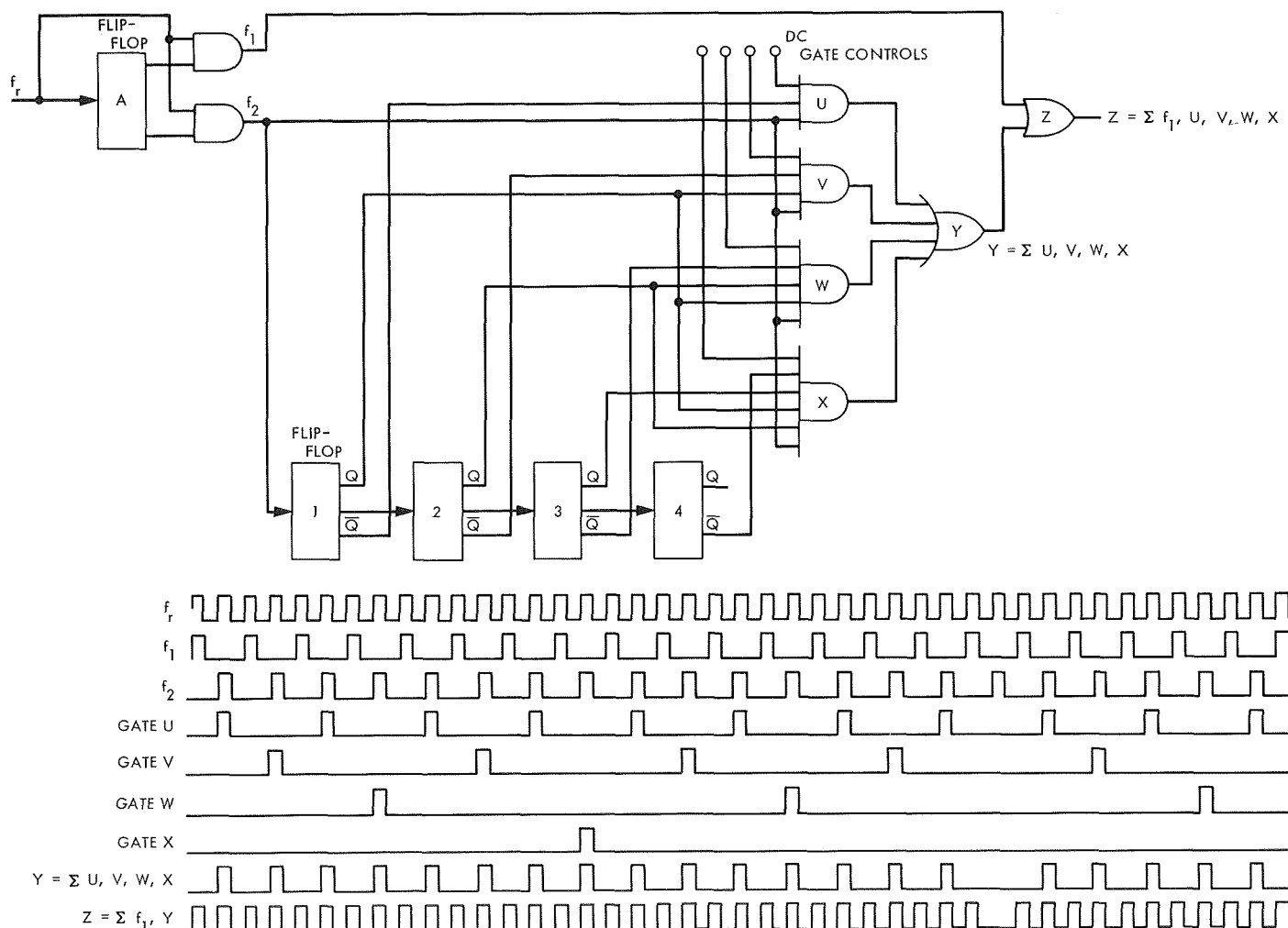
Fig. 4. Rate multiplier and waveforms

a digital frequency synthesizer using both the divide and passive filter technique (Fig. 5).

c. Analysis. The waveform $e(t)$ at the output of the frequency divider contains a phase step of $360/n$ deg as shown between points a and b in Fig. 6. This waveform, as shown in sinusoidal form in Fig. 7a, can be represented by the sum of three waveforms: (1) the basic periodic waveform, (2) a second waveform identical to the basic waveform by 180 deg out of phase, and starting at time t_1, and (3) a third waveform identical to the

basic waveform starting at t_2 (Fig. 7b). In this analysis only the fundamental or sine waveforms have been used for simplicity. This is valid, since the harmonics present in the digital waveform are eliminated in the bandpass filter. The input waveform or excitation signal to the bandpass filter can then be represented by

$$e(t) = \sin \omega_n t\, u(t) - \sin \omega_n(t - t_1)\, u(t - t_1)$$
$$+ \sin \omega_n (t - t_2)\, u(t - t_2) \qquad (1)$$

where ω_n = the angular frequency of the sine waveform.

The Laplace transform of the excitation signal is then

$$E(s) = \frac{\omega_n}{s^2 + \omega_n^2} (1 - e^{-st_1} + e^{-st_2}) \qquad (2)$$

The effect of the filter on the input phase transient of $360/N$, or ϕ, is to integrate this transient over a period of several cycles, because the energy storage qualities of the filter tend to resist sudden input changes in the excitation signal. To calculate the filter response to a phase step superimposed on the excitation signal, a simple bandpass network was used (Fig. 8). The transfer function $G(s)$ of the circuit is

$$G(s) = \frac{s}{RC \left(s^2 + \dfrac{1}{RC} s + \dfrac{1}{LC} \right)} \qquad (3)$$

A transfer function in terms of the filter -3-dB bandwidth BW and its natural resonant frequency ω_n is obtained by

$$\frac{1}{RC} \cdot \frac{2\pi}{2\pi} = 2\pi BW$$

and letting

$$\frac{1}{LC} = \omega_n^2$$

Fig. 5. Digital synthesizer block diagram
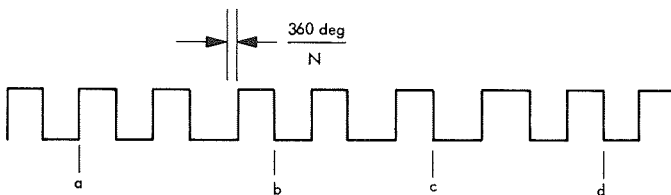
Fig. 6. Divider output waveform
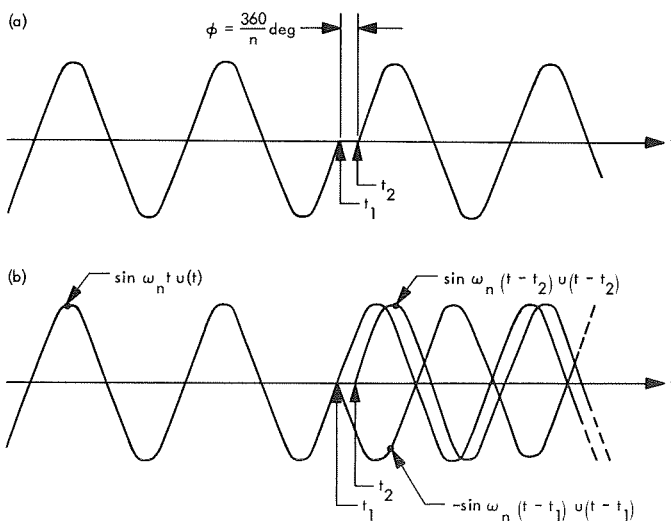
Fig. 7. Bandpass filter excitation
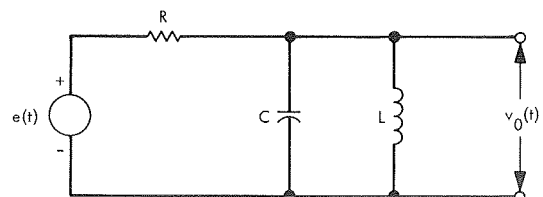
Fig. 8. Bandpass filter

The transfer function is then

$$G(s) = \frac{s}{RC(s^2 + 2\pi BW\, s + \omega_n^2)} \qquad (4)$$

Note that an approximation is made to simplify the analysis; namely, the resonant angular frequency used for the filter is assumed to be the same as for the excitation sine wave.

The transform of the filter output

$$V_0(s) = G(s)\, E(s)$$

$$= \frac{\omega_n}{s^2 + \omega_n^2} \left[\frac{s}{RC(s^2 + 2\pi BW\, s + \omega_n^2)} \right]$$

$$\times\, (1 - e^{-st_1} + e^{-st_2}) \qquad (5)$$

and the inverse transform of the output waveform (assuming a narrow bandwidth filter) is

$$v_0(t) = \sin \omega_n t - \sin \omega_n\,(t - t_1)$$

$$+ \frac{\omega_n}{\omega_D} \exp\left[-\pi BW(t - t_1)\right] \sin \omega_D\,(t - t_1)$$

$$+ \sin \omega_n\,(t - t_1)$$

$$- \frac{\omega_n}{\omega_D} \exp\left[-\pi BW(t - t_2)\right] \sin \omega_D(t - t_2)$$

$$(6)$$

where the damped frequency

$$\omega_D = \left[\omega_n^2 - (\pi BW)^2\right]^{1/2}$$

Expression (6) can be simplified, with very small error, by letting $\omega_n = \omega_D$.

The filter output, from t_1 on, becomes

$$v_0(t) = \exp\left[-\pi BW(t - t_1)\right] \sin \omega_n(t - t_1)$$

$$+ \{1 - \exp\left[-\pi BW(t - t_2)\right]\}\sin \omega_n(t - t_2)$$

$$(7)$$

Expression (7) shows that the filter output voltage at t_1, due to the initial excitation, starts decaying at an exponential rate, and a second output voltage at t_2 starts increasing at an exponential rate, the rates being controlled by the filter bandwidth. The resultant output is a nearly constant amplitude signal which is shifting in phase with time.

The manner in which the filter action distributes the input phase step ϕ was calculated from the vector diagram shown in Fig. 9. The output phase $\theta(t)$ is

$$\theta(t) = -\tan^{-1} \frac{[1 - \exp(-\pi BWt)] \sin \phi}{\exp(-\pi BWt) + [1 - \exp(-\pi BWt)] \cos \phi}$$

$$(8)$$

where $\phi = t_1 - t_2$ and the output phase $\theta(t)$ is measured after t_2. For accuracy, Expression (8) relies on ϕ being small compared to the phase-spreading time period due to the filter. Expression (8) was programmed for a Hewlett-Packard 9100 calculator and for $\theta(t)$ plotted for several filter bandwidths, which are shown in Fig. 10. The input phase step ϕ was set at 0.628 rad, which is equivalent to dividing the rate multiplier output by a factor of 10. In each case $\theta(t)$ approaches ϕ as a limit.

The action of the frequency divider and bandpass filter upon the rate multiplier output waveform can be
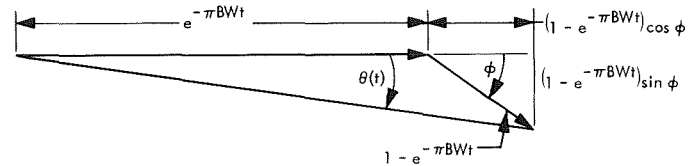
Fig. 9. Vector diagram
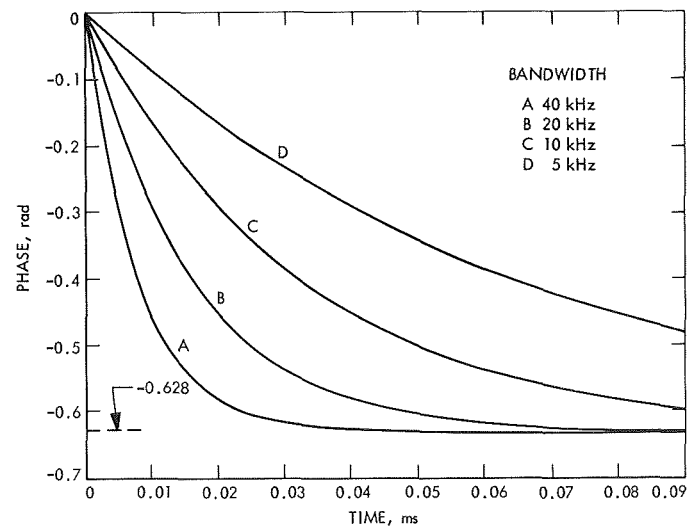
Fig. 10. Phase versus bandwidth
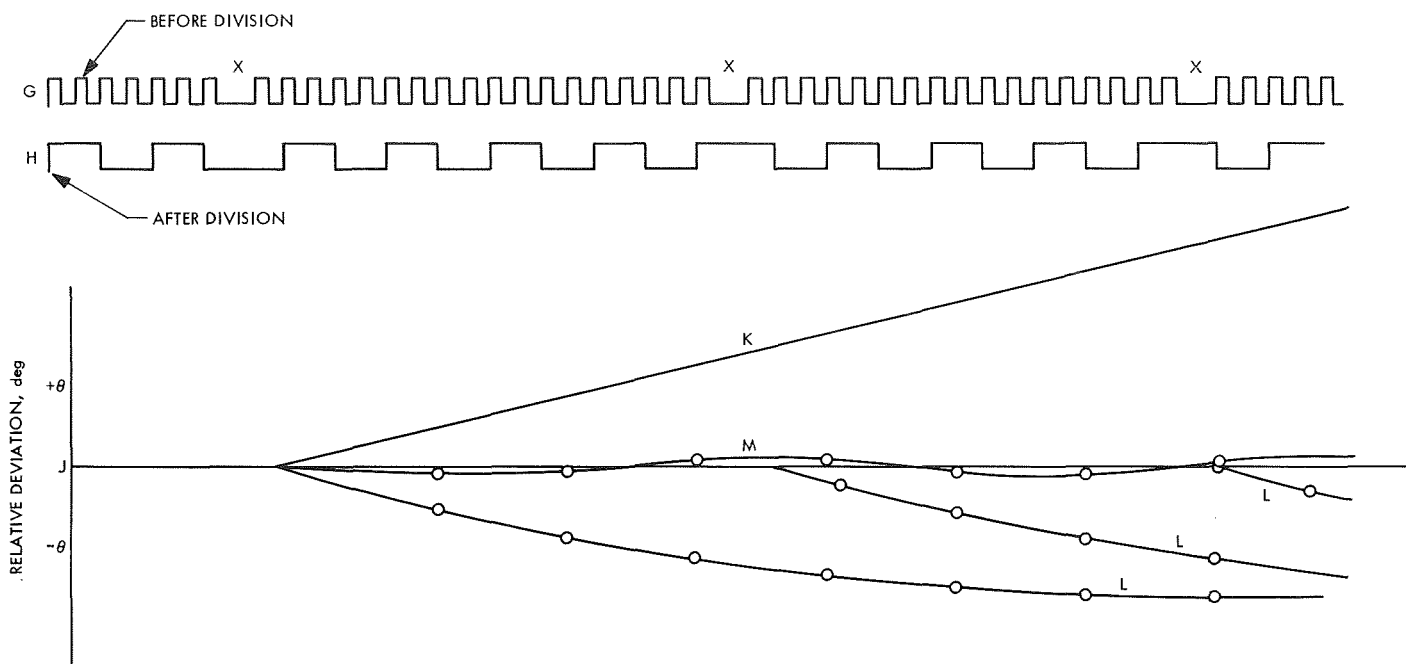
Fig. 11. Effects of filter and divider

illustrated by reference to Fig. 11. The pulse sequence input to the divider is shown in G and the divider output by H. The nominal frequency is designated by the horizontal line shown by J. Except for the exclusion of the pulses marked X, the average pulse rate is slightly higher in frequency than nominal, and the filter output phase deviates linearly from nominal as shown by curve K. Shortly after each X occurs, the divider output has a negative phase step which is integrated by the filter (curves L). The resultant filter output frequency M is the sum of all the integrated phase steps and the negative phase ramp. Curve M shows that the overlapping phase ramps, at the filter output, tend to reduce the peak-to-peak phase ripple on the output frequency.

d. Development. A breadboard digital synthesizer has been constructed and some phase stability measurements have been made on its output signal. The measurements were made in a 20-Hz bandwidth 2295-MHz phase-locked receiver. To generate an S-band test signal, the

500 kHz from the digital synthesizer was mixed with a 23.4-MHz signal from a Hewlett-Packard 5100 synthesizer; the 23.9-MHz sum frequency was then multiplied by 96 to 2295 MHz. The measurements showed no inherent phase instabilities due to the digital synthesizer.

Construction of an improved version of the synthesizer has begun which will allow the output frequency to be varied in much smaller increments than was possible with the breadboard. More evaluation will be performed when construction of the second model is complete.

e. Conclusions. The feasibility of using a rate multiplier followed by a frequency divider and passive bandpass filter for frequency synthesis has been demonstrated. This method of frequency synthesis is relatively simple, since it does not require locked loops or other complex schemes to provide a variable signal source. Since the output frequency is controlled by dc voltages, it can be easily adapted to computer control.

V. Operations and Facilities

A. DSN Operations

1. Radio Science Support, T. Sato, L. Skjerve, and D. Spitzmesser

a. RAES Panel activities. As reported in SPS 37-61, Vol. II, pp. 153–154, radio astronomy experiments to be conducted at DSN facilities are now selected by the Radio Astronomy Experiment Selection (RAES) Panel. Since the last report, three proposed experiments have been submitted to the panel and they are being evaluated.

b. Radio science operations

Very long baseline interferometer experiment. On December 21, 1969, a 24-h very long baseline interferometer (VLBI) experiment was conducted between two Goldstone Deep Space Communications Complex (DSCC) sites (DSSs 11 and 14) and one of the DSN facilities in Australia (DSS 42). The principal observers were Dr. D. S. Robertson[1] at DSS 42 and Dr. A. T. Moffet[2] at the Goldstone DSCC. These observations are the latest of a series conducted by these experimenters (SPS 37-56, Vol. II, pp. 148–149, and Refs. 1 and 2). The characteristics of variable quasars are being investigated in this experiment.

---

[1]Principal Officer of the Space Research Group, Weapons Research Establishment, Adelaide, Australia.

[2]Associated with the Owens Valley Radio Observatory, which is operated by the California Institute of Technology.

The station analog and digital configuration for this observation was similar to previous experiments but the data bandwidth was increased by an order of magnitude from 1.1 to approximately 15 kHz.

The analog subsystem used the standard DSIF receiver with experiment-peculiar elements as shown in Fig. 1. The normal free-running crystal oscillators used in the receivers were replaced by frequency synthesizers driven from the station rubidium vapor frequency standard. This configuration provided the required high stability and phase coherent local oscillator signals. The RF signal is converted to a baseband signal in the 10-MHz telemetry phase detector and further amplified at baseband for processing by the digital data recording system.

The digital processing and recording subsystem (Fig. 2) uses an on-site SDS 920 computer as the major element. This computer normally functions as the digital instrumentation subsystem (DIS) in the standard station configuration.

To process the data of this experiment, it is necessary to add some minor additional external circuitry to the basic DIS. The added circuitry (Fig. 3) consists of a high-speed single-bit analog to digital converter (ADC), a 6-bit shift register, a $\div 6$ counter, and necessary control logic. This external circuitry is connected to the computer Y-buffer.
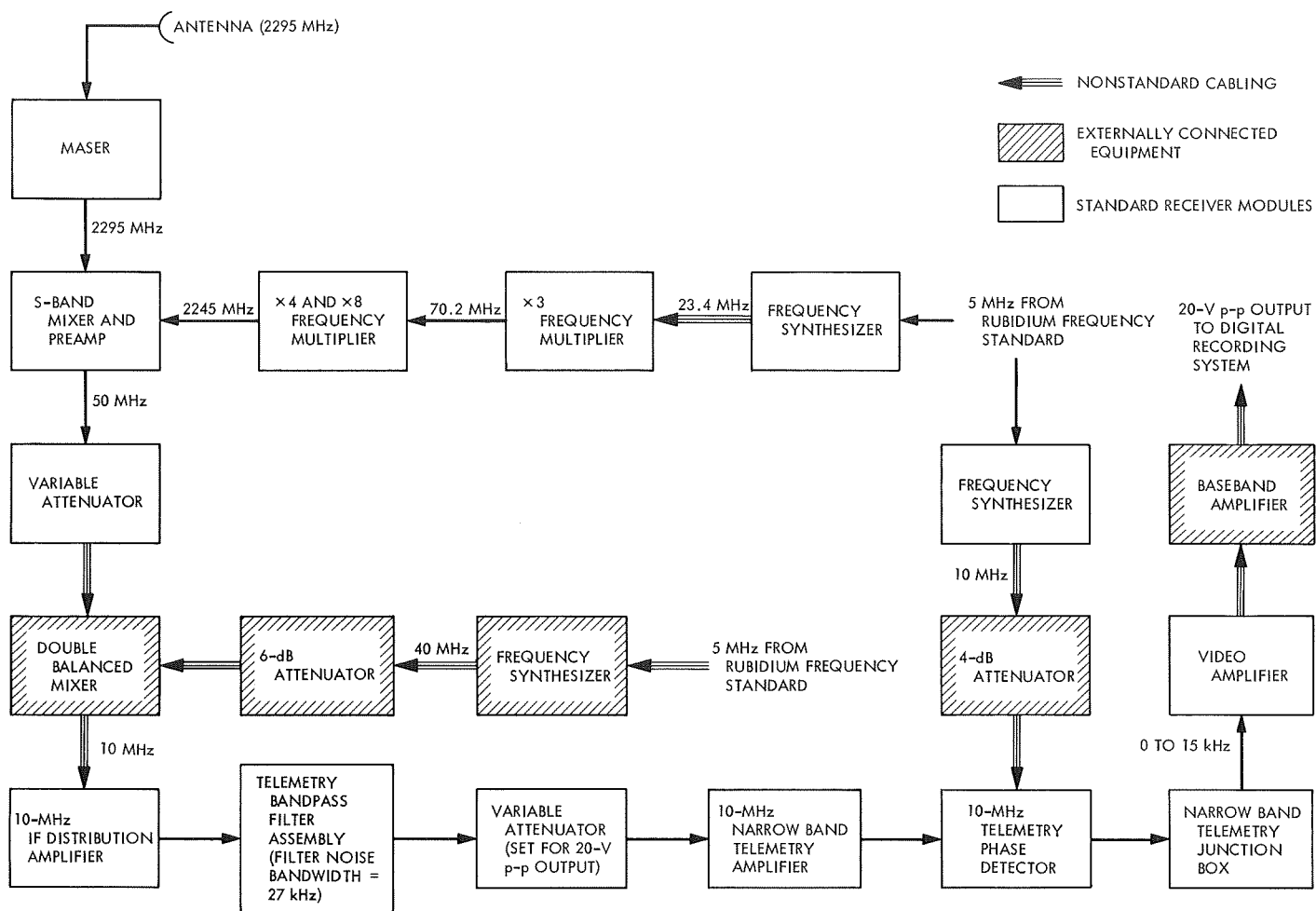
Fig. 1. Analog portion of interferometer system
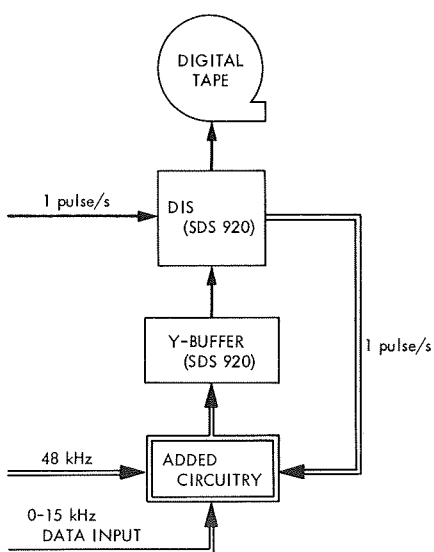
Fig. 2. Digital recording subsystem
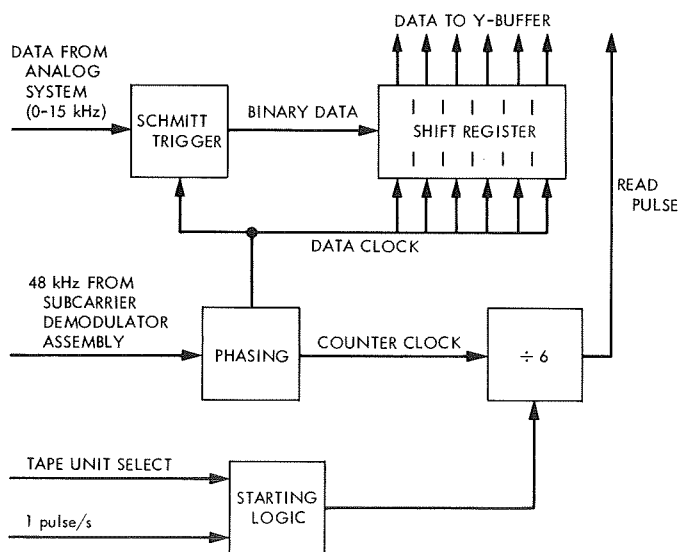
Fig. 3. Added circuitry

The 0 to 15-kHz bandwidth noise spectrum from the analog system is applied to the single-bit ADC and the digitized data are stored in the 6-bit shift register. The 48-kHz sampling frequency clocks the ADC and the shift register and is divided by six to generate a read pulse to transfer the data from the shift register to the computer Y-buffer. The data are then processed by the main computer under control of a special computer program and recorded on magnetic tape at 1-s intervals. One reel of tape can store approximately 12 min of data.

The computer program, as well as the digital recording and processing subsystem, was developed by A. J. Legg of the Space Research Group and was fabricated from spare SDS 920 computer cards.

During this experiment, observations were made on 24 sources and the data are being processed by the experimenters at this time.

Flux measurement observations. The partial results of an earlier (June 1969) VLBI experiment have recently been published (Ref. 3). The DSN facilities that supported this experiment were DSSs 14 and 41. More than 50 sources were observed. In support of this work, additional flux measurements were made on some of these sources on December 30, 1969 using DSS 14. During the December observations, the planet Saturn was detected during a single scan. It is believed that this is the first time Saturn has been detected in this manner.

References

1. Gubbay, J., et al., "Trans-Pacific Interferometer Measurements at 2300 MHz," *Nature,* Vol. 222, No. 5195, pp. 730–733, May 24, 1969.

2. Gubbay, J., et al., "Variations of Small Quasar Components at 2300 MHz," *Nature,* Vol. 224, No. 5224, pp. 1094–1095, Dec. 13, 1969.

3. Cohen, M. H., et al., "Compact Radio Source in the Nucleus of M 87," *Astrophys. J.,* Vol. 158, No. 2, Nov. 1969.

2. An Improved Method of Station Timekeeping, K. Oerke and E. Silva

a. Introduction. Considerable time and effort have been expended to obtain accurate time synchronization and frequency standard drift rates throughout the DSN. The methods used have included the Lunar Bounce Radar Timing System, very low frequency (VLF) reception, portable atomic clocks, Loran C (via MSFN), HF reception, and microwave. Each DSIF submits a weekly timing report so that the timing error factor present in

the tracking data can be accounted for during the tracking data reduction process. The present procedure requires meticulous hourly logging of timing data and weekly reduction of the data to obtain the desired precision. At present, personnel and procedures, rather than equipment, are the weakest link in the chain. The quality of timing data is affected by factors such as personalities, changes of personnel, their acquired knowledge, and station manning schedules, which vary throughout the DSN.

The acquisition of timing data can be automated to obtain consistent, accurate timekeeping. This proposal for automation was developed at DSS 61 with the following restraints:

(1) To keep cost and implementation time at a minimum, only material and modules that are presently available at the station level were used without excessively depleting the station's spares.

(2) Only circuit designs recommended by the computer manufacturer were used.

(3) The method cannot interfere or limit present station capabilities.

(4) Accuracy, dependability, and operational time must all be maximized.

For time synchronization, a time interval counter is the best method for measuring the time difference between standards. Existing counters at the stations for this purpose are not always available and tend to be unreliable in operation if not properly set up. Also, since several standards need to be compared, several counters would be needed or a method developed to multiplex the inputs to one counter. For minimum cost and highest reliability, a binary counter with multiplexed inputs was designed. This simple free-running time interval counter (similar in concept to the millisecond clock in the telemetry and command processor subsystem) can be fabricated from spare computer modules and the spare card cage mounted in the rear of the antenna pointing subsystem (APS) interface rack. The APS was chosen to monitor this counter using its Scientific Data Systems (SDS) 910 computer. Presently this computer is only used in the operational antenna pointing program; therefore, it is possible to automatically log the data needed for time synchronization up to about 98% of the time. The operational program worst-case time utilization is about 80%, which occurs in the seldom used injection condition mode. The computer is down for periodic maintenance for only about 8 h per month. Other computers at the stations are not available for this type of continuous use.

Since the counter does not require computer control, a low priority overfill routine for the APS operational program can sample the counter at random, punch the data on paper tape, and provide an alarm when clock failures occur. It is emphasized that such an overfill routine in no way interferes with the operation of the main APS program. These punched tape data are then reduced periodically on another computer to give daily time synchronization data.

b. Counter theory of operation. The main signal interfaces and the counter control logic are shown in Fig. 4. The counter is a conventional 15-stage binary counter operating as a frequency divider with a sixteenth stage that functions as an overflow indicator.

All counter input signals are conditioned to match SDS logic through either a Schmitt trigger or a logic level converter at the input. Additionally, when a narrow pulse is needed, a single-shot multivibrator (MV) is used. The single-shot MV comprises a differentiator circuit mounted on the interface cable card, followed by a standard SDS amplifier. This is the SDS-recommended solution for obtaining an inexpensive single-shot MV.

The main inputs to the counter are:

(1) The 1-MHz standard DSIF reference which, after being doubled and counted down, provides a time resolution capability of 0.5 μs.

(2) The station master clock at 1 pulse/s (delayed 0.994 s) which starts the counter once during each 10-s period.

(3) The 1 and 2 bits of the tens of seconds of station binary-coded decimal time. These inputs are routed from the APS through the counter interface cable and are used to time multiplex the following four types of stop commands.

(4) The VLF stop command. A 100-Hz square wave from the VLF receiver that is coherent to WWVL is used as a stop command and gives the phase difference between the station's master oscillator and the WWVL reference.

(5) The station time code generator (TCG) stop command. The 1 pulse/s of the TCG can be used as a counter stop command to derive both the time offset of the station secondary clock and the phase

difference between the site primary and secondary frequency standards.

(6) The microwave area clock (UWV). The 1 pulse/s from the UWV area clock is used as a stop command to derive the time offset between the station and area clocks (which can be synchronized via lunar source radar) and the phase difference between the primary DSIF station frequency standard and the area frequency standard.

(7) MSFN (Wing) stop command. The 1 pulse/s from the MSFN Wing, when used as a stop command, gives both the time offset from the station prime clock and the drift rate compared to the MSFN cesium standard. The MSFN clock can be synchronized to Loran C.

(8) Derived from the same source as the multiplexing inputs [see item (3), above], the 8 bit of the units of seconds resets the counter when going true once each 10-s period.

Operation of the counter is controlled by the start enable flip-flop and the control flip-flop. The start count input, a 0.994 pulse, is *and*ed with the reset output of the start enable flip-flop to set the control flip-flop. This arrangement allows only the first 0.994 pulse after the reset pulse to set the control flip-flop. The control flip-flop set output enables the 1-MHz DSIF reference into the doubler. The purpose of the doubler is to obtain a 0.5-μs resolution from the counter. However, only dc-type flip-flops are readily available for use at 2 MHz and the SDS-type dc flip-flops cannot normally be operated as counter stages. The solution adopted is to use a pair of dc flip-flops, one of which forms the counter first stage. The first of the two, referred to as the gating flip-flop, is clocked directly at 2 MHz and enables the second one, which is clocked by the delayed 2 MHz. This second one forms the first stage of the counter. The second counter stage, operating at 1 MHz, and all subsequent stages utilize the standard SDS-type ac-coupled flip-flop modules.

One of the four time-multiplexed stop inputs resets the control flip-flop within the maximum count period of 16383.5 μs. If the stop input is absent, the 8 bit of the units of seconds resets all control and counter stages. A valid readout of the count is only available from the beginning of the first second up to the start of the eighth second of each 10-s period during a minute. This count is converted to negative true logic and applied to the number nine negative true input word of the APS.
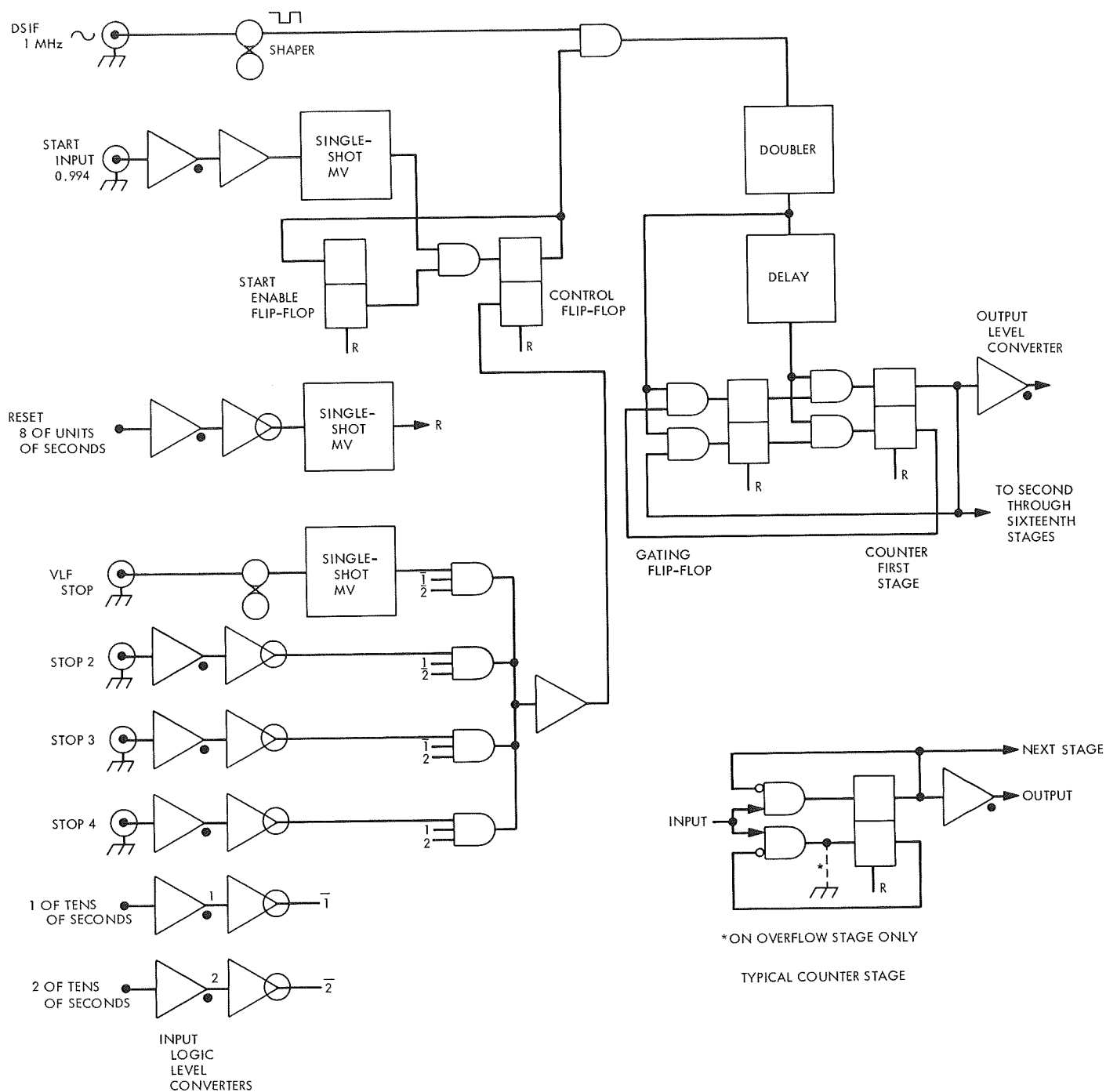
Fig. 4. Time interval counter

The counter output is a 23-bit word that can be accessed by the APS computer under execution of an EOM-30020 command followed by a parallel input command. The time offset data are contained in the 15 low-order bits 8 through 23. Bit 7 is the overflow indicator. Bits 4 through 6 are meaningless and are always zero. Bits 0, 1, and 2 define the source of the stop command for that sample. Bit 3 indicates whether the sample was taken during a valid time period rather than during reset or when counting. Bit 23 has a value of 0.5 μs and the maximum count is 16,282.5 μs. Any period longer than this sets the overflow stage.

Since the counter starts at the end of the 0.994 pulse, there is a time bias of negative 6 ms that allows for clock offsets (from the reference clock) between 6 ms lead and (approximately) 10 ms lag. The overflow indicator will be set by any clock falling outside this range. As clock differences would not normally exceed this range, the overflow counter is a good indicator of a probable clock failure.

The APS test cable, W526 (Test A), is used for interfacing. This cable was originally required for acceptance tests on the APS and is rarely used. Three differentiator circuits are mounted on the cable plug module and do not interfere with the use of the cable for system tests.

c. Programming. The preliminary version of the APS overfill program has successfully demonstrated the concept of time-sharing the APS computer. During program initialization the operating parameters are requested and entered by typewriter. On a low priority basis during normal program idle time, the counter contents are read out and checked. Apparent clock failures are printed out on the APS input–output typewriter. All desired data are stored in APS memory and punched out hourly on tape.

The post-processor program accepts historical data (for previous weeks) and the current week's data from the punched tape. The program checks for continuity of data, and calculates drift rates and clock offset data for each of the timing standards used. The program also compensates for system data anomalies by accepting the operator's evaluation for each specific anomaly. The data outputs from this program are in a format suited for the System Data Analysis group and, furthermore, exceed all the requirements of the present reporting procedure.

B. Facility Engineering

1. Pedestal and Instrumentation Tower Foundation Elements, A. Riewe

a. Introduction. The first 210-ft-diam antenna was installed at DSS 14 of the Goldstone Deep Space Communications Complex. Work has now begun on the fabrication and construction of two additional 210-ft antennas, completion of which will establish the first subnet of 210-ft antenna facilities for the DSIF.

The 85-ft antenna facilities at DSS 42A (Tidbinbilla, Australia) and DSS 61A (Robledo, Spain) are being upgraded to 210-ft antenna facilities. This is the first of a series of progress reports on the 85-ft to 210-ft antenna upgrade project.

b. Design. There is no design as such under this contract. There is, however, a 90-day design review period. This review has been completed by the contractor and all errors and omissions found during this period have been corrected. At the end of this period, the contractor accepted responsibility for all errors and omissions still remaining in the documentation and for antenna performance.

c. Fabrication. Fabrication has been started in all areas except those held by JPL because of planned modification. Examples of this are the reflector and subreflector structure where it is planned to modify the contract to include the tri-cone configuration in place of the present mono-cone system.

Construction. On-site preparation for construction of the 210-ft antenna at DSS 42A started on November 3, 1969. Construction will begin in late spring at DSS 61A.

The initial construction effort will be to excavate for and construct the reinforced-concrete pedestal and the reinforced-concrete instrument tower foundation.

The pedestal of the 210-ft antenna will be a mass reinforced-concrete cylinder with a flat slab top having a concrete collar in the center. The above-grade portion of the pedestal will have the same configuration as the existing 210-ft antenna at DSS 14. The pedestal will be founded 20 ft below finished grade on a 12-ft-wide ring footing. The pedestal walls will be 3 ft 6 in. thick and the total pedestal dead load will be approximately 11,000,000 lb. The pedestal rotation about a horizontal axis for a 45-mph wind has been computed to be 5 arc sec.

The instrument tower will be of reinforced-concrete construction to a height of 35 ft above finished grade. The above-grade portion has the same configuration as the existing DSS 14 antenna. The below-grade portion of the instrument tower consists of a silo-type footing having an outside diameter of 26-ft and an embedment depth of 28.5 ft below finished grade. The rotational motion of the instrument tower about a horizontal axis, due to coupled loads resulting from a 45-mph wind load on the antenna, has been computed to be 1.0 arc sec. The foundation elements of the instrument tower and pedestal are completely separate.

Excavation for the antenna foundations started on November 19, 1969. Dewatering of the foundation area, by pumping from an interceptor trench extending around the perimeter of the pedestal footing and having a diameter on the order of 100 ft, was started on November 25, 1969. Figures 5 and 6 show the excavated area as it appeared on January 5, 1970. Figure 5 shows the antenna excavation in the center foreground with the contractors offices, concrete batch plant, and miscellaneous storage sheds in the background. Figure 6 shows the instrument tower excavation in the center with the pedestal footing staked.

Placement of the instrument tower base concrete was completed on January 27, 1970. The pedestal footing concrete was placed on February 4, 1970. In general, the on-site work at DSS 42A is proceeding on or slightly ahead of schedule.

Due to the presence of ground water, the instrument tower silo footing will be waterproofed by applying a five-ply hot-mopped membrane to the exterior surface of the silo. The waterproofing membrane, which is under the base of the instrument tower, is shown in Fig. 7 prior to placement of reinforcing steel and concrete.

Founding condition. Extensive color photographs were taken of the materials exposed in the foundation excavations and were studied by the foundation consultant, the Donald R. Warren Company of Los Angeles, who did the initial site foundation investigation. Their opinion
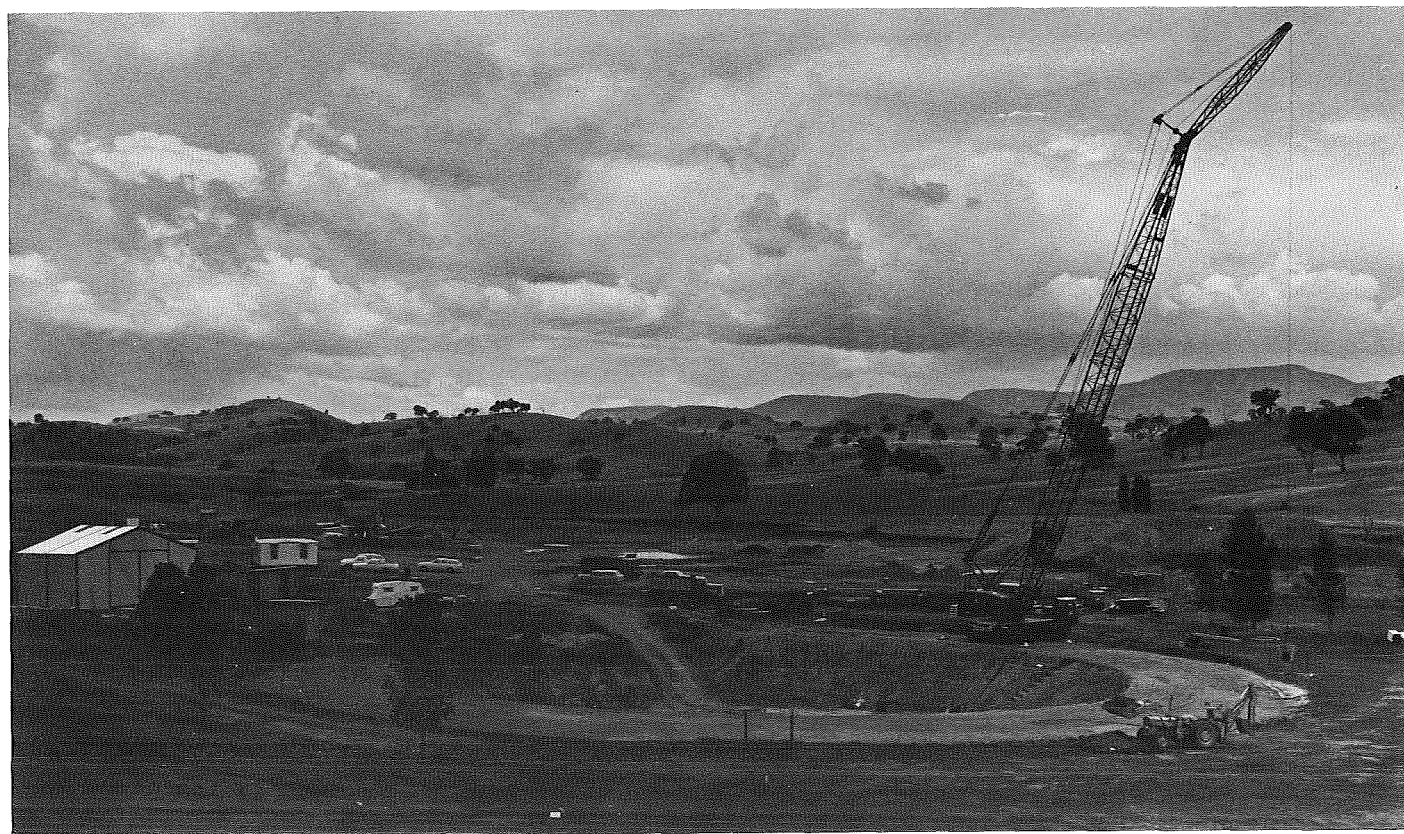
Fig. 5. Construction site and preliminary excavation
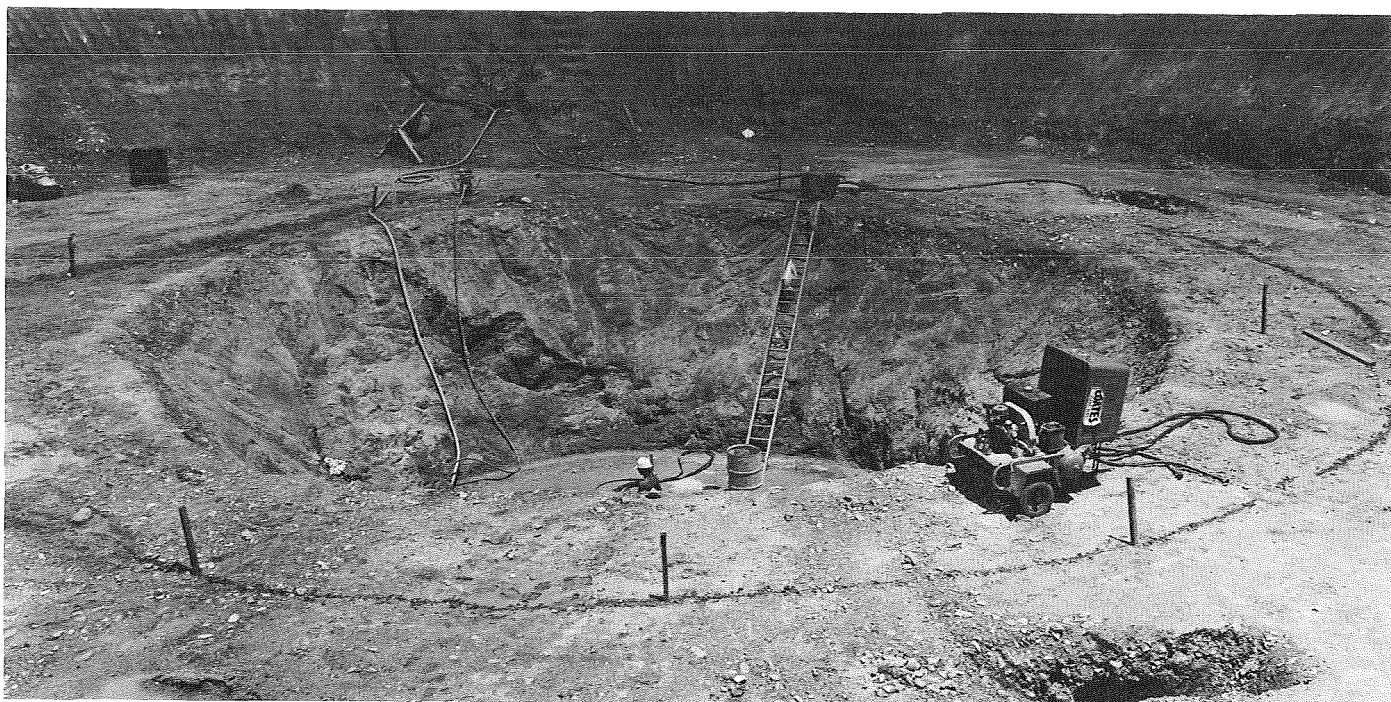
Fig. 6. Pedestal foundation excavation

was that the founding materials exposed in the excavation are representative of those revealed in the test borings, and that the rock joints and fractured zones are generally tighter and less frequent than had been indicated by the test borings. The site is, therefore, somewhat better than had been assumed for the foundation analysis and hence the rotation values are conservative.

Concrete mix design and control. The Snowy Mountains Hydro-Electric Authority Engineering Laboratories, an Australian organization, has been retained by Collins Radio Corp. to design concrete mixes and to control the batching, mixing, and placement of all concrete work on the site. Concrete for construction of the pedestal will be a high-strength, controlled modulus of elasticity mix. The specification requires a minimum ultimate compressive strength of 4000 lb/in.² and a Young's modulus of elasticity concrete is believed to be unique to the 210-ft antenna pedestal design.

Concrete design considerations. The physical properties of the pedestal concrete are governed by requirements of the azimuth hydrostatic thrust bearing which require a very small deflection of the bearing runner under the pad. The runner is grouted directly on the pedestal shoulder and its deflection is a function of the properties of the pedestal concrete. Two specific

requirements were established in the design of the hydrostatic bearing:

(1) The design of the hydrostatic bearing pad and runner and the pedestal were correlated so that their theoretical deflection curves matched within 0.001 in. In the design of the advanced antenna system pedestal, deflection of the runner due to the elastic properties of the concrete was analyzed on the assumption of an edge-loaded plate in a state of plane stress and by a lattice analogy. The runner deflection was analyzed by use of an orthogonal expansion of the flexure equation for a beam on an elastic foundation.

(2) A 0.003-in. maximum was established for the deflection of the runner under the pad due to creep of the concrete under loads to be encountered during construction of the antenna, and before azimuth rotation was possible.

The following additional steps are being taken to minimize the creep problem and to aid in improving long term dimensional stability:

(a) The pedestal wall is designed with extra thickness to minimize stresses.

Fig. 7. Waterproofing instrument tower base

(b) Largest aggregate consistent with feasible placement is used.

(c) A low water–cement ratio is used.

(d) A high cement–aggregate ratio is used.

(e) A low heat cement is used.

(f) Placement and vibration of the concrete will be carefully controlled.

(g) A long wet cure will be provided, followed by special coating to inhibit moisture loss.

Concrete placement control. The specifications for proper placement of concrete are as follows:

(1) Concrete temperature will be limited to not more than 70°F when placed. For air temperatures below 32°F, the surface of the concrete will be required to be protected from freezing.

(2) The concrete will not be allowed to fall freely more than 4 ft. This will require special buckets with long rubber discharge chutes (Tremies) to place the concrete in heavily reinforced areas.

(3) Heavy-duty high-frequency vibrators will be required to disperse the concrete around the reinforcing bars and to fill the forms. The low slump concrete and close reinforcing bar spacing make this a particularly difficult problem.

Inspection sampling and testing will be accomplished as follows:

(1) All materials will be certified by the Snowy Mountains Authority Laboratory.

(2) A minimum of six test cylinders will be taken for each 100 yd³ of concrete placed. Compressive strength tests will be made after 7 and 28 days. Tests will also be made for Young's modulus of elasticity.

(3) Slump tests will be made on each batch of concrete.

Protection and curing will consist of:

(1) Starting immediately, after stripping the forms, the concrete walls and roof deck will be covered with burlap and kept wet for 30 days. After 30 days, the walls and roof deck will be painted with an epoxy base paint.

(2) Construction joints will require special cleaning, wetting, and a modified mix on the next lift to provide plastic concrete at the joint.

Intense rainfalls occurred in the station area on January 17 and 18, 1970, which resulted in flooding of the foundation excavations and caused interruption of the continuous placement of the instrument tower base slab. The water was promptly pumped out and the instrument tower base slab was treated as a cold joint in accordance with JPL specifications prior to continuing the base slab placement. Figure 8 shows the flooded pedestal footing excavation prior to pumping on January 21, 1970.
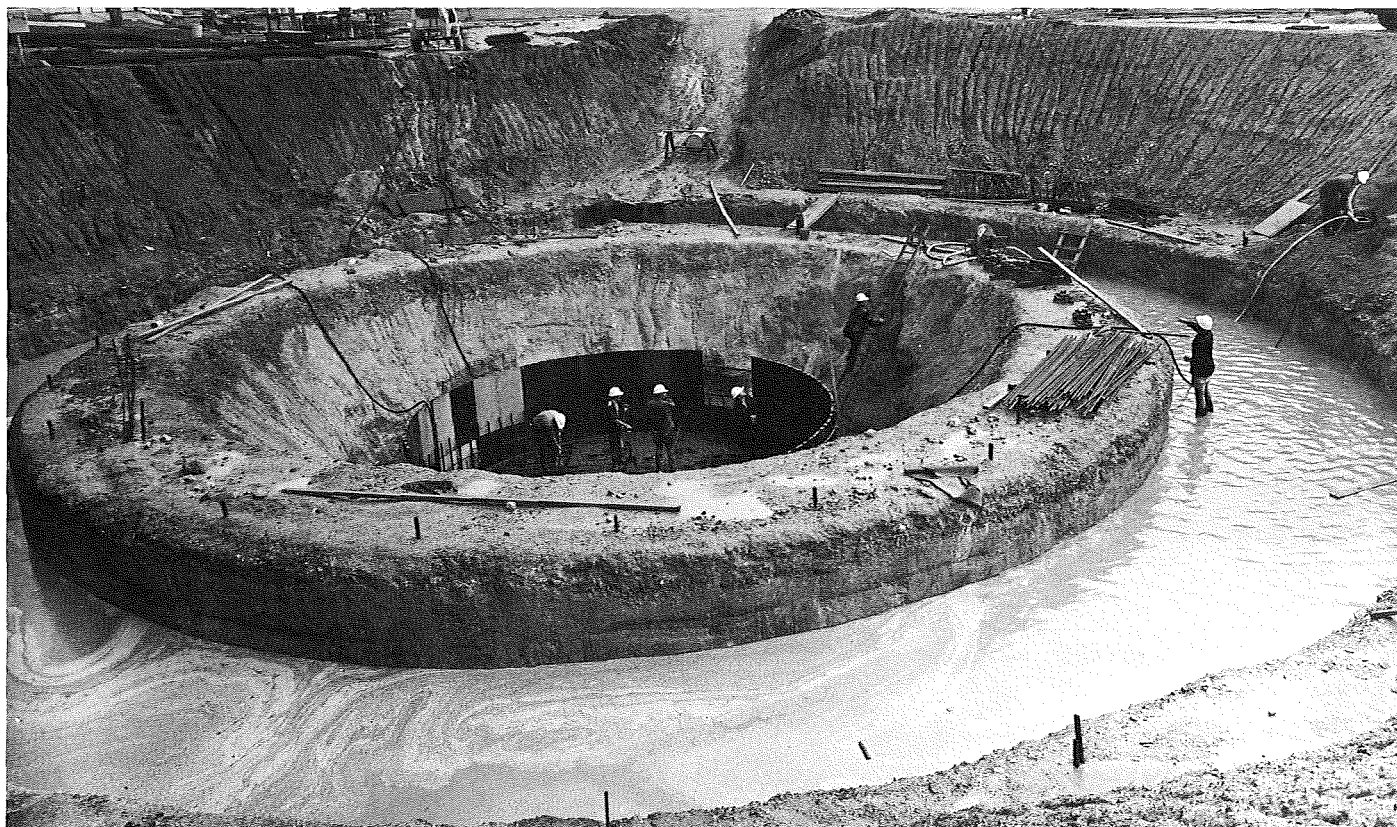
Fig. 8. Pedestal foundation excavation after rain

Subject Index